Seismic monitoring and multiphysics modelling of ground-borne vibrations from small wind turbines

Rachel Fiona Westwood

This thesis is submitted in accordance with the requirements of Keele University for the degree of Doctor of Philosophy in Earth Science

Keele University
March 2012

Do not go where the path may lead. Go instead where there is no path and leave a trail.

Ralph Waldo Emerson

Abstract

Wind energy is planned to play a major role in UK and Scottish Governments achieving renewable energy targets. The Southern Uplands of Scotland are a prime resource for wind and also home to the Eskdalemuir seismological station, a component of the International Monitoring System of the Comprehensive Nuclear-Test Ban Treaty.

Previous work demonstrated that large wind turbines generate vibrations at frequencies significant to Eskdalemuir which are transferred into the ground and can be detected at many kilometres. In order to protect its capabilities, a 50 km consultation zone is enforced around Eskdalemuir for all new wind turbine developments, regardless of size.

In this thesis, an integrated approach combines multiphysics modelling and seismic monitoring to characterise the vibrations from small wind turbines ($<$50 kW) to assess their effect on Eskdalemuir. Four wind turbines, differing in power, hub height and tower structure, have been monitored using a combination of accelerometers and seismometers attached to the tower and buried in the ground at distances up to 200 m from the turbine.

Surface waves are shown to be the predominant wave type originating from the turbines; however, body waves are also present. The waves attenuate at a rate inversely proportional to the distance from the turbine, confirming that the sensors lie within the near-field radiation zone of the tower. Wind speed is shown to affect the tower vibration amplitude differently for each turbine.

Visualisation of the bending modes and radiation patterns in the ground have been obtained through multiphysics modelling and this, together with seismic monitoring, has permitted the frequency peaks in the monitored spectrum to be identified as originating from either the turbine or an alternative source.

Importantly, it has been shown that the algorithm currently used to assess wind farm vibrations around Eskdalemuir may not be suitable for small wind turbines.

Acknowledgements

Firstly, I must thank my supervisor Professor Peter Styles. Thank you for all your encouragement, advice and guidance while I have been at Keele, for your help with fieldwork, trust and belief in me and for reading just about everything I have written while I have been at Keele. I could not have done it without you and I could not have asked for a better supervisor. Thank you.

Sam Toon has been there whenever I needed advice, a laugh or a break (especially if it involved geocaching). For sharing your knowledge with me, being patient and for all your help with fieldwork and Matlab, thank you. I am proud to call you my friend.

I would like to thank the owners of the wind turbines I monitored. Thank you for allowing me access to your wind turbine, for your friendliness and cups of tea. Thanks goes to the manufacturers for initiating contact with the owner and supporting my requests for information.

I am grateful for the assistance from the staff at Keele, especially Dr Ian Stimpson for reading my chapters and providing advice along the way, Dr Jamie Pringle for his ceaseless amounts of encouragement and Dr Stu Clarke for his crash course in Geology. Thanks also to Pauline Weston, Shirley Courthold and Ian Wilshaw for helping with administration related issues and booking vehicles and accommodation for fieldwork and conferences.

Thanks go to Malcolm Wright for his help with fieldwork, your hole digging skills are second to none.

I am grateful to the Earth Science postgraduates that were here at Keele when I started, who made me feel so welcome and with whom I became good friends. To those who have arrived since, thank you for your friendship and support and I wish you the best with your research.

I have been lucky enough to have had my research funded jointly from the Engineering and Physical Sciences Research Council and Keele Acorn and am extremely grateful.

To my friends and family, your support and belief in me has kept me going, especially during my writing-up, thank you.

Mum, Dad, Martin and John, I can't thank you enough, without your love, encouragement and faith in me, this would not have been possible.

Thank you to you all.

Contents

List of Figures

List of Tables

Symbols

α_{dM}	Rayleigh mass damping parameter
β_{dK}	Rayleigh stiffness damping parameter
δ_{k0}	Kronecker delta
ϵ	tensile strain
ϵ_l	Longitudinal extension strain
ϵ_t	Transverse contraction strain
ϕ	the angle of dip
η_{xy}	shear strain
λ	Eigenfrequency of the wave field or wavelength (it will be clear from the context)
ν	Poisson's ratio
θ	the angle of azimuth
ρ	Density
σ	Stress
τ_{xy}	shear stress
ω	angular frequency or angular velocity (it will be clear from the context)
ω_b	central frequency of a bandpass filter
ω_c	the cut-off frequency in a filter

A	the amplitude of a wave or the surface area (it will be clear from the context)
A_0	the amplitude of the signal from the reference turbine at a reference location
A_{far}	signal amplitude from a turbine, at a distant location in the far-field
A_{ij}	predicted signal amplitude at location j from turbine i

A_j	the total predicted amplitude for the entire proposed wind farm
$A_{j,m}$	the total predicted amplitude from turbine m of wind farm j
A_{near}	signal amplitude from a turbine, at a distance close to the turbine
A_{ref}	the reference amplitude used in the Styles et al. (2005) model
A_D	the predicted amplitude of the body waves in the Saccorotti et al. (2011) model
A_R	the predicted amplitude of the surface waves in the Saccorotti et al. (2011) model
A_M	the total predicted amplitude from M wind farms
C_d	drag coefficient
E	Young's modulus
E_d	the maximum or mean energy of a wave
F	a force
F_c	centrifugal force
F_g	gravitation force
G	the Shear modulus
I_t	turbulence intensity
N_0	the number of turbines at the reference wind farm
N_j	the number of turbines at the proposed wind farm
N_M	the proposed number of turbines at Maiden
P_0	the power rating of the reference turbine $\setminus$ wind farm
P_k	the kth spectrogram
P_i	the power of turbine i
P_j	the power rating of the turbine at the proposed wind farm
P_M	the power rating of the turbines at Maiden
Q	the Q-factor, a non-geometric attenuation factor of the wave with distance travelled
R_{far}	the distance from source to the far-field location
R_{ij}	the distance of turbine i from location j
R_{near}	the distance from source to the near location
R_{ML}	the distance from Maiden to LIGO
S_f	the seismic amplitude on the foundation

S_g	the seismic amplitude in the ground at 190/200 m from the turbine
S_r	the seismic amplitude r metres from the turbine
S_t	the seismic amplitude on the wind turbine tower
SS_{res}	the square of the residuals
SS_{tot}	total sum of the squares
T	the period of a wave
V	volume of a material
V_{ref}	wind velocity at reference height
V_h	wind velocity at height h
$\mathbf{K}$	stiffness matrix
$\mathbf{M}$	mass matrix
$\mathbf{S}$	the eigenvalues of the wave field along the diagonal
$\mathbf{V}$	the eigenvectors of the wave field in each column
c	wave velocity
dr	small area on which a force is acting
f	frequency
f_N	Nyquist frequency
g	acceleration due to gravity
k	wave number
n	geometrical spreading coefficient
p	pressure
r	the distance to the wind turbine
r_0	the distance to the turbine producing the A_0 signal
r_i	the distance to turbine i
r_j	the distance to the centroid of the proposed wind farm
t	time
v	velocity

v_0 seismic velocity of the bedrock under the reference turbine

v_i eigenvector describing the shape of the frequency

w wind speed

$\bar{x}$ the mean of x

$\bar{y}$ the mean of y

z_0 surface roughness

Chapter 1

Introduction

In recent years, small wind turbines have become increasingly popular, used by farmers, schools and industry to reduce energy costs and CO_2 footprints.

In the UK, the Southern Uplands of Scotland offer the best resources for wind energy. This is an area of high topography where high wind speeds are prevalent and which lies in close proximity to the main national grid connections between Scotland and England; making the area ideal for both large and small wind turbine developments.

Situated close to Langholm, in the centre of the area, is the Eskdalemuir seismological station (EKA), a component of the Comprehensive Nuclear-Test Ban Treaty (CTBT) International Monitoring System (IMS). The UK is bound by the Treaty to ensure the detection capabilities of the station are not compromised. In February 2004, the UK Ministry of Defence (MoD) introduced a precautionary 80 km exclusion zone around EKA, halting all new wind farm developments within the zone in case they compromised the detection capability of the Eskdalemuir station. This removed a large percentage of the UK's onshore wind capacity.

Subsequently, an Eskdalemuir Working Group was established and the Applied and Environmental Geophysics Research Group at Keele University, funded by the MoD, the Department for Trade and Industry (DTI, now restructured with responsibility passed to the Department of Energy and

Climate Change, DECC) and the British Wind Energy Association (now RenewableUK), were asked to conduct research to investigate the nature and levels of vibration from wind turbines and whether these would interfere with EKA. The study by Styles et al. (2005) focused on twenty-six Vestas V47 660 kW turbines situated on similar geology and topography to Eskdalemuir. The study found that large wind turbines generate vibrations within the frequency band of interest for EKA, which transfer into the ground and propagate many kilometres.

As a consequence of the 2004/5 work, a model was derived to calculate the aggregate vibrational contribution from any planned wind farm in the vicinity of EKA. A maximum permissible aggregate background noise budget of 0.336 nm was introduced and noted by the Comprehensive Nuclear-Test-Ban Treaty Organisation in Vienna. On the basis of the research results and the calculated noise budget, the MoD reduced the exclusion zone to a statutory 50 km consultation zone around EKA (figure 1-1). However, no distinctions were made between different types of wind turbines based on rated power output or hub height.

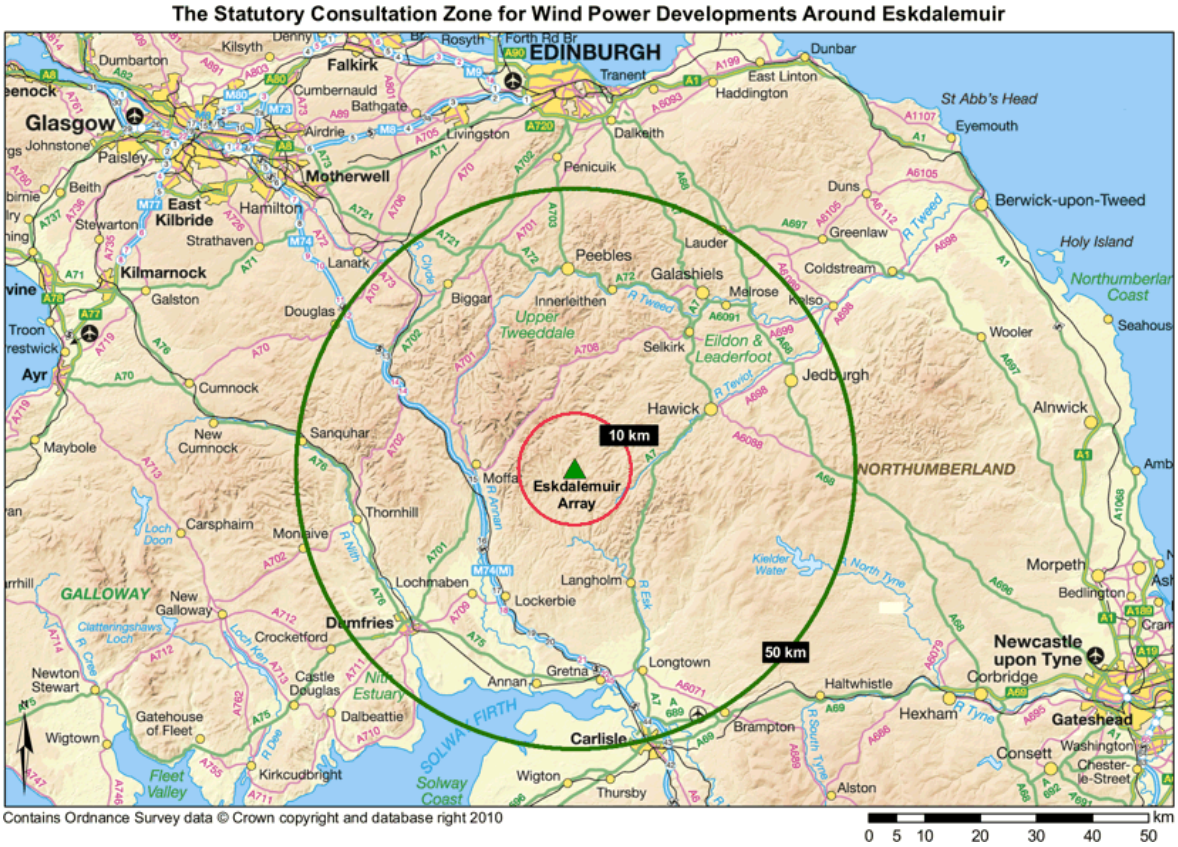

Figure 1-1: *The location of the Eskdalemuir (EKA) seismic station, with the 50 km statutory consultation zone for wind power developments shown by the green circle and the complete exclusion zone at 10 km shown by the red circle.*

1.1 The Eskdalemuir Seismological Station

The Eskdalemuir seismological station is located in the Southern Uplands of Scotland, near Langholm and is a component of the International Monitoring System (IMS) for the Comprehensive Nuclear Test Ban Treaty (CTBT). The CTBT is an international treaty which bans all nuclear explosions, whether for military or peaceful purposes. Although it is not yet in force, the treaty was adopted by the United Nations General Assembly in September 1996. As of the end of February 2012, a total of 182 countries had signed the treaty of which 157 had ratified it, the latest being Indonesia in February 2012 (CTBTO 2012). The Eskdalemuir seismological recording station (EKA) was ratified as an auxiliary station of the IMS in February 2009. It is also a substitute seismic station should a catastrophic failure of a European primary IMS station occur (Bowers 2010, CTBTO 2009).

The array (figure 1-2) consists of twenty broadband seismometers arranged in two perpendicular arms of approximately 10 km long with ten seismometers in each. The two arms cross off-centre at N 55.33° W 003.15° and lie roughly SSW to NNE and WNW to ESE (Güralp Systems Limited 2004).

Each seismometer is housed in a specially constructed pit (figure 1-3). The depths of the pits vary but on average are 2.25 m deep. The base of the pit contains concrete, for levelling, to a depth of 0.15 m . A steel cylinder with 1 m radius sits on top of this and bitumen used to seal it in place. A further layer of concrete 0.15 m deep is placed inside the cylinder and levelled. The cylinder is held rigid at the sides with a concrete back fill and material excavated when creating the pit. A domed lid is bolted in place on top of the cylinder and covered with sandbags (Truscott 1964).

EKA has been operational since May 1962 and has recorded over 400 signals associated (presumably) with nuclear events. The length of operation and geometry of the array means that EKA is the longest serving steerable seismic array in the world (CTBTO 2009).

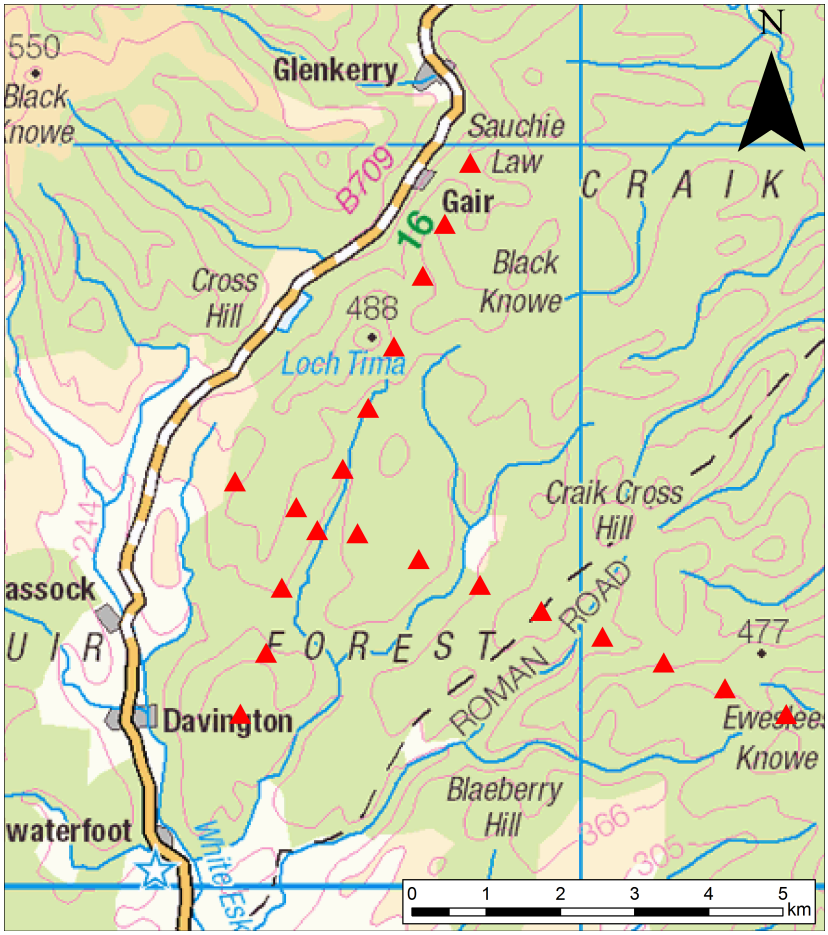

Figure 1-2: *The EKA array geometry, with the individual seismometers indicated by red triangles (Contains Ordnance Survey data. ©Crown copyright and database right 2012.)*

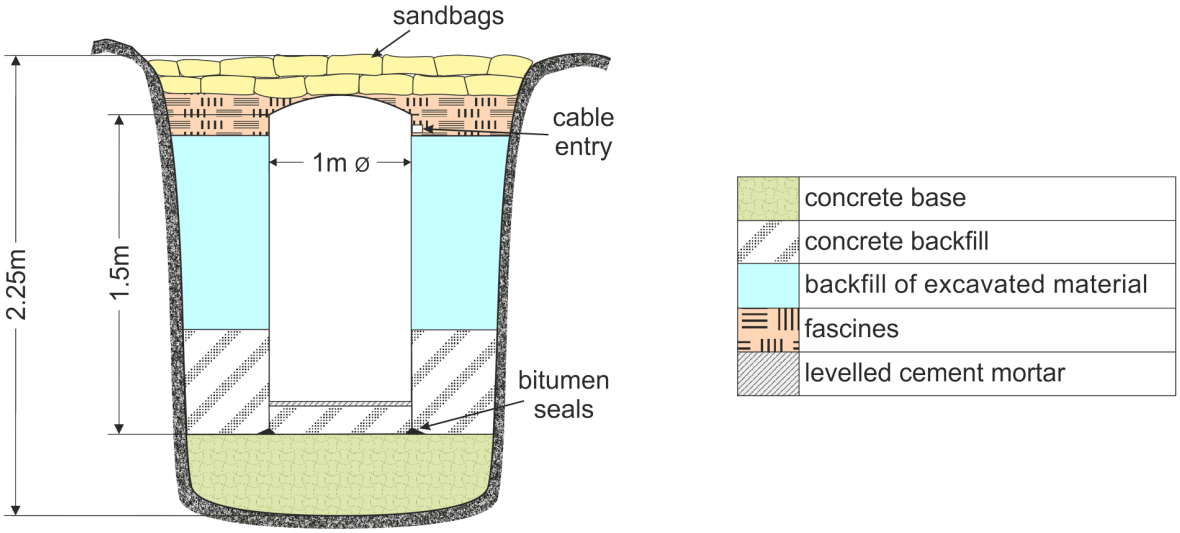

Figure 1-3: *A schematic of a typical seismic pit at EKA (After Truscott 1964)*

1.2 Wind Energy in the UK

The UK government, in line with the Kyoto agreement, has the challenge of reducing carbon emissions in the UK by 60% by 2050. The Scottish Government, more ambitiously, set a target of 80% of the country's energy consumption to be generated from renewable sources and Scottish Renewables (2012) claim that 100% of Scotland's electrical consumption can be generated from renewables by 2020. Wind energy will play a large role in achieving these targets.

On 30 June 2011, there was 5.6 GW of wind capacity (onshore and offshore) operational in the UK and nearly the same again consented and awaiting construction. An additional 3.6 GW were under construction, giving a total of 14.6 GW (RenewableUK 2011b). Of this, 4.2 GW was attributed to operational onshore wind, 1.37 GW under construction and 3.7 GW consented and awaiting construction.

1.2.1 The Small Wind Turbine Market in the UK

There are over twenty manufacturers of small wind turbines in the UK and more abroad. In recent years, demand for small wind turbines has increased considerably, with deployed capacity reaching 14.23 MW in 2010 (figure 1-4), an increase of 65% (5.61 MW) on the previous year (RenewableUK 2011a). In the last two years there has been significant growth in the deployment of 10-20 kW and 50-100 kW machines (figure 1-5). This increase is likely to be due to the introduction of the feed-in tariffs offered by the UK government, which were predicted by RenewableUK (2011a) to further stimulate growth in the small wind market in 2011. The figures for 2011 are not yet available. The values on the graphs in figures 1-4 and 1-5 give the predictions of deployment for 2011 made by RenewableUK.

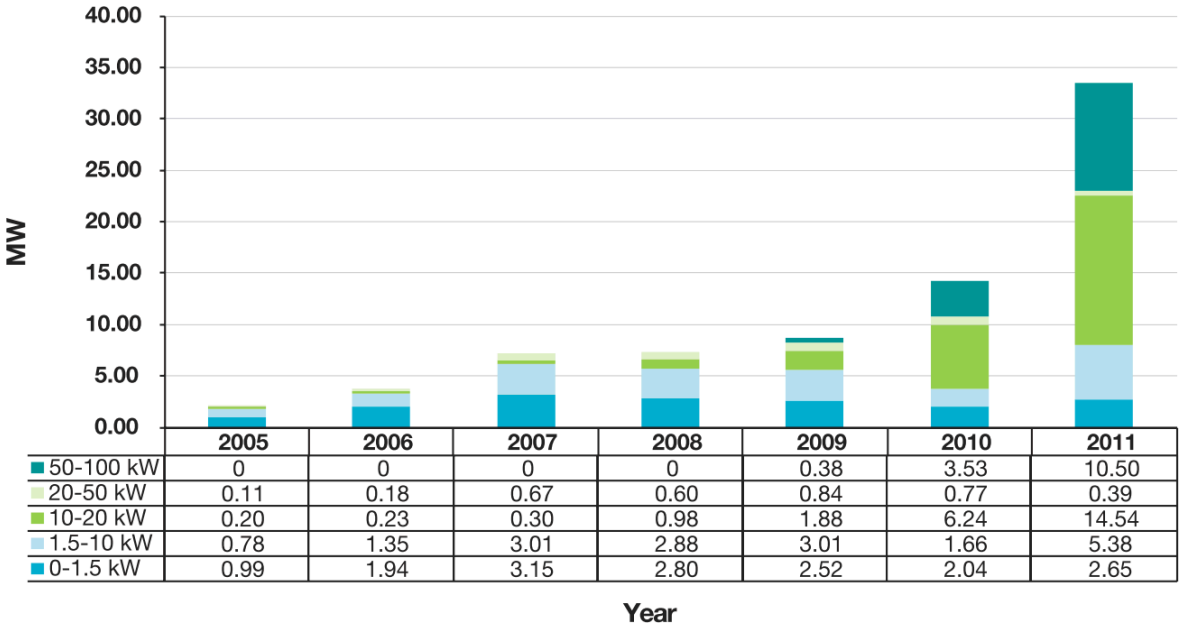

	2005	2006	2007	2008	2009	2010	2011
50-100 kW	0	0	0	0	0.38	3.53	10.50
20-50 kW	0.11	0.18	0.67	0.60	0.84	0.77	0.39
10-20 kW	0.20	0.23	0.30	0.98	1.88	6.24	14.54
1.5-10 kW	0.78	1.35	3.01	2.88	3.01	1.66	5.38
0-1.5 kW	0.99	1.94	3.15	2.80	2.52	2.04	2.65

Figure 1-4: *Annual deployment of small wind turbines in the UK in MW (RenewableUK 2011a)*

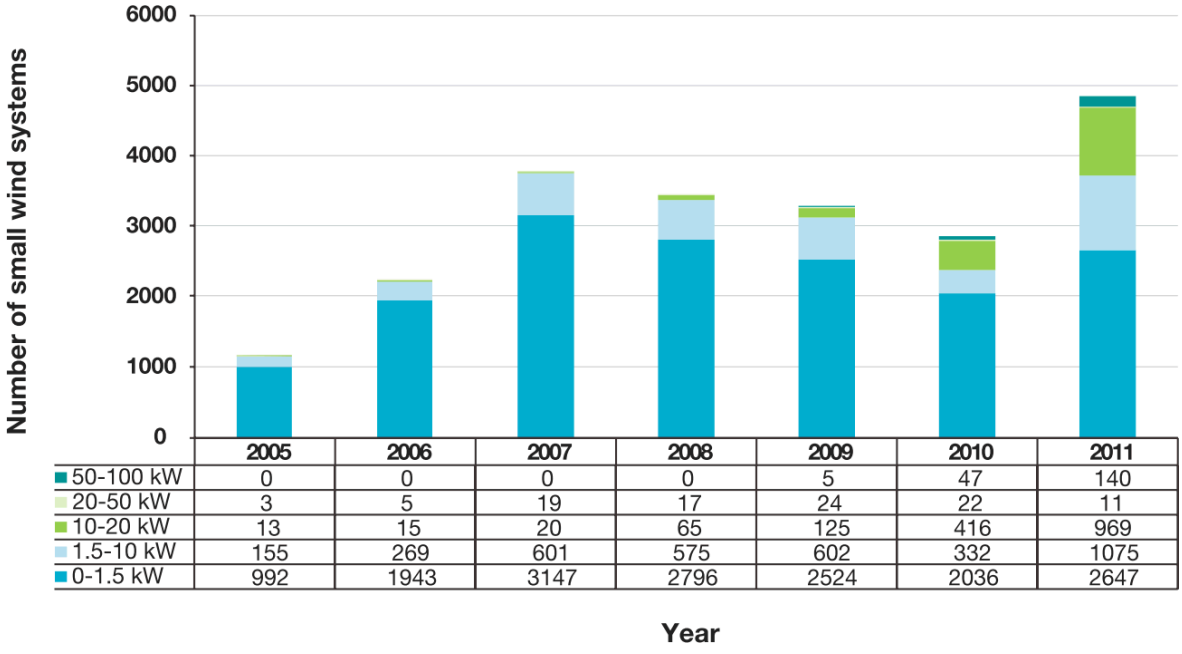

	2005	2006	2007	2008	2009	2010	2011
50-100 kW	0	0	0	0	5	47	140
20-50 kW	3	5	19	17	24	22	11
10-20 kW	13	15	20	65	125	416	969
1.5-10 kW	155	269	601	575	602	332	1075
0-1.5 kW	992	1943	3147	2796	2524	2036	2647

Figure 1-5: *The numbers of small wind turbines deployed annually (RenewableUK 2011a)*

1.2.2 Wind Farms around Eskdalemuir

There are a number of large wind farm developments operational within the consultation zone, with more under construction and in planning (figure 1-6). In addition to these, there are many small wind turbines which are operational or in planning, but are being held up by the restrictions around Eskdalemuir.

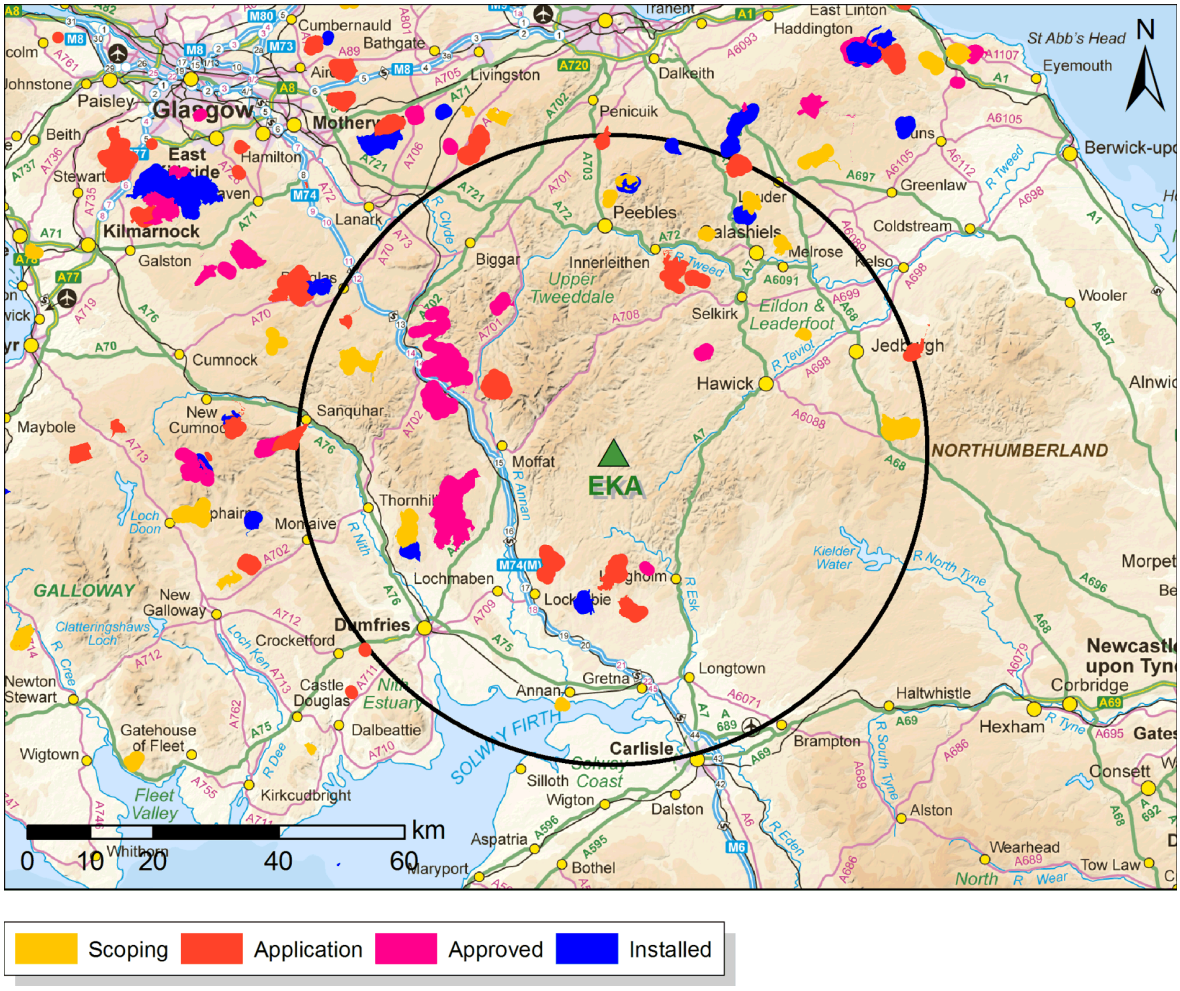

Figure 1-6: *The current number of wind farms around the Eskdalemuir seismological station. The black circle indicates the 50 km consultation zone. (Contains Ordnance Survey data. ©Crown copyright and database right 2012. Wind farm site location obtained from Scottish Natural Heritage (2011))*

1.3 A Brief Introduction to Wind Turbines

A wind turbine is erected for the specific purpose of converting the wind's energy into electricity. This is different to windmills which convert power from the wind into mechanical energy for a specific purpose, such as grinding grain or pumping water. There are arguments over where the first wind turbine originated, some sources (Burton et al. 2001, Endurance Windpower Ltd 2011a) state that it was in America, where Brush constructed a 12 kW DC generator named the "Dynamo" in the early nineteenth century; however, others (Wind Energy Facts 2009, Nixon 2008) claim that it was actually a Scotsman, Professor James Blythe, who in 1887 (shortly before Brush) built a wind turbine, which he installed in the garden of his holiday cottage to power the lighting. Today, wind turbines range in power from a few watts to the current largest, the Enercon E-126, at 7.5 MW and 135 m hub height (Enercon GmbH 2010).

There are two common configurations for wind turbines; horizontal axis wind turbines (HAWT) and vertical axis wind turbines (VAWT). A HAWT has a propeller-type rotor and generator at the top of a tower and depending on whether the machine is upwind or downwind, a tailvane on the downwind side of the nacelle. A VAWT has the main shaft positioned vertically and the generator on the ground (Danish Wind Industry Association n.d.), no tailvane is required as the blades can respond to the wind coming from any direction (BWEA 2005). The wind turbines examined for this research are all HAWTs.

Figure 1-7 shows the inside of the nacelle of a HAWT. Most of the control of the wind turbine is located within the nacelle. As the blades turn, the main shaft operates the generator, which converts the rotation of the shaft to electrical energy using magnetic fields (BWEA 2005). The gearbox increases the speed of the rotor to that required by the generator. However, a gearbox is generally not required for small wind turbines and is becoming less frequent in large wind turbines. Both fixed speed and variable speed wind turbines are available. If the wind turbine is fixed speed, the blades pitch to ensure a constant rotational speed.

A brake is installed as a safety measure and is applied should the wind turbine fail or when the wind speed passes a critical level.

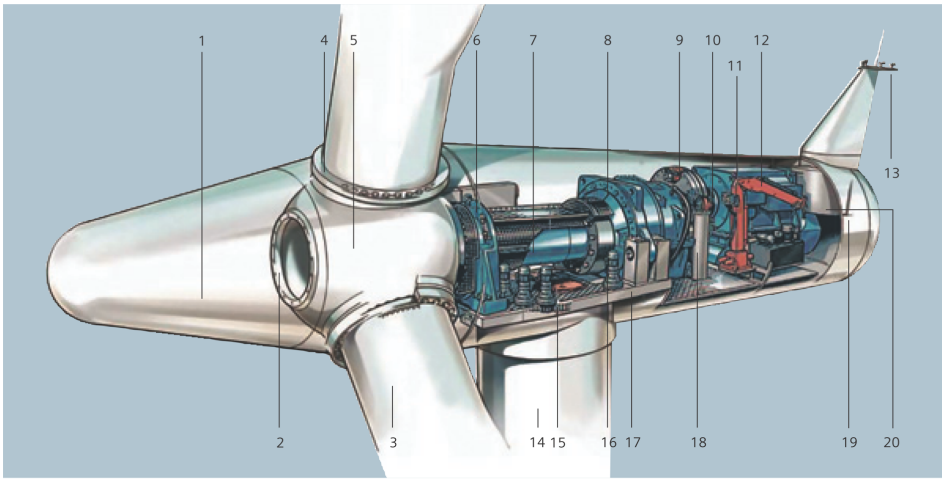

Nacelle arrangement

1. Spinner
2. Spinner bracket
3. Blade
4. Pitch bearing
5. Rotor hub
6. Main bearing
7. Main shaft
8. Gearbox
9. Brake disc
10. Coupling
11. Generator
12. Service crane
13. Meteorological sensors
14. Tower
15. Yaw ring
16. Yaw gear
17. Nacelle bedplate
18. Oil filter
19. Canopy
20. Generator fan

Figure 1-7: *Inside the nacelle of a wind turbine (Siemens 2009)*

The meteorological sensor contains an anemometer which provides wind speed and direction data for controlling the cutting-in and -out of the wind turbine and yawing the nacelle into the wind. Some small wind turbines do not contain this sensor.

Most large wind turbines have three blades and are upwind machines; this means that the blades face into the wind. Small wind turbines vary, with the most popular (including the four turbines investigated for this research) being downwind machines. Those which are upwind generally contain a tail fin which keeps the blades pointing into the wind (Wood 2011).

The IEC Standard for small wind turbine safety, IEC 61400-2, defines a small wind turbine as having a rotor swept area of less than 200 m^2, corresponding to a rated power of around 50 kW. Small wind turbines vary in size and shape (figure 1-8), with the number of blades ranging from two to seven. Some of the main differences between large and small wind turbines are presented in table 1-1.

Figure 1-8: *A selection of small wind turbines. Top left: Gaia-Wind 133. Top right: Proven P35. Middle right: QR5. Bottom right: FuturEnergy Upwind. Bottom left: Skystream 3.7. Centre: Cascade Swift*

	Small wind turbines	Large wind turbines
Siting	Close to the location where the power will be used. Generally only one or two turbines are installed. The area may not be the windiest as proximity to the user is more important.	In windy areas and generally as farms with at least three turbines.
Grid connection	Can be either stand-alone or grid connected depending on the power output of the turbine and the usage requirements of the owner.	Delivers electricity direct to the national grid.
Rotor Configuration	Generally downwind machines	Upwind
Design	Ranges greatly in blade number, nacelle design and tower construction - lattice and tubular towers are available, some tubular towers have internal flanges, some external, others are interlocking, etc.	Generally tubular tower with three blades.
Cost	A few thousand pounds	Hundreds of thousands to millions of pounds
Technical Differences		
Control	Variable pitching system is employed or no pitching system, due to cost. Generator resistive torque must be overcome before the blades will start to turn. The wind turbine brake must be applied manually at the turbine.	Pitch control is generally used to change the angle of attack of the blades. The wind turbine can also be started and stopped remotely.
Yaw drive	Free yaw using a tail fin or downwind blades due to costs	Complex yaw drive mechanism to keep the blades and rotor aligned to the wind.

Table 1-1: *Some differences between large and small wind turbines. (Data obtained from BWEA 2005, Wood 2011, Manwell et al. 2002)*

1.4 Aims and Thesis Outline

This research aims to examine the vibrations from a selection of small wind turbines to find out if they behave in the same way as large wind turbines and whether the vibrations they generate will adversely affect the detection capabilities of EKA. In order to do this, two approaches will be combined: seismic monitoring and multiphysics modelling.

In order to achieve these aims, four wind turbines with different specifications will be monitored, to investigate tower structure and the differences between variable and fixed speed. A selection of analyses will be performed to determine the characteristics of the vibrations. Two of the turbines will be modelled using multiphysics software to examine whether multiphysics modelling can replace monitoring or whether it should be used to complement it in order to obtain additional information.

1.4.1 Thesis Structure

This chapter sets out the aims of the research and provides information on the background to the project. A brief introduction on wind turbines is presented and the main differences are highlighted between large and small wind turbines.

Chapter 2 provides details of background information required for this thesis. Wave theory is explained first, covering harmonic waves with necessary definitions and seismic waves. Elasticity coefficients, with specific emphasis on those required for the finite element modelling of a solid structure are described, before an overview is presented on finite element analysis and the stages of the technique. The two analyses used during modelling are also explained. Aspects of signal processing relevant to this thesis are discussed, including Fourier Analysis, filtering and generating a power spectrum density function using Welch's method. The chapter concludes by looking at the different loads which are present on wind turbines.

A review of previous work related to wind turbine monitoring is provided at the start of chapter 3, followed by a discussion of the findings from each and comparisons between them. The second part of the chapter reviews previous seismic monitoring work around scientific installations.

Details of the equipment, deployment and data processing techniques required for monitoring are provided in chapter 4 and details of the monitoring experiments presented in chapter 5. Chapter 5 is split into sections; one for each turbine, with details of the turbine, test site and results provided in each.

Analysis of the results from chapter 5 is given in chapter 6. In this chapter the effect of tower structure is explored, followed by an analysis of how wind speed affects amplitude. This is considered for both seismic amplitude on the tower and in the ground. The attenuation of the signals from the wind turbine is derived and the wave type explored using polarisation analysis. The chapter ends with a discussion of the techniques and the findings.

Multiphysics modelling is introduced in chapter 7, where a review of previous work involving finite element modelling of wind turbines is presented. An overview of the Comsol modelling software follows, with specific focus on the elements required to model a wind turbine.

Chapter 8 provides a description of the models, examining the build up of a model from a simple hammerhead to a full wind turbine with blades, foundation and the surrounding ground. Two wind turbines are modelled; one with a tubular tower and the other a lattice tower. The effects of soil and bedrock layers in the model are also investigated. A discussion of the models and the results concludes the chapter.

Chapter 9 concludes the thesis, summarising the research and detailing the application of the findings. Recommendations are provided on areas for further work and the implications of the results with respect to the Eskdalemuir seismological station.

Chapter 2

Background Theory

This chapter aims to provide a detailed understanding of the theory required for this thesis. Section 2.1 introduces the concept of wave theory beginning with an explanation of the harmonic wave and its properties before moving on to discuss the different types of wave which propagate through the ground, how they do so and how they attenuate, which is a key area for this thesis.

The elasticity coefficients (section 2.2) of a material describe its stress and strain relationships. These coefficients are particularly relevant to multiphysics modelling where they are used to describe the physical properties of each element within the model. The section on Finite Element Analysis (FEA) presents a brief overview of the Finite Element Method used to ascertain the modal vibrational frequencies of a wind turbine model. The field of FEA is vast and emphasis in this section is on eigenfrequency and frequency response analysis.

The techniques and algorithms required to analyse the data gathered from monitoring a wind turbine are presented in section 2.4, including Fourier Analysis and generation of a power spectrum using Welch's method.

Finally, section 2.5 describes the three main sources of loads on a wind turbine.

2.1 Wave Theory

A wave is a disturbance in both space and time, transferring energy from one point in space to another (Coulson & Jeffrey 1977). Mathematically, a propagating wave is described by a function in the form $f(x \pm ct)$, where x is the origin of the wave and ct is the distance the wave has travelled over time t with speed c. This is a general form for a wave travelling in one dimension and not changing shape.

A harmonic or sinusoidal wave is one of the simplest types of wave and takes the form

$$f(x,t) = A\, e^{i(\omega \pm kx)} = A\, \cos(\omega t \pm kx) + Ai\, \sin(\omega t \pm kx). \tag{2.1}$$

The harmonic wave is characterised by its amplitude, A, angular frequency, ω, and wavenumber k. Consider a simple harmonic cosine wave with

$$f(x,t) = A\cos(\omega t + kx). \tag{2.2}$$

The phase of the wave is described by (kx) and when constant, the value of $f(x,t)$ is constant. The wavenumber describes how the wave oscillation repeats in space per unit length of time. The wavelength, λ (figure 2-1), indicates the distance between two corresponding points in the cycle of a wave. They are related by the equation

$$\lambda = 2\pi/k. \tag{2.3}$$

As wavelength is a distance, measured in centimetres (cm) or metres (m), by equation (2.3) the wavenumber is the inverse measured in cm^{-1} or m^{-1}.

Adjusting the value of kx results in a shift in the position of the wave, with a complete cycle shift equating to a value of 2π and representing no difference in the appearance of the wave. A shift of $-\pi/2$ ($\pi/2$ to the left) produces a sine wave.

The period of a wave (figure 2-1), T, describes how the wave oscillates in time. It is defined by the equation

$$T = 2\pi/\omega, \tag{2.4}$$

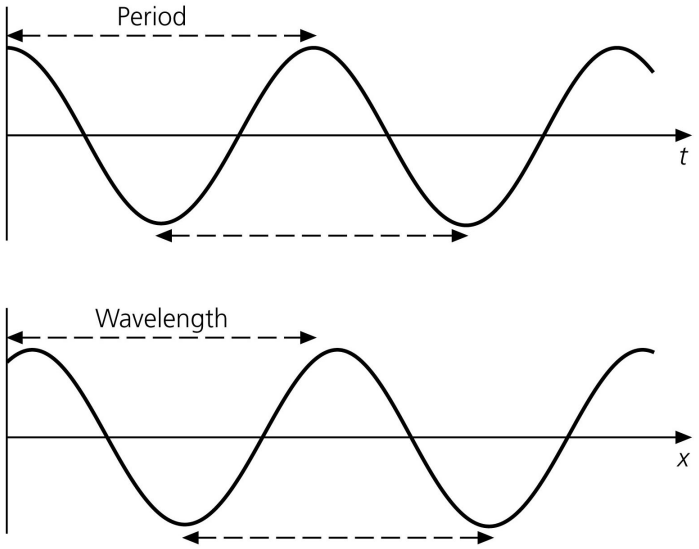

Figure 2-1: *A harmonic wave as a function of time (top) with a fixed position and as a function of position with a fixed time (bottom) (Stein & Wysession 2002).*

and is inversely related to the frequency of the wave by the equation

$$f = 1/T = \omega/(2\pi). \tag{2.5}$$

The angular frequency of the wave is measured in SI units of radians per second (or Hz), meaning the period of the wave has the unit of time (seconds).

The velocity of the wave is the ratio between the angular frequency and wavenumber

$$v = \frac{\omega}{k}. \tag{2.6}$$

2.1.1 Wave Propagation Through the Ground

A seismic wave is generated whenever there is a burst of energy in the ground, such as an earthquake or an explosion. There are two main types of wave which propagate through the ground; body waves and surface waves. Body waves travel through the interior of the Earth, following a path determined by the density and stiffness of the material they are travelling through. Surface waves, as the name dictates, travel along the surface of the Earth and are slower than body waves.

2.1.1.1 Body Waves

Body waves can be either longitudinal or shear (transverse) waves (figure 2-2). Longitudinal waves are compressional and dilational along the direction of propagation, these are known as P (primary) waves and are the first prominent wave to be seen on seismograms. The shear wave, which is not compressional, causes shear of the material it is passing through perpendicular to the direction of propagation. These waves are known as S (secondary) waves and are the second type of wave to be seen, after the P wave (Gubbins 1990, Udías 2000).

Shear waves which are horizontally polarized, with displacement parallel to the Earth's surface are defined as SH. Vertically polarized shear waves, where displacement is in the vertical plane, perpendicular to the Earth's surface are defined as SV. When interacting with a horizontal boundary, P and SV waves couple together, whereas SH waves remain separate (Stein & Wysession 2002). The energy of the waves, which spread three dimensionally, decay with distance r at a rate of $r^{-0.5}$, due simply to geometrical spreading.

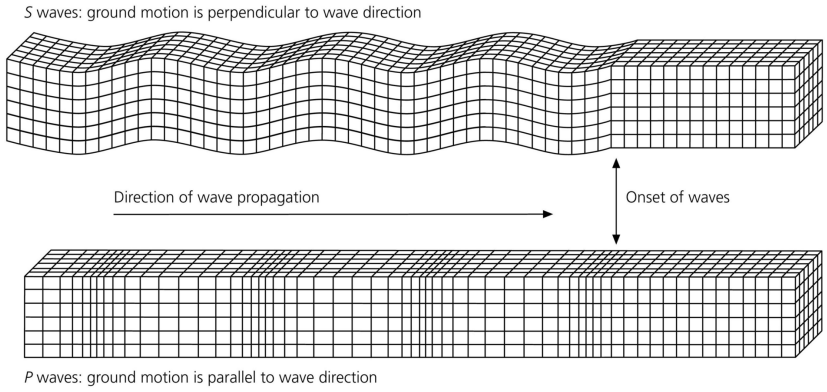

Figure 2-2: *Examples of body waves. The top image is an example S wave and the bottom image a P wave (after Stein & Wysession 2002).*

2.1.1.2 Surface Waves

Surface waves propagate along the surface of the Earth, with their energy spreading two dimensionally and decaying with distance r from the source at approximately r^{-1}. There are two types of surface wave; Love waves and Rayleigh waves (figure 2-3).

Rayleigh waves are named after John William Strutt, Lord Rayleigh (1887) who first predicted their

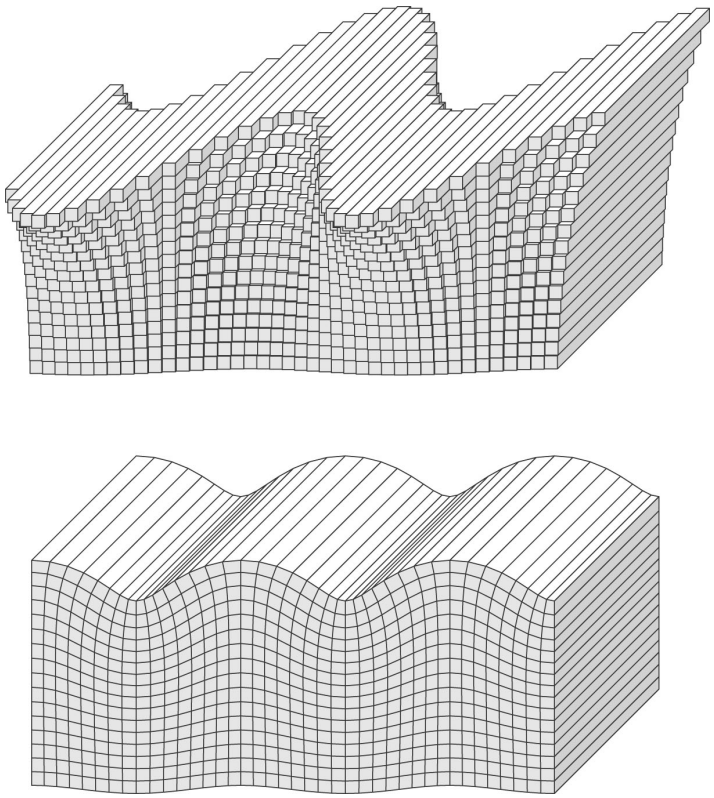

Figure 2-3: *Love (top) and Rayleigh (bottom) waves for horizontal propagation across a surface (Shearer 1999).*

existence. They are formed by the coupling of two inhomogeneous P and SV waves (Shearer 1999) along a free boundary and contain both radial and vertical motion. The motion of a Rayleigh wave is elliptical, changing from retrograde (anticlockwise) at the surface to prograde (clockwise) at depth and passing through a point at which there is no horizontal motion (figure 2-4). This is caused by the horizontal and vertical components of the wave being shifted in phase by 2π (Shearer 1999, Udías 2000).

A Love wave consists only of transverse motion and is formed by the constructive interference of SH waves. In order for Love waves to occur, the velocity of the structure the wave is passing through must vary with depth, therefore Love waves cannot exist in a uniform half space, whereas Rayleigh waves can. The simplest geometry for a Love wave to occur would be a layer of material with finite thickness and velocity underlain by a half space.

For both Rayleigh and Love waves, the amplitude of the wave decreases with depth.

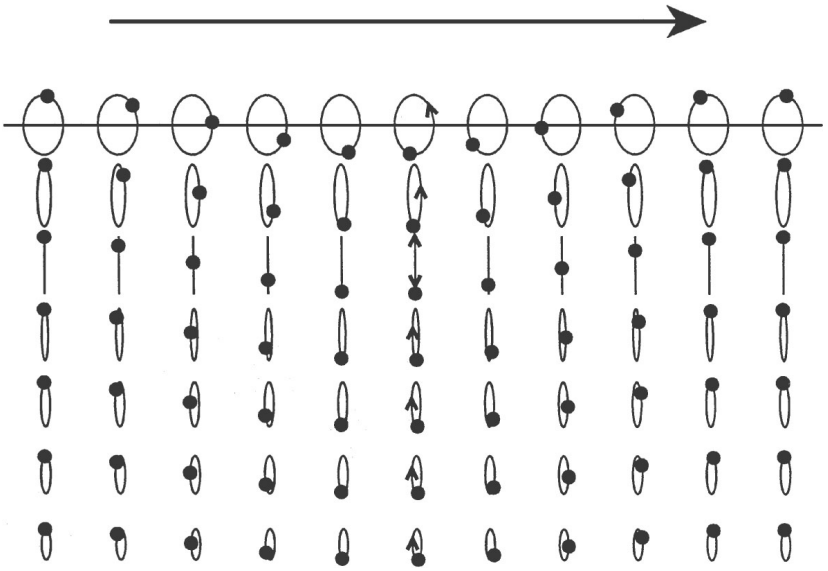

Figure 2-4: *The particle motion for a Rayleigh wave propagating from left to right (Shearer 1999). The dots represent a fixed point in time.*

2.1.1.3 Attenuation

A seismic wave will spread out from the source over a spherical wave front. The area of the wave front at the surface increases proportionally to the radius ($A = \pi r^2$). The energy in the wave front will vary as the wave expands and contracts. This is known as geometrical spreading. A surface wave propagating along the surface of the Earth will have an energy decay at a rate of r^{-1}, where r is the radius of the wave front and an amplitude decrease of $r^{-0.5}$, as the amplitude is proportional to the square root of the energy (Stein & Wysession 2002).

A body wave, which expands with a spherical wave front (spherical spreading) has an area of $4\pi r^2$. This means that the energy within the wave front decays at r^{-2} and the amplitude decreases at r^{-1}. Geometric spreading will be the sole mechanism if the material is homogeneous and non-dissipative. However in reality, this is not the case (Wilson 1994) and additional terms should be included to take into account, for example, loss of energy through the ground or internal friction causing additional decay on the signal. This absorption is related to the dimensionless quality factor, Q, which represents the ratio of the amount of energy dissipated per cycle of harmonic motion, ΔE_d, with frequency ω to the maximum or mean energy, E_d, accumulated during the same cycle. It is defined as (Udías 2000)

$$\frac{1}{Q(\omega)} = \frac{1}{2\pi}\frac{\Delta E_d}{E_d}, \tag{2.7}$$

This is an inverse relationship, meaning that low Q areas attenuate more than high Q areas. For $Q \gg 1$ then the attenuation of the seismic wave can be defined as (Shearer 1999)

$$A(x) = A_0 e^{-\omega x/2Qv}, \tag{2.8}$$

where v is the velocity of the wave and x is the distance the wave has propagated.

When considering the propagation of signals from wind turbines, three attenuation models are usually considered. The first is the $1/\sqrt{r}$ model with linear attenuation and is typical of propagation at the surface of the ground. The $1/\sqrt{r}$ model (no linear attenuation) is similar but lacks the attenuation component, and a $1/r$ model, typical of propagation through the air. Further discussion of these models and the previous works which have considered them can be found in section 3.1.

2.2 Elasticity Coefficients

Hooke's Law states that the displacement of an elastic material is proportional to the force applied upon it. The law is defined by the equation

$$F = -kx, \tag{2.9}$$

where F is the force, x the displacement of the material and k is the spring constant. A material which obeys Hooke's Law has properties known as the elastic moduli, which relate the stress and strain of the material. Some of these moduli are particularly relevant to engineering geophysics, including the bulk modulus, shear modulus, Young's modulus and Poisson's ratio. When modelling a wind turbine in multiphysics software, Young's modulus and Poisson's ratio (along with the density) provide the material properties in an element of the model. Although Young's modulus is generally easy to obtain, it can be calculated in terms of Poisson's ratio and either the bulk modulus or shear modulus. Each of these four properties are described in more detail in the following sections.

2.2.1 Bulk Modulus

The Bulk modulus, K, is the measure of a material's resistance to uniform pressure (compressibility) and is measured in Pascals. It is defined by the equation

$$K = -V\frac{\delta P}{\delta V}, \tag{2.10}$$

where P is pressure and V is the volume of the material.

2.2.2 Shear Modulus

The shear modulus, G, is the measure of a material's resistance to a shear force. The modulus is a ratio of shear stress to shear strain (figure 2-5). Shear stress is the magnitude of the force per unit area of the sheared face, defined with the equation

$$\tau_{xy} = F/A. \tag{2.11}$$

Shear strain is the amount of movement per unit length of the sheared face and is defined with the equation

$$\epsilon_{xy} = \Delta x/L. \tag{2.12}$$

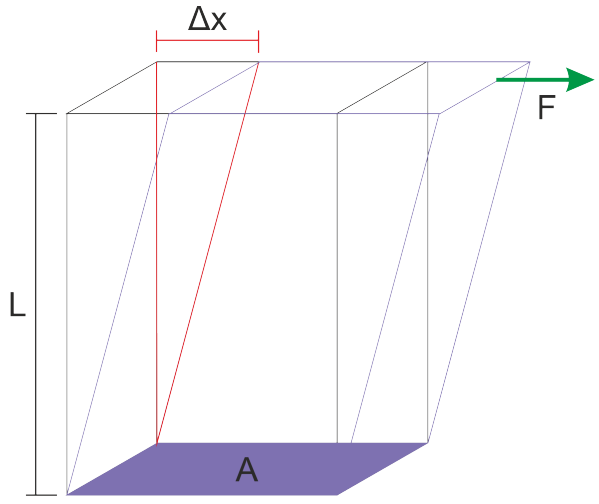

Figure 2-5: *The variables required in order to calculate the shear modulus*

Hence the shear modulus is defined as

$$G = \frac{\tau_{xy}}{\epsilon_{xy}} = \frac{F/A}{\Delta x/L} = \frac{FL}{A\Delta x}. \tag{2.13}$$

The more rigid the material, the larger the modulus will be, as it will require a larger force to displace the material by the same amount.

2.2.3 Poisson's Ratio

Poisson's ratio, ν, is the ratio of transverse contractional strain to longitudinal extensional strain, that is the transverse strain normal to the applied load to the axial stain in the direction of the applied load. For example, if a cylindrical bar is stretched it will increase in length but decrease in diameter. Possion's ratio provides the relationship between the two changes. It is defined by the equation

$$\nu = -\frac{\epsilon_t}{\epsilon_l}, \tag{2.14}$$

where ϵ_t is the transverse contractional strain and ϵ_l longitudinal extension strain. Normal materials generally have a positive ratio value. This is because most materials resist the change in volume when stretched, as determined by the bulk modulus, more than they resist the change in shape, as dictated by the shear modulus.

When applied to wave propagation, the Poisson's ratio of a material influences the speed at which a wave will propagate through it.

2.2.4 Young's Modulus

Young's modulus is the ratio of stress to strain and measures the stiffness of a material. It is defined by the equation

$$E = \frac{\sigma}{\epsilon}, \tag{2.15}$$

where σ is the tensile stress and ϵ is the tensile strain. Young's modulus is measured in pressure units (Pascal in SI) as stress is a pressure but strain is dimensionless.

By the theory of elasticity, Young's modulus is related to the bulk modulus, K, and shear modulus, G, by the equations (Matthews et al. 1997)

$$K = \frac{E}{2(1-2\nu)} \tag{2.16}$$

and

$$G = \frac{E}{2(1+\nu)}, \tag{2.17}$$

where ν is Poisson's ratio.

2.3 Finite Element Analysis

Finite Element Analysis (FEA) is the practical application of the Finite Element Method (FEM), which finds approximate numerical solutions to complex partial differential equations. It is based on the idea of replacing a complex continuous function with smaller simpler and more manageable pieces. FEA was first used to solve structural engineering problems by Hrennikoff (1941) and McHenry (1943) and the term 'finite elements' was first introduced by Clough (1960). However the principles had been used much earlier by geometers to calculate the approximate value of π (Davies 1980).

The technique is now used in many other fields including chemical engineering, electromagnetics and earth sciences. Many commercial computer packages exist to solve problems using FEA in a user friendly manner and combine physics, for example solving a problem which combines acoustics and structural mechanics simultaneously, rather than approaching the problem in two stages. The software used in this thesis is Comsol, a multiphysics modelling package (see section 7.2).

The field of FEA is vast and it is beyond the scope of this thesis to provide detailed information into the mathematics and various techniques which can be applied. This section presents a general summary of the method with emphasis on the areas relevant to the modelling of a wind turbine. For

more detailed information on FEA see Davies (1980), Oden (1981), Cheung & Yeo (1979), Comsol Multiphysics (2008a).

Mathematical models are a theoretical representation of a real-world scenario. The generation of a computational model allows the outcome of a real world situation which is rare or undesired in the real world to be viewed. The model is a simplified version of the real world object, as computational power and time versus accuracy must be considered. The more complex the model, the longer it will take to compute the results. Three dimensional models for FEA can be generated in a computer aided design (CAD) package and imported into the solver software or created directly in the solver software if it contains a CAD module.

The process of FEA is divided into four steps

1. Divide the mathematical model into finite elements and nodes.
2. Specify the physical behaviours of each element (boundary conditions and material properties).
3. Solve the system of equations for each node (eg displacement, velocity).
4. Calculate any desired quantities for each element (eg stress, strain).

2.3.1 Finite Elements

Each finite element is considered individually and does not overlap with any other element. The overall mathematical model is solved approximately by connecting all elements and nodes. Each individual element has a set of properties associated with it, which a computer solver will use to perform the necessary calculations. These are (Felippa 2010):

- Dimensionality - each element can have one, two or three dimensions and a model can be constructed from a mixture of elements with different dimensions. For example, a 1D bar can be used to construct a model in 2D or 3D.
- Nodes - nodes define the geometry and are usually located on the corner or end of the element (see figure 2-6).

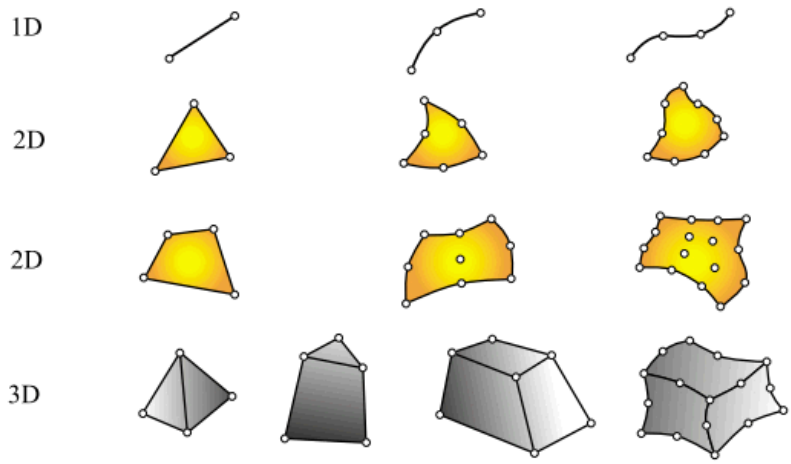

Figure 2-6: *An example of possible finite elements in one, two and three dimensions (Felippa 2010)*

- Geometry - generally most elements have fairly simple geometry. In one-dimension, this could be straight lines or curves, in two-dimensions, a triangle or quadrilateral and in three-dimensions, a tetrahedra, pentahedra or hexahedra (see figure 2-6).
- Degree of freedom - this is the state of the element and defines the way forces are transmitted through nodes. For example, two beams connected together will behave like a welded joint and will transmit three forces (one axial, two shear) and three moments (one torsion and two bending). Whereas a beam connected to a truss will only transmit one force (axial).
- Engineering properties - these specify the mechanical behaviour of the element and include Young's modulus and Poisson's ratio (see section 2.2).
- Fabrication properties - These are mechanical properties linked to the fabrication of the element. For example, the cross-section diameter of a beam or the thickness of a shell.

2.3.2 Boundary Conditions

Boundary conditions (BC) are important to the way a solver manages what happens at a boundary or interface within a model. One of the main functions of a boundary condition is to set constraints on the boundary which affect the amount of the displacement the boundary can have, for example, the boundary may be rigid and fixed and not move at all or only have movement in one direction.

The multiphysics modelling package, Comsol (section 7.2) has a choice of two types of BC; Dirichlet

conditions or generalised Neumann conditions. Dirichlet conditions specify the value of the solution on the boundary. For an ordinary differential equation, they take the form

$$y(0) = \alpha_1; \tag{2.18}$$

$$y(1) = \alpha_2. \tag{2.19}$$

Neumann conditions are second order and specify the value of the derivative of the solution on the boundary. For an ordinary differential equation, Neumann conditions take the form

$$\frac{\partial y}{\partial x}(0) = \alpha_1; \tag{2.20}$$

$$\frac{\partial y}{\partial x}(1) = \alpha_2. \tag{2.21}$$

For a PDE on the domain $\Omega \in \mathbb{R}^n$ then Dirichlet BC will take the form in equation (2.22) and Neumann BC will take the form in equation (2.23).

$$y(x) = f(x) \forall x \in \Omega, \tag{2.22}$$

$$\frac{\partial y}{\partial n}(x) = f(x) = \nabla y(x) \cdot \mathbf{n}(x), \tag{2.23}$$

where **n** denotes the vector normal to the boundary. The Robins BC or generalised Neumann BC are a combination of the Dirichlet and Neumann BC in that they specify a linear combination of the value the solution should take and its derivatives.

2.3.3 Meshing

Discretisation of a model into finite elements is termed meshing. The idea is to keep the mesh as simple as possible using the simplest elements. A mesh on the model should be relatively fine in areas which have a significant change and are prone to stresses and strains and coarse in other areas. For example, changes in thickness or material properties, corners and sharply curved edges should all have a fine mesh (figure 2-7). It is important that elements do not cross interfaces, see figure 2-8. For more information on meshing, especially in relation to Comsol, see Comsol Multiphysics (2008b, chapter 5).

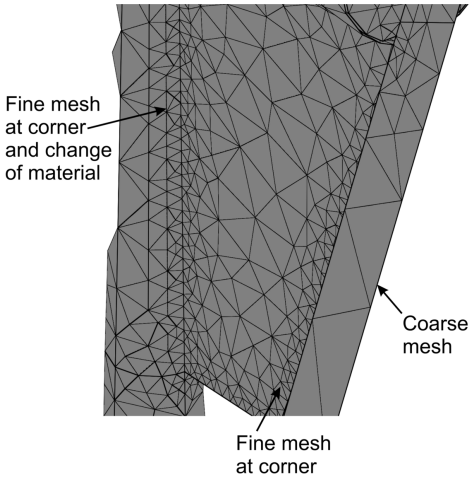

Figure 2-7: *An example of how meshing changes from fine to coarse at corners and changes of material.*

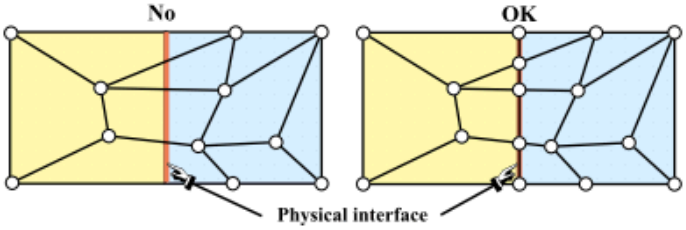

Figure 2-8: *An example of good (right) and bad (left) meshing at an interface (Felippa 2010).*

2.3.4 Eigenfrequencies

The eigenfrequencies of a system are the characteristic frequencies of the system, that is those which describe the natural vibration (normal modes) of the system. For a stiffness matrix, **K**, mass matrix **M**, and modal frequency analysis problem in the form

$$\mathbf{K}v_i = \lambda_i \mathbf{M} v_i, \tag{2.24}$$

then v_i is the eigenvector describing the shape of the frequency (bending mode) and λ_i the eigenvalue corresponding to v_i.

The eigenfrequencies, f, or corresponding angular frequency, ω, of a system are related to the eigenvalues as

$$\omega = 2\pi f = i\lambda. \tag{2.25}$$

Comsol solves the FE problem and calculates the eigenvalues of the system, returning either the

eigenfrequencies or eigenvalues. See Comsol Multiphysics (2008a,b) for more information of the eigenfrequency solver and the Comsol solvers in general.

2.3.5 Frequency Response Analysis

A frequency response analysis will find solutions to the system over a range of frequencies at discrete intervals, in a parametric fashion. This enables a solution of the model to be visualised which is equivalent to generating a power spectral density plot (see section 2.4.4) of raw experimental data.

2.4 Signal Processing

A wave is a continuous analogue signal. In order to acquire the signal in a digital form, the incoming wave must be discretised (Scherbaum 1994), which involves sampling and recording the signal at constant time intervals over a finite period of time. The result is a time series, generally represented by a vector of real numbers.

2.4.1 Fourier Analysis

In 1804 Baron Jean Baptiste Joseph Fourier (1768-1830), a French physicist and mathematician, began work on a memoir entitled The Propagation of Heat in Solid Bodies, which he completed in 1807 and published in 1822 in *Théorie Analytique de la Chaleur*. In this he expanded functions as trigonometrical series to solve boundary-value problems of partial differential equations, introducing what is now known as the Fourier series.

For a signal with a finite duration, the Fourier series, over a time interval $-T/2 < t < T/2$, is defined as (Stein & Wysession 2002)

$$f(t) = a_0 + \sum_{n=1}^{\infty} a_n \cos\left(\frac{2n\pi t}{T}\right) + \sum_{n=1}^{\infty} b_n \sin\left(\frac{2n\pi t}{T}\right), \tag{2.26}$$

where a_0 is a constant and T/n is the period of the signal. The function $f(t)$ is a series of sine and cosine terms with varying periods. The sine and cosine functions in the series are orthogonal, which

means that the integral of the product of two different terms over the interval $-T/2 < t < T/2$ is always zero. Therefore, to solve for the coefficients a_n or b_n, both sides of equation (2.26) should be multiplied by the respective sine or cosine term and integrated (Stein & Wysession 2002). On this basis the coefficient a_n is

$$a_n = \frac{2 - \delta_{n0}}{T} \int_{-T/2}^{T/2} \cos\left(\frac{2n\pi t}{T}\right) f(t)dt, \tag{2.27}$$

where δ_{n0} is the Kronecker delta. Similarly

$$b_n = \frac{2}{T} \int_{-T/2}^{T/2} \sin\left(\frac{2n\pi t}{T}\right) f(t)dt. \tag{2.28}$$

Equation (2.26) can be simplified using the angular frequencies $\omega_n = 2n\pi/T$. Expanding the sine and cosine terms into complex exponentials gives

$$f(t) = a_0 + \frac{1}{2} \sum_{n=1}^{\infty} \left\{(a_n - ib_n)e^{it\omega_n} + (a_n + ib_n)e^{-it\omega_n}\right\}, \tag{2.29}$$

which by defining, $F_n = (a_n - ib_n)/2, F_0 = a_0$ and $F_{-n} = (a_n + ib_n)/2$ becomes

$$f(t) = F_0 + \sum_{n=1}^{\infty} F_n e^{it\omega_n} + \sum_{n=1}^{\infty} F_{-n} e^{-it\omega_n} = \sum_{n=-\infty}^{\infty} F_n e^{it\omega_n}, \tag{2.30}$$

with

$$F_n = \frac{1}{T} \int_{-T/2}^{T/2} f(t) e^{-it\omega_n} dt. \tag{2.31}$$

For a signal with an infinite duration, the Fourier series in equation (2.30) is extended to become the Fourier transform (Stein & Wysession 2002).

2.4.1.1 The Discrete Fourier Transform

The Fourier transform is a way of converting a signal in the time domain into the frequency domain. For a continuous signal, this is done using the equation

$$F(x(t)) = X(f) = \int_{-\infty}^{\infty} x(t)\, e^{-2\pi i f t} dt. \tag{2.32}$$

For a discrete time signal, the Fourier transform simplifies to

$$F(x_m) = \sum_{n=-\infty}^{\infty} x_n\, e^{-2\pi i m n}, \text{ for } m \in \mathbb{Z}, \tag{2.33}$$

where x_n is a discrete time signal defined for infinitely many samples. However in reality, like the signals processed in this thesis, the signal will be finite. In this case, the Discrete Fourier Transform (DFT) is used and defined as

$$F(x_m) = \sum_{n=0}^{N-1} x_n\, e^{-2\pi i m n/N}, \text{ for } m = 0, 1, ...N-1. \tag{2.34}$$

The signal is continuous and samples are taken at an interval of Δt, then the discrete frequencies, ω_m, which relate to $F(x_m)$ are given by

$$\omega_m = \frac{2\pi m}{\Delta t\, N}. \tag{2.35}$$

2.4.2 The Nyquist Frequency

The Nyquist frequency equates to half the sampling rate of a signal and is the highest frequency which can be used in order to be able to fully reconstruct a signal and recover all Fourier components. It is defined as

$$f_N = \frac{\Delta t}{2}. \tag{2.36}$$

If the sample period is too large, then samples are skipped in the original signal, creating an alias and giving the impression of a longer period (figure 2-9).

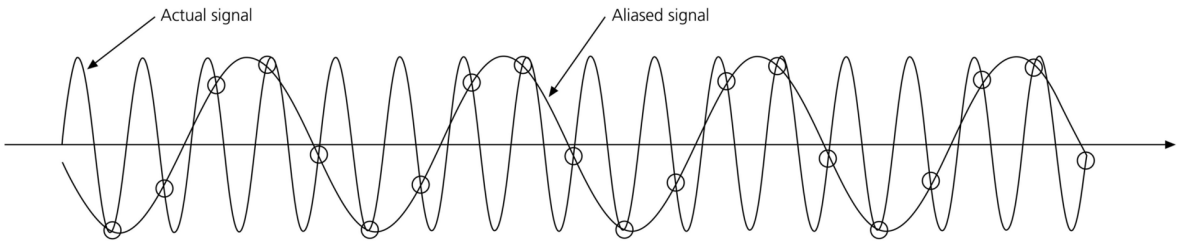

Figure 2-9: *At least two samples per wavelength are required in order to accurately reconstruct a signal. If the frequency is higher than the Nyquist, the signal becomes aliased producing a signal with a longer period (After Stein & Wysession 2002)*

2.4.2.1 The Fast Fourier Transform

The Fast Fourier Transform (FFT), developed by Cooley & Tukey (1965), reduces the time and complexity required to compute a Fourier Transform. The FFT assumes that there are N data points, such that

$$N = 2^q \text{ for } q \in \mathbb{Z}. \tag{2.37}$$

If this is not the case then zero padding can be used to add an arbitrary number of zeros to the head or tail of the signal. The algorithm works by recursively breaking down the DFT in equation (2.33) into two parts of size N_1 and N_2 such that $N = N_1 N_2$, until $N = 1$. The most common FFT algorithms divide the DFT into two parts of size $N/2$ (Stoica & Moses 1997, Aki & Richards 1980).

Let

$$W = e^{\frac{-2\pi i}{N}}, \tag{2.38}$$

then the DFT in equation (2.33) simplifies to

$$F(x_m) = \sum_{n=0}^{N-1} x_n W^{mn}, \tag{2.39}$$

and

$$X_m = \sum_{n=0}^{N/2} x_n W^{mn} + \sum_{n=N/2+1}^{N} x_n W^{mn} = \sum_{n=0}^{N/2} \left(x_n + x_{n+N/2} \right) W^{mN/2} \Big) W^{mn}, \tag{2.40}$$

This operation is performed recursively until $N/2 = 1$, which is possible as N is a power of 2. For

more information on the method and its application to digital signal processing see Aki & Richards (1980), Pickering (1986).

Matlab (section 4.4.2) contains a built-in function, *fft* for computing the DFT of a signal using the FFT algorithm.

2.4.3 Filtering

When applied to a signal, a filter allows part of the signal to pass (the passband) and attenuates the rest of the signal. The requirements of a filters performance influence the type, shape and design of filter which should be implemented. For example it may be necessary to have a filter which can achieve requirements with a minimum filter order or have a certain amount of ripple or flatness on the passband.

The passband controls the frequencies which the filter allows to 'pass'. A low-pass filter will only allow frequencies below a certain value (the cut-off frequency, ω_c), whereas a high-pass filter is the opposite, allowing only frequencies above a certain value. Alternatively a band pass filter allows all parts of the signal between two given frequencies to pass, centralised about the frequency ω_b. The opposite of this is the band-stop filter which allow all parts of the signal except those in a specified frequency band. For example, a requirement to remove all noise above 25 Hz on a data sample recorded at 100 Hz would require a low-pass filter. Figure 2-10 shows an example of each of the basic types of filter.

There are two types of filters used in digital signal processing; Infinite Impulse Response (IIR) and Finite Impulse Response (FIR). The IIR filter contains a feedback loop and will return an infinitely long result, whereas the FIR will only return the same number of samples as the signal entering the filter. An IIR filter uses less memory and calculations than an FIR filter, so is more efficient, however they are not suitable for all types of applications.

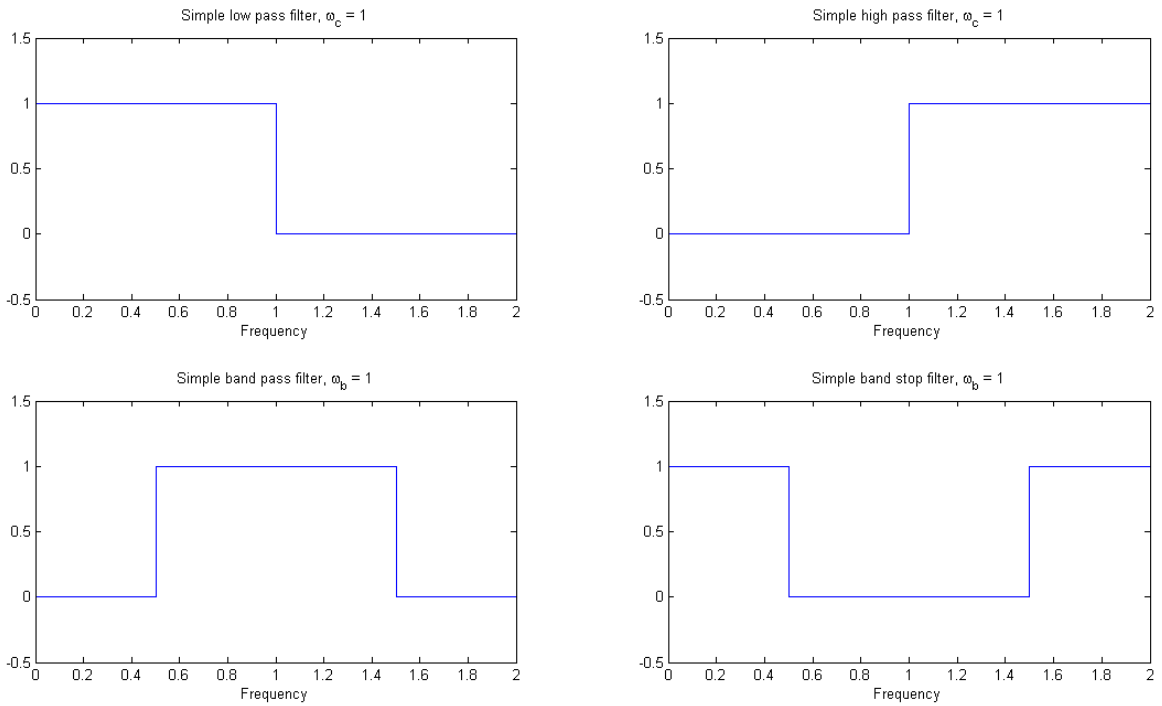

Figure 2-10: *Examples of the four basic filter types. The cut-off frequency and centre-band frequency is fixed at 1Hz.*

2.4.3.1 The Butterworth IIR Filter

The Butterworth filter (Butterworth 1930) has a tapered cut-off and is designed to have a maximally flat frequency response in the passband. The transfer function, representing the frequency response, for the low-pass nth order Butterworth filter is given as (Gubbins 2006)

$$|F_l(\omega)|^2 = \frac{1}{1 + (\omega/\omega_c)^{2n}}, \tag{2.41}$$

where ω_c is the cut-off frequency and n is the order of the filter. Figure 2-11 shows how varying the value of n affects the sharpness of the roll-off. A high-pass filter has the opposite effect to the low-pass and is simply defined as

$$F_h(\omega) = 1 - F_l(\omega). \tag{2.42}$$

Shifting the function and centering about ω_b will produce a band pass filter

$$|F_b(\omega)|^2 = \frac{1}{1 + ((\omega - \omega_b)/\omega_c)^{2n}}. \tag{2.43}$$

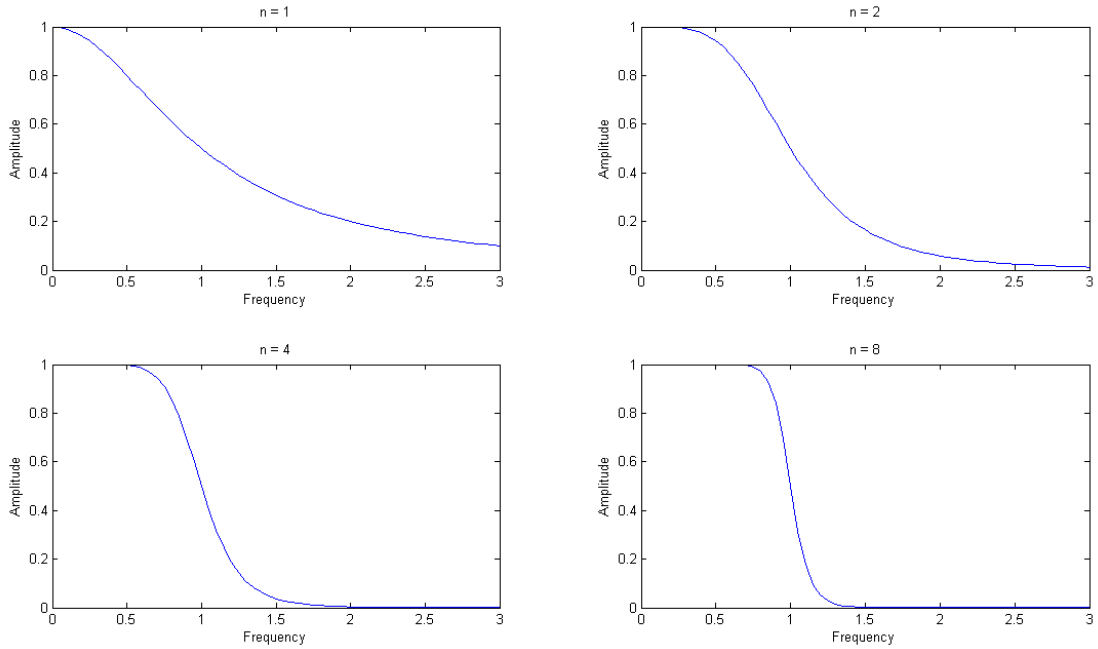

Figure 2-11: *Butterworth filter defined by equation* (2.41) *with variation in* n*. The cut-off frequency is fixed at 1 Hz (After Gubbins 2006).*

2.4.4 Welch's Method

The power spectral density function (PSD) details the amount of power in a signal distributed over a range of frequencies. This can be visualised by plotting the function against frequency (figure 2-12).

The PSD is produced using Welch's method (Welch 1967) as follows:

1. Split the samples into M overlapping segments, each with length L and D samples apart, such that

$$(M-1)D + L = N \tag{2.44}$$

2. Each of the M samples is windowed using data windows $W(\xi)$, for $\xi = 0...L-1$ and the Finite Fourier Transform performed on the sequences $X_1(\xi)W(\xi)...X_M(\xi)W(\xi)$ to obtain $B_1(n)...B_M(n)$. The M periodograms[1] are obtained using,

$$B_m(n) = \frac{1}{L}\sum_{\xi=0}^{L-1} X_m(\xi)W(\xi)e^{-2mi\xi n/L}, \tag{2.45}$$

where $m = 1...M$ and $n = 0...L/2$.

[1] an estimate of the spectral density of a signal. The term was first used by Schuster (1898).

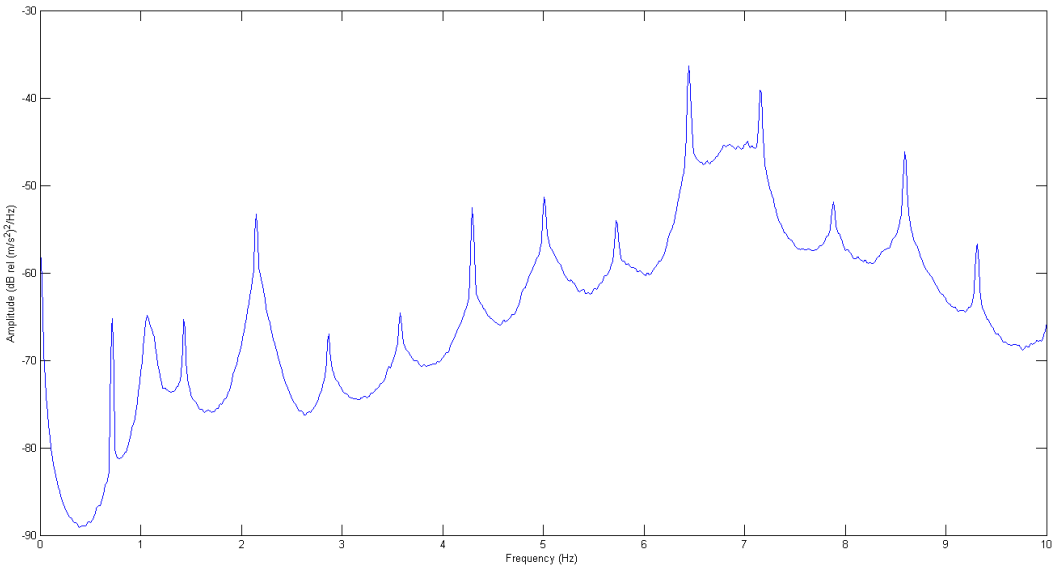

Figure 2-12: *Example power spectral density plot*

3. The spectrum is an average of the periodograms,

$$\hat{I}_k\left(\frac{N}{L}\right) = \frac{1}{M}\sum_{m=0}^{M}\frac{L}{U}\left|B_m(n)\right|^2, \tag{2.46}$$

where

$$U = \frac{1}{L}\sum_{\xi=0}^{L-1} W^2(\xi).$$

The result is an array of power measurements (dB) vs. frequency (Hz).

2.4.5 Converting between Acceleration, Velocity and Displacement PSD

It is possible to convert between acceleration, velocity and displacement power spectral density functions. As velocity is the derivative of displacement, then given the velocity PSD, $S_v(f)$, then the displacement PSD $S_x(f)$ is defined as

$$S_x(f) = \frac{S_v(f)}{4\pi^2 f^2}, \tag{2.47}$$

This is achieved due to the Fourier harmonics being related such that

$$V(f) = -2\pi i f X(f), \tag{2.48}$$

where $X(f)$ is the Fourier transform of the displacement (see section 2.4.1) and $V(f)$ the Fourier transform of the velocity.

To convert from acceleration into velocity, equation (2.47) holds, with S_x being replaced with S_v and S_v with the acceleration PSD function S_a. Applying equation (2.47) results in an equation for the displacement PSD function in terms of the acceleration PSD function, such that

$$S_x(f) = \frac{S_a(f)/4\pi^2 f^2}{4\pi^2 f^2} = \frac{S_a(f)}{16\pi^4 f^4}. \tag{2.49}$$

2.5 Loads on Wind Turbines

There are three main sources of loads present on a wind turbine:

1. Gravitational loading,
2. Inertial loading,
3. Aerodynamic loading.

These loads have an impact on the efficiency and fatigue of the wind turbine and must be considered when the turbine is designed. The equations for each are used when generating a multiphysics model of a wind turbine, in order to generate as accurate a model as possible.

2.5.1 Gravitational Loading

Gravitational loading is the effect due to gravity and is the most basic load affecting a wind turbine, specifically the blades. Due to Newton's second law,

$$F_g = mg, \tag{2.50}$$

where m is the mass of an object, g the acceleration due to gravity and F_g is the force acting on the object. The loading due to gravity on the blades results in a sinusoidal bending moment. When the blade is travelling downward, the leading edge has a tensile stress acting upon it and the trailing edge

a compressive stress. In the upward direction, these are reversed with the leading edge exposed to a compressive stress and the trailing edge to a tensile stress. Loading under gravity is a major source of fatigue (Burton et al. 2001).

2.5.2 Inertial Loading

When the blades rotate, a centrifugal load generates a tensile stress on the blades. The force acting on the blade at a radius r from the rotor is defined as

$$F_c = \omega^2 r m, \tag{2.51}$$

where m is the mass of the blade and ω the angular velocity of the rotor. The force acts perpendicular to the rotor. Due to the bending (or coning) of the blades, the force has two components which are perpendicular, $F_c \sin\varphi$, and parallel, $F_c \cos\varphi$, to the blades (Hansen 2008) as shown in figure 2-13.

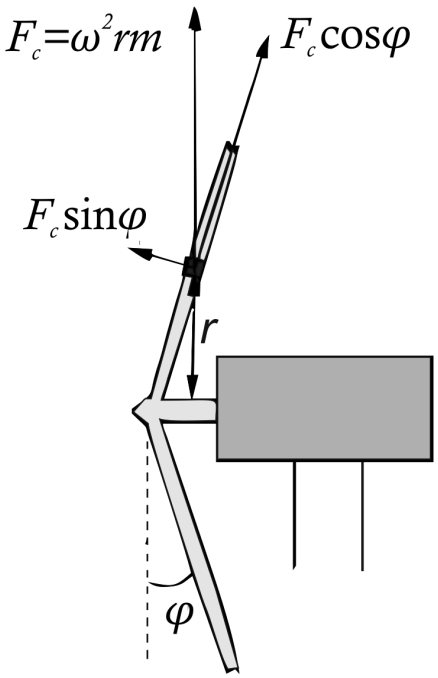

Figure 2-13: *Centrifugal forces acting upon the blades (After Hansen 2008)*

2.5.3 Aerodynamic Loading

On an upwind turbine, wind flow past the blades and tower causes a force to impact on the structure. Wind speed varies with height above the ground. This wind speed profile means that there will be a different speed on the part of the blade nearest thee ground, compared to the top of the blade tip. Wind velocity is calculated at height h using a power law (Hansen 2008):

$$V_h = \frac{\log(h_{ref}/z_0)V_{ref}}{\log(h/z_0)}, \tag{2.52}$$

where V_{ref} is the wind velocity at a fixed reference height h_{ref}, V_h is the wind velocity at height h and z_0 is the surface roughness length. The surface roughness length provides a characterisation of the landscape, table 2-1 provides details of the values for a selection of terrain.

The force on all areas of the turbine exposed to the wind is given by

$$F = \frac{1}{2}C_d A \rho I_T v_h^2, \tag{2.53}$$

where C_d is the drag coefficient, A is the surface area, ρ is the density of air (1.225 kg/m^3) and I_t is the turbulence intensity (equal to 0.13 (Marmo & Buckingham 2011)).

This force occurs on the blades and tower as a pressure such that

$$p = \frac{1}{2}C_d \rho (I_T v_h)^2. \tag{2.54}$$

Roughness length z_0 [m]	Landscape
0.0002	Water
0.0024	Completely open terrain with a smooth surface, such as concrete runways in airports
0.03	Open agricultural area without fences and hedgerows and very scattered buildings, only softly rounded hills
0.055	Agricultural land with some houses and 8 meter tall sheltering hedgerows within a distance of about 1.25 km
0.1	Agricultural land with some houses and 8 meter tall sheltering hedgerows within a distance of about 500 m
0.2	Agricultural land with many houses, shrubs and plants or 8 meter tall sheltering hedgerows within a distance of about 250 m
0.4	Villages, small towns, agricultural land with many or tall sheltering hedgerows, forests and very rough and uneven terrain
0.8	Larger cities with tall buildings
1.6	Very large cities with tall buildings and skyscrapers

Table 2-1: *Surface roughness lengths (After Ragheb 2012)*

Chapter 3

A Review of Seismic Monitoring of Wind Farms and Seismically Sensitive Installations

3.1 Microseismic Monitoring of Wind Farms

Very few studies on the microseismic vibrations from wind farms have been carried out in either the UK or abroad. This section details in chronological order the different studies from the UK related to microseismic monitoring of wind farms, Europe and the US since the first work in the mid 1990s.

3.1.1 Llandinam

From 1989 to 2000, the University of Liverpool Microseismic Research Group operated a seismic station, providing real time monitoring of local and worldwide earthquakes. The station consisted of a single three-component seismometer, located at the Powys Observatory, near Knighton in Wales. When plans were submitted to build a wind farm on a neighbouring hill, the group suspected that the wind turbines might interfere with their seismic station.

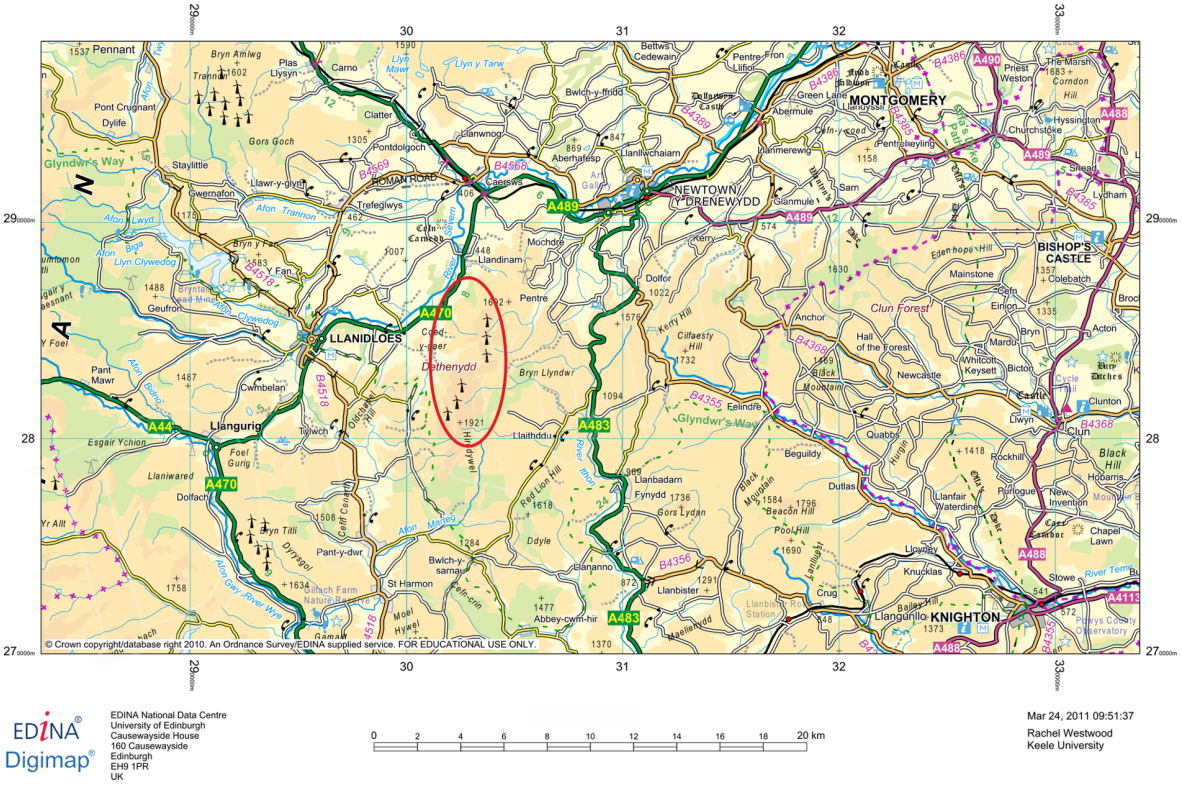

Figure 3-1: *The location of the Penrhydlan & Llidiartiwaun wind farm in relation to surrounding towns*

Preliminary experiments were conducted near the Penrhydlan & Llidiartiwaun (P&L; figures 3-1 and 3-2) wind farm in Llandinam, Wales, using a selection of accelerometers, seismometers and geophones which were deployed 1 km away from the wind farm (10 km south of Newtown, Powys). The P&L wind farm, operated by CeltPower Ltd, was commissioned in January 1993 and contained 103 Mitsubishi 300 kW wind turbines. At the time of construction it was Europe's largest wind farm in terms of both the number of turbines and generating capacity. Data was gathered during September 1994 and subsequently during 1996 at a nearby farm, Y Graig (figure 3-2). The study (Rushforth et al. 1997) showed that during high wind periods (figure 3-3) frequencies between 0.5 Hz and 1 Hz and at approximately 4.5 Hz are clearly seen, but are greatly reduced when there is no wind (figure 3-4).

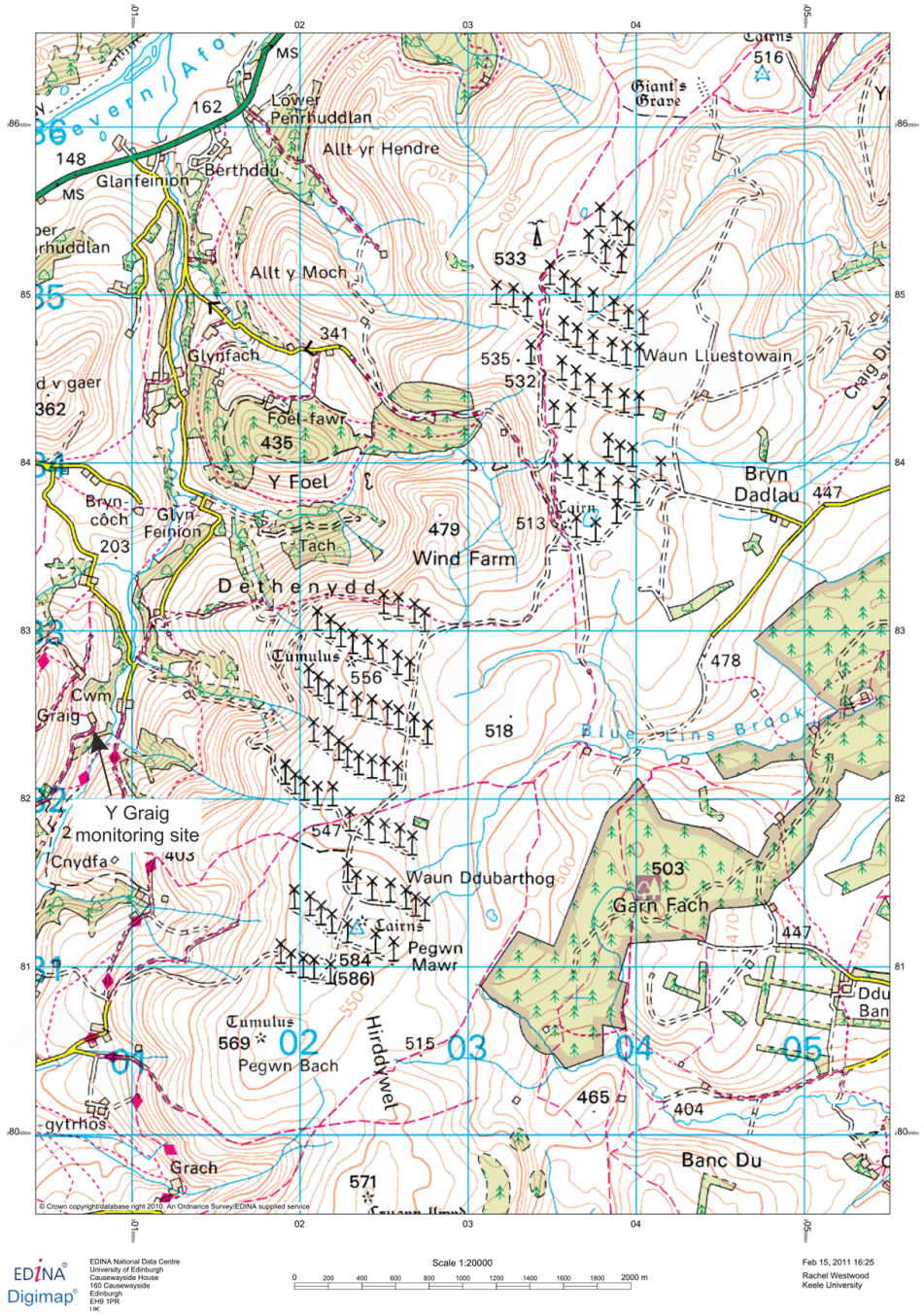

Figure 3-2: *Detailed view of the Penrhydlan & Llidiartiwaun wind farm with the Y Graig monitoring site used in 1996 highlighted*

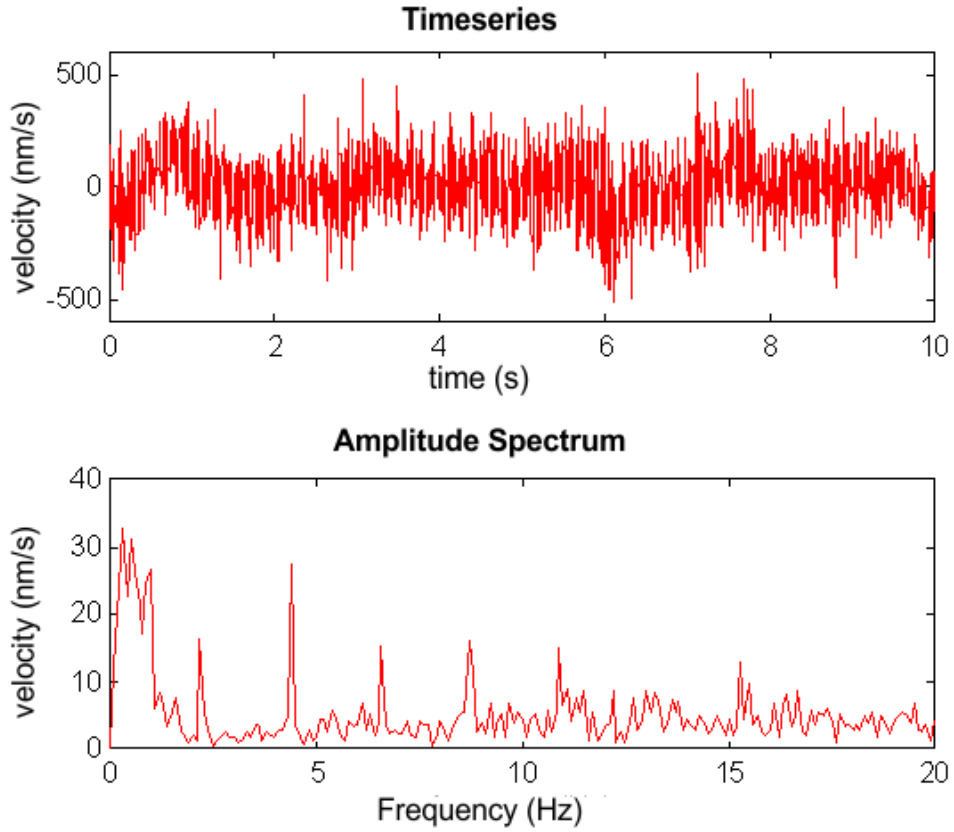

Figure 3-3: *Data recorded at Y Graig in 1996 during a period of high (but undetermined) wind speeds (After Rushforth et al. 1997)*

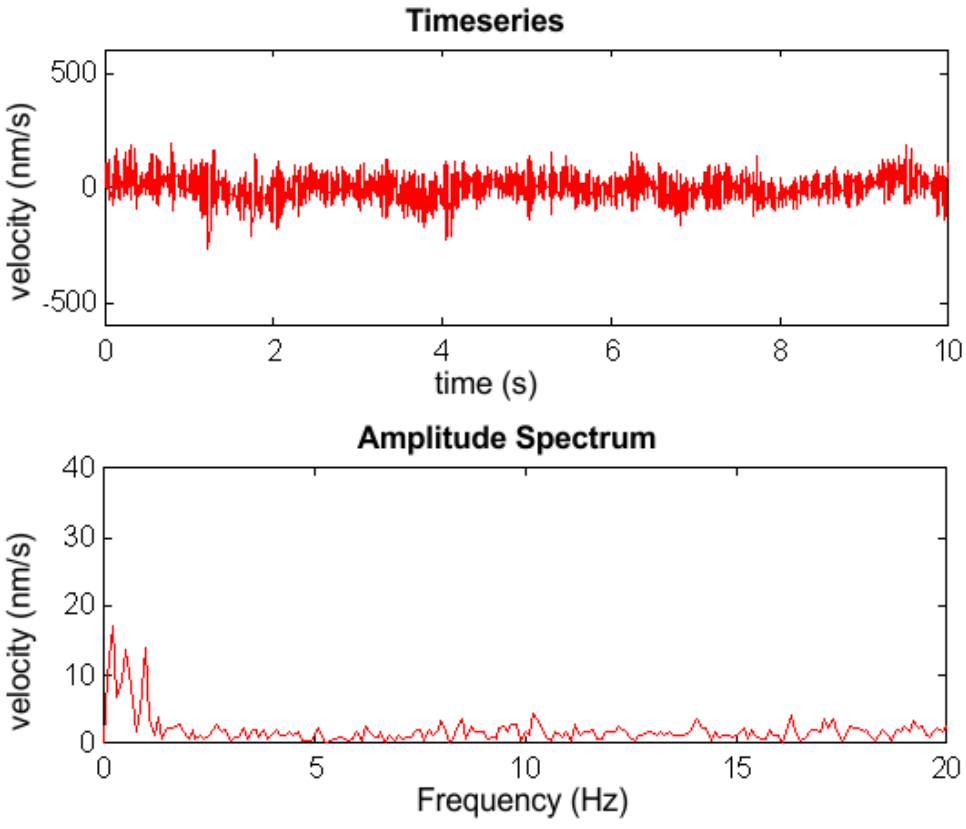

Figure 3-4: *Data recorded at Y Graig in 1996 during a period of no wind (After Rushforth et al. 1997)*

3.1.2 St Breock Downs

As a consequence of the work at Llandinam, the Environment Technologies Support Unit (ETSU) and Powergen commissioned the University of Liverpool Microseismic Research Group to carry out research to investigate whether low frequency seismic signals from wind farms were transmitted through the ground and to further characterise any signals present (Styles 1996, Snow 1997). The Group carried out experiments at St Breock Downs wind farm in Cornwall (figure 3-5), owned by Powergen. The wind farm contained eleven Bonus 450 kW turbines, which were commissioned in July 1994. Measurements were recorded using Lennartz LE-3D/1 three-component seismometers over a period of ten days at distances of 25 m, 50 m and 100 m from Turbine 1. An additional sensor, a Geosense DV-1, was deployed at a distance of 1 km from the wind farm and a B&K 8316 accelerometer placed at the base of Turbine 1. The numbering of the turbines on the site is shown in figure 3-6.

As part of the experiment measurements were recorded over a range of wind speeds and directions. A sequential shut down of the wind farm was also carried out. It was found that harmonic components

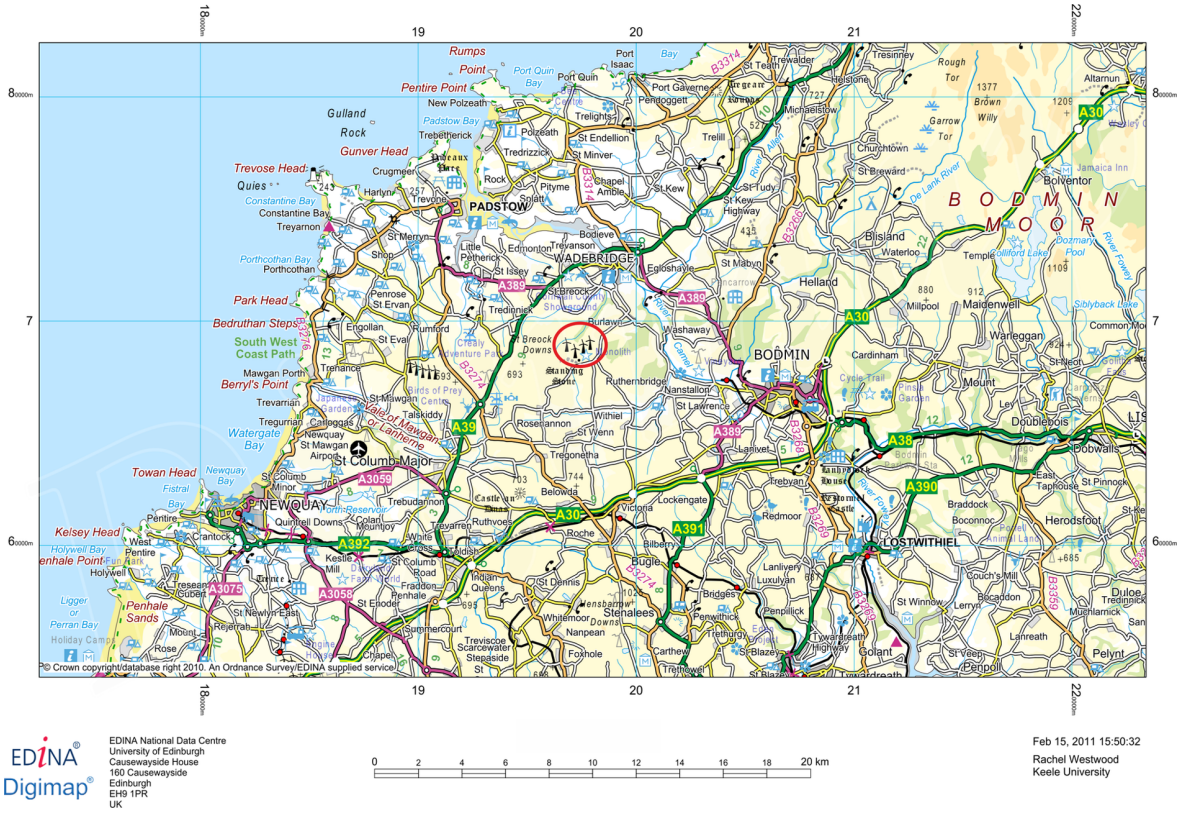
PADSTOW
WADEBRIDGE
BODMIN
NEWQUAY
LOSTWITHIEL
St Columb Major
St Breock Downs
Rumps Point
Pentire Point
Trevose Head
Park Head
Bedruthan Steps
Gunver Head
Gulland Rock
Towan Head
Kelsey Head
Penhale Sands
South West Coast Path
Berry's Point
Watergate Bay
Constantine Bay
Porthcothan Bay
Holywell Bay
Fistral Bay
Newquay Bay
Padstow Bay
Port Quin Bay
Jamaica Inn
Bolventor
Blisland
Helland
Maidenwell
Warleggan
Cardinham
Mount
Doublebois
Dobwalls
Herodsfoot
Braddock
Boconnoc
Lanreath
Pelynt
Duloe
Looe
Polperro
Golant
Tywardreath
Par
Fowey
Lerryn
St Winnow
Lostwithiel
Bugle
Stenalees
Roche
Victoria
Lockengate
Redmoor
Indian Queens
St Dennis
St Columb Road
St Columb Minor
St Ervan
St Eval
Rumford
Trevarrian
Tregurrian
Carloggas
Trebudannon
Quintrell Downs
Crantock
Pentire
Holywell
Penhale
Perran Bay
Mawgan Porth
Trenance
Ruthernbridge
Nanstallon
St Lawrence
Lanivet
Trebyan
Tregonetha
Wadebridge
Egloshayle
St Mabyn
Washaway
Millpool
Common Moor
Temple
Waterloo
Dozmary Pool
Siblyback Lake
Colliford Lake
De Lank River
Rough Tor
Brown Willy
Garrow Tor
Altarnun
Tresinney
Trewalder
Port Isaac
Port Gaverne
Pendoggett
Michaelstow
Churchtown
St Breward
St Kew
St Tudy
Trelill
Trelights
Polzeath
New Polzeath
St Endellion
St Minver
Tredrizzick
Trebetherick
Crugmeer
Harlyn
Trevone
Pityme
Chapel Amble
Bodieve
Trevanson
Edmonton
Little Petherick
St Issey
Tredinnick
Penrose
Ergollan
Rumford
Trenance
Mawgan Porth
Trevarrian
Tregurrian
Carloggas
Taskiddy
Newquay Airport
St Mawgan
Trevemper Reservoir
Quintrell Downs
Crantock
Pentire
Holywell
Kestle Mill
Fraddon
Penhale
St Enoder
Summercourt
Treviscoe
Scarcewater
Stepaside
Foxhole
Nanpean
Whitemoor
Carthew
Trethewel
Penwithick
Penpillick
Bridges
Luxulyan
Lanlivery
Bilberry
Castle an Dinas
Belowda
Trebyan
Braddock
Boconnoc
Herodsfoot
Doublebois
Dobwalls
Warleggan
Cardinham
Mount
Helland
Maidenwell

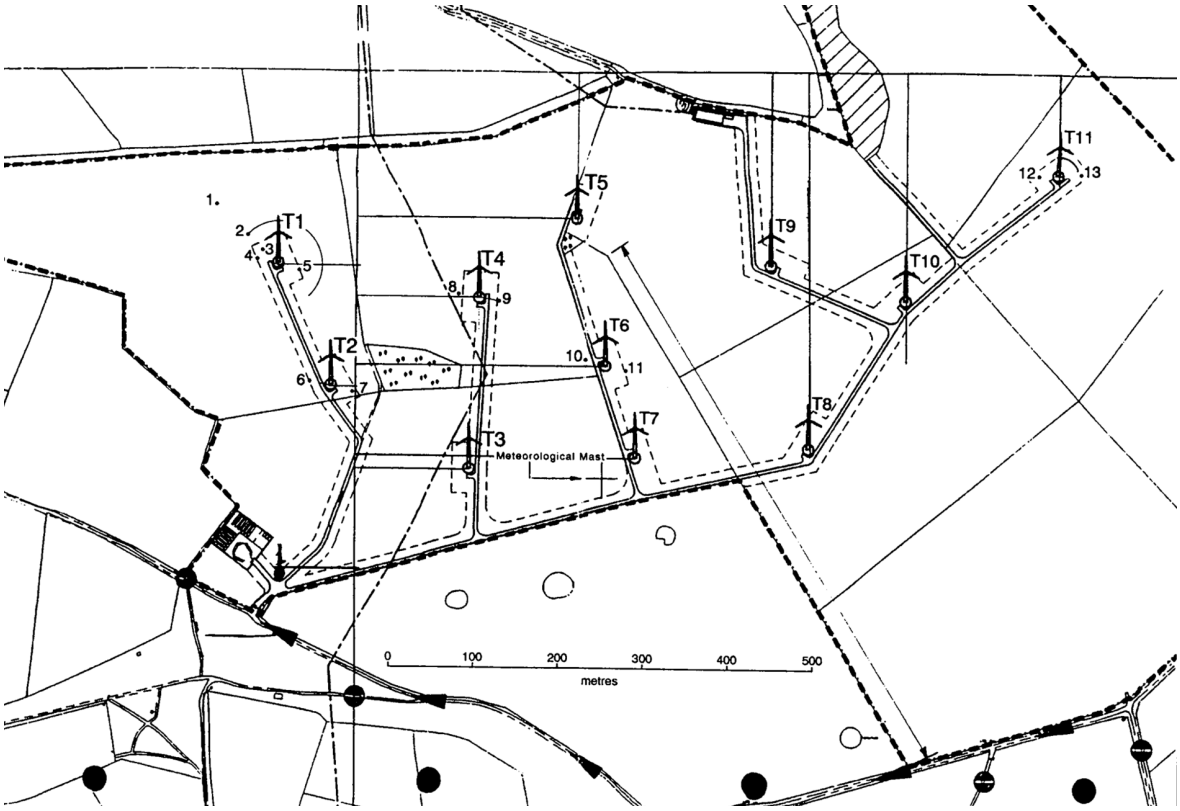

Figure 3-6: *The location of the turbines at St Breock Downs wind farm and the microseismic measuring stations 1 to 13 (Styles 1996).*

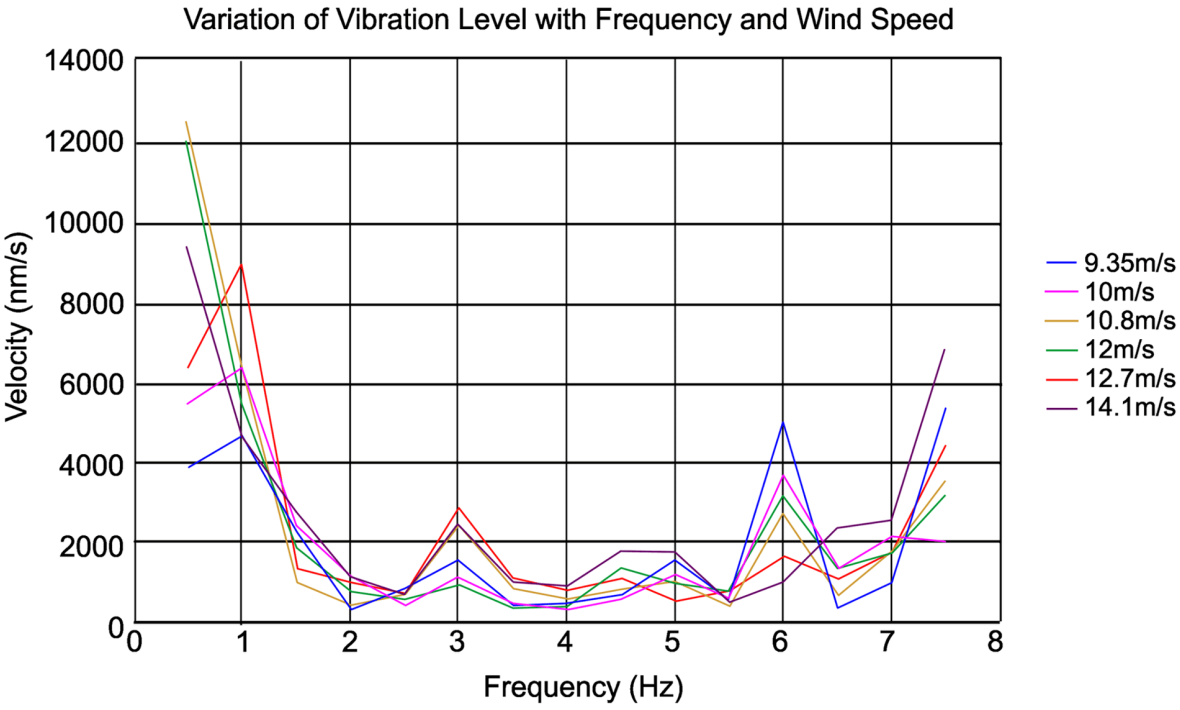

Figure 3-7: *Vibration levels against frequency for varying wind speeds at St Breock Downs wind farm (After Styles 1996)*

at multiples of 0.5 Hz were transmitted through the ground with particular peaks occurring at 0.5 Hz, 3 Hz, 4.5 Hz, 6 Hz and 7.5 Hz, as well as higher frequencies. Above 3 Hz, the frequencies attenuated with distance, with higher frequencies decaying fastest. The peak at 0.5 Hz was still visible at a distance of 1 km from the wind farm.

The amplitude of these prominent frequencies was found to differ with wind speed (figure 3-7), with different frequencies being more dependent on different wind speeds. Measurements were taken at a constant wind direction over a range of wind speeds from 9 m/s to 14 m/s. Generally the amplitude increased with wind speed, however the amplitude for the 6 Hz peak decreases with increasing wind speed. Variations in seismic amplitude at a constant wind speed of 10 m/s were seen depending on wind direction.

When the turbines were switched off the levels of vibration dropped; however the lowest frequencies were still present even when all turbines on the wind farm were shut down. This may be due to these frequencies originating from a source other than the wind turbine. Alternatively, as the tower vibrates at its resonant frequencies all the time, be it at much lower amplitudes when the blades are not turning and exciting the tower, it may be the first bending mode which is visible.

3.1.3 Stateline

In the USA, Schofield (2002) conducted a study to determine whether the seismic signals from the proposed Maiden wind project would be detrimental to the Laser Interferometric Gravitational Wave Observatory (LIGO) on the Hanford Reservation. LIGO actively searches for gravitational waves which are created when supernovas collapse to form neutron stars and black holes (LIGO 2010). The study focused on measurements of the vibrations from the Stateline Wind Project in Oregon, which consists of 399 Vestas V47, 660 kW wind turbines and found results consistent with the work carried out at St Breock Downs. Measurements were obtained at ten sites around the Stateline wind farm, using Güralp CMG-40T three-component seismometers. One of the seismometers was located on the concrete base of one of the turbines, with a second positioned 24 m SW of the same turbine. The third sensor was mobile and recordings were taken at distances of 50 m, 100 m, 150 m, 710 m, 1660 m (1 mile), 3 km, 11 km and 18 km away from the most north-eastern turbine.

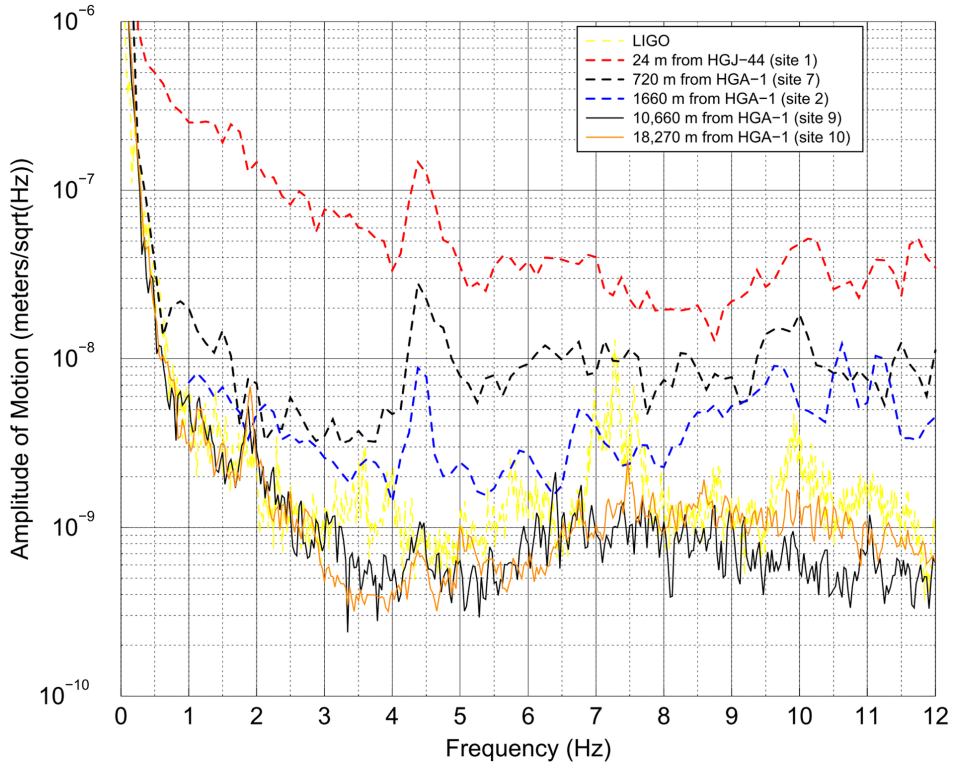

Figure 3-8: *The horizontal motion frequency spectrum at increasing distances (Schofield 2002).*

Schofield identified peaks which increased in frequency as the rotational rate of the turbines increased, before stabilising at high wind velocities when the turbines run at a nearly constant rotational rate. These frequencies were harmonic components of the blade passing frequency of 0.49 Hz and occurred predominantly at 1.47 Hz, 2.95 Hz, 4.34 Hz, 5.88 Hz and 7.35 Hz (figure 3-8). Peaks at 0.669 Hz and 11 Hz were constant and visible when the turbines were both operational and shut down.

In order to predict the amplitudes at LIGO from the proposed wind farm, Schofield tests three attenuation models. The $1/\sqrt{r}$ model (equation (3.1)) assumes that the relationship between the amplitude of a signal in the far-field, A_{far} and at close to the source, A_{near}, contains no linear attenuation and is directly related to the ratio of the distances to the far-field, R_{far}, and near-field, R_{near}, locations. This model assumes propagation along the surface.

$$A_{far} = A_{near}\sqrt{\frac{R_{near}}{R_{far}}}. \tag{3.1}$$

The $1/\sqrt{r}$ with linear attenuation model (equation (3.2)) adds a linear attenuation factor to the $1/\sqrt{r}$

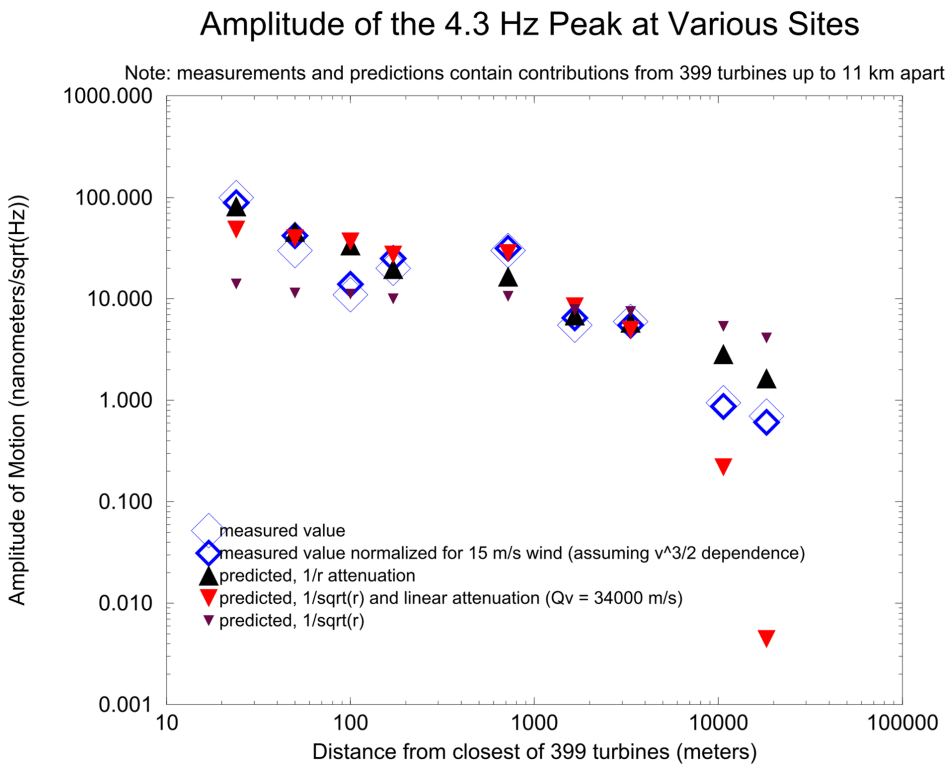

Figure 3-9: *A comparison of the three predictive amplitude models with two sets of real data from Stateline at 4.3Hz (Schofield 2002).*

model, incorporating the Q-factor and wave velocity of the underlying geology,

$$A_{far} = A_{near}\sqrt{\frac{R_{near}}{R_{far}}}e^{\left(\frac{\pi f}{Q_v}\left(R_{near}-R_{far}\right)\right)}. \tag{3.2}$$

The $1/r$ model (equation (3.3)) is a model of propagation through a volume, such as air and therefore contains no square root function,

$$A_{far} = A_{near}\frac{R_{near}}{R_{far}}. \tag{3.3}$$

When combining the signal to take into account multiple turbines, Schofield assumes that the signals sum in quadrature. From the three models, the $1/r$ model, is selected as working best for the 4.3 Hz peak (figure 3-9), which had the highest amplitude of the harmonics, relative to the background noise (figure 3-8).

A final model of the amplitude of the signal is given which takes into consideration the power rating difference of the turbines proposed at the Maiden wind farm (GE 1.5 MW wind turbines) and those

at Stateline (660 kW) and the number of turbines on the proposed site. The model is defined as

$$A_j = A_0 \left(\frac{v}{15}\right)^{1.5} \sqrt{N_M} \sqrt{\frac{P_M}{P_0}} \frac{r_0}{R_{ML}}, \tag{3.4}$$

where A_j is the predicted amplitude at LIGO from the Maiden wind farm, A_0 is the amplitude of the signal from one turbine at Stateline measured at 18 km, v the wind speed, N_M the proposed number of turbines at Maiden, P_M the power rating of the turbines at Maiden, P_0 the power rating of the turbines at Stateline, r_0 the distance to the turbine producing the A_0 signal and R_{ML} the distance from Maiden to LIGO.

The model generates only an estimate of the amplitude and Schofield states that there is a high degree of uncertainty. This is due to the differences between the turbines at Stateline and Maiden, which may cause the predominant peak at 4.3 Hz to change in amplitude and/or frequency. In addition the turbines proposed for the Maiden project are variable speed, which, suggested Schofield, may result in a lower signal level at LIGO. Other uncertainties arise due to topography. He recommended testing the turbines to be installed at Maiden to ensure his assumptions hold.

3.1.4 Dun Law

In 2004, the Ministry of Defence (MoD), the British Wind Energy Association (now RenewableUK) and the Department for Trade and Industry (DTI) commissioned and funded research to be carried out by the Applied and Environmental Geophysics Research Group at Keele University, in order to investigate the nature and levels of vibration from wind turbines and whether these would interfere with the Eskdalemuir seismic station, EKA (section 1.1). The study (Styles et al. 2005, England 2007) focused on Dun Law wind farm in the Scottish Borders (figure 3-10) which contained twenty six fixed-speed Vestas V47 (660 kW, 40 m hub height and 47 m rotor diameter) wind turbines (figure 3-11) and was situated on similar geology (Silurian shales) and topography to Eskdalemuir.

Ten Güralp CMG-6TD seismometers were deployed at locations of up to 17 km away from Dun Law (figure 3-12) for a period of four months. In addition, six Güralp CMG-5U accelerometers were mounted on the north, south, east and west inside walls and inside of one of the turbines, on the floor, to the northerly and southerly edges.

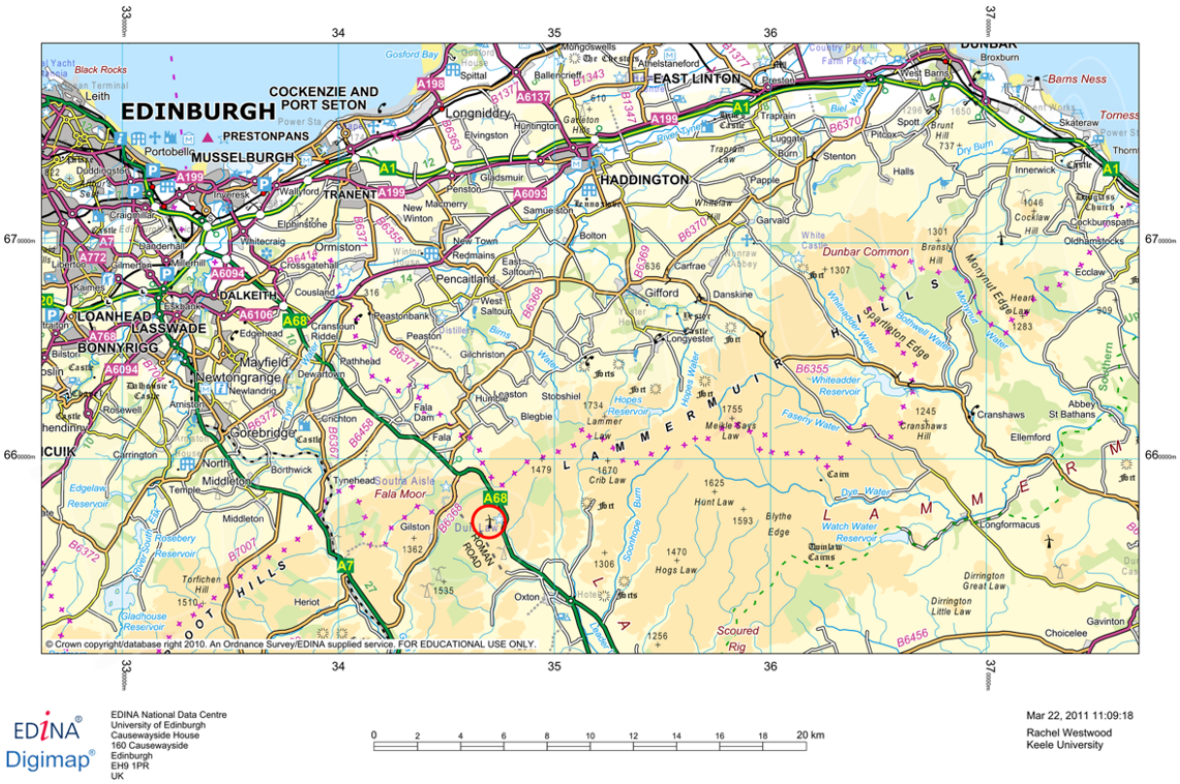

Figure 3-10: *The location of Dun Law wind farm in the Scottish Borders*

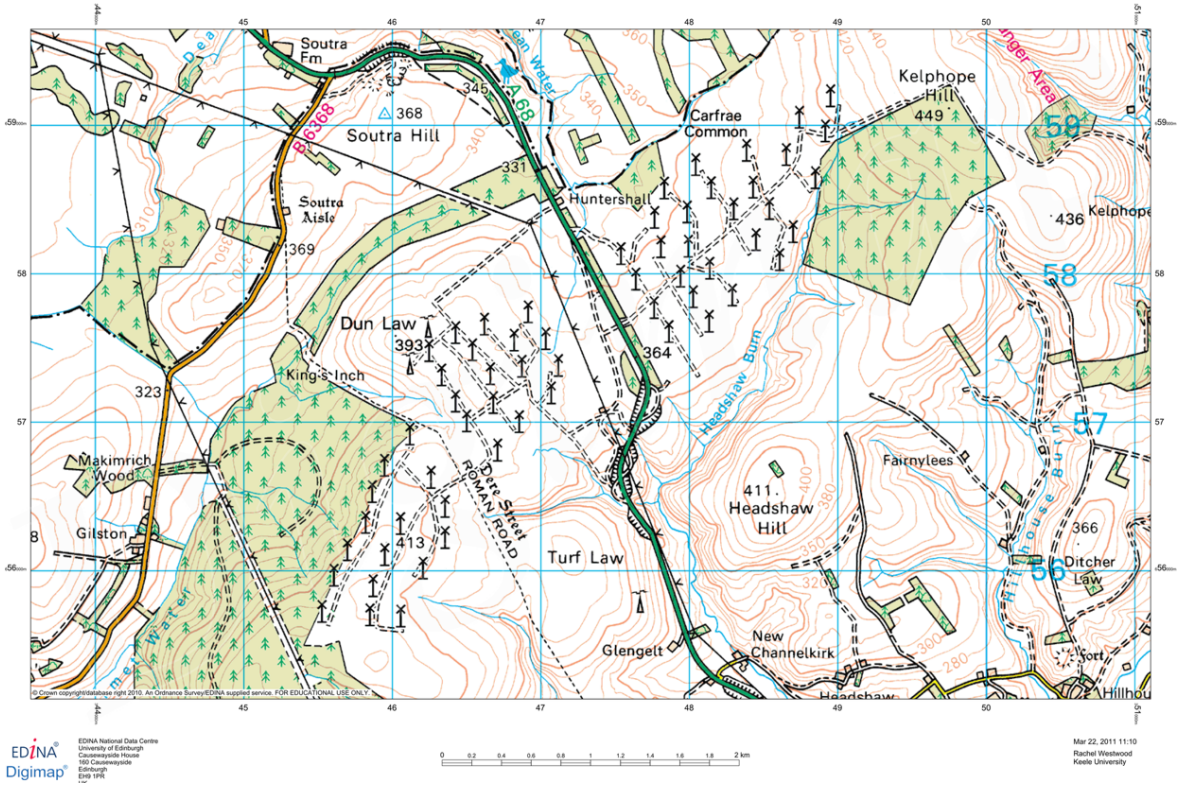

Figure 3-11: *The layout of Dun Law wind farm*

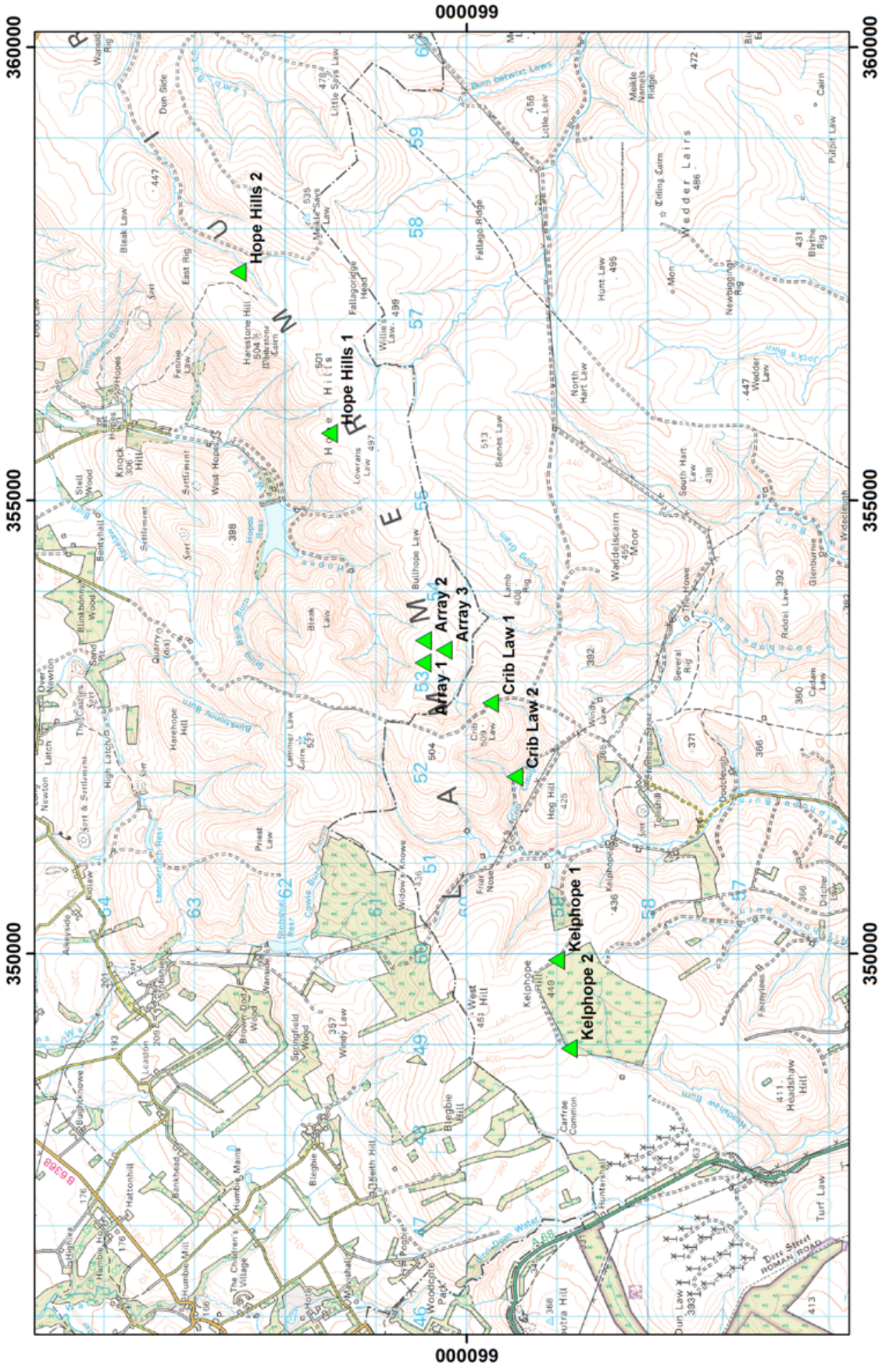

Figure 3-12: *The locations of the seismometer sites and on-turbine measurements in relation to Dun Law wind farm (After Styles et al. 2005).*

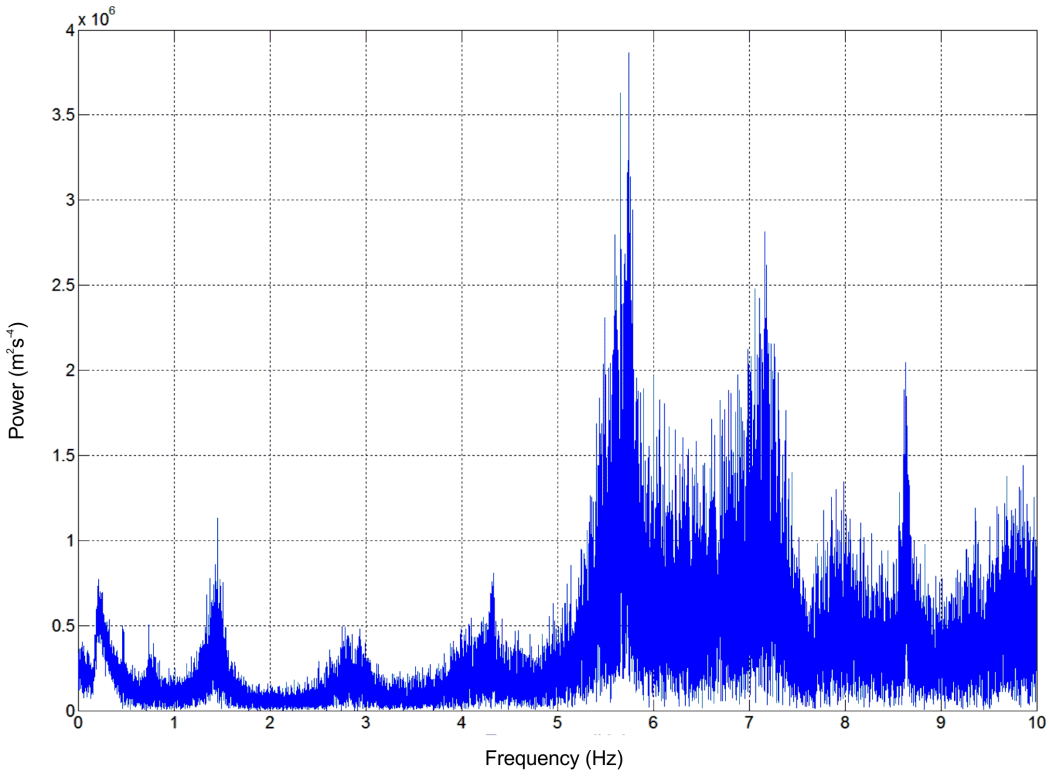

Figure 3-13: *A frequency Spectrum using data obtained on the turbine (After Styles et al. 2005).*

Prominent peaks were found to be present at 1.4 Hz, 2.8 Hz, 4.3 Hz, 5.7 Hz, 7.1 Hz and 8.5 Hz in the data recorded on the accelerometers attached to the turbine (figure 3-13) and the seismometers away from the turbine, including Kelphope 1 at 1.2 km (figure 3-14) and Crib Law 2 at 4.4 km (figure 3-15).

As part of the study a series of shut-off experiments were carried out on the site to establish the spectral content of the vibrations from an individual turbine. During the shut-off period the amplitude of the frequency spectrum from measurements recorded on the turbine clearly dropped (figure 3-16), but the resonant frequencies were still visible, although at a much lower amplitude.

Measurements were recorded over a large range of wind speeds. It was found that at very low wind speeds (around 3.5 m/s) when the wind farm was not generating, the harmonic frequencies could not be seen, however additional frequencies at 4 Hz and 6.7 Hz were apparent. At low wind speeds (around 4.6 m/s), when the wind farm was generating, there were clear signals and side bands on the frequencies possibly due the turbine cutting in and out due to the low wind speed. As the wind picks up (around 7.3 m/s), the harmonic signals were consistently present and could be seen on several of the seismometers. In high wind speeds averaging 11.2 m/s, the signals were very clear and the amplitude increased. Figure 3-17 shows spectrograms from Kelphope 1, 1.2 km from the wind farm,

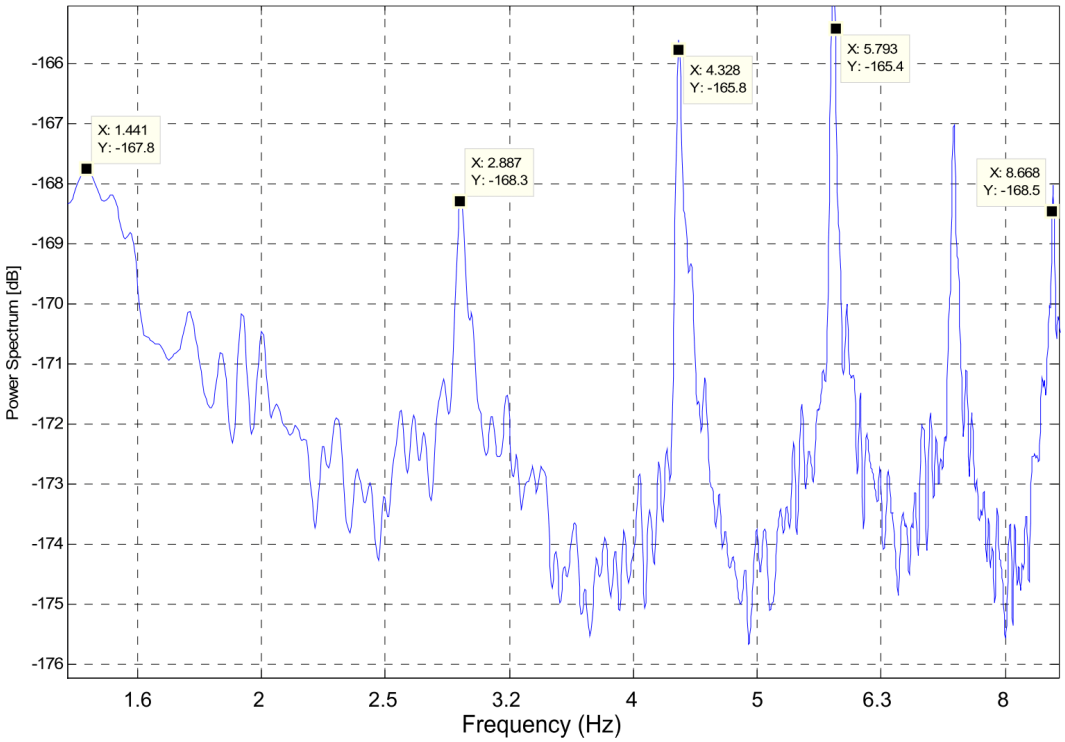

Figure 3-14: *A frequency spectrum (with a log scale on the x-axis) using data obtained at Kelphope 1, 1.2 km from Dun Law (After Styles et al. 2005).*

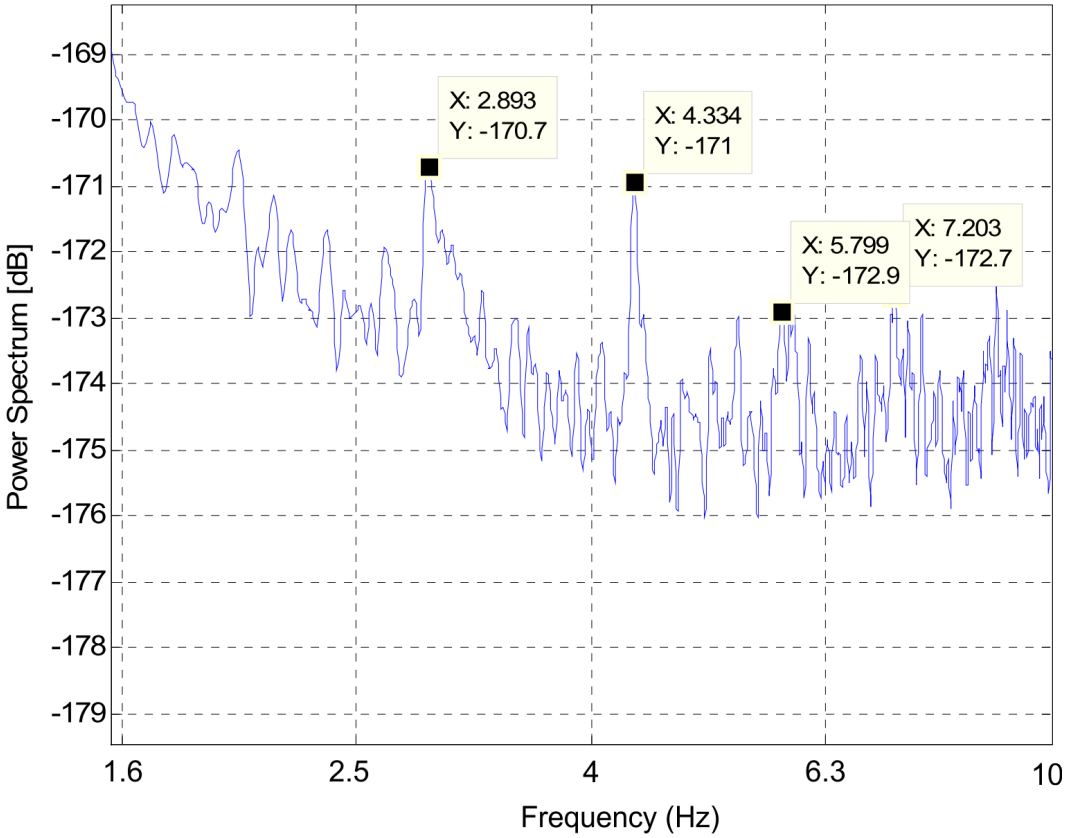

Figure 3-15: *A frequency spectrum (with a log scale on the x-axis) using data obtained at Crib Law 2, 4.4 km from Dun Law (After Styles et al. 2005).*

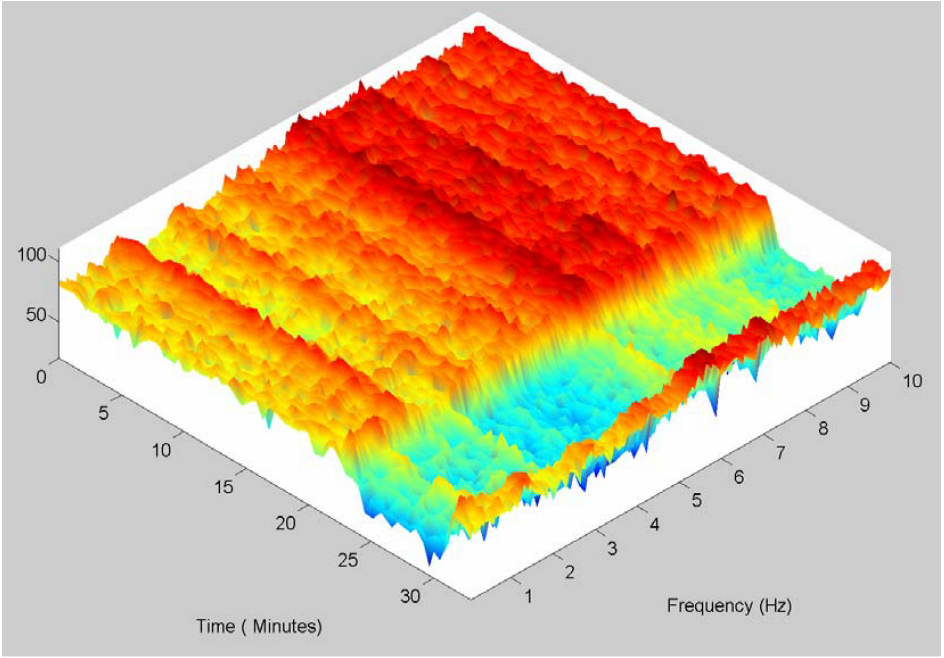

Figure 3-16: *A spectrogram from an on turbine sensor over a shut-down period (starting at 22 minutes) at Dun Law (Styles et al. 2005).*

for the four previously described wind speeds.

Styles et al. (2005) used a $1/\sqrt{r}$ with linear attenuation model (equation (3.5)) to calculate the projected amplitude of a signal at Eskdalemuir from any given wind farm. It is applicable to surface waves radiating out from the turbine uniformly. Different models were tested using the data obtained from field studies and the one presented in Styles et al. (2005) was found to be the best fit and most sensible (Styles, pers comm.).

The model relates the amplitude of the signal at a location far from the turbine, A_{far} to the amplitude of a signal close to the turbine, A_{near}, incorporating the distance the two locations are away from the turbine, the Q-factor and the wave velocity of the underlying geology.

$$A_{far} = A_{near}\sqrt{\frac{R_{near}}{R_{far}}}e^{\left(\frac{\pi f}{Qv}\left(R_{near}-R_{far}\right)\right)}. \tag{3.5}$$

The following statements were made about the model:

- The Stateline wind farm was used as a reference term, with the knowledge that at 1 km, the amplitude is 24 nm. Stateline consisted of 399 wind turbines, rated at 660 kW each. The

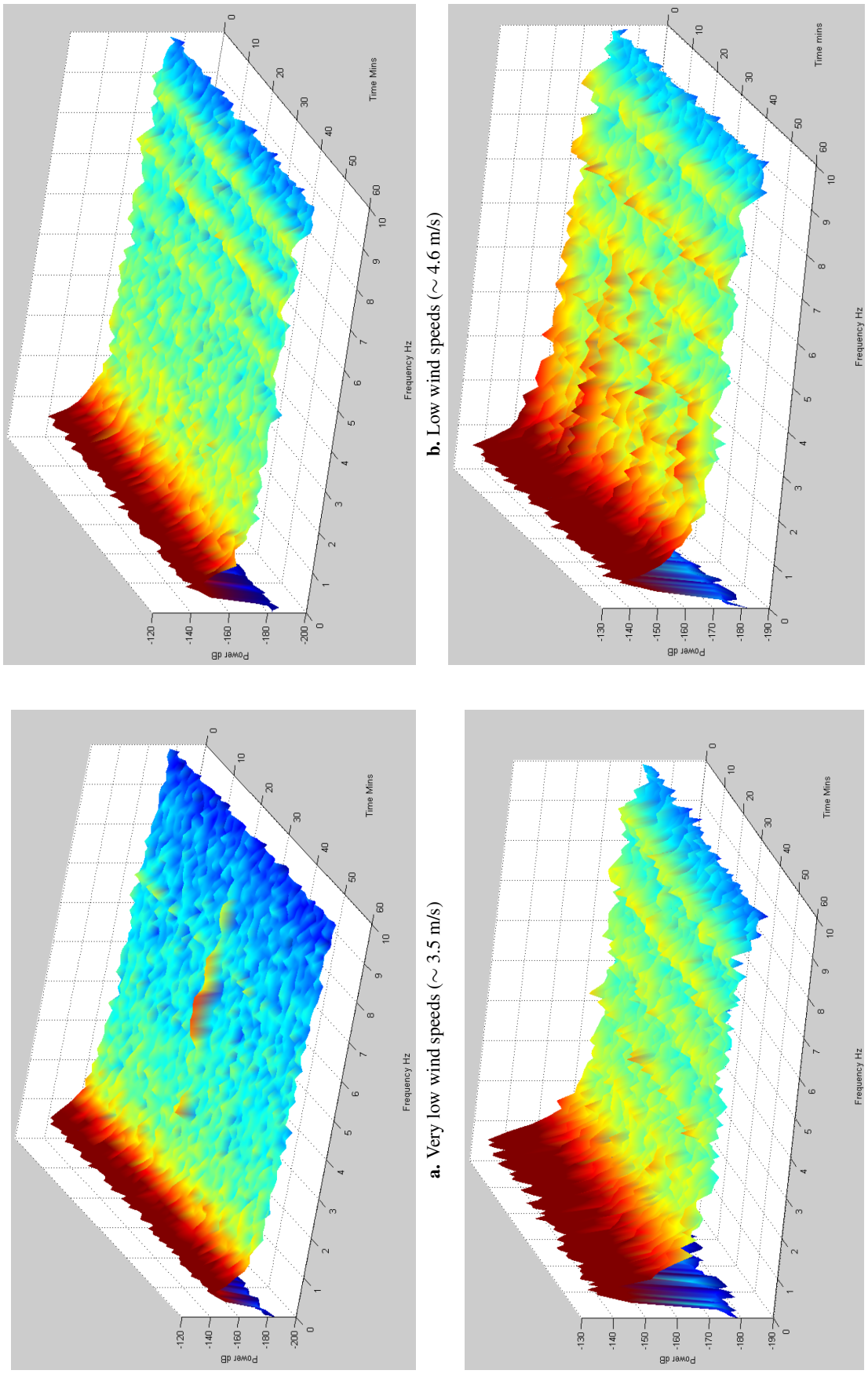

a. Very low wind speeds ($\sim$ 3.5 m/s)

b. Low wind speeds ($\sim$ 4.6 m/s)

c. Medium wind speeds ($\sim$ 7.3 m/s)

d. High wind speeds ($\sim$ 11.2 m/s)

Figure 3-17: *Spectrograms from Kelphope 1, 1.2km from Dun Law, from a range of wind speeds (Styles et al. 2005).*

reference amplitude is defined as

$$A_{ref} = A_0\sqrt{r_0}e^{\left(\frac{-\pi f r_0}{Qv}\right)}. \tag{3.6}$$

- The vibrations generated from the wind turbine were assumed proportional to the power of the turbine. Therefore a power ratio term for the proposed wind farm in relation to Stateline was included within the model.
- It was assumed that the signals from each individual turbine on the wind farm were quasi-random and that the turbines were not in phase. For a wind farm with N_j wind turbines, the model in equation (3.5) would contain an additional $\sqrt{N_j}$ term to account for this. As Stateline was used as a reference, this value is proportional to the total number of wind turbines at Stateline, N_0, giving the ratio $\sqrt{N_j/N_0}$.
- The turbines only exceeds 60% utilisation 20% of time, so a multiplier was included to account for this.

With these points in mind the total amplitude, A_j, at Eskdalemuir from a proposed wind farm at a distance of r_j km away is given by

$$A_j = 0.6A_0\sqrt{\frac{r_0}{r_j}}e^{\left(\frac{-\pi f(r_0-r_j)}{Qv}\right)}\frac{P_j}{P_0}\sqrt{\frac{N_j}{N_0}}, \tag{3.7}$$

where A_0 is the reference amplitude at Stateline, r_0 is the reference distance at Stateline, P_0 is the power of the turbines at Stateline, N_0 is the number of turbines at Stateline, f is the frequency, Q is the Q-factor, v is the ground velocity, r_j is the distance from Eskdalemuir to the proposed wind farm and N_j is the number of turbines on the proposed wind farm.

Multiple wind farms, as with individual turbines do not operate in phase. As such, the total amplitude from M wind farms will sum in quadrature, such that

$$A_M = \sqrt{\sum_{m=1}^{M}(A_{j,m})^2}, \tag{3.8}$$

where A_M is the total predicted amplitude at Eskdalemuir from M wind farms and $A_{j,m}$ is the amplitude of the signal for wind farm m.

As a consequence of the work at Dun Law, a noise budget of 0.336 nm was proposed, equivalent to the noise levels measured at Eskdalemuir on a windy day (Trodd 1998) and applicable to all proposed wind farms within the vicinity of the seismic station. The work at the Stateline wind farm (section 3.1.3) by Schofield (2002) was used as a calibration factor in the extended model to calculate the noise budget. Using the calibrated model, the amplitude of any proposed wind farm could be obtained to see whether the wind farm development would take the total additional noise over the noise budget.

In addition to the noise budget, Styles et al. (2005) proposed the following:

- No wind turbine developments of any kind should be permissible within a 10 km radius of the Eskdalemuir station.
- It was advised that wind turbines of the design that were common at the time of the study should not be permitted within 17.5 km of Eskdalemuir and that in order to maximise capacity this should ideally be 25 km.
- Between 17.5 km and 50 km wind farms could be built providing the total noise budget of 0.336 nm, for all wind farms in the area, was not exceeded.
- Beyond 50 km, it was envisaged that a normal wind farm development would not have a detrimental effect on the station.

3.1.5 Schliekum

There are two gravitational wave detectors in Europe: VIRGO near Pisa, Italy, a joint venture between Italy and France and GEO600 near Hannover, Germany, a joint venture between Germany and Britain. Fiori et al. (2006, 2009) carried out work in 2005 at the Schliekum wind farm near GEO600, 25 km south of Hannover, with the aim of generating a model to predict the effect of a wind farm planned to be constructed near VIRGO. The Schliekum wind farm consists of eight turbines, from two different manufacturers, ranging in size and power. Table 3-1 provides details of the turbines. The average distance from each turbine at Schliekum to the north and central buildings of GEO-600 is 1 km and 1.6 km respectively (figure 3-18).

Manufacturer and Model	N. of turbines	Names	Power [MW]	Tower height [m]	Rotor diameter [m]
Nordex N90	3	Domink, Olem, Malte	2.3	100	90
Nordex S77	2	Daniela, Kerstin	1.5	85	77
EnronWind 1.5s	2	Lutz, Robert	1.5	85	65
EnronWind 1.5	1	Isabelle	1.5	85	65

Table 3-1: *Technical data about each of the wind turbines at the Schliekum wind farm (Fiori et al. 2009)*

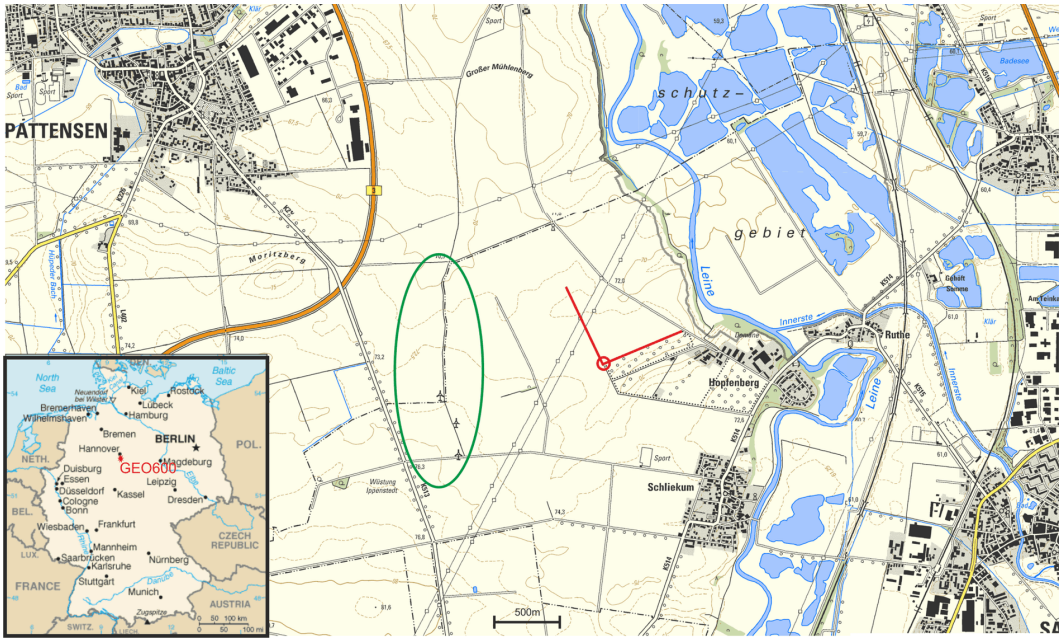

Figure 3-18: *The location of the Schliekum wind farm (green circle) in relation to GEO600 (red circle and lines) (base map courtesy of Outdooractive.com). Inset: Location of GEO600 in Germany (Map courtesy of www.cia.gov).*

Two sets of measurements were obtained during the study. Sercel L-4 1 Hz geophones were used in the first, placed horizontally and vertically on the foundations of each turbine and measurements were taken during a variety of wind conditions. A frequency spectrum for each turbine individually was calculated using the acquired measurements (figure 3-19). Additionally, an assessment was made as to how the spectrum changes with increasing wind speeds (figure 3-20). Fiori et al. (2009) identified the first and second modes of each turbine as listed in table 3-2. The wind speed data show that the general amplitude of the spectrum increases with wind speed and that even when the turbine is not operational, some peaks are still visible, agreeing with the finding made at St Breock Downs and Dun Law (sections 3.1.2 and 3.1.4).

The second experiment involved deploying three Strecheisen STS2 low frequency three-component accelerometers on the floor of each GEO600 building and two Lennartz 3D/5s seismometers to take measurements for at least eight hours continuously, at thirteen locations up to 5 km away from the

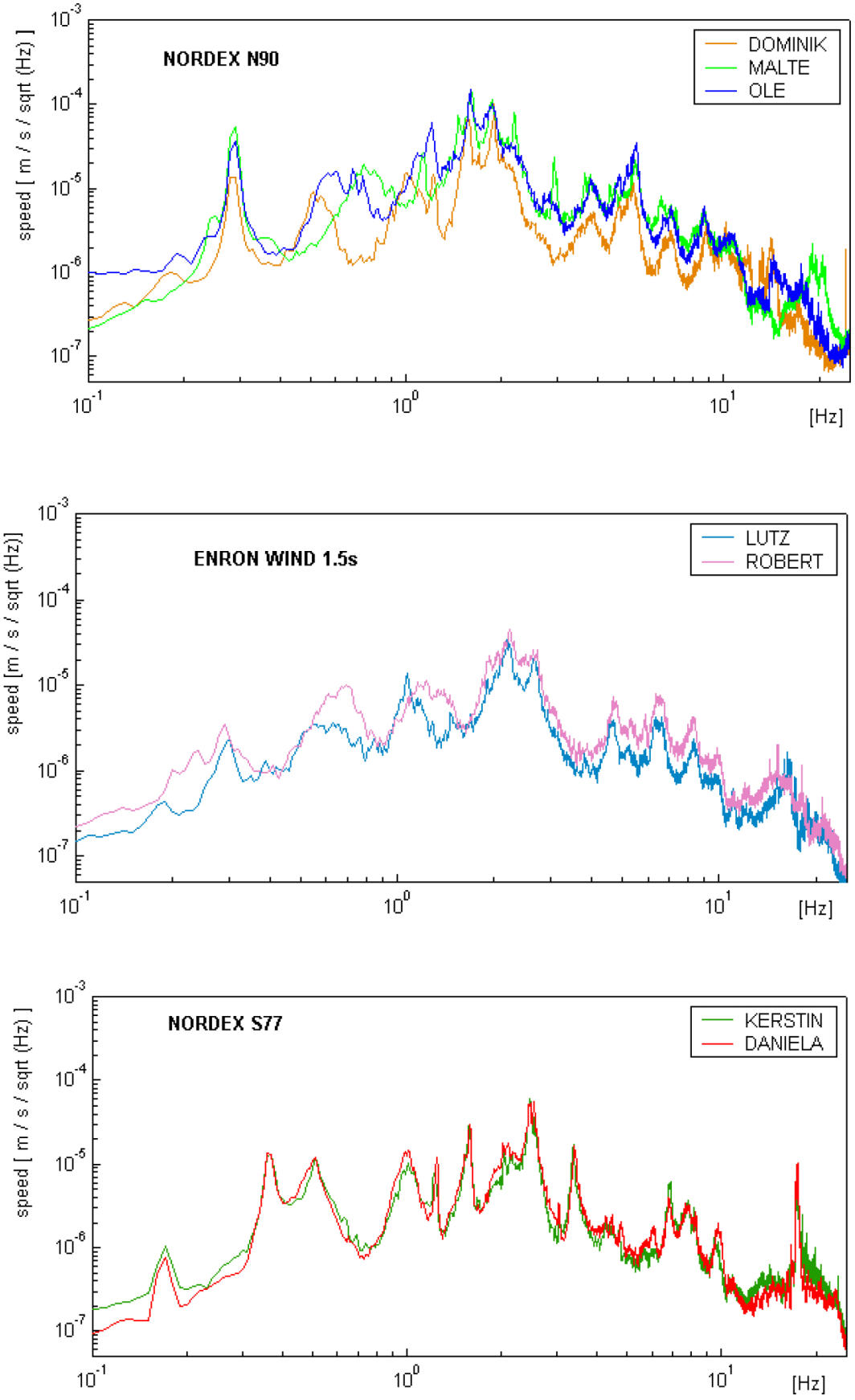

Figure 3-19: *The individual frequency spectra from the Schliekum turbines (Fiori et al. 2009)*

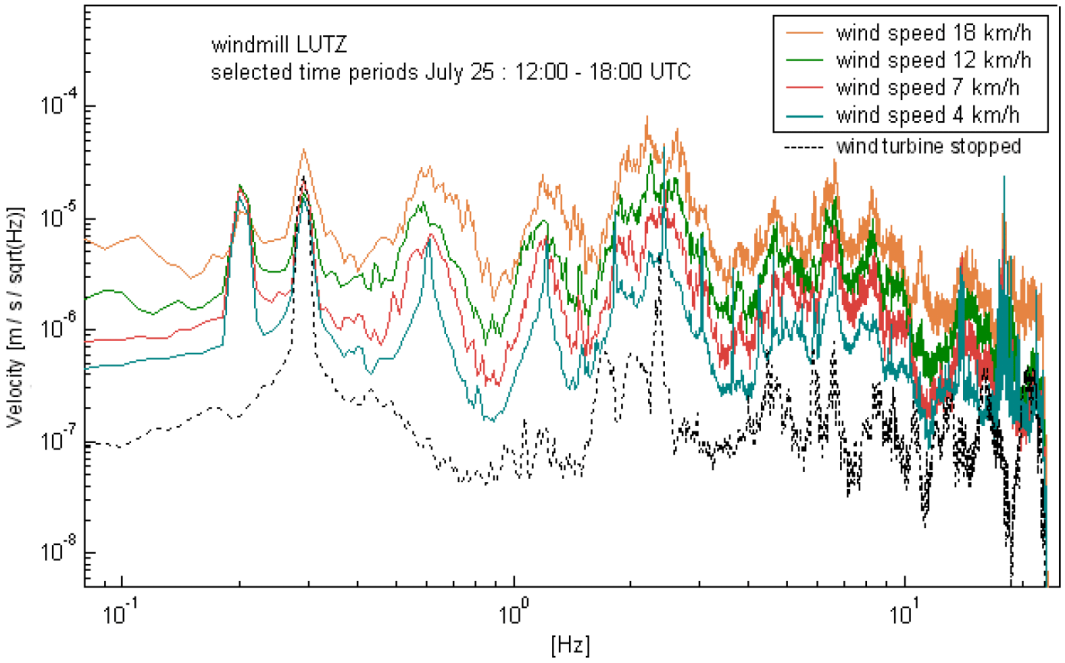

Figure 3-20: *A frequency spectra generated from measurements obtained at the base of one of the EnronWind 1.5s wind turbines on the Schliekum wind farm under different wind conditions (Fiori et al. 2009).*

Turbine	First mode	Second mode
Nordex S77	0.37	2.45
Nordex N90	0.29	1.9
EnronWind 1.5	0.29	2.3
EnronWind 1.5s	0.29	2.2

Table 3-2: *The first and second bending mode frequencies for each of the turbine models at Schliekum as identified by Fiori et al. (2009).*

wind farm. These distances mean that most of the measurements were recorded in the near-field of the wind farm. Fiori et al. (2009) find a distinct peak at 0.3 Hz, with the amplitudes of the spectral components between 2 Hz and 10 Hz generally decreasing with distance.

In order to calculate the effects of the proposed wind farm on VIRGO, a $1/\sqrt{r}$ with linear attenuation model (equation (3.2)) was used. The model was calculated with respect to a reference turbine of power P_0, producing a signal with amplitude A_0 at a reference distance r_0, such that

$$A_{ij} = \frac{K}{\sqrt{R_{ij}}} P_i e^{\left(\frac{-\pi f R_{ij}}{Q v}\right)}, \tag{3.9}$$

where A_{ij} is the predicted amplitude of the signal at location j from turbine i, R_{ij} is the distance of turbine i from location j, P_i is the power of turbine i, f is the frequency of interest, Q is the Q-factor, v is the wave velocity through the underlying geology of the proposed wind farm and

$$K = A_0\sqrt{r_0}\frac{1}{P_0}e^{\left(\frac{-\pi f r_0}{Q v}\right)}. \tag{3.10}$$

Multiple turbine signals are combined in quadrature so that the total amplitude of the complete wind farm is given by

$$A_j = \sqrt{\sum_i (A_{ij})^2}. \tag{3.11}$$

Using this model and a reference turbine on the Schliekum wind farm, Fiori et al. (2009) calculated that the proposed wind farm would have an effect on VIRGO if placed within 4 km and recommended a minimum distance of 6 km from each of the VIRGO buildings.

The proposed farm was installed by mid-2008 and plans had been submitted for an additional three 2 MW turbines. In 2009, Saccorotti et al. (2011) conducted measurements at VIRGO to determine the nature and attenuation of the seismic signals from the existing wind farm. A combination of three component seismometers and accelerometers were placed at fourteen locations, of which three were fixed for the entire three week recording period.

Prominent peaks at approximately 1.7 Hz, 3 Hz, 4 Hz, 5.5 Hz and 7 Hz were seen on a frequency spectrum (figure 3-21) generated using data gathered on a seismometer located at site 931E (shown in relation to VIRGO and the wind turbines in figure 3-22). The spectrum generated during the night using data collected during the day from the same site is more noisy and broadband, which Saccorotti et al. (2011) attribute to human noise.

When comparing the data against wind speed, Saccorotti et al. (2011) state that there is a good correlation between this and seismic amplitude above 1 Hz. However this was not the case for the peak at 0.45 Hz where it was suggested that ocean noise is the most likely source.

Comparison of two data sets collected on different sensors, one under the turbine and the other at 931E, over wind speeds of around 3 m/s and 11 m/s, lead to the conclusion that the peaks other than the one at 1.7 Hz are either not related to the wind farm or are reflected, modifying the spectral composition of the signal.

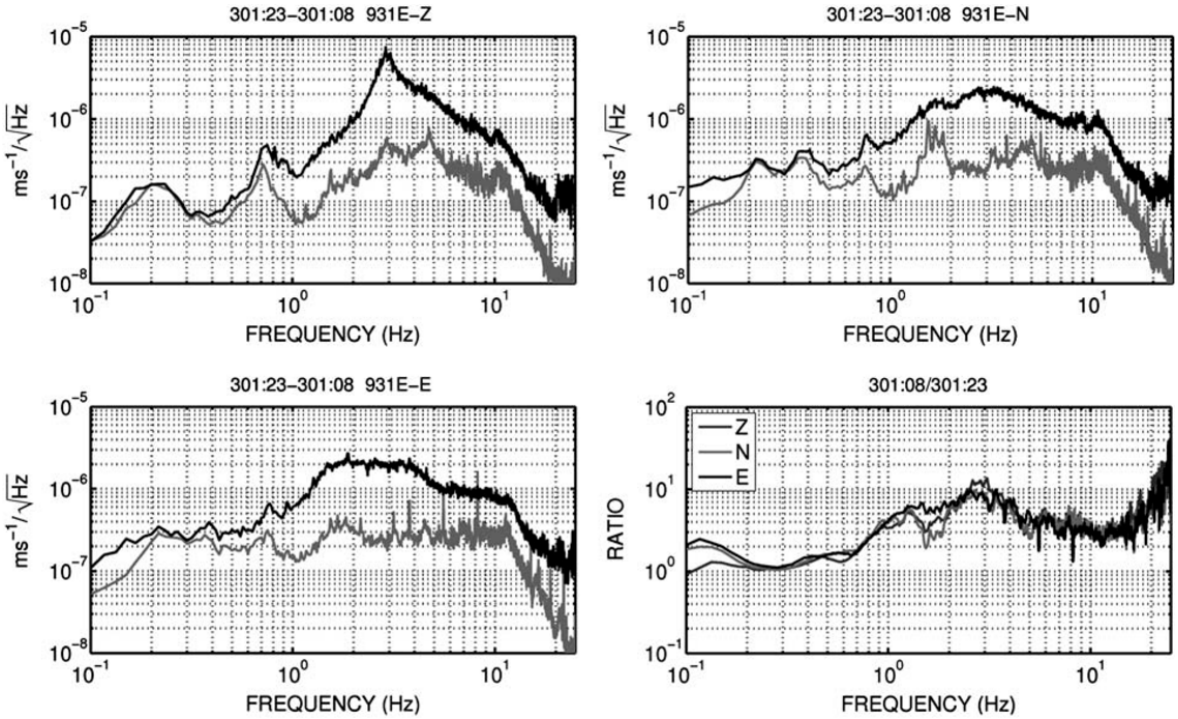

Figure 3-21: *A comparison of day and night frequency spectra for the three-components of the 931E sensor. The fourth image (bottom right) is the spectral ratio between the day and night measurements for each component (Saccorotti et al. 2011).*

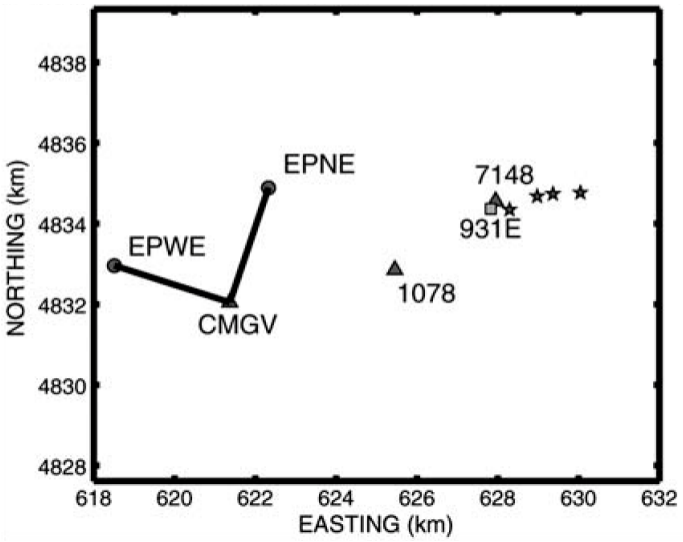

Figure 3-22: *The configuration of the VIRGO antenna and locations of the monitoring sites. Triangles are Güralp CMG-40T broadband seismometers, Square is a Lennartz Le3D-5s seismometer and the stars are the positions of the four wind turbines (Saccorotti et al. 2011).*

Saccorotti et al. (2011) made the following assumptions when deriving a model which incorporated surface and body waves.

1. the turbines all generate a signal with the same amplitude;
2. the signals from the turbines are in phase, which means that they will constructively interfere;
3. the energy is split equally between body and surface waves;
4. local effects on the amplitude of the signal are negligible.

The general $1/\sqrt{r}$ with linear attenuation model was used for surface waves, such that

$$A_D = A_0\sqrt{r_0}e^{-\frac{\pi f r_0}{Q_0 v_0}}, \tag{3.12}$$

but the model expanded for body waves, such that

$$A_R = A_0(2r_1 + r_2)^{-n}e^{\left(-\frac{2\pi r_1 f}{Q_1 v_1} - \frac{2\pi r_2 f}{Q_2 v_2}\right)}, \tag{3.13}$$

where A_0 is the reference amplitude at location r_0, n is the geometrical spreading coefficient, Q_1 and v_1 are the Q-factor and shear-wave velocity through the middle layer and Q_2 and v_2 are the Q-factor and shear-wave velocity through the half-space (figure 3-23).

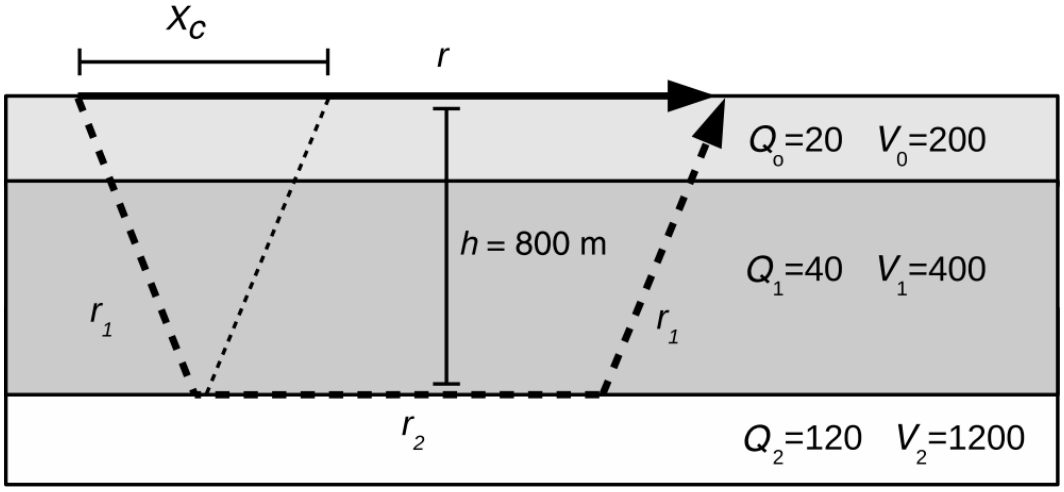

Figure 3-23: *A sketch of the Saccorotti et al. (2011) propagation model, assuming that waves from the turbine propagate as surface and body waves, refracted at an interface. Q_n and v_n are the Q-factor and wave velocity for each layer respectively, x_c is the critical distance, r is the distance from the wind turbine to the sensor and h is the thickness of the middle layer.*

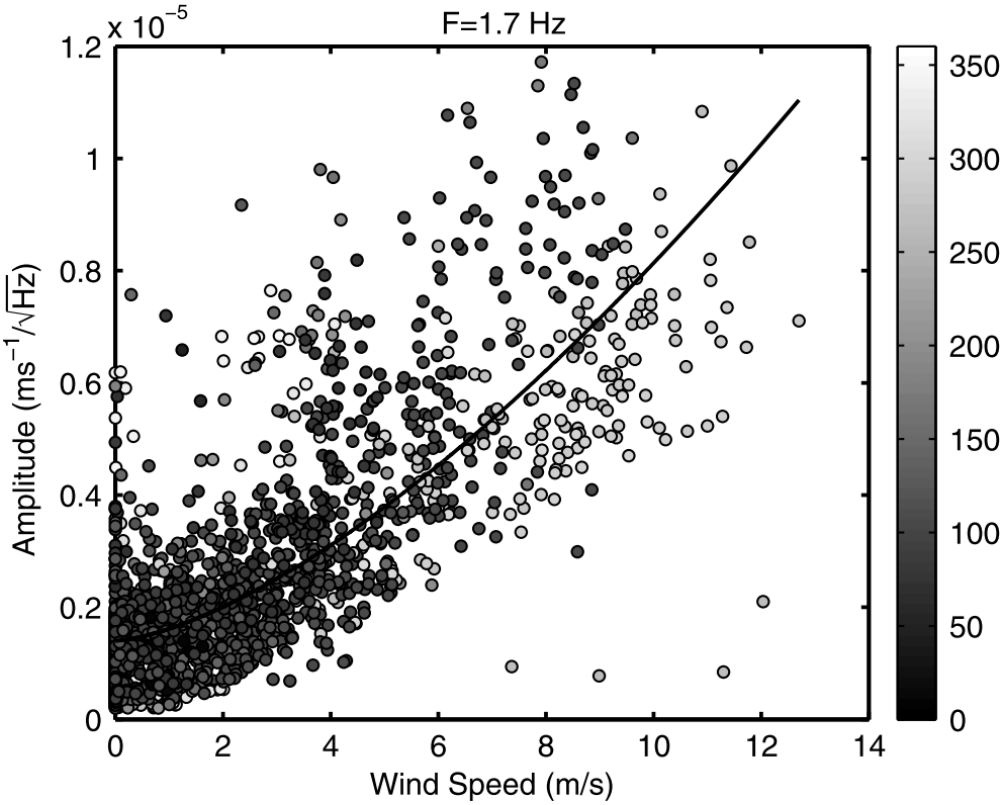

Figure 3-24: *The relationship between seismic amplitude and wind speed with a power curve fitted to the data (Saccorotti et al. 2011).*

For a wind farm of N turbines, each vibrating with an amplitude A_0 and located at distance r_i, $i = 1 \ldots N$, then the amplitude would be

$$A_j = A_0 \sum_{i=1}^{N} \left(A_{D,i} + A_{R,i} \right). \tag{3.14}$$

By defining a power law which relates seismic amplitude to wind speed (figure 3-24) as

$$A_s = c + aW^{3/2}, \tag{3.15}$$

and substituting this value into equation (3.14), Saccorotti et al. (2011) derived a model which relates seismic amplitude to wind speed for any configuration of wind turbines.

3.1.6 Discussion

Previous studies have shown that large wind turbines generate low frequency vibrations which are propagated many kilometres through the ground. However, the frequencies that are generated are not consistent through all turbine types. Table 3-3 provides a summary of the prominent frequencies generated by different turbines.

Apart from the EnronWind turbine, the frequency spectrum for each of the other turbines contains a peak at around 0.5 Hz. Similarly the turbines other than the Nordex contain peaks at around 4.5 Hz. This is in the middle of the frequency band of concern for the Eskdalemuir station.

The Nordex S77 and the EnronWind 1.5s both have the same power and hub height, but the only frequencies common to both occur at 1Hz, 2.2-2.4 Hz and 6.5-6.9 Hz, these may be the resonant frequencies of the tower, which could explain the similarity. Likewise, the Mitsubishi and Bonus wind turbines have very close hub heights and frequencies which agree at around 0.5 Hz and 4.5 Hz, so it is likely that these relate to the first and second bending modes of the tower. The Vestas, just 8 m taller than the Mitsubishi and Bonus has frequencies close to these at 0.669 Hz and 4.34 Hz.

This shows that all large turbines generate vibrations of about the same frequency. Further research looking at turbines of different power, hub height and rpm could refine the attenuation algorithms discussed in section 3.1.6.1 or exclude certain types of turbine from the restrictions at Eskdalemuir if they do not generate this frequency.

Turbine	Power	Hub Height	Diameter	rpm	Frequencies (Hz)
Mitsubishi	0.3MW	31m	29m	43	0.5, 1, 2.15, 4.3, 6.5, 8.7, 10.8
Bonus	0.45MW	32m	35m	34	0.5, 3, 4.5, 6, 7.5
Vestas V47	0.66MW	40m	47m	28.5	0.669, 1.47, 2.95, 4.34, 5.88, 7.35, 11
Nordex S77	1.5MW	85m	77m	9.9-17.3	0.37, 0.51, 1, 1.2, 1.5, 2.45, 3.4, 6.9
EnronWind 1.5s	1.5MW	85m	65m	11-20	0.29, 1, 2.2, 4.5, 6.5, 8
Nordex N90	2.3MW	100m	90m	9.6-16.8	0.29, 0.45, 1.2, 3, 5.1, 6.8, 8.9

Table 3-3: *The respective prominent frequencies of various wind turbines (Data from Styles 1996, Schofield 2002, Styles et al. 2005, Fiori et al. 2006)*

3.1.6.1 Attenuation Models

Four of the studies (Schofield 2002, Styles et al. 2005, Fiori et al. 2009, Saccorotti et al. 2011) have proposed attenuation models to calculate the total amplitude of signals from a wind farm on a proposed site.

Schofield (2002) investigated three base attenuation models and opted for the $1/r$ model, due to this fitting best at 4.3Hz. This selection contradicts what is stated later in the paper, as this model is for propagation through a volume, such as air and as such would mean that frequencies are transmitted in the form of infrasound which couples to the ground, but Schofield states that infrasound coupling could not account for the peak.

Styles et al. (2005) and Fiori et al. (2009) both apply a $1/\sqrt{r}$ with linear attenuation base model, thus assuming propagation along the surface, with the signal attenuating linearly as surface waves, then

$$A_{ij} = A_0 \sqrt{\frac{r_0}{R_{ij}}} e^{\left(\frac{-\pi f(R_{ij}+r_0)}{Qv}\right)}. \tag{3.16}$$

The final models obtained by Fiori et al. (2009) and Styles et al. (2005) have been rearranged into a one line equation, so that they are easier to compare and are summarised in equations (3.17) and (3.18) respectively,

$$A_{ij} = A_0 \frac{\sqrt{r_0}}{\sqrt{R_{ij}}} e^{\left(\frac{-\pi f(r_0-R_{ij})}{Qv}\right)} \frac{P_i}{P_0}, \tag{3.17}$$

$$A_j = A_0 \sqrt{\frac{r_0}{r_j}} e^{\left(\frac{-\pi f(r_0-r_j)}{Qv}\right)} \frac{P_j}{P_0} \sqrt{\frac{N_j}{N_0}}. \tag{3.18}$$

The main difference between these two models is that the Fiori et al. (2009) model (equation (3.17)) is for a single turbine, with multiple turbines added in quadrature. Whereas the Styles et al. (2005) model (equation (3.18)) is based on a wind farm, with multiple wind farms added in quadrature. As this model is defined relative to the Stateline wind farm, there is an additional $\sqrt{\frac{N_j}{N_0}}$ term which represents the number of wind turbines at the wind farm as a ratio to the number of turbines at Stateline.

Saccorotti et al. (2011) claimed that the vibrations from turbines are propagated as both surface and body waves, with the equation for seismic amplitude as a function of frequency and distance being

$$A_j = A_0 \left(\frac{1}{\sqrt{r_0}} e^{\left(-\frac{\pi f r_0}{Q_0 v_0}\right)} + (2r_1 + r_2)^{-n} e^{\left(-\frac{2\pi r_1 f}{Q_1 v_1} - \frac{2\pi r_2 f}{Q_2 v_2}\right)} \right). \tag{3.19}$$

This is based on the following assumptions holding

1. the amplitude generated by each of the wind turbines is identical;
2. the signals from the turbines are in phase and will sum constructively;
3. there is an equal split between body and surface waves and no other type of wave;
4. local effects on the amplitude of the signal are negligible.

Other work (Fiori et al. 2009) has shown that the amplitude of the signal generated by different turbines of the same type is not always consistent (figure 3-19), hence contradicting item 1 above. In addition, wind turbines do not sum constructively and are not in phase. They are quasi-random sources and sum in quadrature (Schofield 2002, Styles et al. 2005), not linearly as assumed by item 2. Saccorotti et al. (2011) state this to be the case in their conclusions and that assuming an in-phase scenario would provide an overestimation of the amplitude for each of the turbines, however when comparing this overestimation with the assumptions in items 3 and 4, they claim that the overestimation is not relevant.

3.1.6.2 Wind Speed and Direction Analysis

The power law established by Saccorotti et al. (2011), which defines seismic amplitude as proportional to wind to the power $3/2$, agrees with Schofield (2002). However, it is not well constrained, as shown in figure 3-24 on page 64 and much scatter is present in the field data, with the possibility of many curves appearing to fit the data. Neither Saccorotti et al. (2011) nor Schofield (2002) analysed wind direction with respect to seismic amplitude, which may better constrain the power law. Each of the papers that discuss the effect of wind in relation to seismic amplitude use a narrow range of wind speeds, ie 9 m/s to 14 m/s at St Breock Downs and comparison of wind speed of 3 m/s and 11 m/s at two different locations in Saccorotti et al. (2011). Although Saccorotti et al. (2011) use a range

of wind speeds from 0 m/s to 12 m/s for the power law derivation, the predominant speeds are only 0 m/s to 5 m/s, the data points are less dense and the scatter greater in the higher wind speeds. In order to gain a better understanding of the effect of wind speed on seismic amplitude, a broader range of wind speeds would be required using a larger dataset.

3.2 Microseismic Monitoring of Ground Vibration and its Effects on Sensitive Scientific Equipment

Some scientific equipment can be very sensitive to small movements in the ground. At these facilities, general ground vibration measurements of the site can assist in the choice of site location or in developing techniques to mitigate any vibrations which may be present. This is particularly relevant to synchrotron radiation centres, where the accelerator components related to the beams are particularly sensitive to ground motion. The techniques used in these studies are similar to those used when studying the effects of wind farm vibrations.

3.2.1 Diamond - the UK's National Synchrotron Facility

The Diamond Light Source is the UK's national synchrotron facility and is located at the Harwell Science and Innovation Campus in Oxfordshire. The Diamond facility was opened in 2007 and is used for industrial and academic research, with over 200 researchers using the facility (Diamond Light Source 2011).

Studies of the ground vibration at Diamond have been carried out in order to improve the beam stability of the facility and to aid in designing systems to mitigate the vibrational effects. Balmer et al. (2000) took measurements at locations adjacent to the building housing the Synchrotron source, on the edge of the site near a busy road and on a quiet part of the site during the night. All recordings were made using a Güralp CMG-3T triaxial seismometer.

A displacement power spectral density (PSD) function (section 2.4.5) was used to analyse the results (figure 3-25). This shows that during the night the amplitude of frequencies above 1 Hz drops. Above

10 Hz, there are a broad range of frequencies which can be attributed to the nearby major road. Some peaks were visible at all sites and Balmer et al. (2000) attribute this to noise from the operation of the synchrotron itself.

Bartolini et al. (2008) report on an investigation using mini-seismometers attached to the ground and machine girders of Diamond. Fast acquisition beam position data was used to obtain measurements of the beam position. There are prominent peaks visible in the displacement power spectral density graph generated from the measured data (figure 3-26), through all sensors. The peak at 16 Hz is identified as originating from air conditioning units and circulating pumps were identified as the dominant source of the 25 Hz peak. No prominent peaks in the ground motion data are seen above 30 Hz.

Both works identify sources linked to the operation of the synchrotron as contributing significantly to the vibrations detected during the experiments.

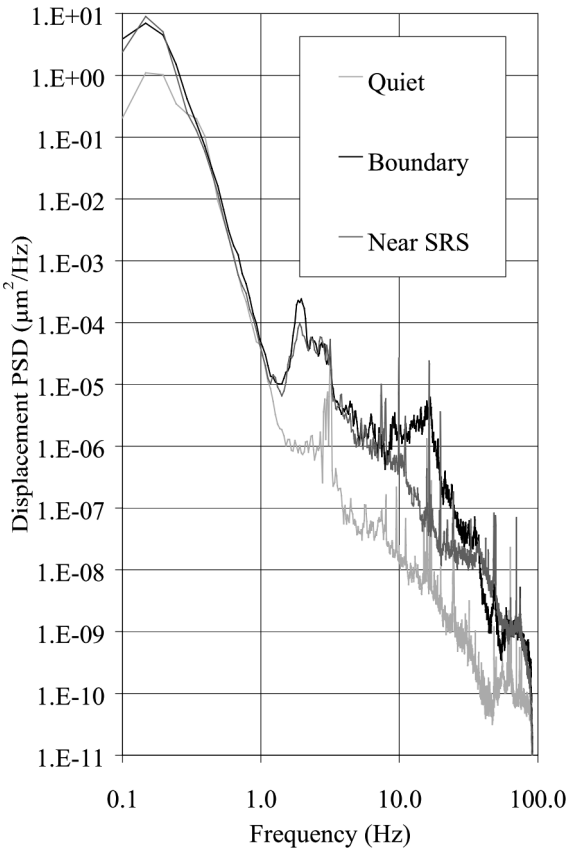

Figure 3-25: *Displacement PSD from measurements taken at Daresbury Laboratory (Balmer et al. 2000).*

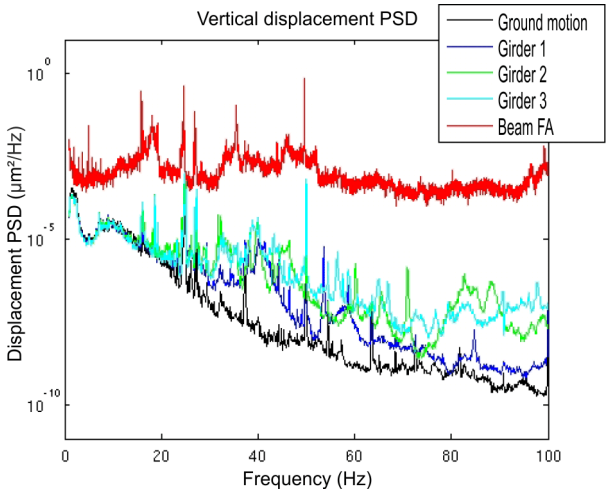

Figure 3-26: *Vertical PSD from measurements taken on the ground, girder and beam motion at Diamond (Bartolini et al. 2008).*

3.2.2 European Synchrotron Radiation Facility (ESRF)

The European Synchrotron Radiation Facility (ESRF) is located in Grenoble, France and is a joint venture between twelve European countries. Zhang (2000) conducted an investigation to measure the ground vibration at ESRF and compared the results with measurements recorded simultaneously at two other synchrotron facilities, SuperACO and Orme des Merisiers near Paris.

Data were collected over a period of sixty hours at the three sites using a RefTek 72A-06 data acquisition system combined with a Güralp CMG-3ESP seismometer and a Mark Products L4C geophone. Time integration and high-pass filtering was performed on the data in order to obtain the peak-to-peak displacement (figure 3-27).

Frequency spectra were calculated for each site, using an FFT window length of 16.384 seconds (4096 data points) and a window overlap of fourteen seconds, in order to find the principal frequencies (figure 3-28), which vary considerably between sites. The spectrum for ESRF contains two main peaks at 2.92 Hz and 16.4 Hz, whereas the two Paris sites contain more, with Orme des Mersiers having peaks at 12.2 Hz, 24.3 Hz, 49.3 Hz and SuperACO having peaks at 6.9 Hz, 12.7 Hz, 24.8 Hz, 33.1 Hz, 34.2 Hz, 46 Hz and 48.5 Hz. Possible sources of these vibrational peaks are identified by Zhang & Lesourd (2005) as being from either internal sources, such as vacuum pumps or water cooling sources, or external sources such as an earthquake, the sewer covers in the road surface near the site or large machinery nearby.

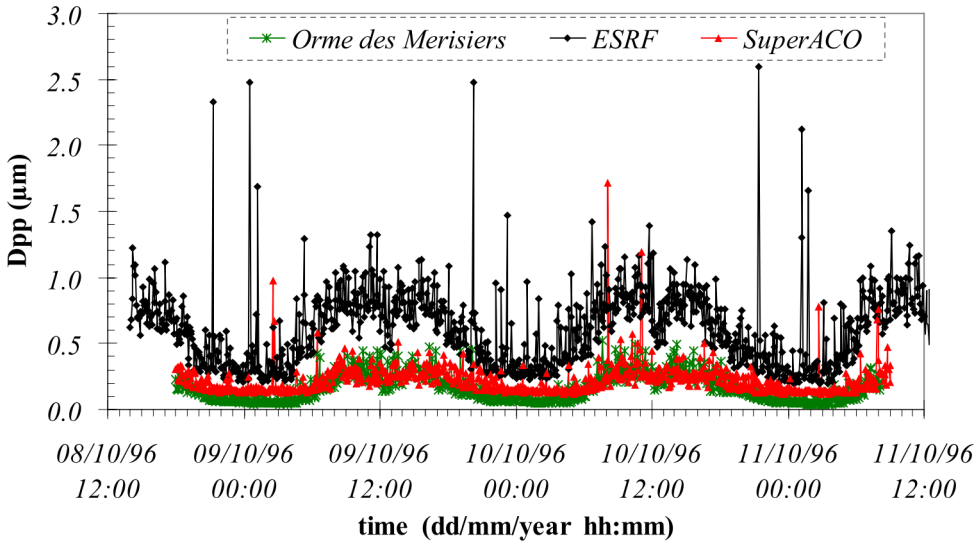

Figure 3-27: *Peak-to-peak displacement at ESRF, Orme des Mersiers and SuperACO with respect to time (Zhang 2000)*

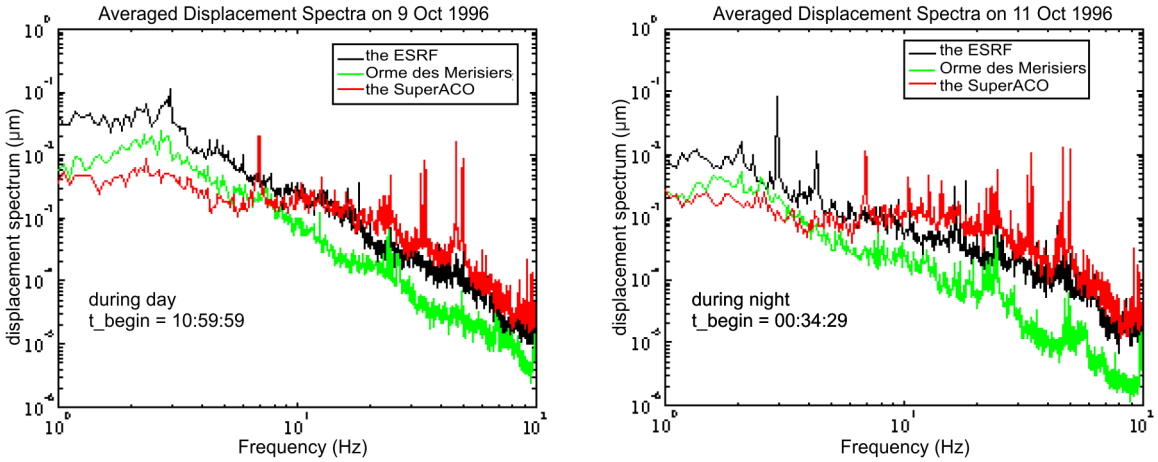

Figure 3-28: *Spectral displacement plots at the three sites (Zhang 2000)*

In order to reduce the effect of these vibrations on ESRF, damping has been applied to the machine girder and mirrors. Further measurements, conducted by Zhang & Lesourd (2005), show that these mitigation techniques have reduced the vibrational effects on the equipment significantly. By installing a damping plate on the machine girder, the frequency response is reduced by a factor of ten (see figure 3-29) and the damping links on the mirrors remove many of the prominent frequency peaks (see figure 3-30).

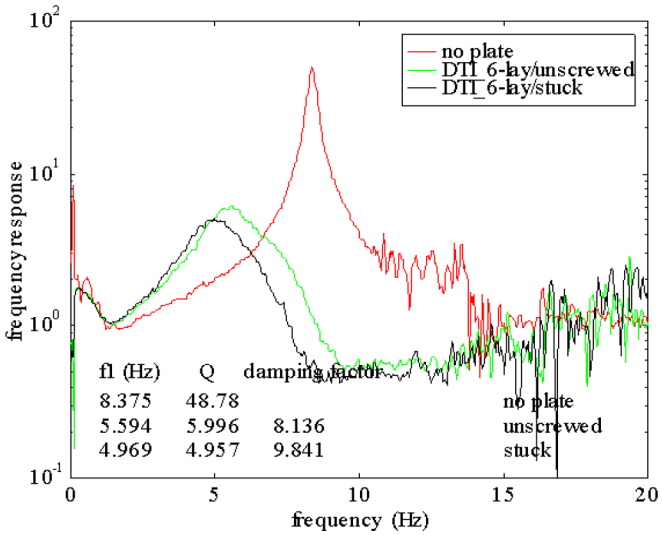

Figure 3-29: *Frequency spectra before and after damping plates were applied to the machine girder at ESRF (Zhang & Lesourd 2005).*

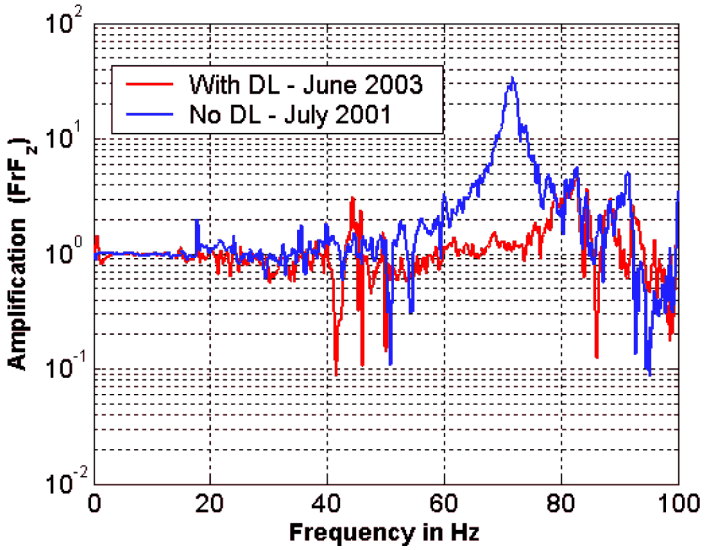

Figure 3-30: *Frequency spectra before and after the damping link (DL) was applied to the mirrors at ESRF (Zhang & Lesourd 2005).*

Chapter 4

Equipment and Data Processing

Four small wind turbines (the Gaia-Wind 133 tubular tower at Wigton, Cumbria, the Gaia-Wind 133 lattice tower near Melrose in the Scottish Borders, the Proven 35-2 at Kilmarnock in East Ayrshire and the Endurance E-3120 near Hayle in Cornwall) have been monitored at locations around the UK in order to assess the vibrations they generate and the propagation of them through the ground. The turbine specifications, location, sensor deployment and results of the monitoring are discussed in chapter 5.

There are certain procedures which are common to the monitoring of each of the wind turbines, these are discussed in the rest of this chapter. It is important that sites are selected carefully and section 4.1 provides the site selection criteria used for the turbines in this project. Section 4.2 details the equipment used for monitoring and is followed by an explanation of the standard deployment of each piece of equipment in section 4.3. In order to ensure that the results from each site can be compared precisely, standard field data processing procedures are defined. These are explained in section 4.4. Finally the predicted spectral content for each turbine is given in section 4.5.

4.1 Site Selection Criteria

The sites of the turbines were chosen based on a number of criteria:

1. Permission from the landowner to access the wind turbine and request for them to keep all livestock away from the turbine and sensors for the monitoring period.
2. A secure site where sensors can be left for a week without being tampered with. Ideally the site should be away from public footpaths.
3. A seismically quiet site is required in order to be able to detect signals, however it is not always possible to tell this until the data is analysed.
4. The further the site can be away from main roads, railway lines, etc, the better, as any additional sources of vibration can interfere with or mask the signals.
5. The site should not be close to any other wind turbines or farms, which is becoming much more difficult.

It was not always possible to achieve all of these criteria for each site, as contact with the land owner was initially established through the manufacturer of the turbine and the number of sites they provided to choose from for each wind turbine was limited.

At the start of the project access to mains electricity within 100 m of the turbine was also required. This was needed in order to power the CMG-DM24S12AMS. However, as the project developed, new equipment was purchased - the CMG-DM24S6EAM - which is powered from 12v batteries, eliminating this requirement.

4.2 Equipment

In this study, a combination of broadband seismometers, three-component and single-component accelerometers and an anemometer are used when monitoring a wind turbine.

The investigations by Schofield (2002), Styles et al. (2005) and Fiori et al. (2006, 2009) have all used broadband seismometers to study ground-borne vibrations from wind turbines. These were shown

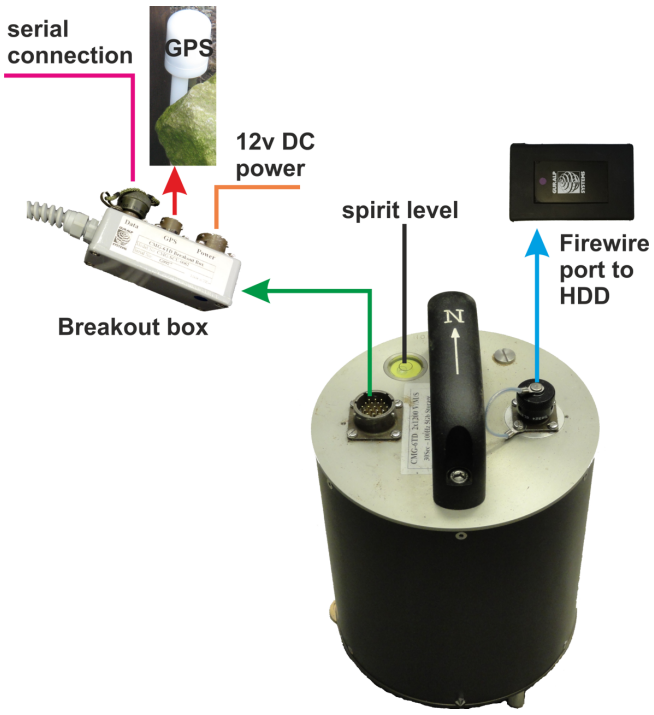

Figure 4-1: *The Güralp CMG-6TD broadband seismometer with details of the input and output ports*

to work well for this type of investigation, so a Güralp CMG-6TD was deployed at each site. The Güralp CMG-5U single-component accelerometers are small enough to be able to be attached to the tower without interfering with the vibrations and can also be used in the ground, although they are more suited to strong motion areas (like on the tower). They have a higher noise floor than the 6TD, making them not as sensitive in the ground as 6TDs.

4.2.1 Broadband Seismometer

The Güralp CMG-6TD is a lightweight three-component broadband seismometer (figure 4-1). Three-component seismometers have the ability to measure the horizontal (north/south and east/west) and vertical components simultaneously. The CMG-6TD has axes orthogonal to within a tolerance of less than 0.1°. It contains an on-board 24-bit digitiser which converts ground motion to digital data and internal flash memory which enables data to be stored continuously to disk or transmitted via the serial data connection. The seismometer is low power, enabling it to be powered from a single 12v car battery for a month. It is ideally suited to medium-noise sites (Güralp Systems Limited 2010). The seismometer is attached to an external GPS antenna for accurate time synchronisation.

4.2.2 Single- and Three- Component Accelerometers

The Güralp CMG-DM24S12AMS acquisition system contains two, six-channel 24-bit digitisers and has the ability to record from up to 12 analogue CMG-5U single-axis accelerometers and six digital inputs, such as the three-component CMG-5TD accelerometer. Figure 4-2 shows a typical set up of inputs and outputs.

The system contains a built-in laptop with Güralp's Scream! software installed. The software provides the capability to view and record incoming data from the sensors. The box is powered from a 110-250v AC mains supply or 12v DC power source.

The Güralp CMG-DM24S6EAM is a low noise digitiser combined with a USB hard disk drive. It has the capability to record data from two three-component instruments connected directly or six single-component sensors via two external junction boxes. The digitiser can record in GCF (section 4.4.1.1) or miniSEED format and is controlled via a web interface. It is powered from a 12v DC power source. Figure 4-3 shows a typical set up of inputs and outputs.

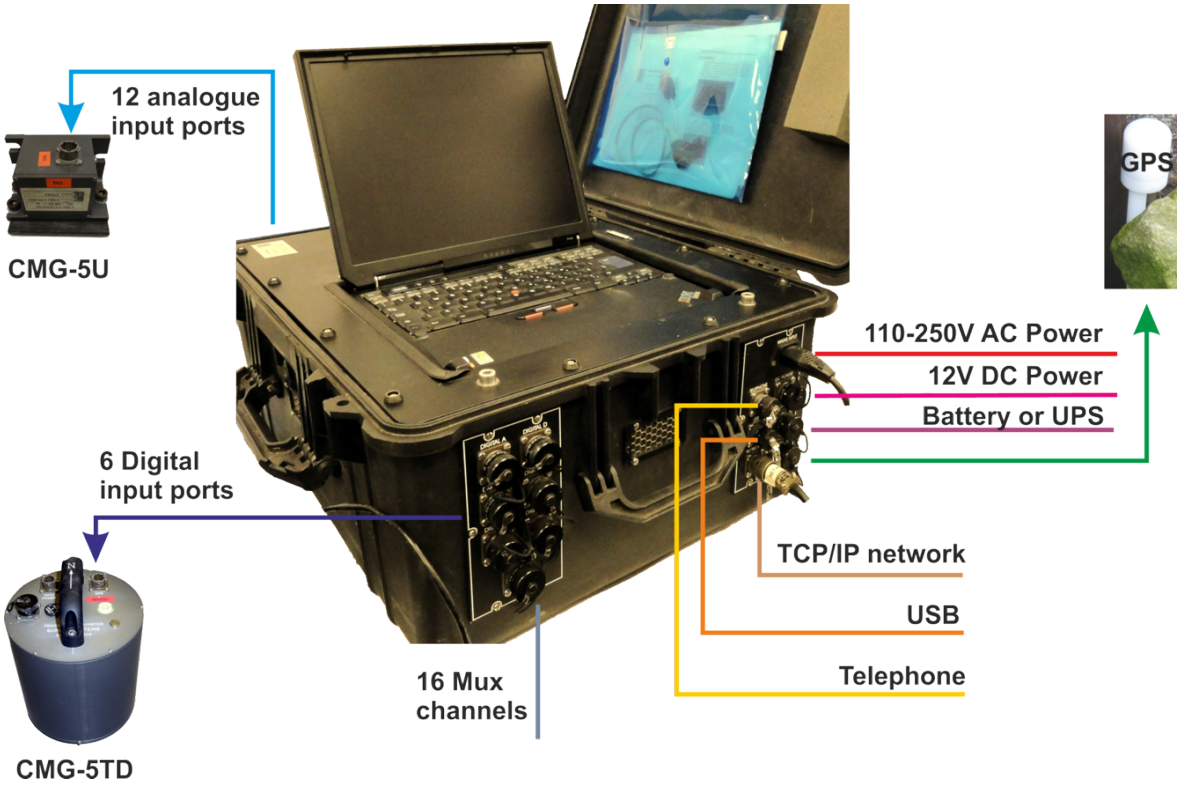

Figure 4-2: *The Güralp CMG-DM24S12AMS acquisition system with details of the input and output ports available*

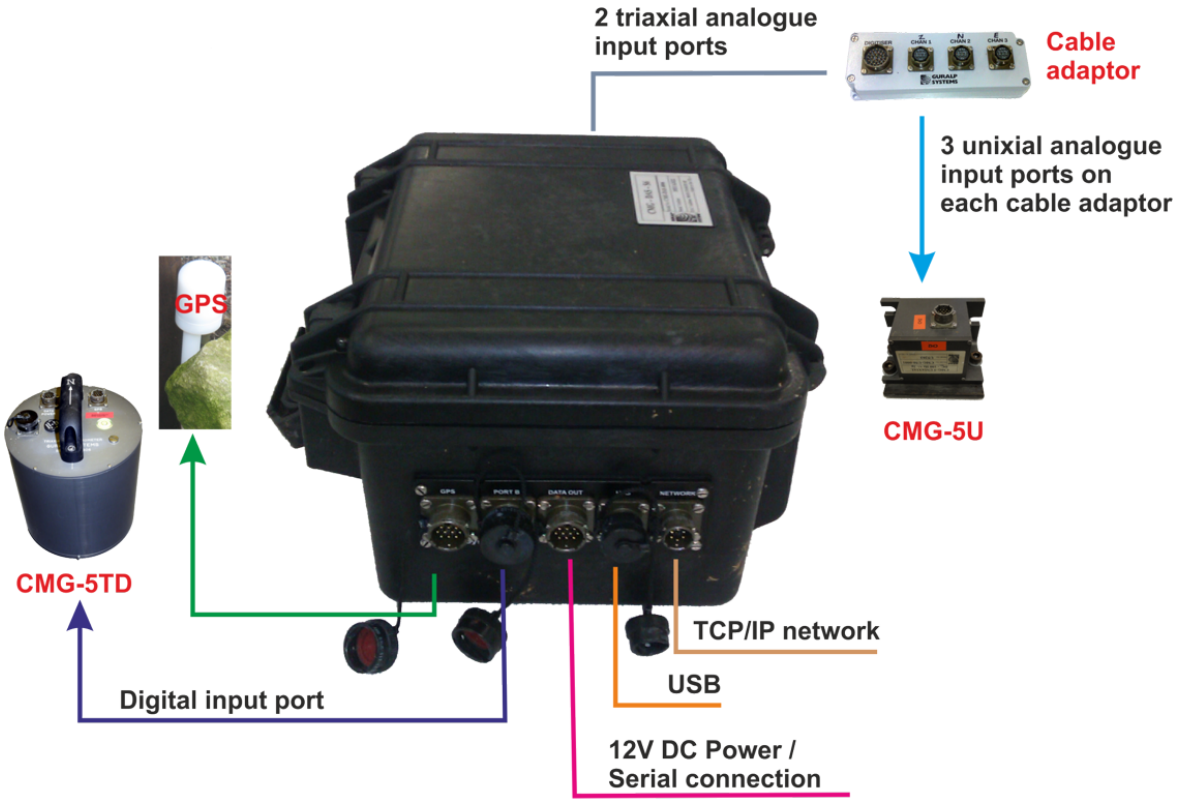

Figure 4-3: *The Güralp CMG-DM24S6EAM digitiser and storage system with details of the input and output ports available*

The single-component accelerometers are Güralp CMG-5U devices which record in a single direction only, but can be deployed either horizontally or vertically. These do not contain on-board digitisers and connect to either of the digitisers described previously. There is a maximum cable length of 50m from the accelerometer to the digitiser. The sensors are low noise, waterproof and relatively small, measuring just 75x75x125 mm.

The Güralp CMG-5TD is a low noise three-component strong motion accelerometer. It can be bedded in a hole surrounded by sand and levelled using the spirit level on the top of the sensor or positioned securely on a concrete surface (eg a wind turbine base). Recording at sample rates from 1 to 200 samples per second, the 5TD contains an on-board 24-bit digitiser module, the CMG-DM24. The 5TD is connected to either of the digitisers which provides power, data storage and GPS time synchronisation. There is a maximum cable length of 100m from the accelerometer to the digitiser.

4.2.3 Anemometer

The Power Predictor anemometer (figure 4-4) records both wind speed and direction. It uses a three cup, pulse anemometer which is accurate to $\pm 3\%$. It is low power, requiring just a single 9V battery. The data logger stores ten minute averaged data on an SD card and can be attached to a 5 m or 12 m mast. In addition to wind data, solar and temperature information are also recorded.

Figure 4-4: *The Power Predictor anemometer*

4.3 Standard Deployment

This section describes the standard deployment of each piece of equipment. Where appropriate the kit was deployed following the SeisUK guidelines described in Brisbourne et al. (2010).

4.3.1 CMG-6TD Seismometer

The Güralp CMG-6TD is a standalone waterproof seismometer containing its own digitiser and is powered by a 12v battery (see section 4.2.1). The seismometer is buried in a hole of approximately 1 m deep and 30 cm diameter and lined with clean builders sand. The sand provides a platform in which to level the sensor and hold it in place, it also increases the coupling between the sensor and the ground. By burying the sensor, it is sheltered from some of the effects of the wind. In order to further protect the sensor from very wet conditions, it is placed in plastic bags and sealed before burying. The

6TD is set up using a laptop with Scream! installed following the procedure outlined in Brisbourne et al. (2010). Recording commences automatically once power has been connected to the sensor.

The sensor is deployed in the same way at each site. Figure 4-5 shows the 6TD in the ground prior to sealing the plastic bags and once it has been deployed with GPS and power supply. The power supply is placed in a plastic box and sealed to prevent water ingress.

Figure 4-5: *The CMG-6TD sensor in the ground. Inset: CMG-6TD deployed under the grass tuft with GPS and battery power supply connected.*

4.3.2 CMG-5TD Accelerometer

The Güralp CMG-5TD is deployed in a similar manner to the CMG-6TD, in a hole lined with clean builders sand and levelled using the spirit level on top of the sensor. Power is provided via a 100 m cable connected to a CMG-DM24S12AMS or CMG-DM24S6EAM (section 4.2.2) and the data recorded on the digitiser using Scream! software. The digitiser and power extension reels are placed in a tent to keep them dry (figure 4-6). The cable attaching the sensor to the digitiser is also buried just under the surface to prevent any animals from gnawing it.

Figure 4-6: *The CMG-DM24S12AMS digitiser in the tent with the GPS antenna nearby and accelerometer cables.*

4.3.3 CMG-5U Accelerometers

On the tower, two CMG-5U accelerometers are attached horizontally and perpendicularly using magnets (figure 4-7). The accelerometers can also be buried in the ground, in shallow pits lined with builders sand. Although the sensors are waterproof, as with the two three-component sensors, the CMG-5U is placed in a plastic bag to provide further protection. The sensor lies horizontally in the pit (figure 4-8) and is levelled before covering with more sand. The sensors are connected to either a CMG-DM24S12AMS or CMG-DM24S6EAM (section 4.2.2) via a 50 m cable, which is embedded just under the surface, ground material permitting.

4.3.4 Anemometer

The BetterGeneration Power Predictor anemometer is mounted on a 5 m mast. It is held vertical with guy ropes and positioned using a compass, with the arrow on the top of the anemometer pointing north. The data logger is held in place on the mast or other suitable nearby support using cable ties and gaffer tape, out of reach of any nearby animals.

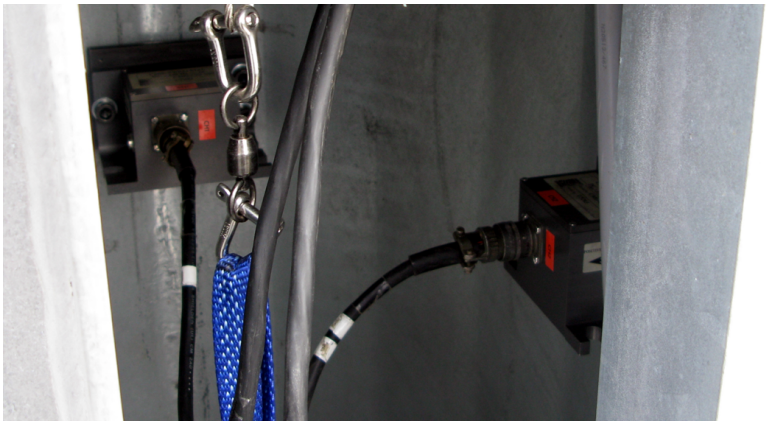

a. Attached to a tubular tower

b. Attached to a lattice tower

Figure 4-7: *Two CMG-5U accelerometers attached to a tower using magnets.*

Figure 4-8: *A CMG-5U in the ground, levelled, but prior to covering with sand.*

4.4 Field Data Processing

4.4.1 File Formats

There are two file formats which are used for recording data when monitoring the turbine. The first is the Güralp GCF Data Format which contains data from the seismic equipment. The other is an ASCII file containing weather data generated by the Power Predictor.

4.4.1.1 Güralp GCF Data Format

Seismic equipment from Güralp use the Güralp Compressed Format (GCF) to store data. The format uses a series of blocks to store either status information in ASCII format or data records. Each block can be up to 1024 bytes long, with a 16 byte header. The header determines the type of data stored within the body of the block. The header consists of four 4 byte fields representing the system ID, which identifies the original system; the stream ID, a unique six character label identifying the device the data was recorded on; the date code, consisting of the time and date when the block starts and the data format defining the format of the block. The system ID and stream ID are each encoded as a base 36 number and the date code as a 32-bit number. The data format field is split into four elements: a reserved field, the sample rate of the data records, a compression code defining the compression format of the block and the number of data records contained within the block. For further information on the Güralp Compressed Format, see Guralp (2008).

4.4.1.2 Power Predictor Output Data File

The Power Predictor anemometer by Better Generation records wind and solar data every ten minutes. The data is stored in a ASCII text file with a header at the top, detailing the type of data in each column. There are seven columns containing data for date and time, wind pulses per interval, wind direction average, raw solar average, raw on board solar average, raw temperature average and wind direction variance. Each data value is separated using a tab delimiter.

4.4.2 Matlab

Matlab is a mathematical programming language which contains built in commands and functions to aid the processing of many different types of data. In addition to the basic Matlab commands, toolboxes can be added to the software to increase functionality. The Signal Processing toolbox contains a number of functions, commands and GUI tools specific to signal processing and useful when post-processing the measurement data for this research.

As well as the built in functions and toolboxes, Matlab has the ability for bespoke functions and

scripts to be developed for a specific purpose. The post-processing of the measurement data for this research and the subsequent generation of graphs all involve the use of Matlab and bespoke scripting.

Object-orientated programming in Matlab is a relatively new feature which was only added in release 2008a. The ability to program with objects means that code can be reused for each wind turbine simply by creating a new object. Classes have been created to manage and post-process the measured data from the sensors and the anemometer. A detailed description of the methods and properties contained within each class can be found in appendix A.

Using the classes and a wrapper script, the data is processed in the same manner for each turbine:

1. The data is split into 10 minute blocks and a displacement power spectral density (PSD) function (section 2.4.4) calculated for each block;
2. The wind data times are checked against the measured data to ensure correlation;
3. Displacement PSD plots are generated for analysis based on wind speed and direction, time of day and distance from the wind turbine.

4.4.2.1 Averaging the PSDs

The block class (appendix A.3) contains a method for calculating the displacement power spectral density function (PSD) of each block (10 minute time period) of data. When analysed, the blocks are filtered based on a specific criteria, for example wind speed or direction. The resultant matrix contains m columns of PSDs. There are a number of ways of statistically obtaining a single PSD vector representative of the entire data set. Figure 4-9 shows the results of applying different methods to the PSD matrix. The grey PSD plots in the background show each individual vector.

The mode is calculated using the most frequently occurring value for each frequency. When there are multiple values which occur equally, the smallest value is used (MathWorks 2010a). This means that the mode tends to sit around the smallest of the individual PSDs. The median returns the middle value at each frequency, if they are sorted into order. The arithmetic mean is the sum of all values at a particular frequency divided by the number of values. It is influenced by extreme values occurring at high or low amplitudes which can bias the value one way or the other. A trimmed mean attempts to

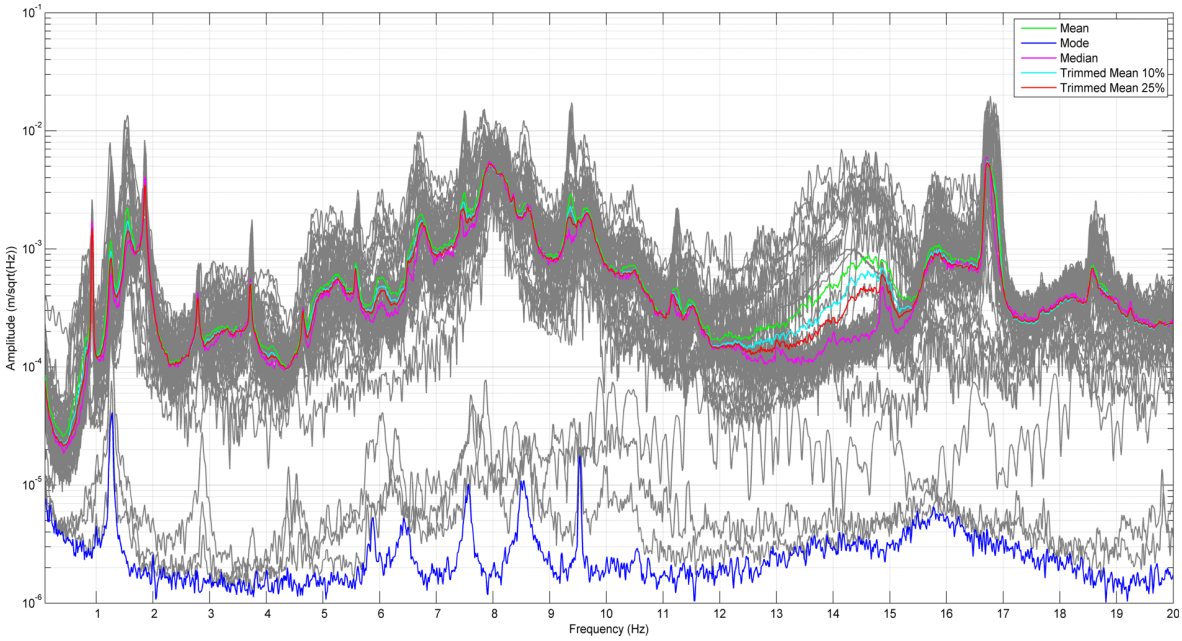

Figure 4-9: *The result of running different averaging on a set of PSD. The grey plots are the original set of PSDs.*

account for this by discarding a given percentage of values at either end of the data set. For example, a 10% trimmed mean will calculate an arithmetic mean from the central 90% of the data, discarding the highest and lowest 5% of values.

The median, although using the extreme values, takes the middle value, so the result is not directly influenced in the same way as the mean. Additionally, the median tends to display more detail than the mean. For these reasons, the median will be used in the following chapters to display the results. However, it should be noted that any calculated equations are within a small error due to a combination of sensor and rounding errors.

For some of the graphs in chapters 5 and 6 nonlinear regression is performed on the data to obtain an equation representative of the trend in the data. If the data is plotted on a log-log scale, then a straight line implies a power law of the form

$$y = ax^b. \tag{4.1}$$

Taking a logarithm of both sides gives

$$\ln y = \ln a + b \ln x \tag{4.2}$$

Similary for an exponential fit in the form

$$y = ae^{bx}, \tag{4.3}$$

Taking the natural logarithm of both sides gives

$$\ln y = \ln a + bx. \tag{4.4}$$

Equations (4.2) and (4.4) are now linear and simple linear regression can be applied to estimate the values of a and b.

For a set of data y of length N and dependent on the values x, the parameters $A = \ln(a)$ and b can be estimated using the functions (Shaw & Wheeler 1994)

$$b = \frac{\sum (y - \overline{y})(x - \overline{x})}{(\sum x - \overline{x})^2}, \tag{4.5}$$

$$A = \overline{y} - b\overline{x}, \tag{4.6}$$

where $\overline{x}$ and $\overline{y}$ are the mean of x and y respectively.

The correlation of determination, R^2, provides an indication on the variability in the data and how well the equation fits to the data. It is related to the square of the residuals, SS_{res} and the total sum of squares, SS_{tot}, such that for the modelled values $\hat{y}$ (MathWorks 2011)

$$SS_{res} = \sum (y - \hat{y})^2, \tag{4.7}$$

$$SS_{tot} = (N-1)\operatorname{Var}(y) = (N-1)(\mathrm{E}[y^2] - \mathrm{E}[y]^2) = (N-1)\frac{\sum y^2}{N}\left(\frac{\sum y}{N}\right)^2, \tag{4.8}$$

$$R^2 = 1 - \frac{SS_{res}}{SS_{tot}}. \tag{4.9}$$

The value of R^2 lies between 0 and 1, with 1 being a perfect fit.

Some of the plots also display error bars. These indicate the range of the data.

4.5 Predicted Spectral Content

The results in Styles (1996) and Styles et al. (2005) show that the blade passing frequency and its harmonics are clearly visible in the monitored data. Therefore it is expected that these will be seen in the results for the wind turbines monitored here. The turbines monitored in these reports were fixed speed machines. Table 4-1 shows all possible harmonics of the blade passing frequency, up to 10 Hz, for the Gaia and Endurance wind turbines, the fixed speed turbines monitored for this thesis. The Proven wind turbine is variable speed, meaning that the blade passing frequency will shift depending on the rotation speed (rpm) of the turbine. The previous studies highlight that the blade-passing frequency excites the vibrations.

	Gaia (56 rpm)		Endurance (43 rpm)	
Rotation Rate Harmonic	Blade Passing Harmonic	Hz	Blade Passing Harmonic	Hz
1		0.93		0.72
2	1	1.867		1.43
3		2.8	1	2.15
4	2	3.73		2.87
5		4.67		3.58
6	3	5.6	2	4.3
7		6.53		5.02
8	4	7.47		5.73
9		8.4	3	6.45
10	5	9.33		7.17
11				7.88
12			4	8.6
13				9.32

Table 4-1: *Blade passing frequencies of the Gaia and Endurance wind turbines*

Chapter 5

Monitoring and Results

This chapter describes the monitoring of each of the four turbines. Information about the turbine, a description of the site and the results from the sensors and wind data are presented for each turbine. Section 5.5 provides a summary and discussion of the findings. Further analysis of the data is provided in chapter 6.

5.1 Gaia-Wind 133 Tubular Tower at Wigton, Cumbria

The Gaia-Wind 133 11 kW wind turbine was developed in Denmark in the early 1990s, with the first turbine going operational in 1993. Unlike most wind turbines, the Gaia contains only two blades which are attached to a unique 'teeter' hub. This allows the blades to be oversized and tilt about a small angle. According to Gaia-Wind Ltd (2011a) the teeter hub allows the turbine to run more smoothly than an equivalent three blade machine. The turbine has a rotor diameter of 13 m and generates power at wind speeds between 3.5 m/s and 25 m/s.

The Gaia is available on either a lattice or monopole tubular tower, with heights of 15 m (lattice), 18 m (monopole or lattice) or 27 m (monopole). Both of the Gaia turbines monitored for this project are mounted on 18 m towers. There is an anemometer connected to the upwind side of the nacelle, which is used for monitoring the wind speed at hub height and controlling the cutting in and out of the

turbine but the values are not logged. The turbine operates at a constant speed of 56 rpm. Table 5-1 provides further information on this wind turbine.

The tubular tower (figure 5-1) is a tapered cylinder with the widest diameter at the base. It is made from grey galvanised steel and consists of three sections connected together with external flanges.

Type	Downwind
Blades	2, constant speed 56 rpm nominal
Blade material	Glass fibre
Tower	Hutchinson self-supporting monopole
Tower height	18 m or 27 m
Rotor diameter	13 m
Rated speed	9.5 m/s
Rated power	11 kW
Cut-in wind speed	3.5 m/s
Max wind speed	54 m/s
MCS certified at time of testing	Yes
Phase	three-phase

Table 5-1: *Information about the Gaia-Wind 133 tubular tower wind turbine*

Figure 5-1: *The Gaia Wind 133 wind turbine at Wigton*

5.1.1 Site Information and Deployment

The Gaia-Wind 133 tubular tower wind turbine, monitored for this thesis, is situated on private land at a farm just outside the village of Wigton in Cumbria, 13 km south-west of Carlisle and outside the Eskdalemuir exclusion zone (figure 5-2). The turbine powers a dairy farm and is located in a field to the rear of the property. It is north-west of the main farm building and approximately 40 m from the Carlisle to Barrow-on-Furness rail line (figure 5-3).

Measurements were recorded over seven days from 7th September 2010 to 13th September 2010. A combination of CMG-5U's, (section 4.2.2), a CMG-6TD (section 4.2.1), a CMG-5TD, (section 4.2.2) and the DM24S12AMS digitiser were deployed to monitor the wind turbine, following the procedures described in section 4.3.

At the site, two single component accelerometers were placed horizontally and perpendicularly inside the turbine , attached to the tower with strong magnets. A third was placed in the ground at the base of the tower. A further three, single-component accelerometers were positioned in a line at 10 m, 20 m

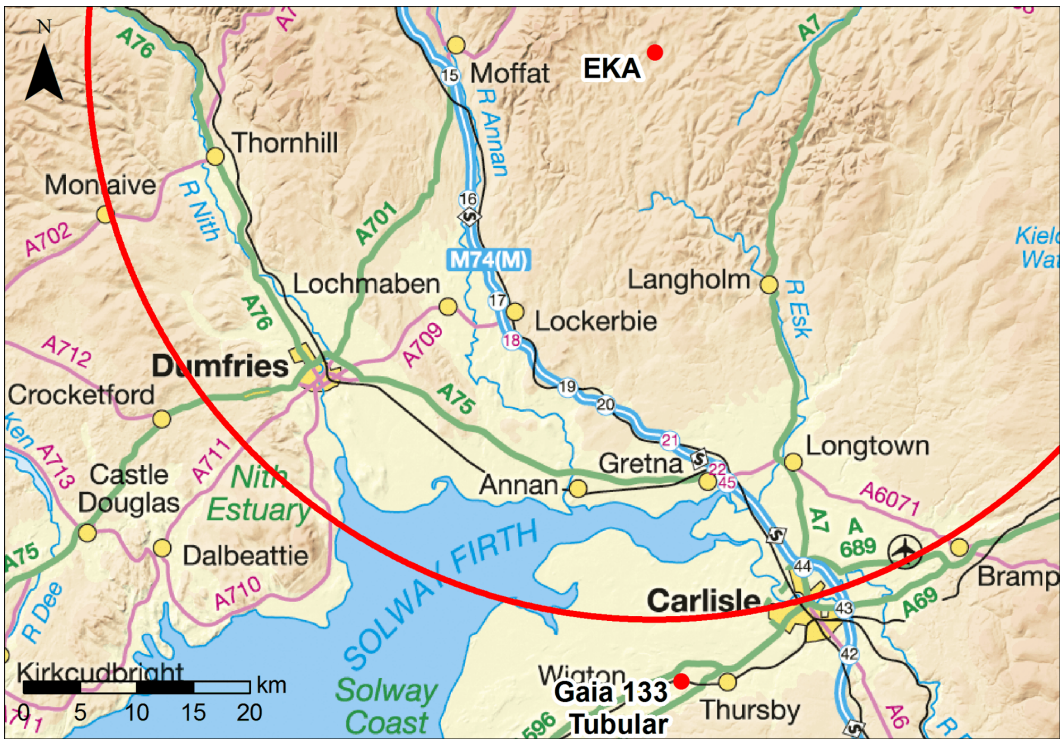

Figure 5-2: *The location of the Gaia-Wind 133 tubular tower at Wigton in Cumbria in relation to EKA and the exclusion zone. Contains Ordnance Survey data ©Crown copyright and database right 2011*

and 30 m away from the tower in a north-westerly direction. These three sensors were shallowly buried, orientated horizontally and aligned radially to the tower. The three-component accelerometer was buried south of the turbine, 70 m away and the three-component seismometer placed on the other side of the railway, 190 m north-east of the turbine. The sensor locations in relation to the turbine and nearby farm buildings are shown in figure 5-4.

Figure 5-3: *The location of the Gaia-Wind 133 tubular tower wind turbine at Wigton, in relation to the nearby railway line*

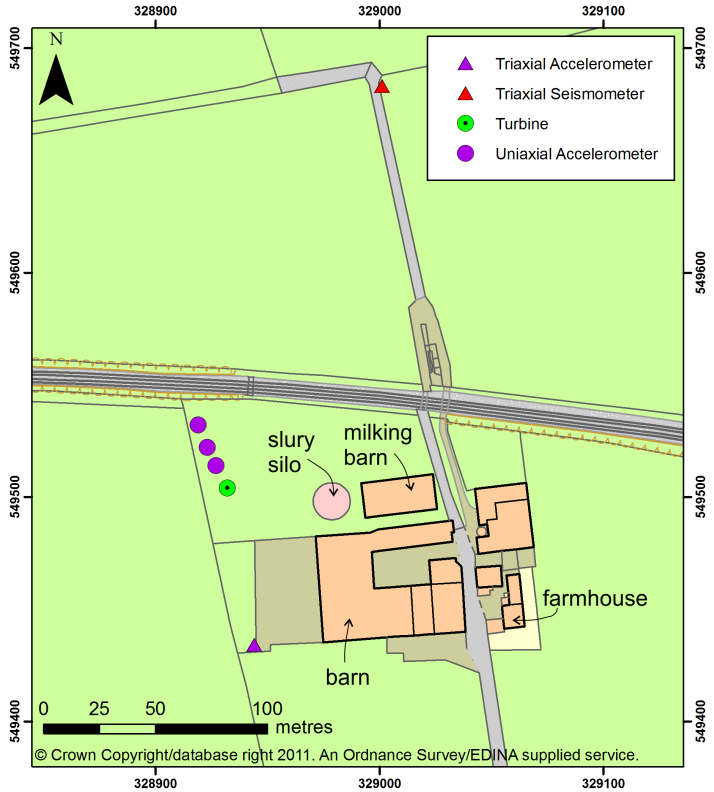

Figure 5-4: *The sensor locations for the monitoring of the Gaia-Wind 133 tubular tower turbine near Wigton. The anemometer at Wigton was positioned 2 m away from the turbine. Coordinates are given in OSGB.*

5.1.2 Wind Variation

The wind speed and direction for the monitoring period are shown in figure 5-5. The Gaia-Wind 133 turbine contains an AC power supply, to which the DM24S12AMS digitiser was connected. However a thunderstorm during the morning of 9th September 2010 cut power to both the turbine and the digitiser. Therefore there is no accelerometer data available after this point. The seismometer remained operational for the entire period, powered from a 12v battery and was not affected by the storm.

The highest wind speed up to the point of the power cut was 5.1 m/s, occurring on 7th September at 16:00. The pie charts in figures 5-6 and 5-7 show the percentage distribution of 1 m/s periods of wind speed prior to the power cut and for the entire monitoring period. After the power cut, the wind speed increased, with a maximum of 7.8 m/s for the period. Prior to the power cut, the predominant wind speed is less than 2 m/s. However, for the entire period, the speeds are much more evenly distributed.

The wind direction changed as the storm came in. Prior to the power cut, the predominant winds were south easterly. When the weather system changed and the storm approached, these changed to westerly followed by north-westerly.

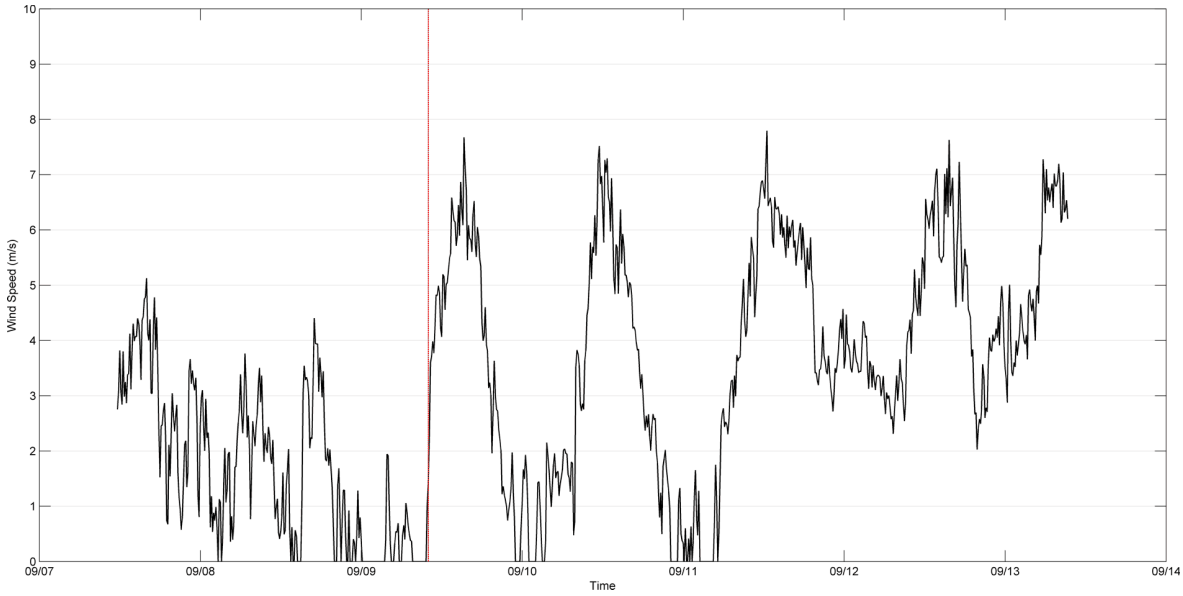

a. Wind speed

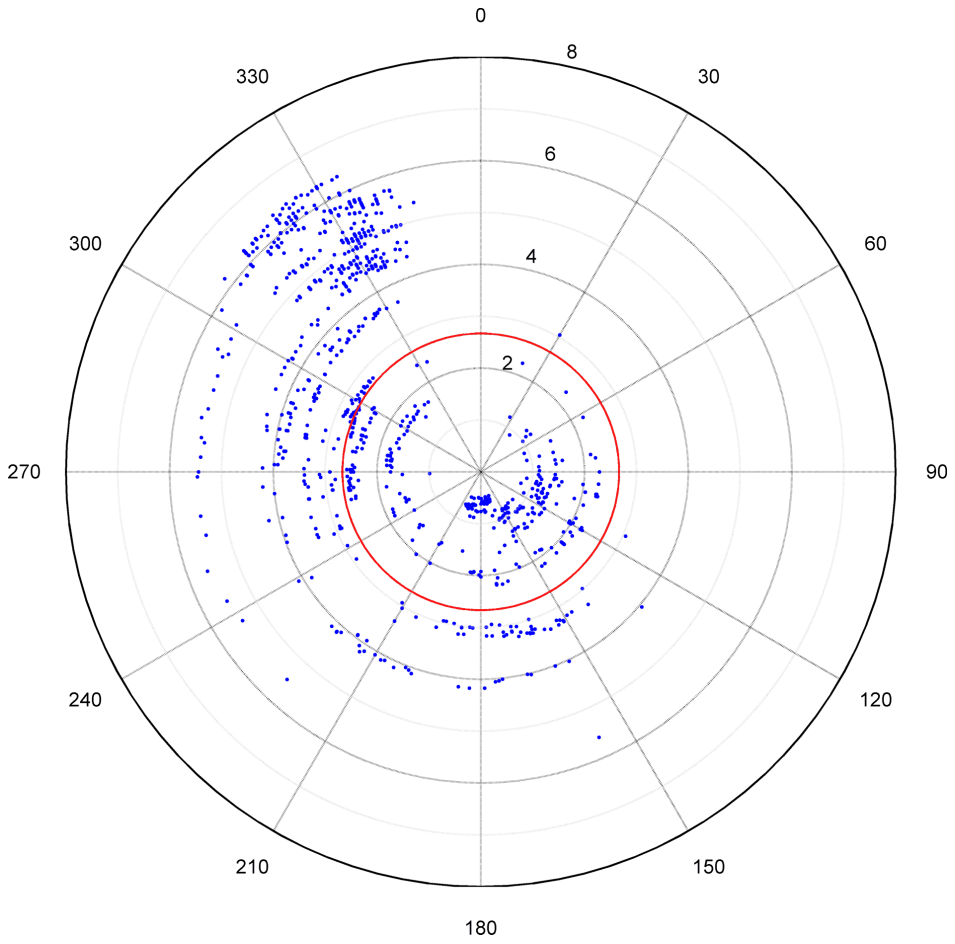

b. Wind direction, with days since the start of monitoring given by the radius

Figure 5-5: *The wind speed and wind direction for the monitoring period at Wigton. The red line on each plot indicates the power cut to the turbine and the digitiser. The distance from the centre of the circle on the wind direction plot indicates days since the start of monitoring*

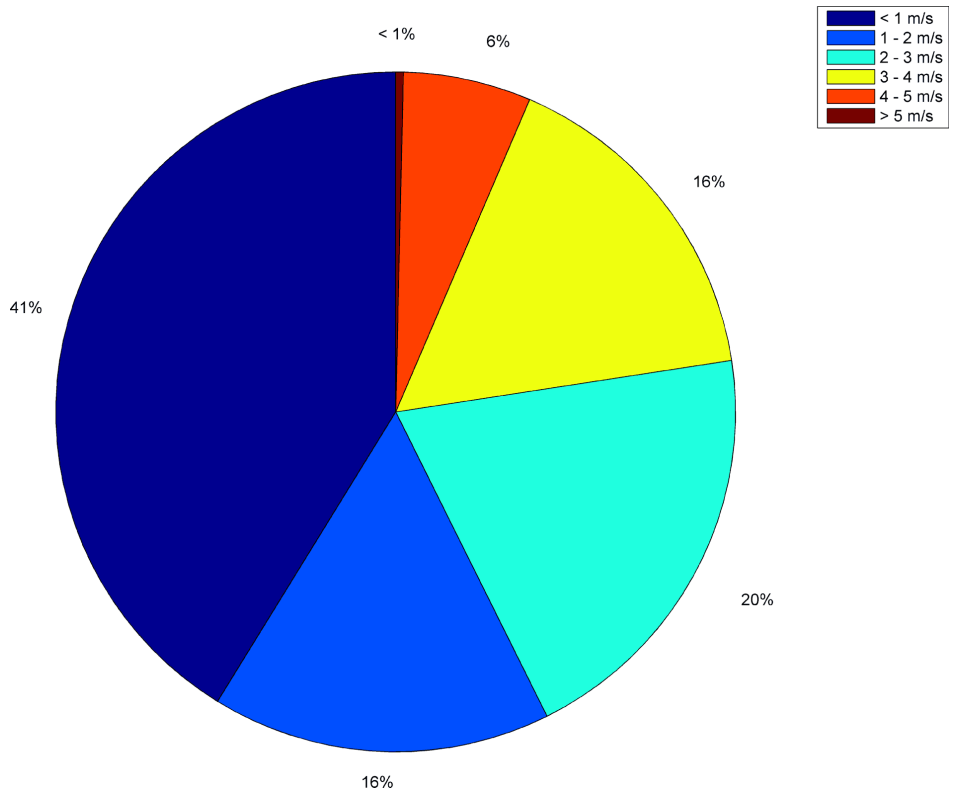

Figure 5-6: *The distribution of wind speeds at the Gaia-Wind 133 tubular tower site prior to the power cut*

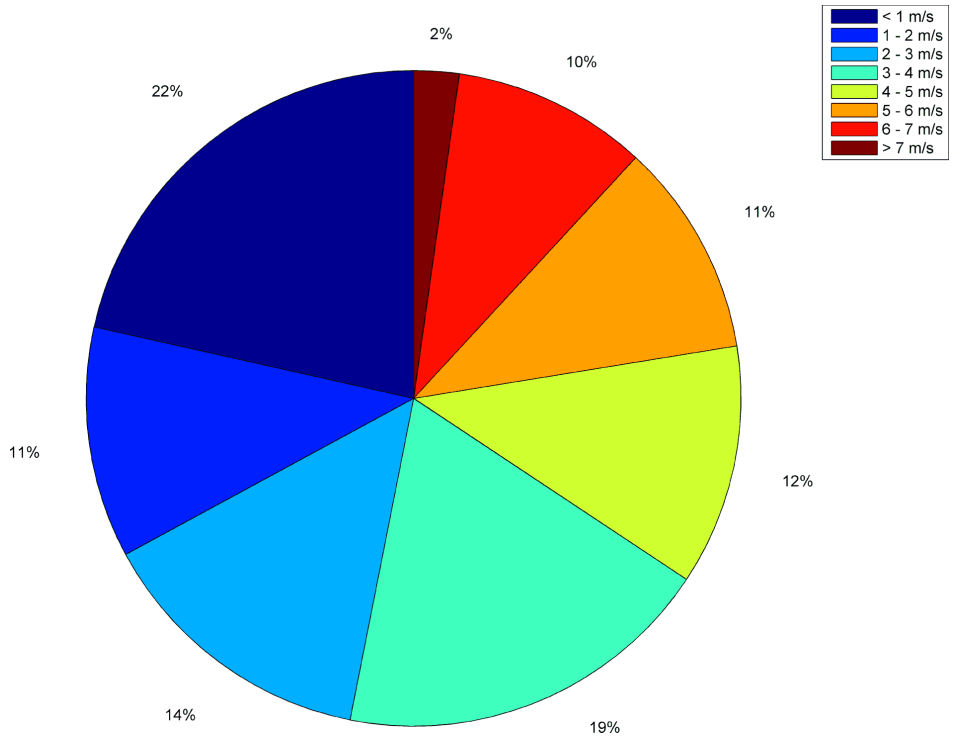

Figure 5-7: *The distribution of wind speeds at the Gaia-Wind 133 tubular tower site for the entire monitoring period*

5.1.3 Results

The Gaia-Wind 133 has a starting speed of 2.5 m/s and cut-in speed of 3.5 m/s, meaning that the blades will start turning at 2.5 m/s but the turbine will not start generating power until the winds reach 3.5 m/s. Data obtained from the accelerometers attached to the tower is available for the period leading up to the power cut. Figure 5-8 shows the displacement frequency spectra for when the turbine was stationary (wind speeds less than 2.5 m/s, hereafter referred to as wsLow and shown as blue on the graphs), starting to turn (wind speeds of 2.5 m/s - 3.5 m/s, hereafter referred to as wsMid and shown as green on the graphs) and generating (wind speeds greater than 3.5 m/s, hereafter referred to as wsHigh and shown as red on the graphs) for a sensor on the tower and figure 5-9 the equivalent graphs at 10 m and 200 m away from the turbine.

The difference between the turbine being non-operational at wind speeds below 2.5 m/s and starting to turn at 2.5 m/s is around a factor of 100. In the ground, this difference decreases with distance, as the amplitude of the operational spectra decreases. At 10 m, at frequencies up to 5 Hz, only the sensor noise of the accelerometer is visible and the maximum difference between wsLow and wsMid is down to a factor of 10. The 6TD is more sensitive to lower frequencies than the 5U and at 190 m peaks can be seen at frequencies above 1 Hz. However, by this distance the difference in amplitude between wsLow and wsMid is only a factor of two.

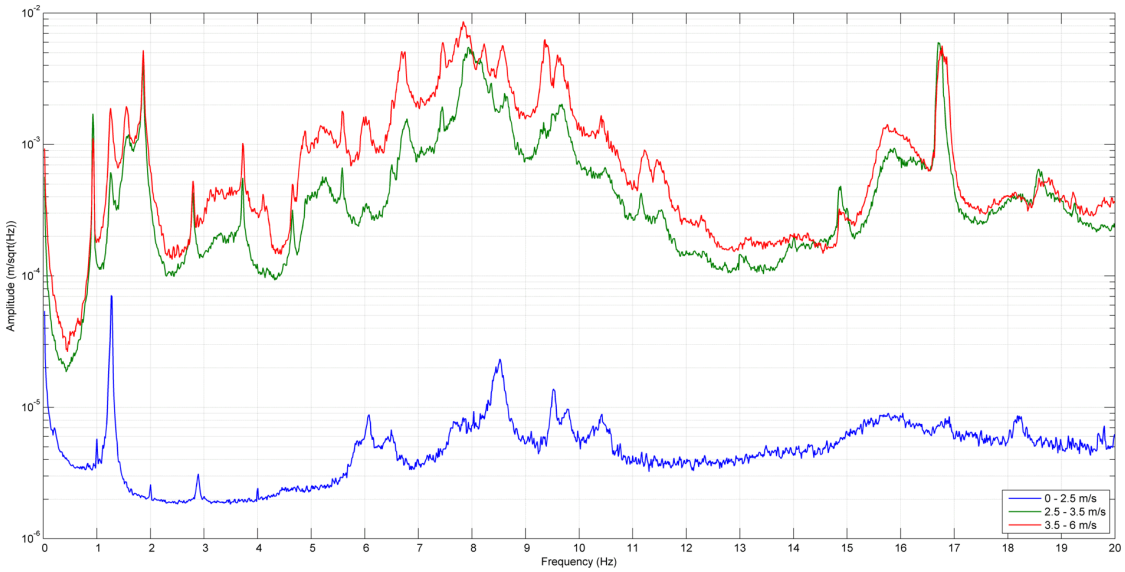

Figure 5-8: *The displacement frequency spectra from data recorded on the tower of the Gaia-Wind 133 tubular tower turbine, at three wind speed ranges: when the turbine is idle, just started up and at speed and generating*

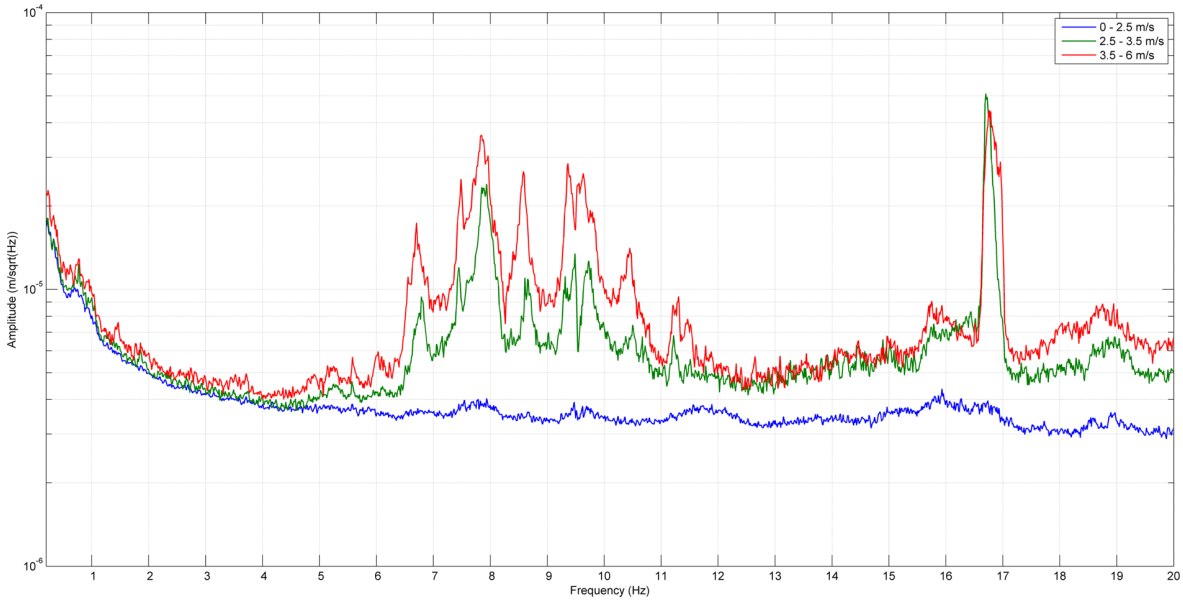

a. 10 m from the turbine

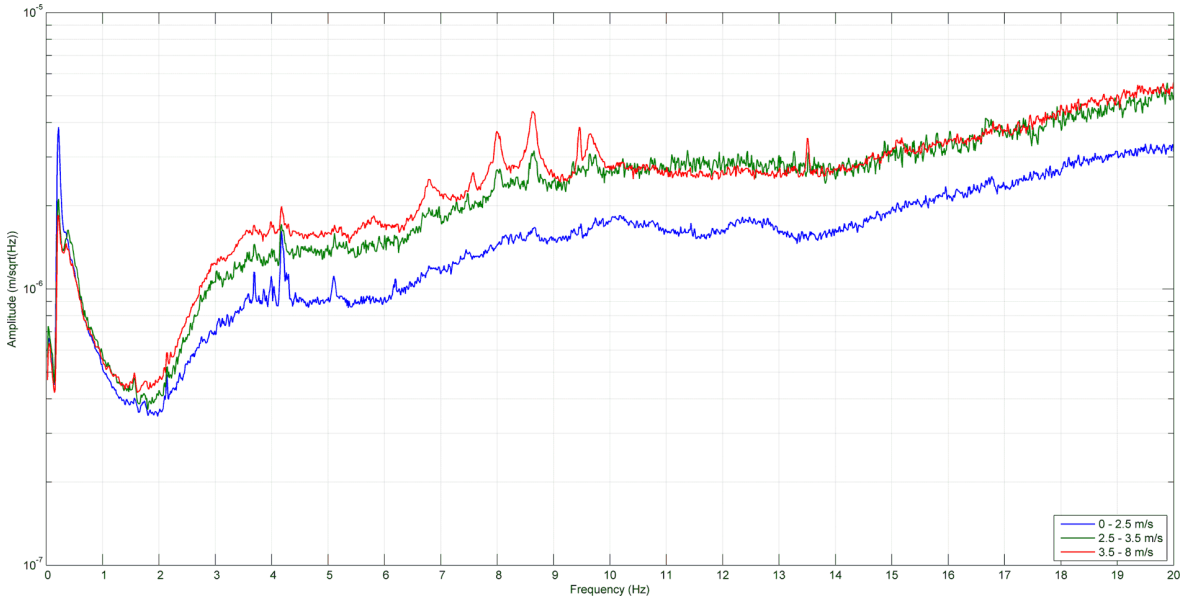

b. 190 m from the turbine

Figure 5-9: *The displacement frequency spectra at three wind speed ranges (when the turbine is idle, just starting up and at speed and generating) using data recorded on two sensors in the ground at the Gaia-Wind 133 tubular tower site*

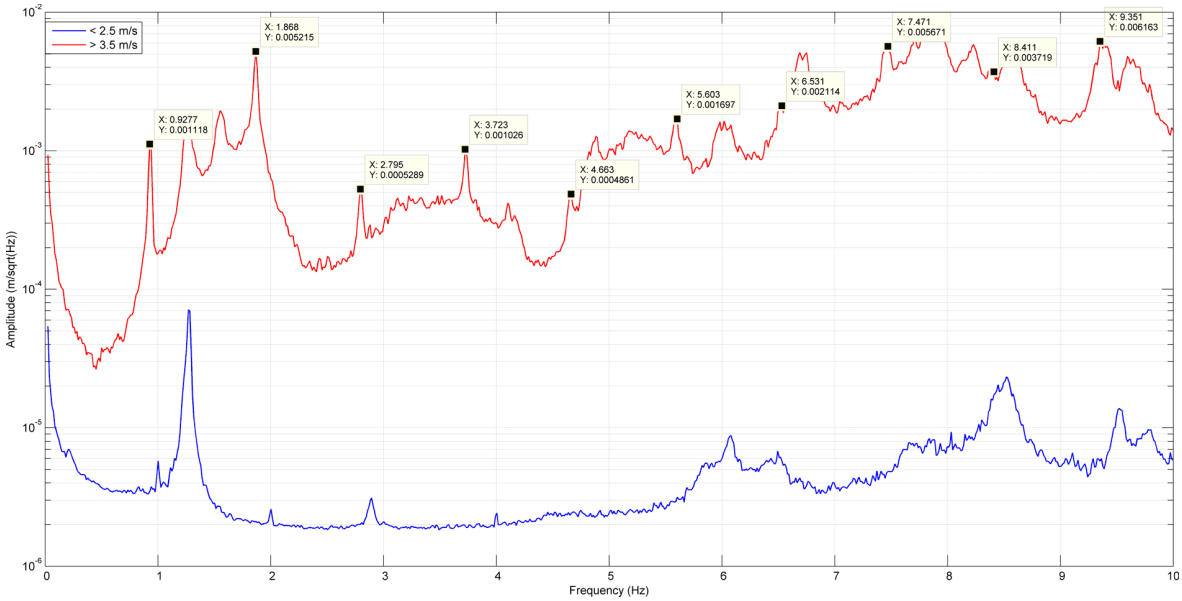

Figure 5-10: *The displacement frequency spectra using data recorded on the tower of the Gaia-Wind 133 tubular tower turbine at wind speeds above 3.5 m/s and below 2.5 m/s with the rotation frequency and harmonics identified*

Above 2.5 m/s, ie when the blades are turning, there are significant peaks on the tower at 0.9 Hz, 1.86 Hz, 3.73 Hz, 5.6 Hz and higher, which agree with the predicted rotation frequency and harmonics (section 4.5). These frequencies do not show in the on-tower spectrum at the low wind speeds (figure 5-10).

Figure 5-11 shows the displacement spectra for all the sensors at wind speeds greater than 3.5 m/s. The sensors in the ground show little below 5 Hz with the main frequency peaks occurring between 6 Hz and 11 Hz. The blade passing frequencies at 7.47 Hz and 9.33 Hz are visible through to 70 m and may possibly just be made out above the background levels at 190 m.

The amplitude on the foundation is a factor of one hundred lower than on the tower and for the peaks between 6 Hz and 10 Hz has dropped by a further factor of ten with respect to the accelerometer at 10 m. The peak at 6.7 Hz is visible on all sensors when the wind speed is greater than 3.5 m/s. Picking the tip of this peak and recording the amplitude at each distance allows the attenuation of the wave to be calculated. This is shown in figure 5-12, where the log-log plot gives an equation for the attenuation at Wigton, for wind speeds greater than 3.5 m/s, of $0.0002r^{-1}$, where r is distance from the wind turbine. This is different to the Styles et al. (2005) model which uses an $r^{-\frac{1}{2}}$ model, although the findings correspond with that of Schofield (2002) at Stateline. However, the Styles et al. (2005) model was calculated using seismometers positioned in the far-field, whereas the sensors used

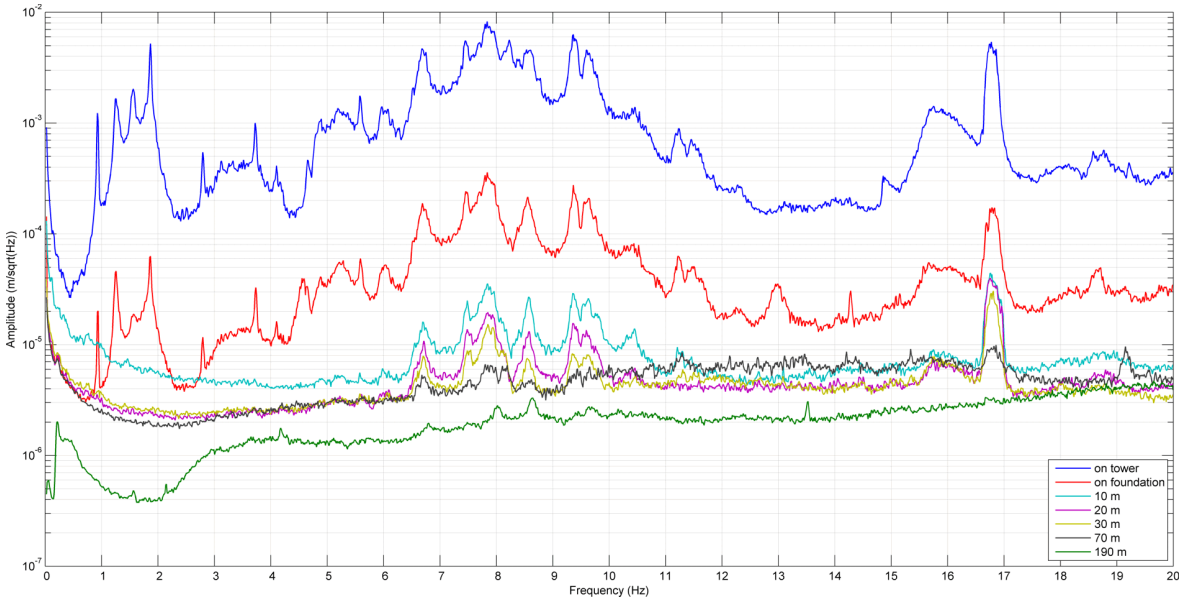

Figure 5-11: *The displacement frequency spectra from data recorded on sensors at a range of distances from the Gaia-Wind 133 tubular tower wind turbine, when the wind was greater than 3.5 m/s*

in this project were positioned close to the turbine in the near-field, this may affect the attenuation calculation. This is discussed further in chapter 6.

When the wind speed is less than 2.5 m/s, the background noise levels on the accelerometers in the ground rise above the amplitude of the sensor attached to the tower. Peaks that are visible on the tower are not clearly seen in the ground (figure 5-13). However, this does not necessarily mean that the vibrations are not present at these distances, only that they are contributing to the ambient background noise.

The plot in figure 5-14 shows how wind speed affects the displacement spectrum on the tower. The colour indicates amplitude with lighter areas being the frequencies and wind speed of highest amplitude and the dark areas the lowest. There is an obvious change in amplitude between 6 Hz and 10 Hz at 3.5 m/s. Below 1 m/s there is little activity, with stronger peaks appearing around 1.5 m/s at 2 Hz, 8 Hz and 17 Hz. This latter peak is a steady frequency between 1.5 m/s and 3.5 m/s, after which it displays a sinusoidal effect with an approximate 1 m/s period.

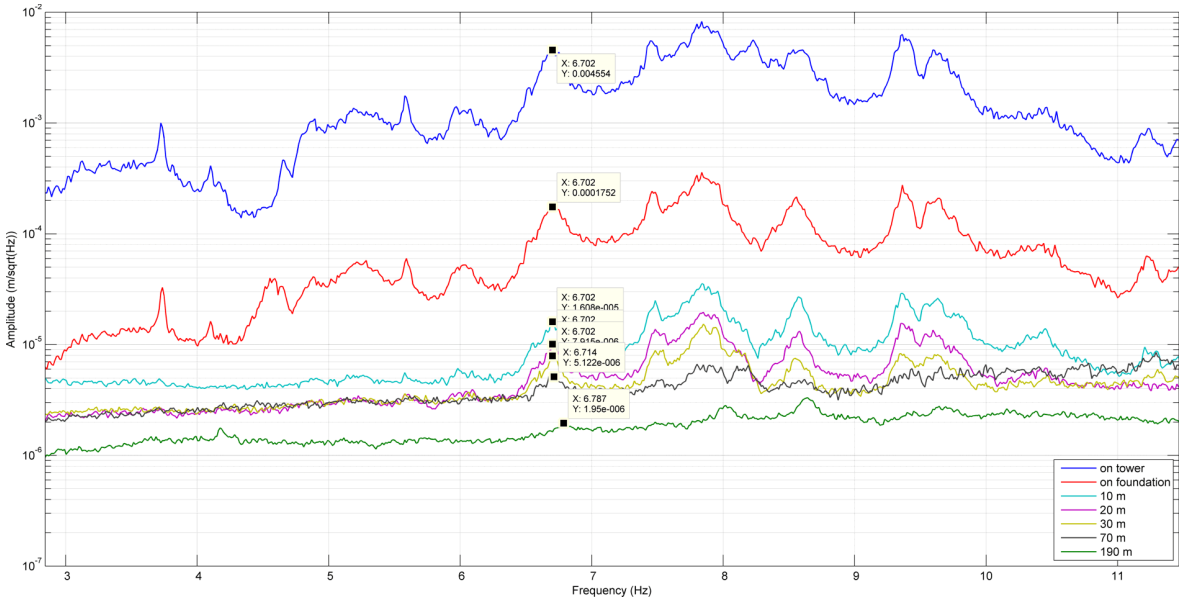

a. Picked peaks at 6.7 Hz

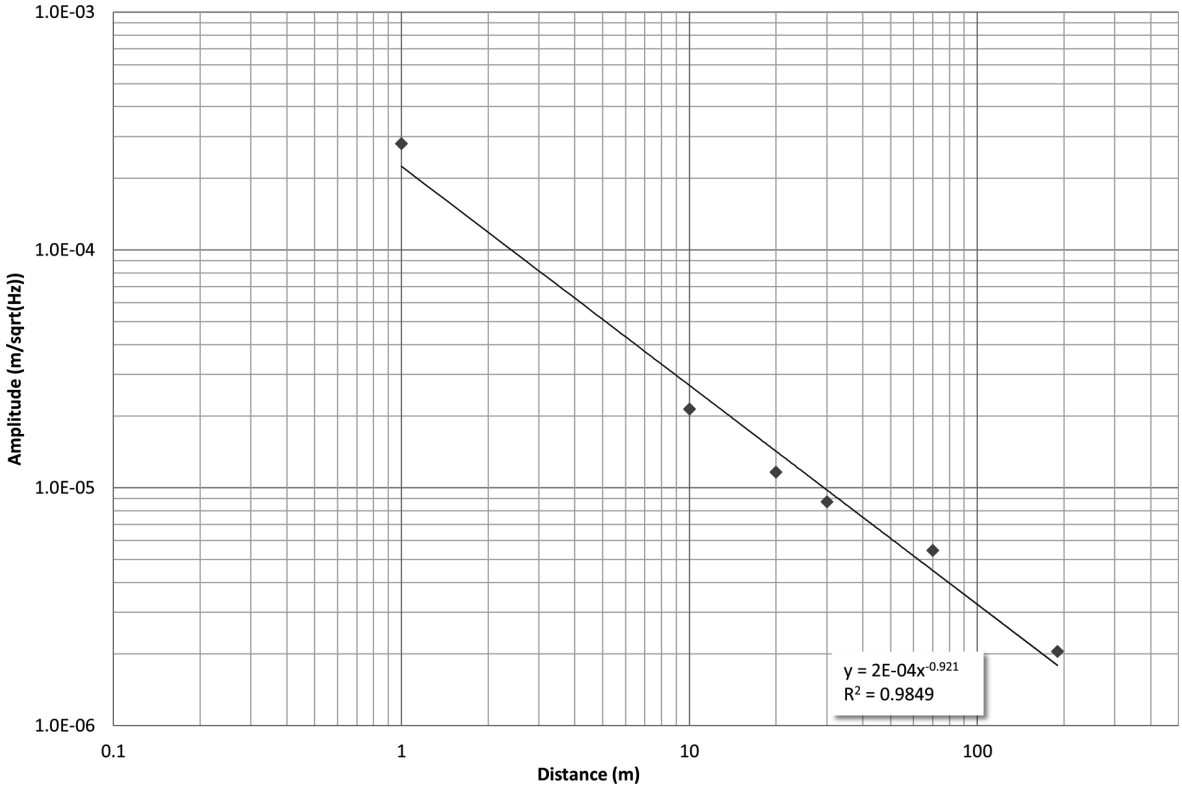

b. A log-log plot of distance to amplitude for the 6.7 Hz peak

Figure 5-12: *The distance-amplitude log-log plot and picked peaks at 6.7 Hz from the sensors at the Gaia-Wind 133 tubular tower site when the wind speed is above 3.5 m/s and the turbine at rated rpm*

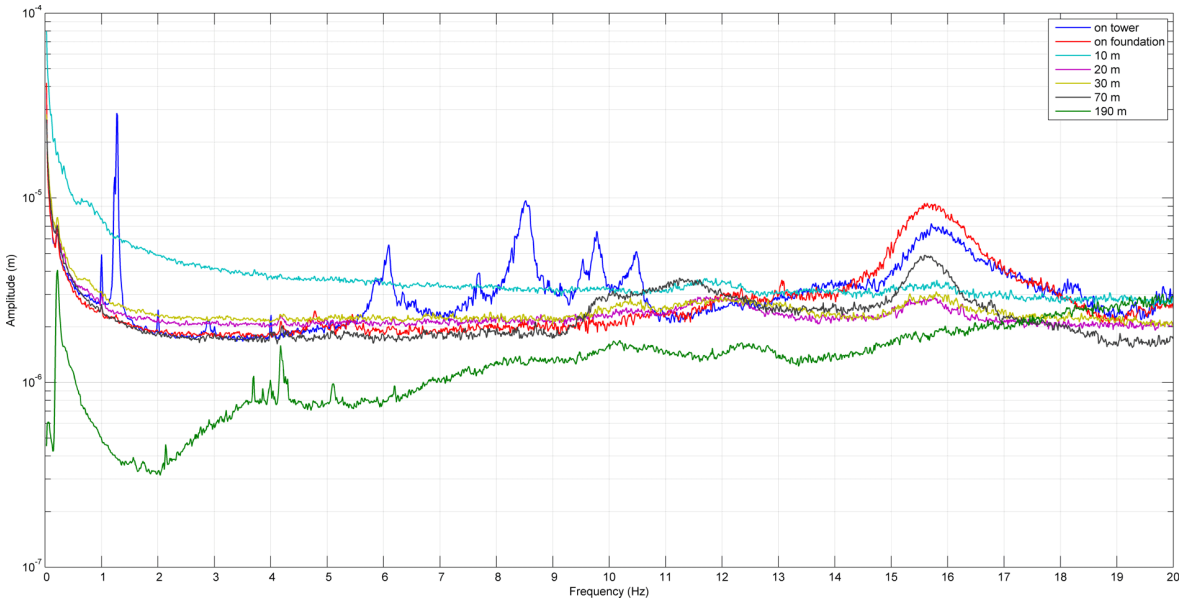

Figure 5-13: *The displacement frequency spectra from data recorded on sensors at a range of distances from the turbine, when the wind was less than 2.5 m/s*

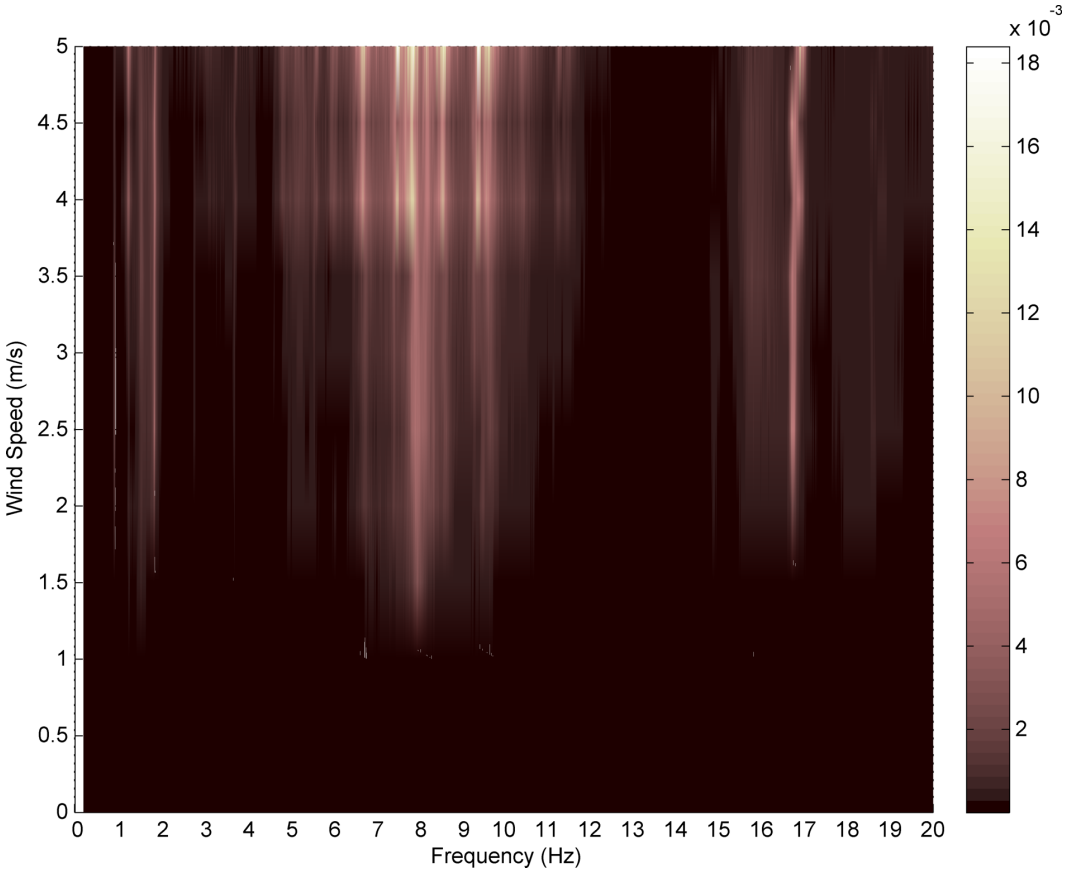

Figure 5-14: *A waterfall plot of wind speed and frequency with colour representing amplitude (m/sqrt(Hz)) from the on tower accelerometer. Data recorded on the tower of the Gaia-Wind 133 tubular tower.*

5.2 Gaia-Wind 133 Lattice Tower near Melrose in the Scottish Borders

The Gaia-Wind 133 lattice tower wind turbine has the same power, rotation speed, blades and hub as the tubular tower model described in section 5.1. The main difference between the two models is the tower design and height. The lattice tower is available in two heights of 15 m and 18 m. Table 5-2 provides further information on the turbine. The tower is constructed from steel beams welded together and mounted on four legs which are embedded in to a concrete foundation (Gaia-Wind Ltd 2008). The monitored lattice tower wind turbine near Melrose is shown in figure 5-15.

Figure 5-15: *The Gaia-Wind 133 near Melrose*

Type	Downwind
Blades	2, constant speed 56 rpm nominal
Blade material	Glass fibre
Tower	Lattice design
Tower height	15 m or 18 m
Rotor diameter	13 m
Rated speed	9.5 m/s
Rated power	11 kW
Cut-in wind speed	3.5 m/s
Max wind speed	54 m/s
MCS certified at time of testing	Yes
Phase	three-phase

Table 5-2: *Information about the Gaia-Wind 133 lattice tower wind turbine*

5.2.1 Site Information and Deployment

The Gaia-Wind 133 lattice tower wind turbine monitored for this thesis is situated on private property, inside the Eskdalemuir consultation zone near Melrose in the Scottish Borders, 6 km south-east of Selkirk (figure 5-16). The turbine is situated on the top of a hill away from any buildings, more than a kilometre away from the nearest minor road and over 3 km from the nearest main road, the A7.

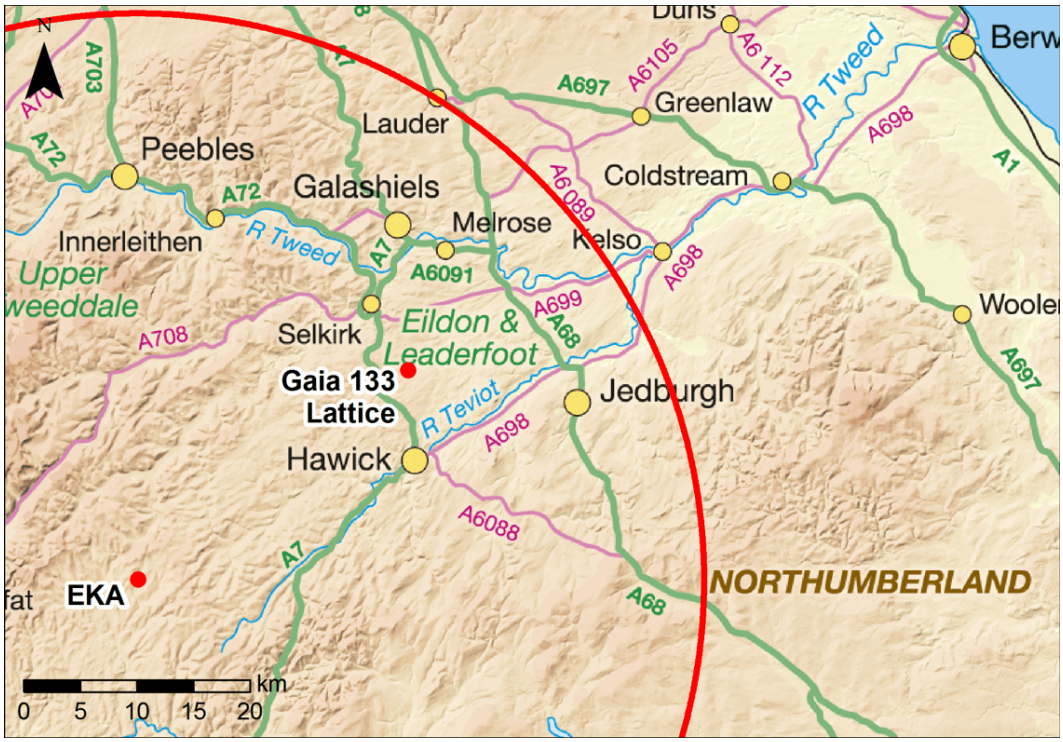

Figure 5-16: *The location of the Gaia-Wind 133 lattice tower at Melrose in Cumbria in relation to EKA and the exclusion zone. Contains Ordnance Survey data ©Crown copyright and database right 2011*

Figure 5-17: *The position of the accelerometers on the turbine and at the base*

Measurements were recorded over seven days from 31st August 2010 to 6th September 2010. Six CMG-5Us, (section 4.2.2), a CMG-6TD (section 4.2.1), a CMG-5TD (section 4.2.2) and the CMG-DM24S12AMS digitiser were deployed to monitor the wind turbine. Two of the single-component sensors were attached to the turbine, as shown in figure 5-17, one was positioned in the ground in the centre of the turbine and the remaining three radially in a line at 10 m, 20 m and 30 m away from the tower respectively in a north-easterly direction. The 5TD was sited 90 m north-east of the turbine, down a slight slope in a field adjoining the turbine and separated from the turbine by barbed wire (figure 5-18). The 6TD seismometer was placed at the far end of the field containing the turbine, 190 m south-west. The sensor locations in relation to the turbine and nearby buildings are shown in figure 5-19.

Figure 5-18: *A view of the accelerometers placed in the ground and the 5TD in the distance from the wind turbine.*

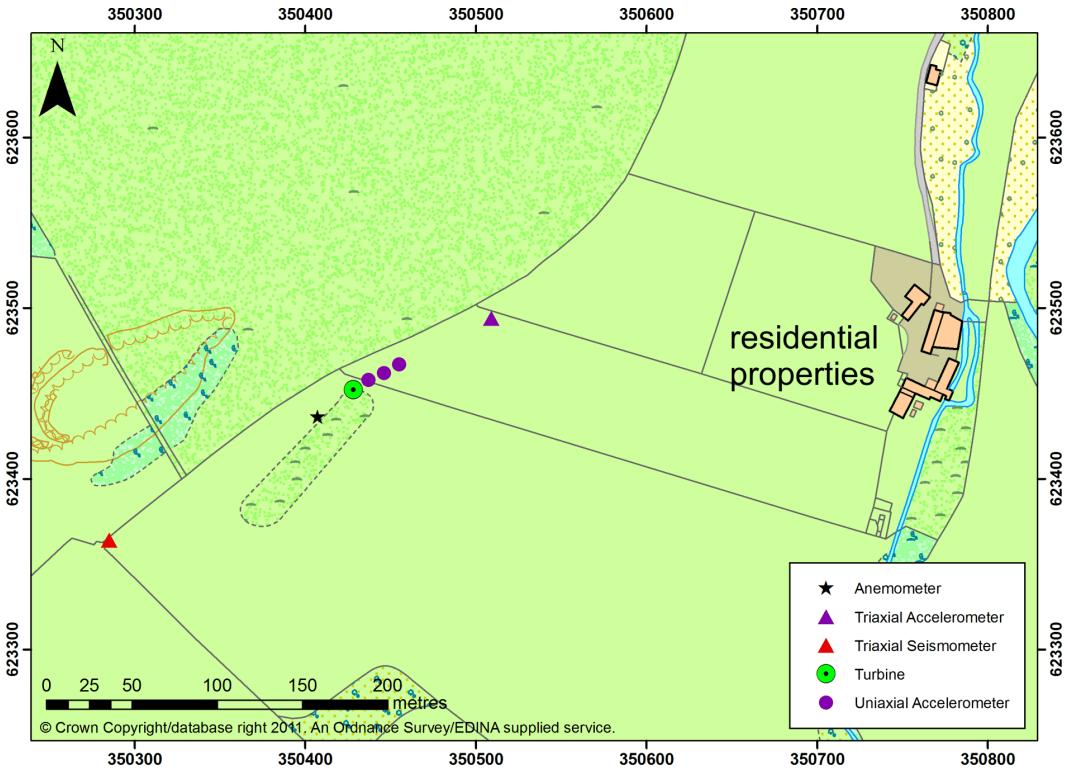

Figure 5-19: *The sensor locations for the monitoring of the Gaia-Wind 133 lattice tower wind turbine near Melrose. Coordinates are given in OSGB.*

5.2.2 Wind Variation

The wind speed and direction for the monitoring period is shown in figures 5-20 and 5-21. The highest wind speed was 9.5 m/s occurring on 6th September 2010 at 13:10. For most of the week, the wind speed did not exceed 5 m/s, however for the last twenty-four hours of monitoring, this changed and wind speeds were obtained between 5 m/s and 9.5 m/s. The pie chart in figure 5-22 shows the distribution of wind speeds in 1 m/s bins.

The predominant winds were north/north-westerly when the wind speed was below 5 m/s. As the wind picked up, the direction changed to a relatively constant south-westerly wind for the last twenty-four hours of monitoring.

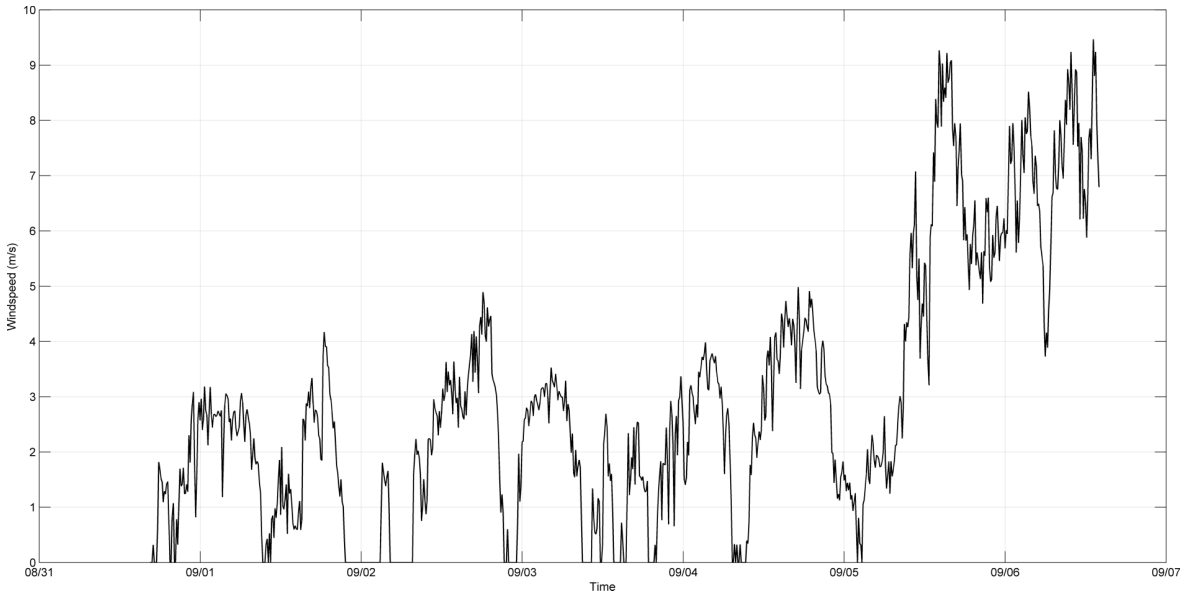

Figure 5-20: *The wind speeds during the monitoring period at Melrose*

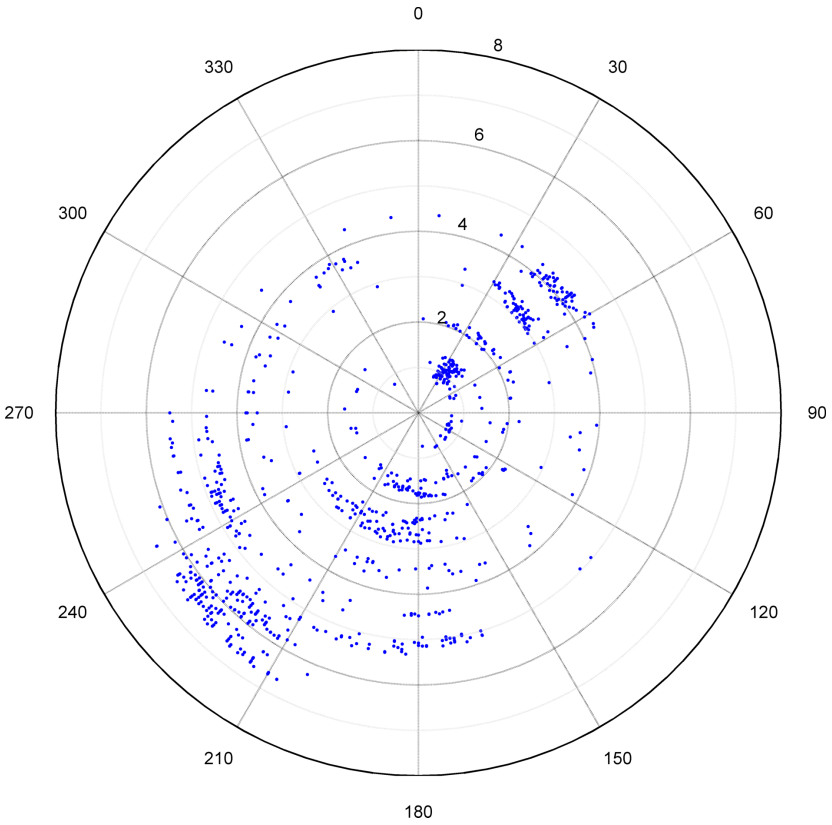

Figure 5-21: *The wind direction during the monitoring period at Melrose. The distance from the centre of the circle indicates days since the start of monitoring*

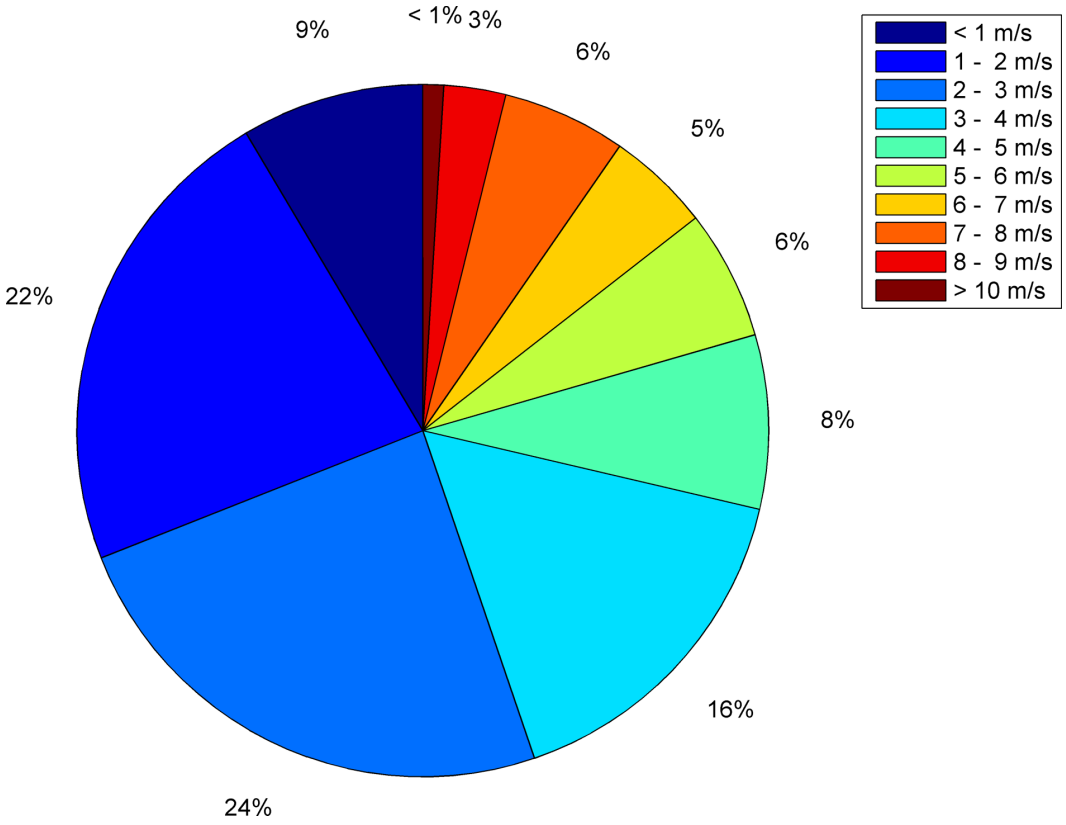

Figure 5-22: *The distribution of wind speeds at Melrose during the monitoring period of 31st August 2010 to 6th September 2010*

5.2.3 Results

The Gaia-Wind 133 starts generating power when the wind speed reaches 3.5 m/s and the blades will rotate at a constant 56 rpm. However at a wind speed of 2.5 m/s the blades will start turning in order to reach the required rpm by the time the winds reach 3.5 m/s. Figure 5-23 shows graphs of the frequency displacement spectra for data recorded on the single-component accelerometers placed on the tower and in the ground in the middle of the tower when the turbine was stationary (wind speed less than 2.5 m/s, hereafter referred to as wsLow and shown as blue on the graphs), starting to turn (wind speeds of 2.5 m/s to 3.5 m/s, hereafter referred to as wsMid and shown as green on the graphs) and generating (wind speeds greater than 3.5 m/s, hereafter referred to as wsHigh and shown as red on the graphs). Figure 5-24 shows the equivalent graphs for data from the two sensors in the ground at 10 m and 190 m respectively.

On the tower, the difference in amplitude between the blades being stationary at wind speeds below 2.5 m/s and starting to turn at 2.5 m/s is less than a factor of ten. On the foundation, for frequencies up to 10 Hz, this has dropped to a factor of two. At 10 m only sensor noise is visible, however the CMG-6TD at 190 m is more sensitive to lower frequencies than the single-component accelerometers and peaks can be seen above 1 Hz. The difference in amplitude between wsLow and wsMid is less than a factor of two.

The shape of the spectrum for wsMid follows the shape of the spectrum when the blades are stationary at wsLow, with only one extra peak appearing at about 7.5 Hz on the tower. At rated rpm when wind speeds are at and above 3.5 m/s additional peaks emerge and some broaden or shift slightly. This can be seen in the on-tower and base spectra.

In the on-tower spectrum for wsHigh, all of the blade rotation frequency harmonics up to 10 Hz are visible (figure 5-25). Below 10 Hz there are two peaks at 2.5 Hz and 3.2 Hz which can not be attributed to blade rotation harmonics. Neither of these peaks can be easily picked out at 10 m or 190 m. As would be expected, at wsLow when the blades are not turning the blade rotation frequencies are not seen. However, other frequencies are visible at 2.3 Hz, 2.45 Hz, 3 Hz, 4.2 Hz, 5.8 Hz, 8.9 Hz and 9.25 Hz.

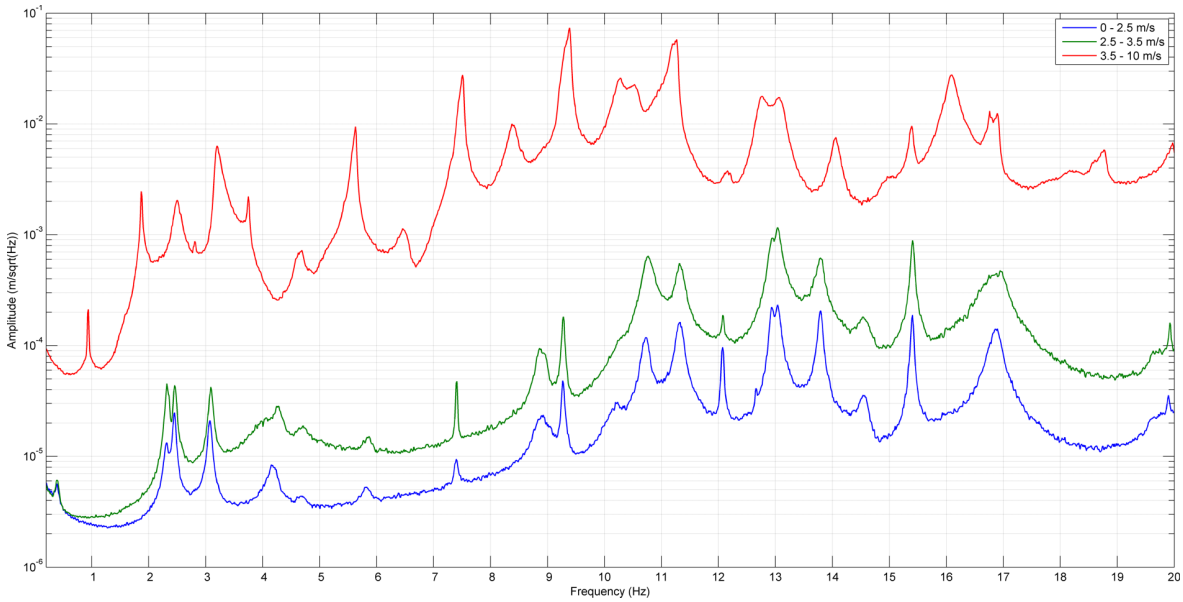

a. On the tower

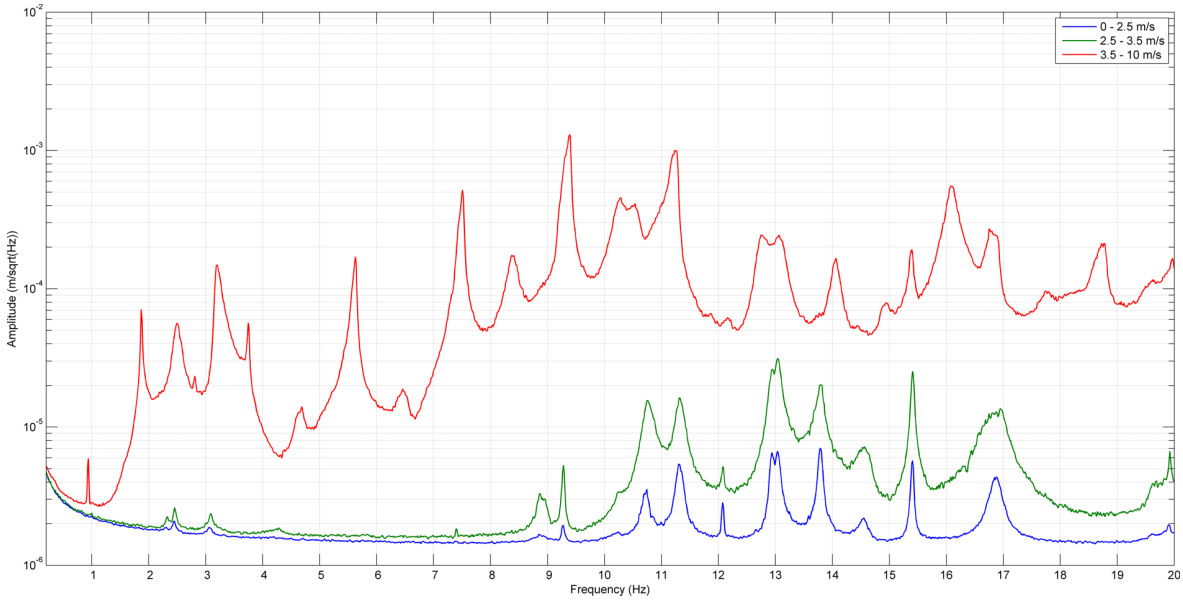

b. On the foundation

Figure 5-23: *The displacement frequency spectra for data recorded from two sensors monitoring the Gaia lattice tower: one on the tower and one on the foundation in the ground in the centre of the tower. Spectra are shown for three wind speed ranges: when the turbine is idle, just starting up and at speed and generating*

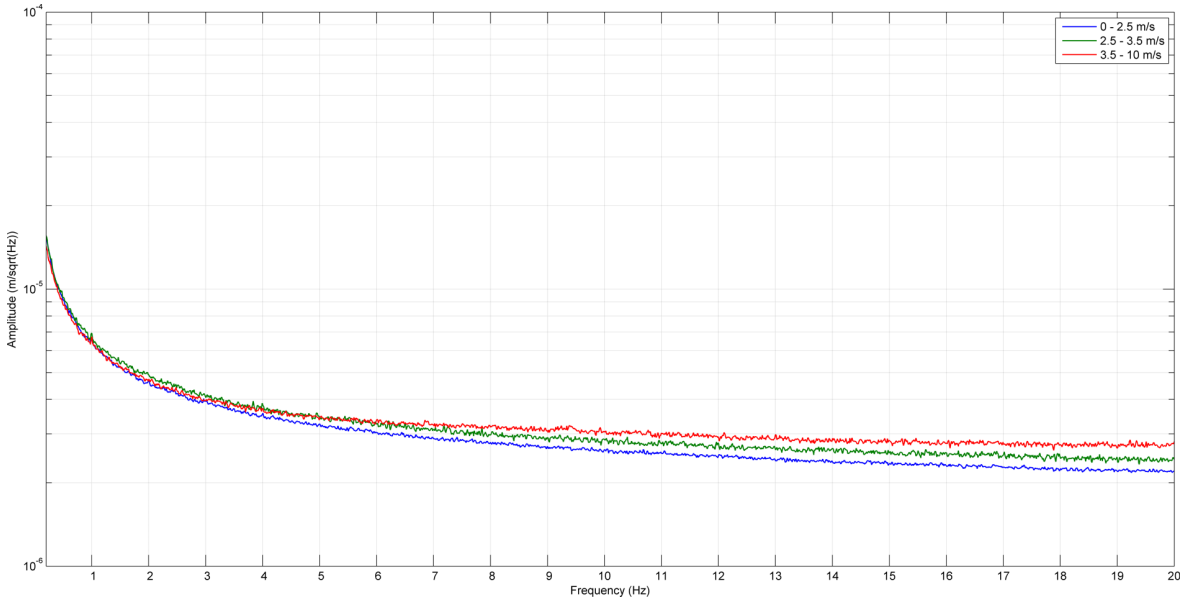

a. 10 m

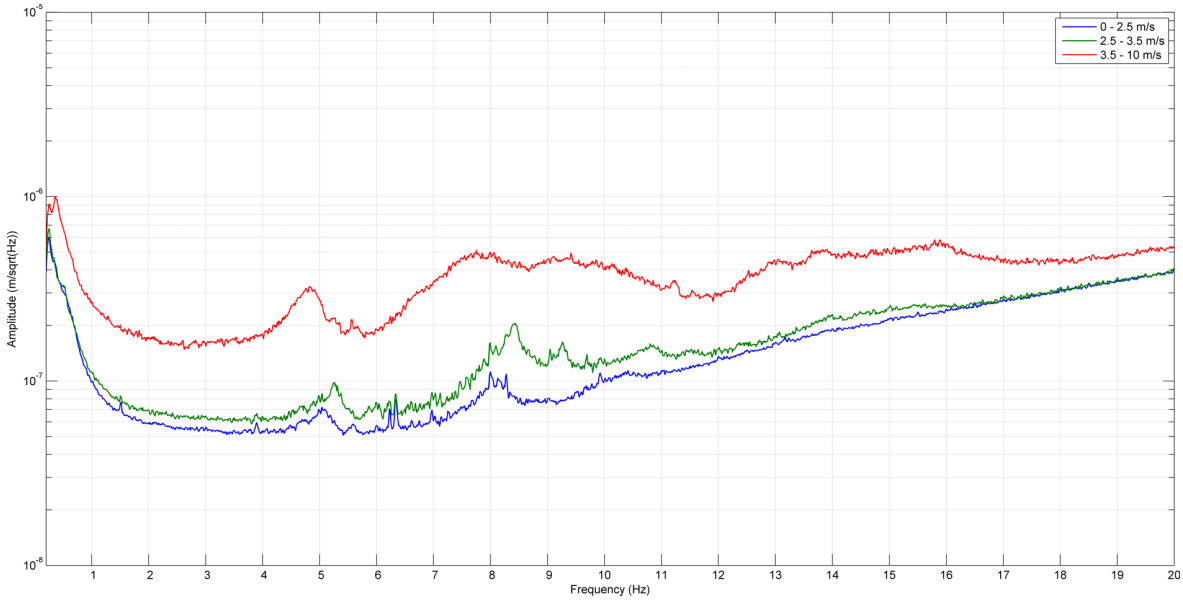

b. 190 m

Figure 5-24: *The displacement frequency spectrum for data recorded from two sensors in the ground at the Gaia-Wind 133 lattice tower site. Spectra are shown for three wind speed ranges: when the turbine is idle, just starting up and at speed and generating*

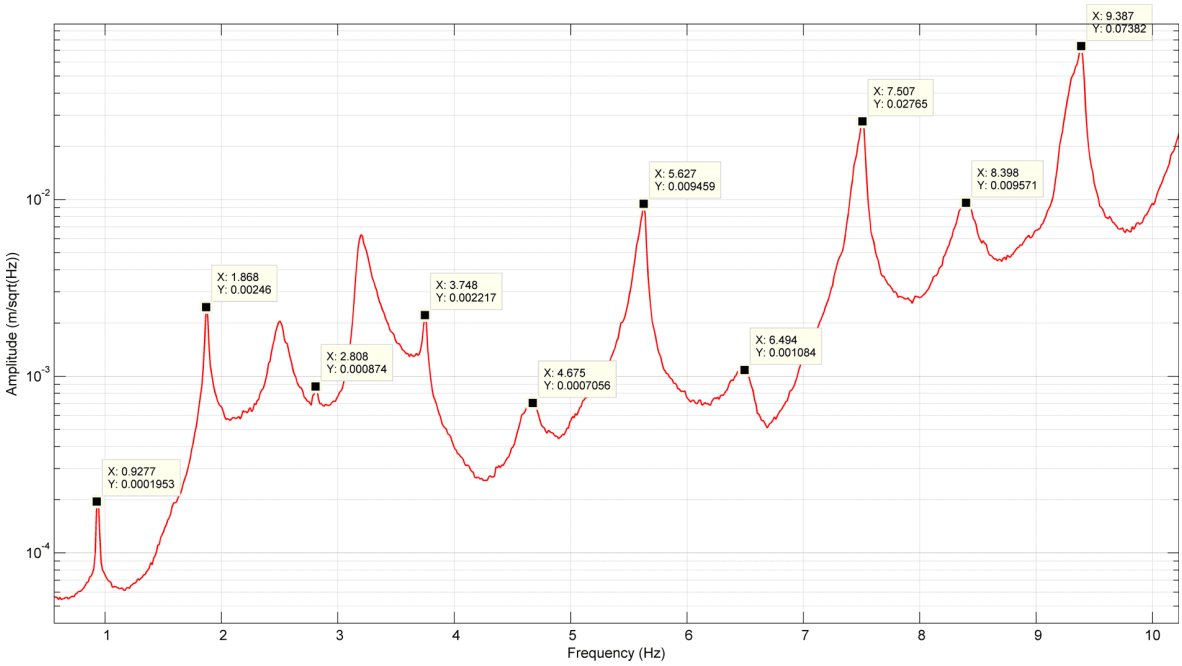

Figure 5-25: *The picked peaks of the Gaia-Wind 133 blade rotation frequency harmonics on the lattice tower*

Figure 5-26 shows the displacement spectra for all the sensors when the wind speed is above 3.5 m/s. The sensor at 10 m only shows sensor noise; however there are peaks visible in the other two accelerometers in the ground at 20 m and 30 m respectively. At 20 m there is a small peak visible at around 7.5 Hz matching the on-tower and base spectra. Both sensors show quite visible peaks at 9.3 Hz and 11.1 Hz. These frequencies are also present in the vertical component of the sensor at 170 m, as is the 7.5 Hz peak, although the amplitude is a factor of ten below the 5TD. There is a drop in amplitude by just under a factor of 100 from the tower to the base, then a further drop of between a factor of 100 and 1000 to the sensor at 20 m, depending on the frequency. The sensor at 170 m, being more sensitive to lower frequencies, also detected a broad peak at 4.7 Hz in both the horizontal (north) and vertical components. Higher frequencies can also be seen on the vertical component which match the on tower and base spectra at 13.1 Hz, 15 Hz, 16.9 Hz and 18.8 Hz respectively.

Picking the tip of the peak common to most of the sensors at 9.3 Hz allows the attenuation of the wave to be calculated, as shown in figure 5-27. An equation from a trendline placed on the log-log plot is calculated as $0.0001r^{-1}$, where r is the distance to the wind turbine. Although different to the Styles et al. (2005) model, the r^{-1} model agrees with the results found for the Gaia-Wind 133 tubular tower at Wigton (figure 5-12 on page 98) and Schofield (2002) at Stateline.

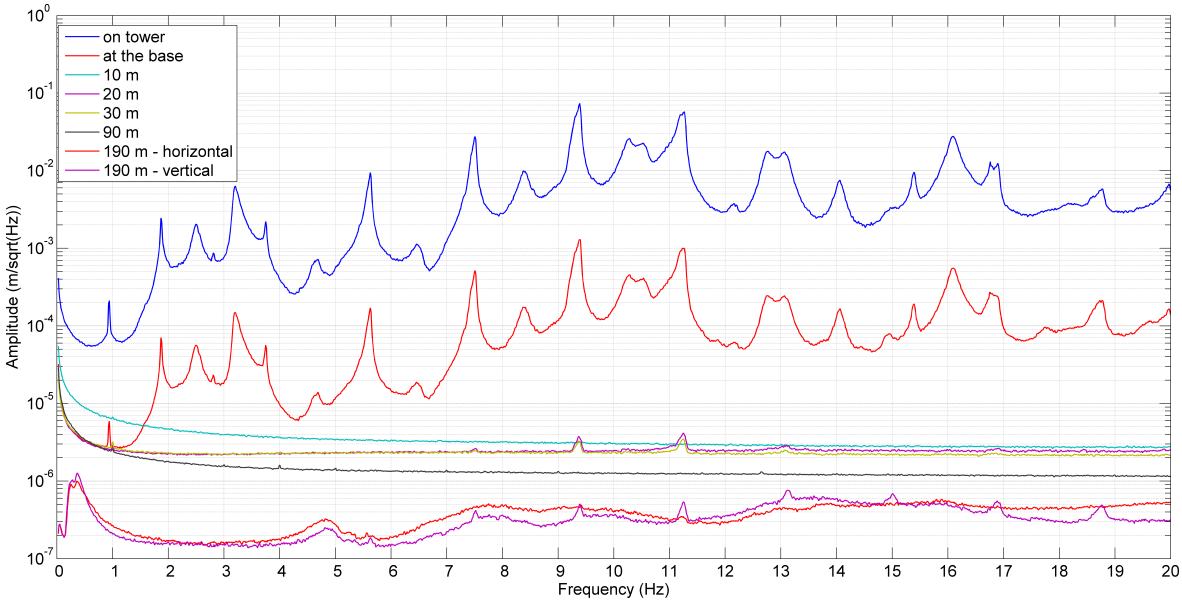

Figure 5-26: *The displacement frequency spectra for data recorded on sensors at a range of distances from the Gaia-Wind 133 turbine at Melrose, when the wind was greater than 3.5 m/s*

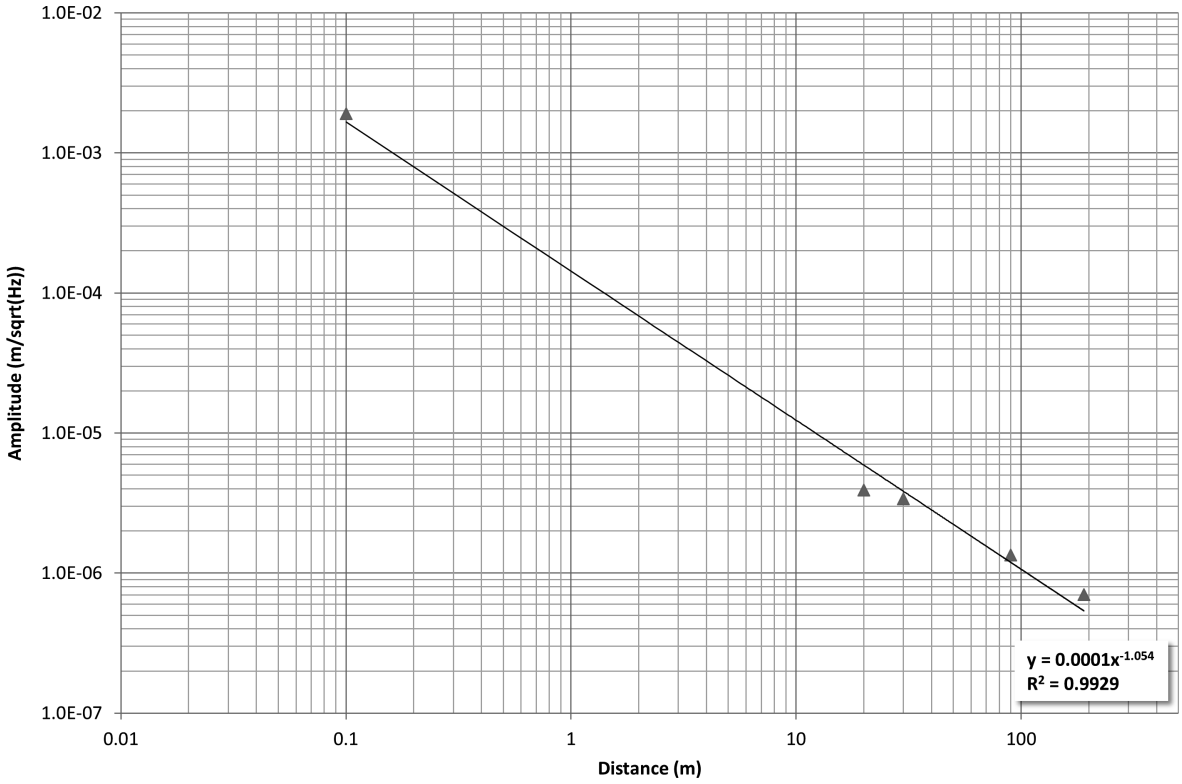

Figure 5-27: *A log-log plot of distance to amplitude for the 9.3 Hz peak when the wind speed is above 3.5 m/s*

A waterfall plot showing how wind speed affects the displacement frequency spectrum is given in figure 5-28. The colour indicates amplitude with the light areas being the frequencies and wind speed of highest amplitude and the dark areas the lowest. The change in amplitude occurs most obviously when the wind speed hits 3.5 m/s and the blades reach full speed, with the most prominent high amplitudes occurring at 9.3 Hz and 11.1 Hz. The frequencies which increase in amplitude at 3.5 m/s, remain visible for higher wind speeds. The 7.5 Hz, 9.3 Hz and 11.1 Hz peaks increase in amplitude further when the wind speed reaches 4.5 m/s.

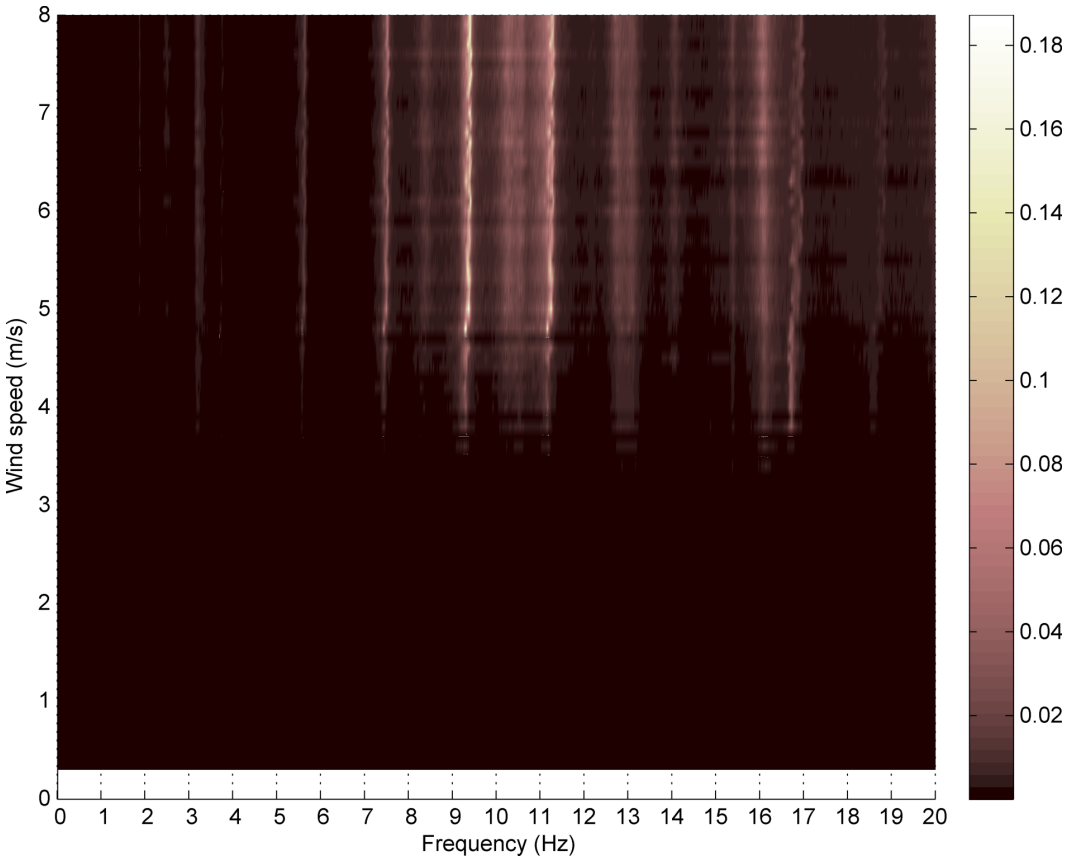

Figure 5-28: *A waterfall plot of wind speed and frequency with colour representing amplitude (m/sqrt(Hz)) from data recorded on the on-tower accelerometer on the Gaia-Wind 133 lattice tower turbine.*

5.3 Proven 35-2 at Kilmarnock, Ayrshire

Proven Energy Ltd was established in Scotland in 1980 by Gordon Proven, with the aim of creating a robust wind turbine capable of generating power in all wind conditions. Their first commercial turbine was installed in 1993. There are three types of Proven turbine, the 7, 11 and 35-2, with rated powers of 2.5 kW, 5.2 kW and 12.1 kW respectively. The Proven 35-2 is a three-blade machine and is the most popular of the three turbines. Unlike the Gaia-Wind 133 and the Endurance E-3120, the

Proven turbines are self-regulating. The blades pitch and cone to regulate the speed. This, Proven states, allows them to operate in storms and very high wind conditions.

The tower, which is made from grey galvanised steel, is icosaganol (twenty-sided) and consists of three interlocking sections, with the diameters of the cross-section faces decreasing with height. The top section of the tower is cylindrical and fits into the icosaganol section using four 'wing' plates. These fit in slots through the outer tower and hold the inner section in place. The hub sits on the top of the cylindrical section. The tower is available in three heights, 15 m, 20 m and 25 m; the Proven 35-2 monitored for this thesis is mounted on a 15 m tower and is shown in figure 5-29.

The Proven 35-2 has a rotor diameter of 8.5 m and operates at wind speeds between 3.5 m/s and 54 m/s. The direction the blades face is controlled by a rudder made from a glass thermoplastic composite known as Twintex. This fits over the hub and round the top section of the tower. Further information on the turbine is given in table 5-3.

Figure 5-29: *The Proven 35-2 wind turbine at Kilmarnock*

Type	Downwind
Blades	3, variable speed self-regulating
Blade material	Glass thermoplastic composite
Tower	Hutchinson self-supporting monopole
Tower height	15 m, 20 m or 25 m
Rotor diameter	8.5 m
Rated speed	11 m/s
Rated power	12.1 kW
Peak power	13.7 kW
Cut-in wind speed	3.5 m/s
Cut-out wind speed	54 m/s
MCS certified at time of testing	Yes
Phase	three-phase

Table 5-3: *Information about the Proven 35-2 wind turbine. After Proven Energy (2010).*

5.3.1 Site Information and Deployment

The Proven 35-2 turbine monitored for this thesis is located on farmland approximately 9 km east of Kilmarnock in East Ayrshire, Scotland (figure 5-30). The site is 2.8 km north of the main A71 road and 1.5 km east of the A719. The wind turbine is used to power a farm and is located approximately 200 m south of the main farm buildings (figure 5-31), in a field that is normally used for grazing cattle.

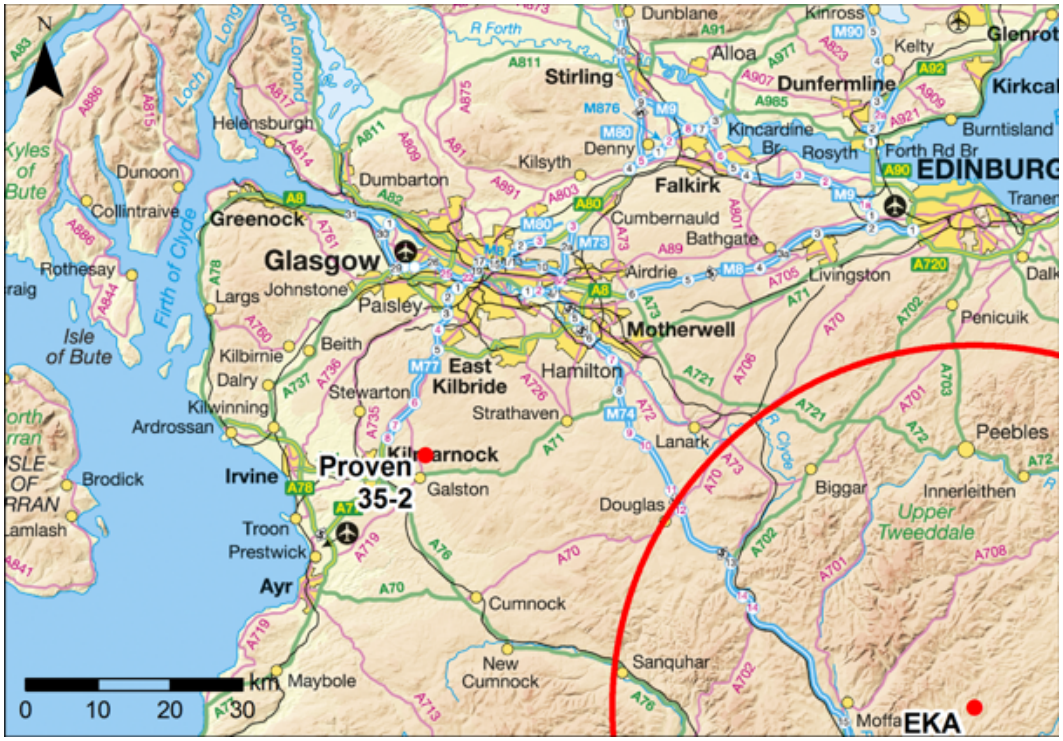

Figure 5-30: *The location of the Proven 35-2 turbine near Kilmarnock in East Ayrshire. Contains Ordnance Survey data ©Crown copyright and database right 2011*

Vibrations were measured over several days from 19th to 25th May 2011, using two uniaxial CMG-5U accelerometers fixed to the turbine and one on the concrete foundation at the base, covered with soil and rocks. The three CMG-5Us which had been placed in the ground radially from the turbine when monitoring the Gaia-Wind turbine were not used for this testing, as it was found during pre-field testing, that the DM24S12AMS digitiser was not producing reliable results on these channels. The CMG-5TD was placed in the ground 100 m north-east of the turbine and the CMG-6TD seismometer buried a further 100 m in the same direction, in a field on the other side of a farm track. Figure 5-31 shows the locations of the sensors in relation to the turbine and farm buildings.

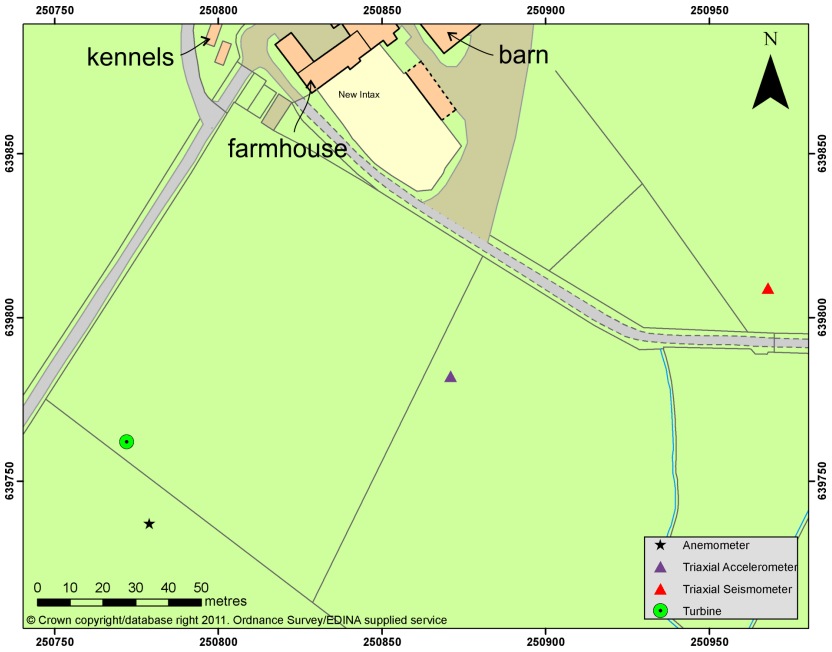

Figure 5-31: *The sensor locations for the monitoring of the Proven 35-2 wind turbine near Kilmarnock. Coordinates are given in OSGB.*

5.3.2 Wind Variation

The wind speed and direction for the monitoring period is shown in figure 5-32. The wind speed at Kilmarnock ranged between 2 m/s and 8 m/s for the first four days of the monitoring period. On 23rd May 2011, the winds picked up and as had previously occurred at Wigton when monitoring the Gaia-Wind 133 tubular tower wind turbine, a power cut occurred, switching off the DM24S12AMS digitiser. Therefore there is no accelerometer data available after this point. The seismometer powered from a 12v battery remained operational for the entire period and was not affected by the power cut.

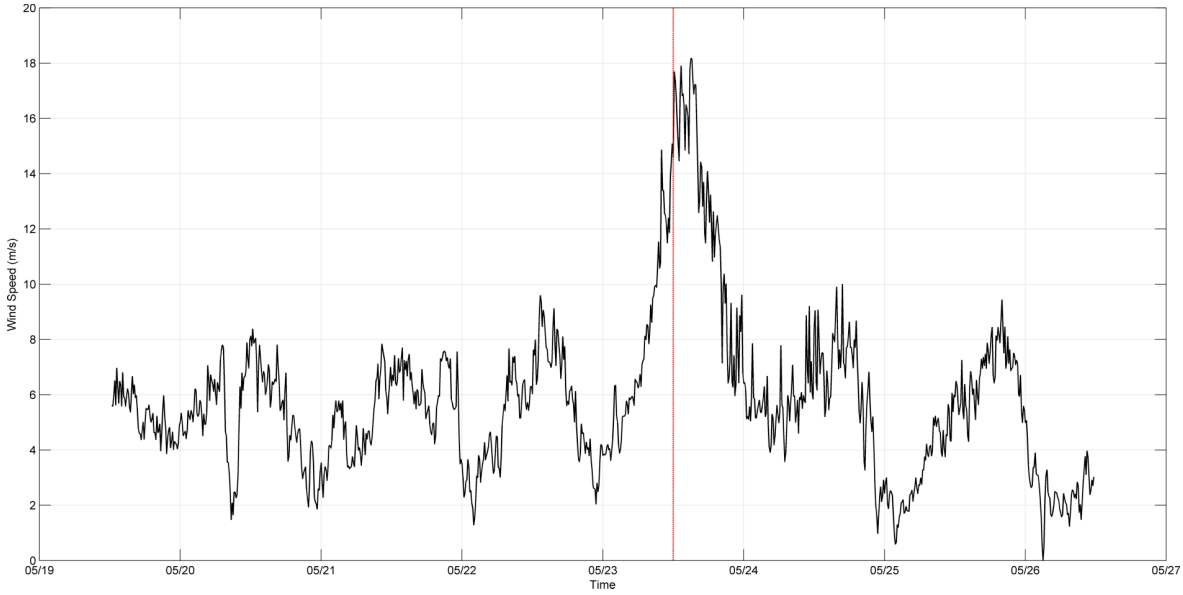

a. Wind speed

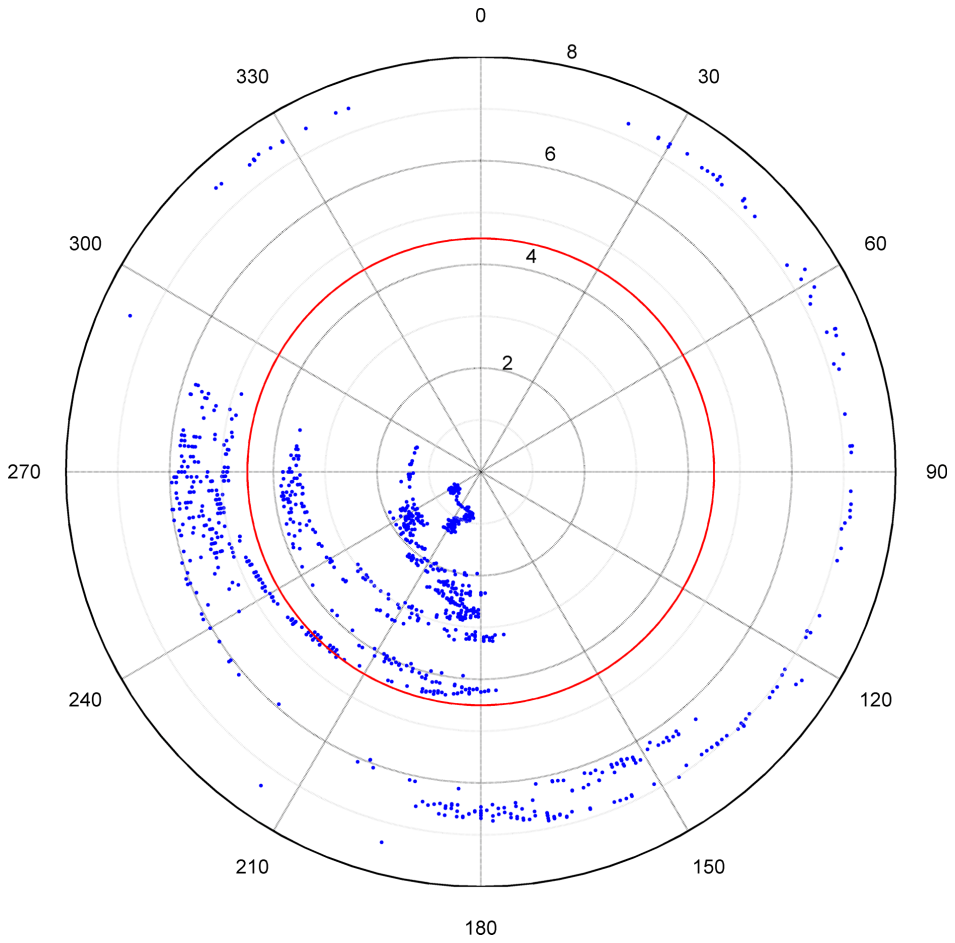

b. Wind direction, with days since the start of monitoring given by the radius

Figure 5-32: *The wind speeds and direction for the monitoring period at Kilmarnock. The red line and circle indicate the power cut to the digitiser.*

The maximum wind speed recorded during the monitoring period was 18.2 m/s and occurred in the afternoon of the 23rd May, after the digitiser had lost power. Prior to the cut-out the maximum speed had been 14.9 m/s. At both of these wind speeds the turbine is generating at or above rated power (figure 5-33). The pie charts in figures 5-34 and 5-35 show the percentage distribution of 2 m/s periods of wind speed prior to the power cut and for the entire monitoring period. Both before the power cut and for the monitoring period as a whole, the predominant wind speeds are between 2 m/s and 8 m/s. The wind direction is predominantly south/south-westerly until 24th May when it moves to a slight westerly for twenty-four hours before changing over the following twenty-four hours to become northerly at the end of the week.

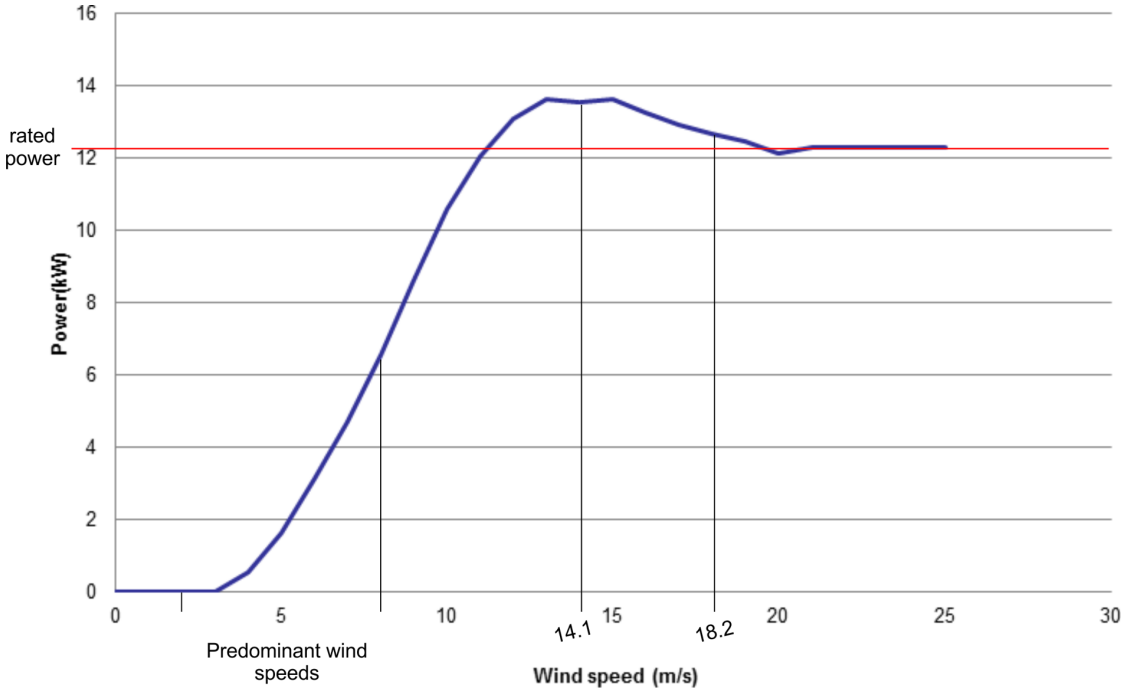

Figure 5-33: *The power curve of the Proven 35-2 wind turbine. The red line indicates rated power. (After Proven Energy, pers. comm.)*

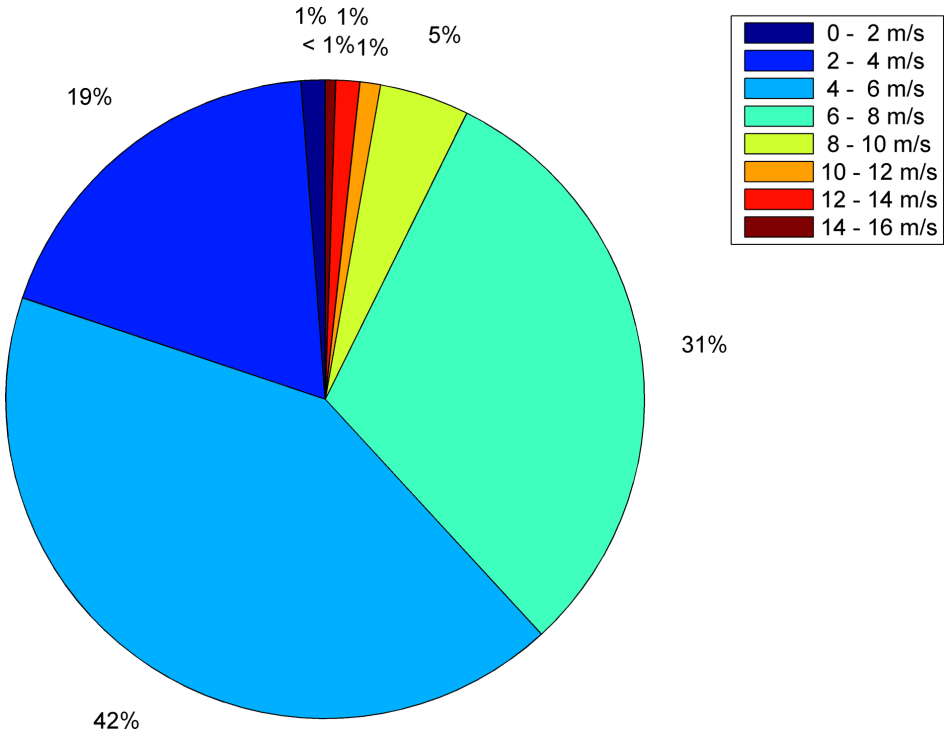

Figure 5-34: *The distribution of wind speeds prior to the power cut*

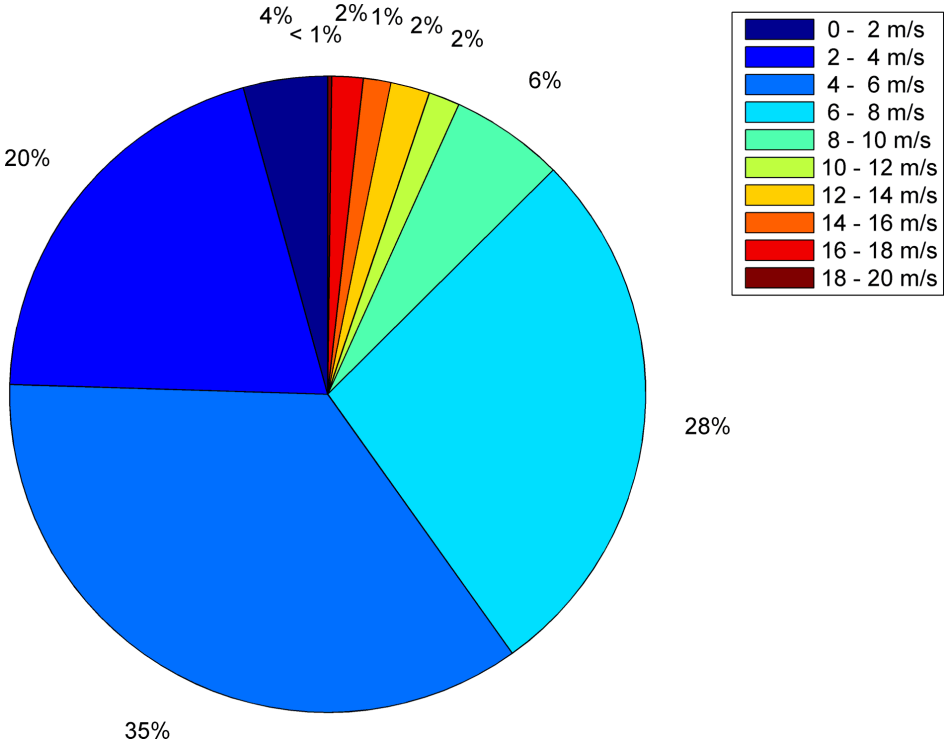

Figure 5-35: *The distribution of wind speeds for the entire monitoring period*

5.3.3 Results

The Proven 35-2 is a variable speed wind turbine, with a cut-in wind speed of 3.5 m/s. Accelerometer data from the sensors on the tower is available for the period leading up to the power cut. Figure 5-36 shows the displacement frequency spectra for the period up to the cut-in speed and then at 2 m/s intervals up to the maximum wind speed. Figure 5-37 shows the equivalent graphs for the sensors in the ground at 100 m and 200 m from the turbine.

Rated power for the Proven 35-2 is reached at a wind speed of 11 m/s. On the tower, below 9.5 m/s, the spectrum changes with each range of wind speeds. This is demonstrated in the 1 Hz to 3 Hz band on the tower, where the peak shifts to the right as the wind speed increases up to 9.5 m/s. At wind speeds greater than this the spectrum stabilises in amplitude and shape. There is a peak at 1.1 Hz which does not shift with wind speed; this is likely to be the first bending mode of the tower and is not affected by the blade rotation rate. At this frequency, there is a difference of a factor of fifty in the amplitude between the spectra when the wind speed is <3.5 m/s and 11.5 m/s.

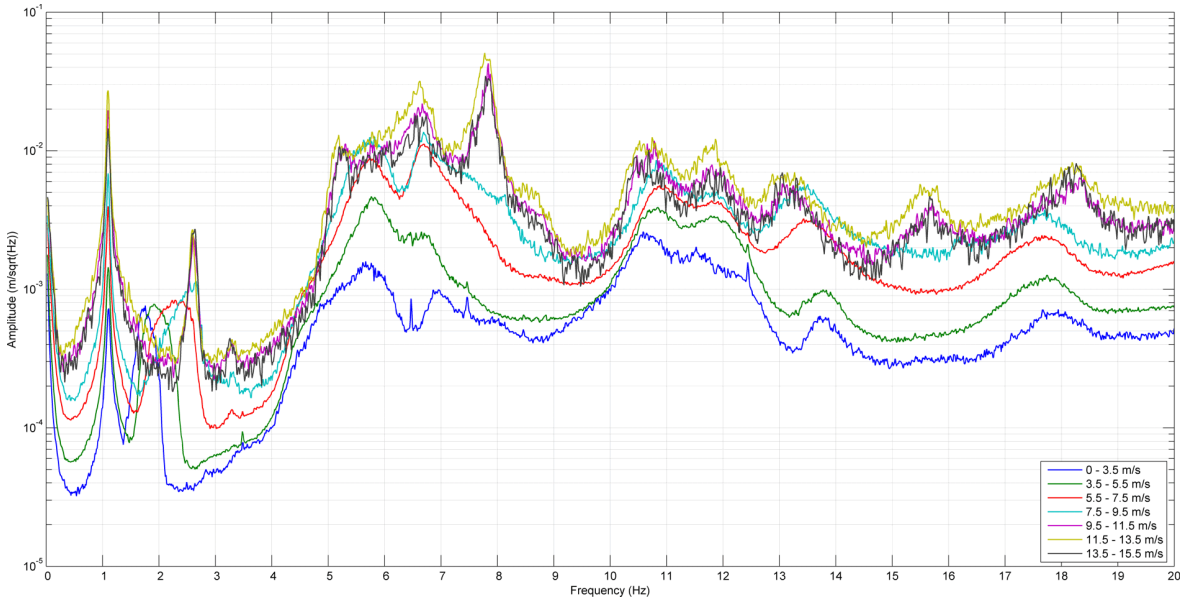

Figure 5-36: *The displacement frequency spectrum from data recorded on the tower of the Proven 35-2, at 2 m/s ranges*

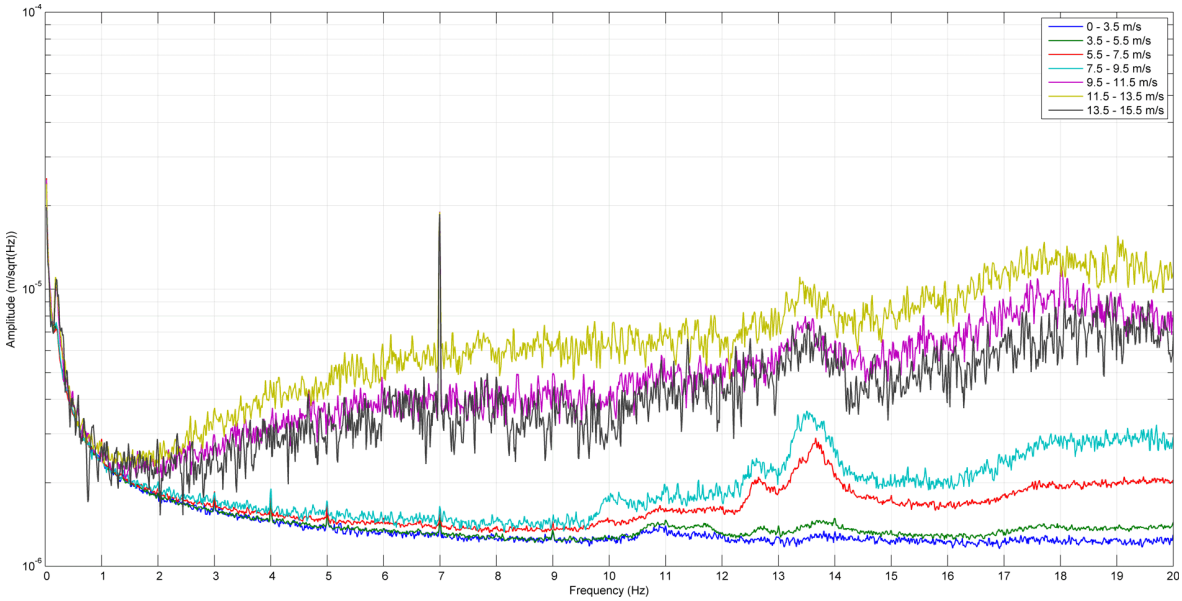

a. 100 m from the turbine

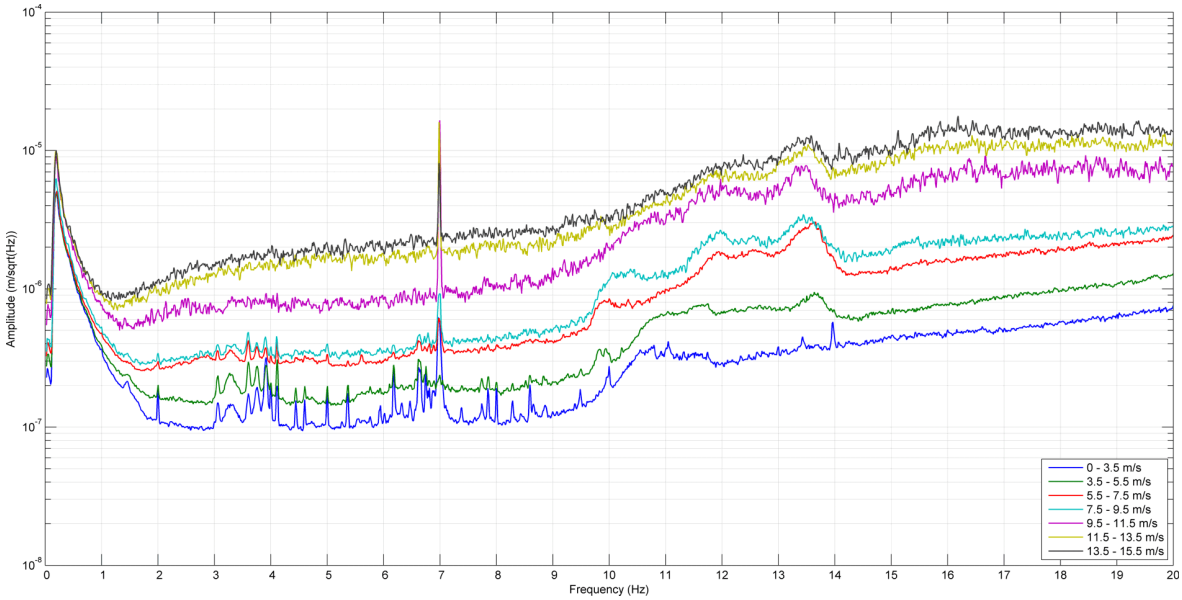

b. 200 m from the turbine

Figure 5-37: *The displacement frequency spectrum from data recorded on two sensors in the ground at the Proven 35-2 site. Spectra are displayed at 2 m/s wind speed ranges.*

On the sensor at 100 m, below 9 Hz, the amplitudes are very similar with small peaks identifiable at 4 Hz, 5 Hz and 7 Hz. Above 9 Hz, the spectral amplitude diverges increasing with wind speed. At higher wind speeds the amplitude is between a factor of two and five greater than the 0 - 5.5 m/s amplitudes depending on frequency. Any peaks visible at lower wind speeds (other than 7 Hz) are masked by the rise in background noise levels.

The sensor at 200 m is more sensitive at low frequencies and the rise in amplitude with wind speed is seen more clearly than on the 100 m sensor. There are about ten peaks visible through low wind speeds between 2 Hz and 7 Hz. However as the wind speed increases, the background noise levels increase and the definition of the peaks decreases. At speeds above 9.5 m/s, most of the peaks have been masked by the background noise.

Figure 5-38 shows the displacement spectra for all the sensors at wind speeds between 9.5 m/s and 15.5 m/s. The sensors in the ground show little above the background noise, apart from the prominent spike at 7 Hz. This is not seen in the data from the on-tower or foundation sensors, which indicates that it originates from a source other than the wind turbine.

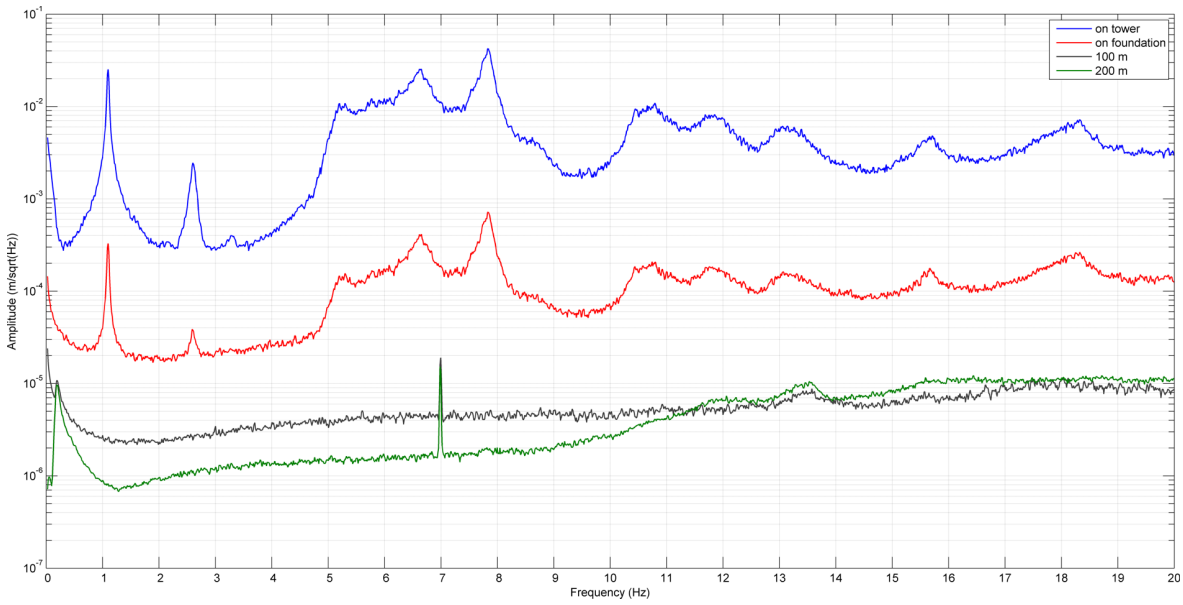

Figure 5-38: *The displacement frequency spectra using data recorded on the sensors at a range of distances from the turbine when the wind speed was between 9.5 m/s and 15.5 m/s*

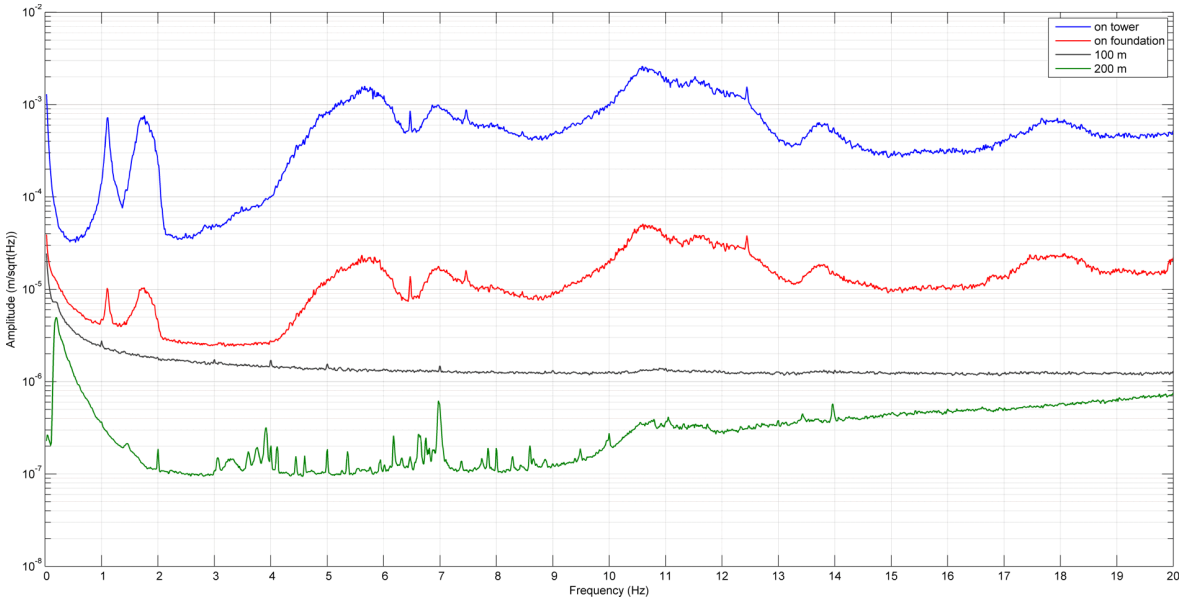

Figure 5-39: *The displacement frequency spectra using data from sensors at a range of distances from the turbine, when the wind speed was less than 5.5 m/s*

The amplitude on the foundation is a factor of one hundred lower than on the tower and has dropped by a further factor of ten by 100 m away from the turbine. Up to 9 Hz, the seismometer at 200 m from the tower is a factor of two lower in amplitude than the accelerometer at 100 m. Between 9 Hz and 11 Hz, the amplitude converges with the accelerometer spectrum.

At lower wind speeds the peaks in the spectra from the data recorded on the tower and on the foundation are broader. However, more peaks can be seen above background noise in the data from the seismometer at 200 m (figure 5-39). Some small peaks are visible in data from the accelerometer at 100 m which correspond with peaks in the seismometer spectrum, however they do not correspond to peaks in the on tower or foundation spectra. There is a drop in amplitude between the data from the accelerometer on the tower and the seismometer at 200 m of over a factor of one thousand.

The plots in figure 5-40 show how wind speed affects the displacement spectrum on the tower. The colour indicates amplitude, lighter areas being the frequencies and wind speed of highest amplitude and the dark areas the lowest. The highest amplitudes occur at wind speeds greater than 8 m/s at 7.9 Hz. At 1.1 Hz there is a constant spike across all wind speeds, corresponding to the first bending mode of the tower. There is also a constant, medium amplitude peak at 6 Hz appearing when the wind speed reaches 5 m/s and remaining for higher wind speeds. Between 2 Hz and 3 Hz, the shift in frequency with wind speed is clearly visible.

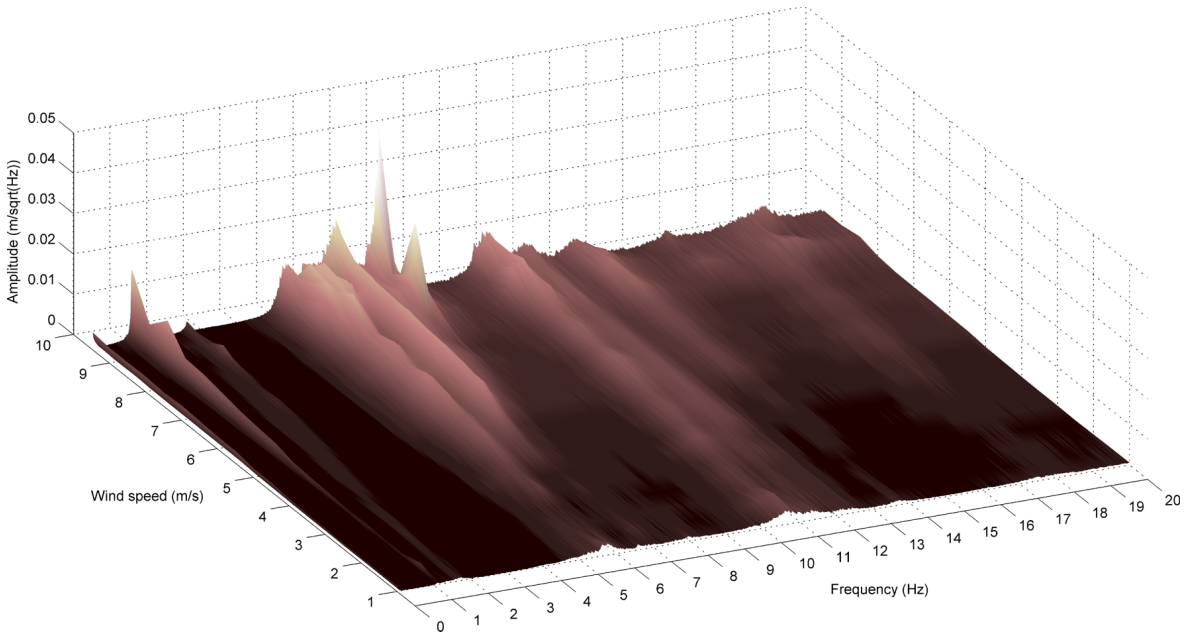

a. 3D

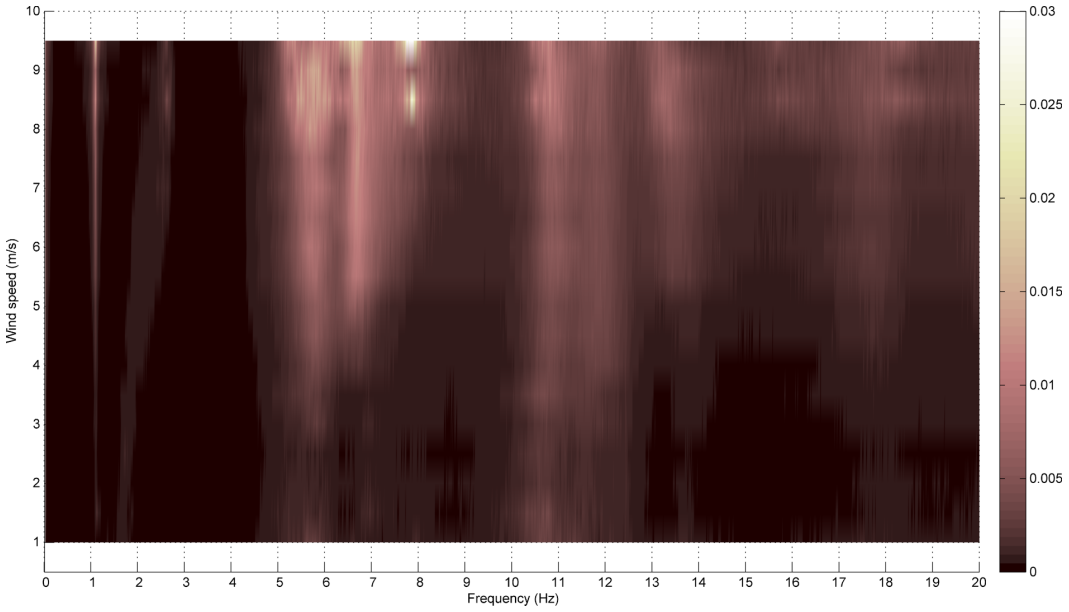

b. 2D

Figure 5-40: *The effect of wind speed and frequency on displacement, with colour representing amplitude (m/sqrt(Hz)). Data is recorded on the tower of the Proven 35-2.*

5.4 Endurance E-3120 near Hayle, Cornwall

Endurance Windpower is an American manufacturer of 5 kW, 35 kW and 50 kW wind turbines; however only the E-3120 model is available in the UK. It is a three blade small wind turbine with a rated power of 50 kW, at the upper limit of the definition of a small wind turbine. As with the Gaia-Wind 133, the E-3120 is fixed speed, operating at 43 rpm and has a rotor diameter of 19 m. There is an anemometer connected to the upwind side of the nacelle. This is used by the on-board computer system to control the cutting-in and -out of the turbine.

The turbine comes on a monopole tower at a height of either 24 m or 36.5 m. The E-3120 monitored for this thesis is mounted on the 24 m tower. The tower is an elongated conical shape with the widest diameter at the base and is made from intersecting units connected by external flanges. Further information on the turbine is given in table 5-4.

Type	Downwind
Blades	3, constant speed 43 rpm nominal
Blade material	Fibreglass/Polyester
Tower	Free-standing monopole
Tower height	24 m or 36.5 m
Rotor diameter	19.2 m
Blade length	9 m
Rated speed	9.5 m/s
Rated power	50 kW
Cut-in wind speed	3.5 m/s
Cut-out wind speed	25 m/s
Max wind speed	52 m/s
MCS certified at time of testing	No
Phase	three-phase

Table 5-4: *Information about the Endurance E-3120 wind turbine. After Endurance Windpower Ltd (2011b).*

5.4.1 Site Information and Deployment

Lanyon Farm and holiday cottages are located 4 km east of Hayle in Cornwall (figure 5-41). The nearest main road, the A30 is 1.7 km away. The wind turbine is located in a field belonging to the farm and is used to power the farm and cottages.

Figure 5-41: *The location of the Endurance E-3120 near Hayle in Cornwall. Contains Ordnance Survey data ©Crown copyright and database right 2011*

Measurements were recorded over several days from 31st August 2011 to 6th September 2011 using the DM24S6EAM digitiser with six CMG-5U accelerometers connected to it. Two of the sensors were attached to the inside of the turbine, on either side of the door, 80 cm above ground level. One sensor was orientated to point north east and the other south east. A third accelerometer was placed inside the turbine in the centre of the foundation pointing west. The remaining three accelerometers were placed radially in a line at 10 m, 20 m and 30 m away from the tower in a south-westerly direction (figure 5-42). The CMG-6TD seismometer was buried 200 m north-east of the turbine, in a field next to the main track to the cottages. The sensor locations in relation to the turbine and nearby buildings are shown in figure 5-43.

Figure 5-42: *A view of the accelerometers placed in the ground and the Endurance E-3120 wind turbine*

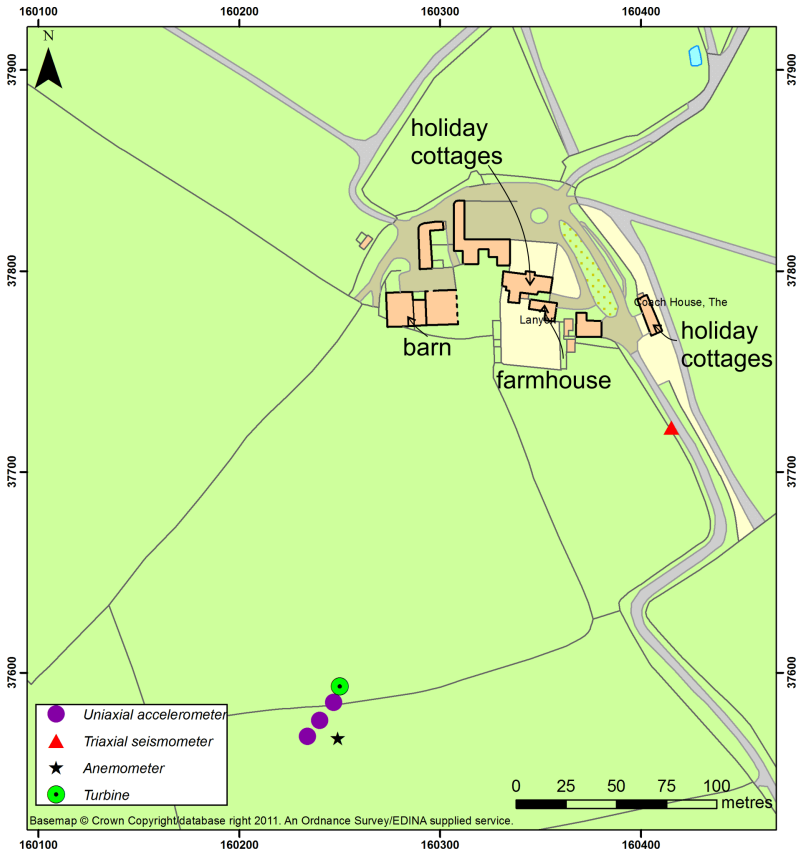

Figure 5-43: *The sensor locations for monitoring the Endurance wind turbine near Hayle. Coordinates are given in OSGB.*

5.4.2 Wind Variation

The wind speed and direction for the monitoring period are shown in figure 5-44. The DM24S6EAM digitiser runs off a 12v battery and should stay operational for the entire monitoring period. However, a faulty battery caused the digitiser to turn off at midnight between 4th and 5th September 2011. Therefore there is no accelerometer data available after this point. The seismometer recorded for the entire period, powered from its own 12v battery.

The highest wind speed up to the point of the power cut was 7.1 m/s, occurring on 1st September at 15:30. After the power cut, the wind speed began to rise, with a maximum speed of 10.3 m/s occurring on 6th September at 07:10. At this wind speed, the turbine was generating more than rated power (figure 5-46).

The wind direction varied throughout the week. Initially for the first two days the winds were south easterly, changing to south westerly for the following two days. Toward the end of the week the direction was variable, ranging from south-west, through west round to northerly.

The pie charts in figures 5-47 and 5-48 show the percentage distribution of 1 m/s periods of wind speed prior to the power cut and for the entire monitoring period. For both periods, the wind speeds are evenly distributed, with small percentages occurring at the higher end (greater than 7 m/s).

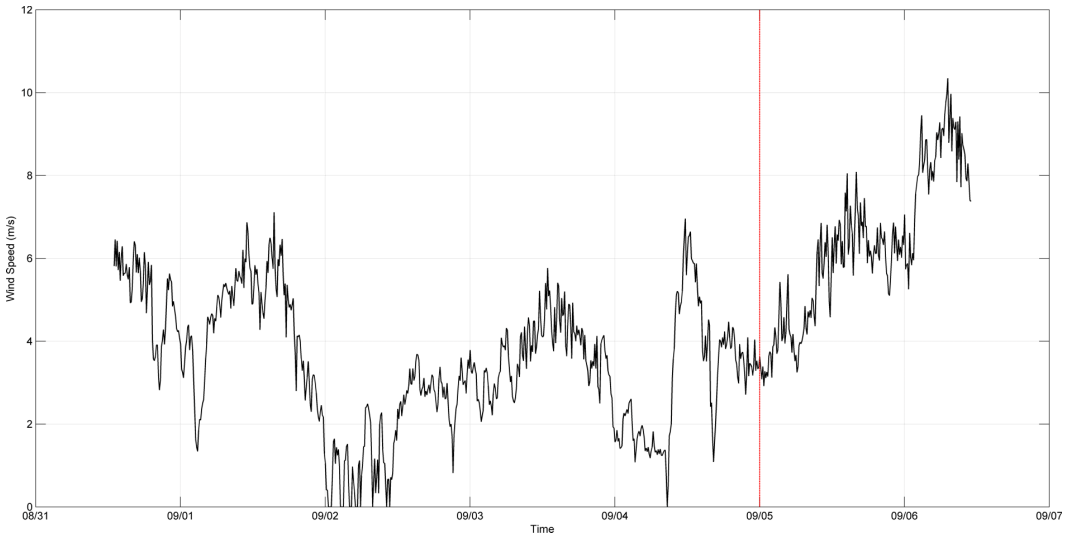

Figure 5-44: *The wind speed for the monitoring period at Hayle. The red line indicates the power cut to the digitiser*

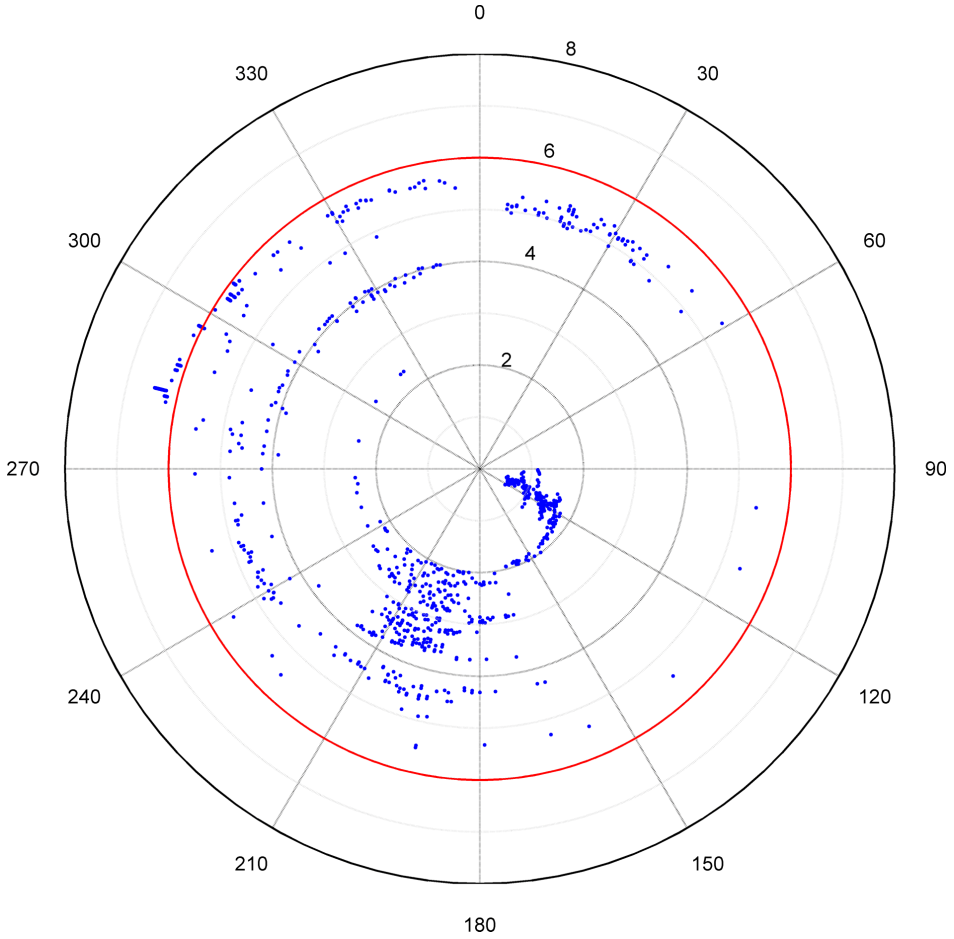

Figure 5-45: *The wind direction for the monitoring period at Hayle. The red circle indicates the power cut to the digitiser and the distance from the centre of the circle the days since the start of monitoring*

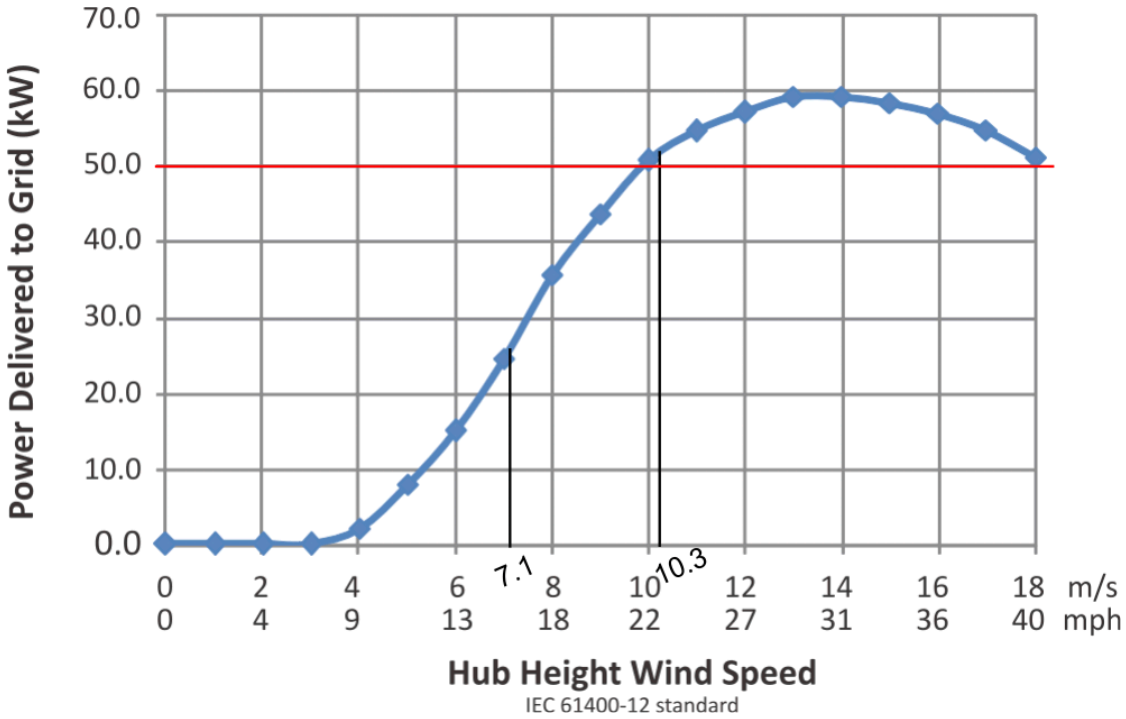

Figure 5-46: *The power curve of the Endurance E-3120 wind turbine (After Endurance Windpower Ltd 2011b). The red line indicates rated power.*

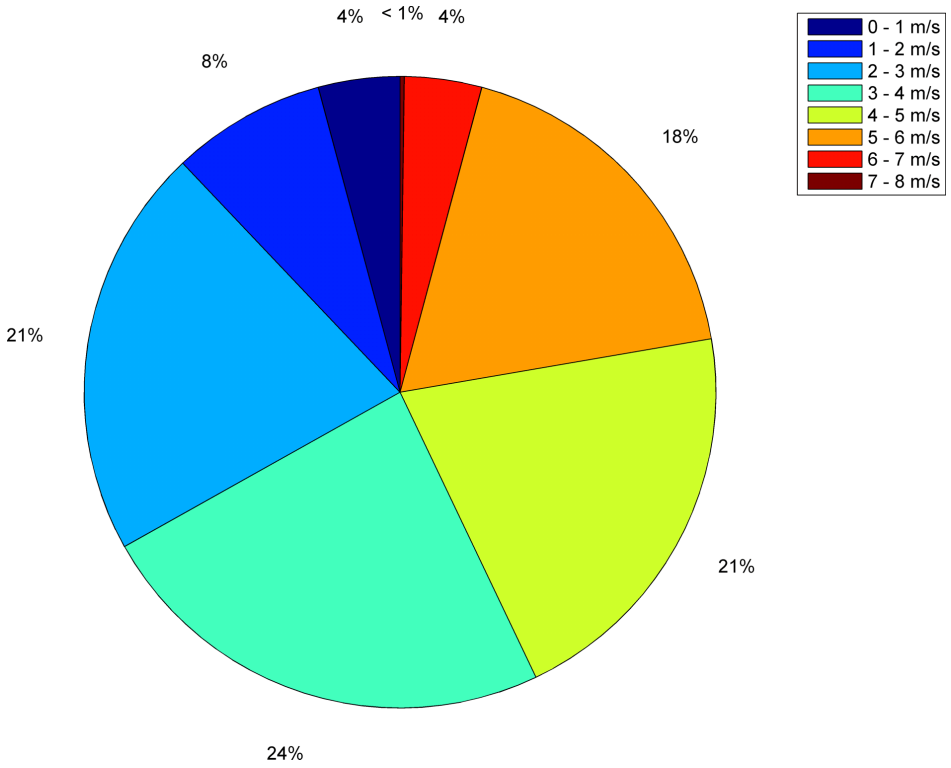

Figure 5-47: *The distribution of wind speeds at Hayle prior to the power cut*

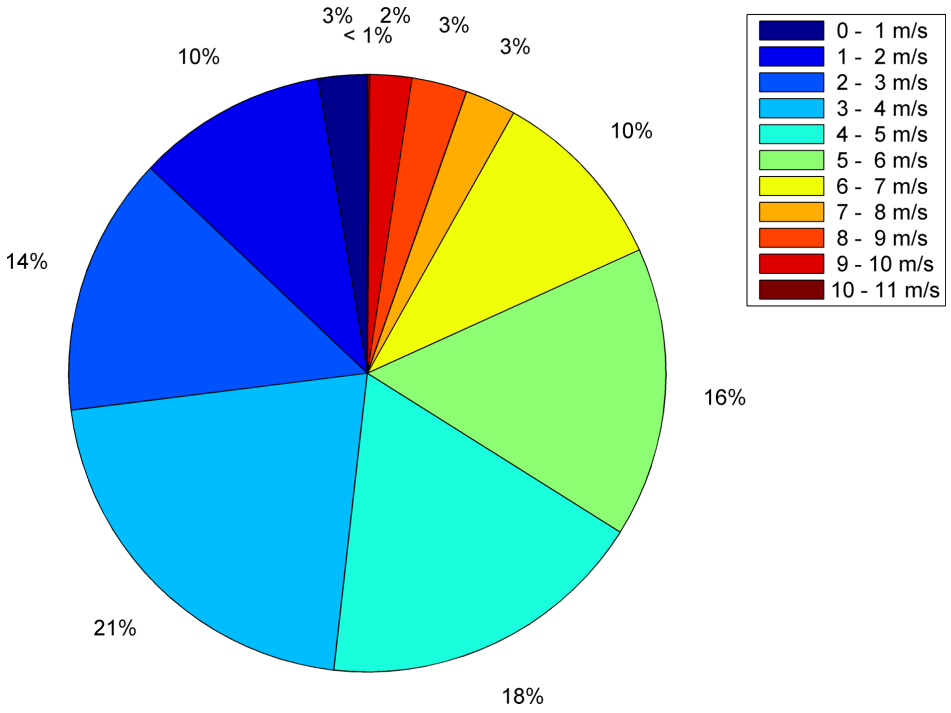

Figure 5-48: *The distribution of wind speeds at Hayle for the entire monitoring period*

5.4.3 Results

The Endurance E-3120 has a cut-in wind speed of 3.5 m/s. It is at this point that the blades will start to turn and the turbine will start generating and delivering power to the grid. At 25 m/s the turbine will cut-out and the brake will be automatically applied, as the force of the wind at speeds above this can cause damage to the rotor. Figure 5-49 shows the displacement frequency spectra at 1 m/s intervals up to the maximum wind speed achieved during the week. Figure 5-50 shows the equivalent graphs for the sensors in the ground at 10 m and 200 m from the turbine.

On the tower, as the wind speeds increase, the amplitude of the spectrum increases, with the main difference in amplitude occurring between the 2 m/s to 3 m/s range and 3 m/s to 4 m/s range. However, the difference in amplitude between the minimum and maximum spectra is at most a factor of ten (dependent on frequency). Peaks are well defined at all wind speeds, however when all the spectra are compared, the spectrum for speeds of less than 1 m/s is noisier, this may be due to less data being available for this wind speed range than the others.

At 10 m from the turbine, the amplitudes have dropped by a factor of one hundred. At low wind speeds, the amplitude is low and additional peaks appear every 1 Hz. The root cause of this has not been identified, but it may be linked to the pulse per second from the GPS and a grounding issue. Many of the peaks visible in the data recorded on the tower are also seen in these spectra.

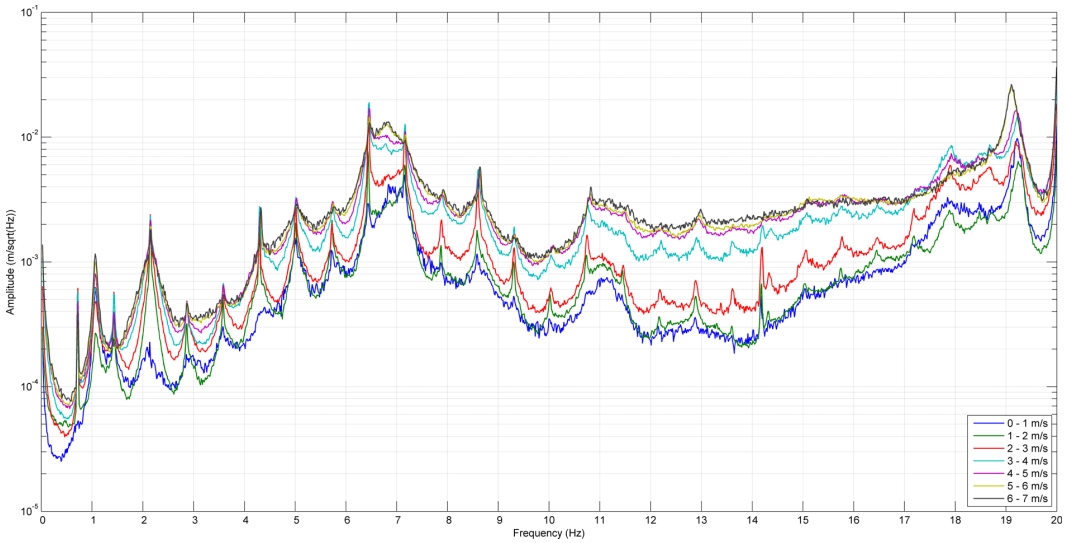

Figure 5-49: *The displacement frequency spectrum from data recorded on the tower of the Endurance E-3120, at 1 m/s ranges*

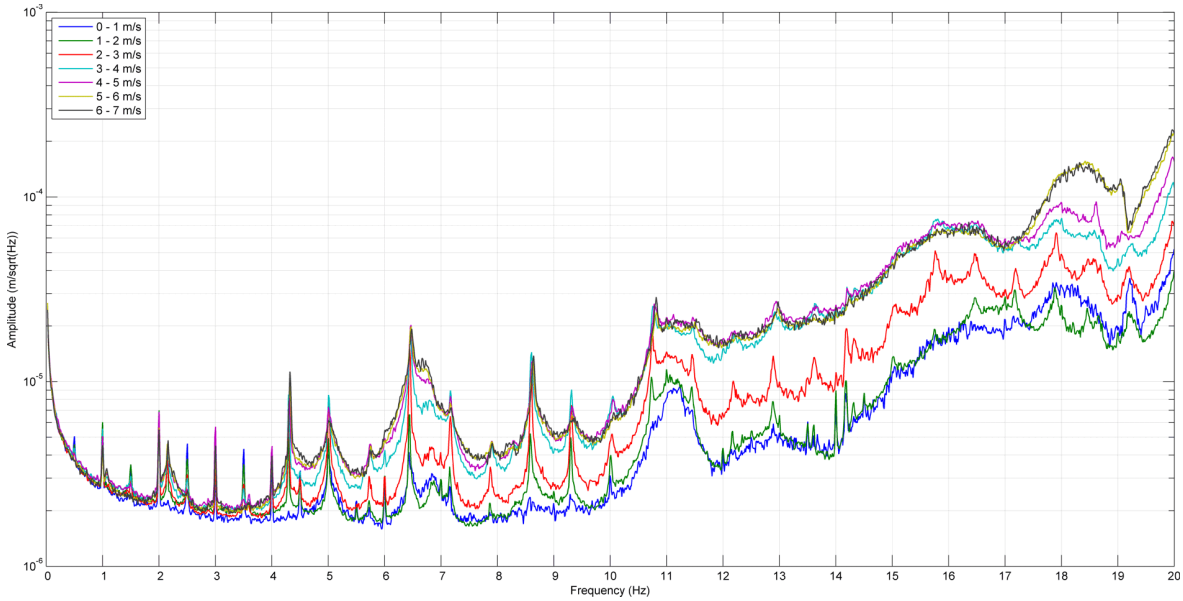

a. 10m

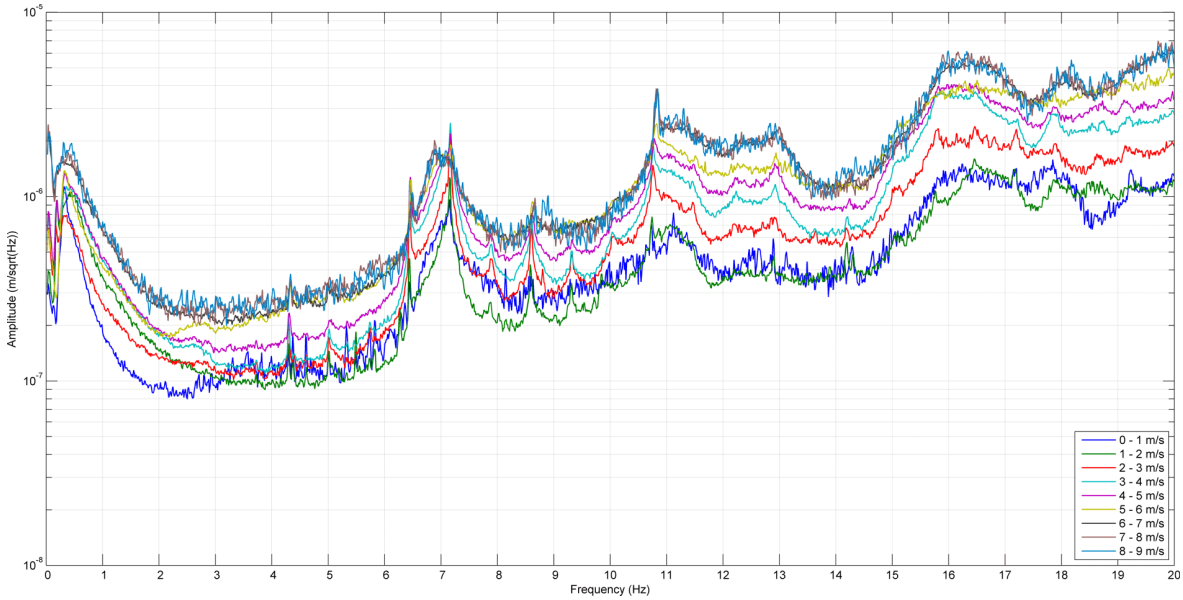

b. 200m

Figure 5-50: *The displacement frequency spectra, at 1 m/s ranges, for data recorded on two of the in-ground sensors at 10 m and 200 m from the Endurance E-3120 respectively*

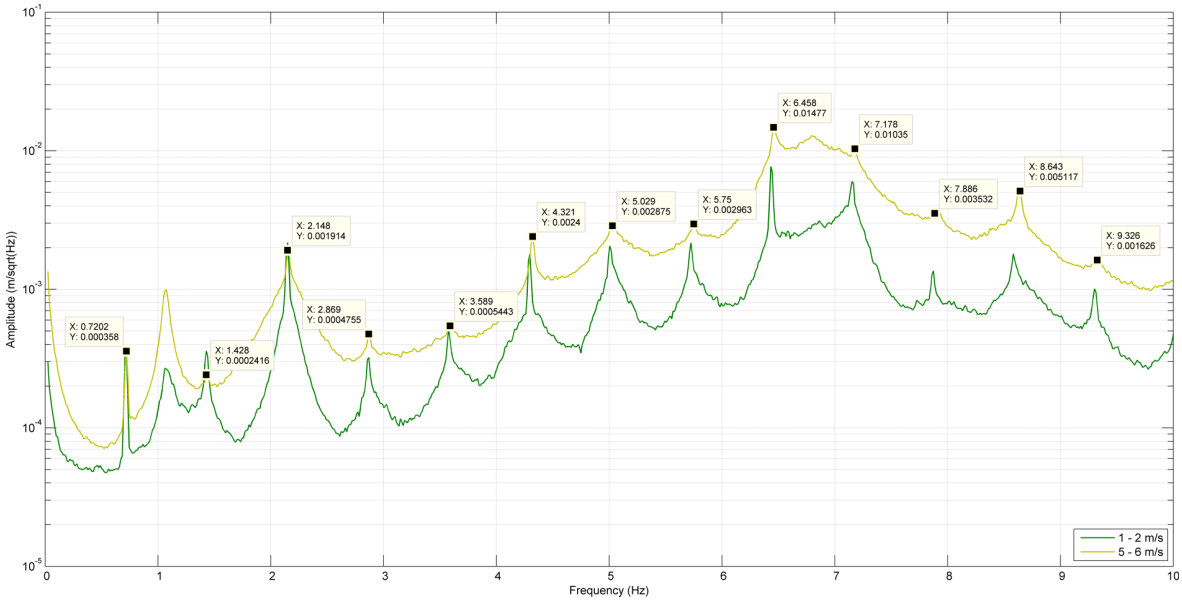

Figure 5-51: *Picked peaks of the Endurance E-3120 blade rotation frequency harmonics*

At 200 m the spectra are visibly noisier, although peaks can still be seen. The difference in amplitude between the maximum and minimum wind speeds has fallen to a factor of five. At frequencies up to 6 Hz, the amplitude of the 0 - 1 m/s spectrum is above the spectra up to 3 m/s. Above 6 Hz, the increase in amplitude with wind speed trend returns for wind speeds greater than 2 m/s. The amplitude of the 0 - 1 m/s spectrum is at or above the amplitude of the 1 - 2 m/s spectrum for all frequencies greater than 3 Hz.

In the on-tower spectrum for all wind speeds, the blade rotation frequency harmonics up to 10 Hz are visible (Figure 5-51). This indicates that although the turbine does not start generating power until the wind speed reaches 3.5 m/s, the blades start turning at lower wind speeds or there are bending modes of the tower at or very close to the same frequencies. The peak at 1.1 Hz cannot be attributed to the blades and is likely to represent the first bending mode of the tower. This peak can just be made out in the sensor at 10 m but can not be easily picked out at 200 m. Additionally there is a broader peak seen when the turbine is generating at 6.8 Hz, but this is not clearly visible in the spectra for wind speeds between 1 m/s and 3 m/s.

Figure 5-52 shows the displacement spectra for all the sensors at wind speeds between 3.5 m/s and 10 m/s. Peaks are visible on all sensors. The 1 Hz artefact peaks visible on the sensor at 10 m are also present on the sensors at 20 m and 30 m. These three sensors were connected to the same port on the digitiser. However, there are also other peaks visible on these sensors which are present on the

foundation and the tower. At 10 m, there are peaks at 1.1 Hz, 2.1 Hz, 4.2 Hz, 5 Hz, 5.8 Hz, 6.3 Hz, 7.1 Hz, 7.9 Hz, 8.6 Hz and higher frequencies. The 4.2 Hz peak and those at 5.8 Hz and above are also present on the sensors at 20 m and 30 m. Out at 200 m the 4.2 Hz, 5 Hz, 6.3 Hz, 7.1 Hz, 7.9 Hz, 8.6 Hz and other frequencies above 10 Hz are still seen. Generally on all sensors, the peaks at higher frequencies above 10 Hz tend to be broader than the lower frequencies.

From the tower to the foundation, the amplitude of the spectrum has dropped by a factor of ten. By 10 m away from the turbine, this has dropped by a further factor of one hundred and the seismometer at 200 m, is a factor of ten down on this. By picking the tip of a peak common to most of the sensors (4.3 Hz), the attenuation of the wave can be calculated (figure 5-53). An equation using linear regression on the log-log plot is calculated as $0.00007r^{-1}$, where r is the distance to the wind turbine. The R^2 value is very good, showing that the equation is a good match to the data. This result agrees with those for the two Gaia-Wind 133 turbines in sections 5.1 and 5.2. However the result does not agree with Styles et al. (2005), possible reasons why are discussed in chapter 6.

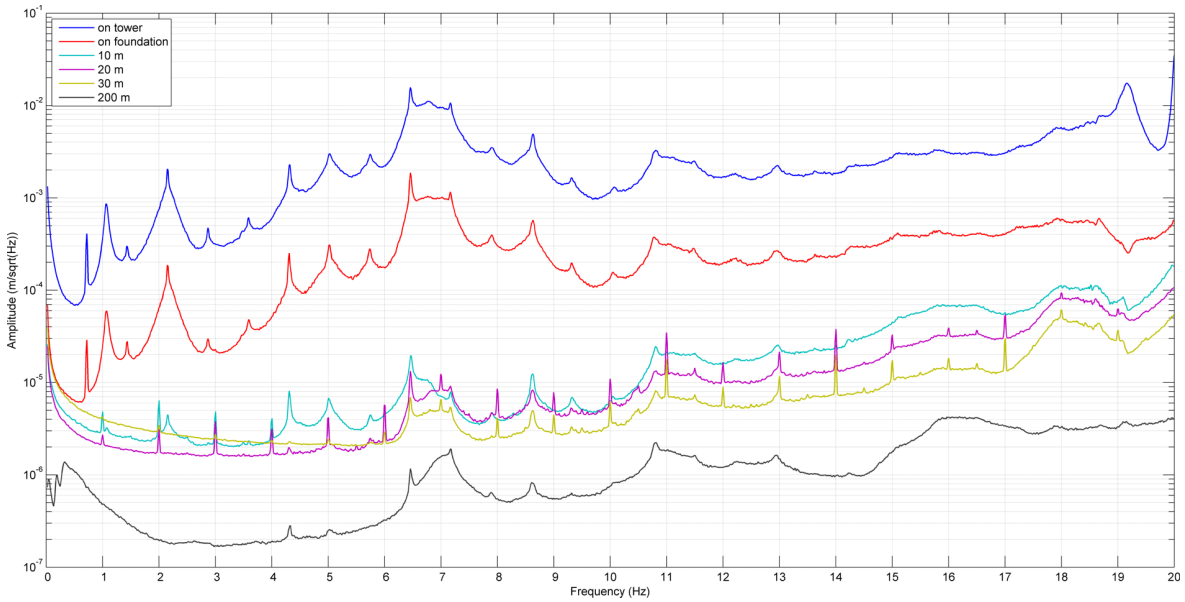

Figure 5-52: *The displacement frequency spectra for sensors at a range of distances from the turbine, when the wind speed was was between 3.5 m/s and 10 m/s*

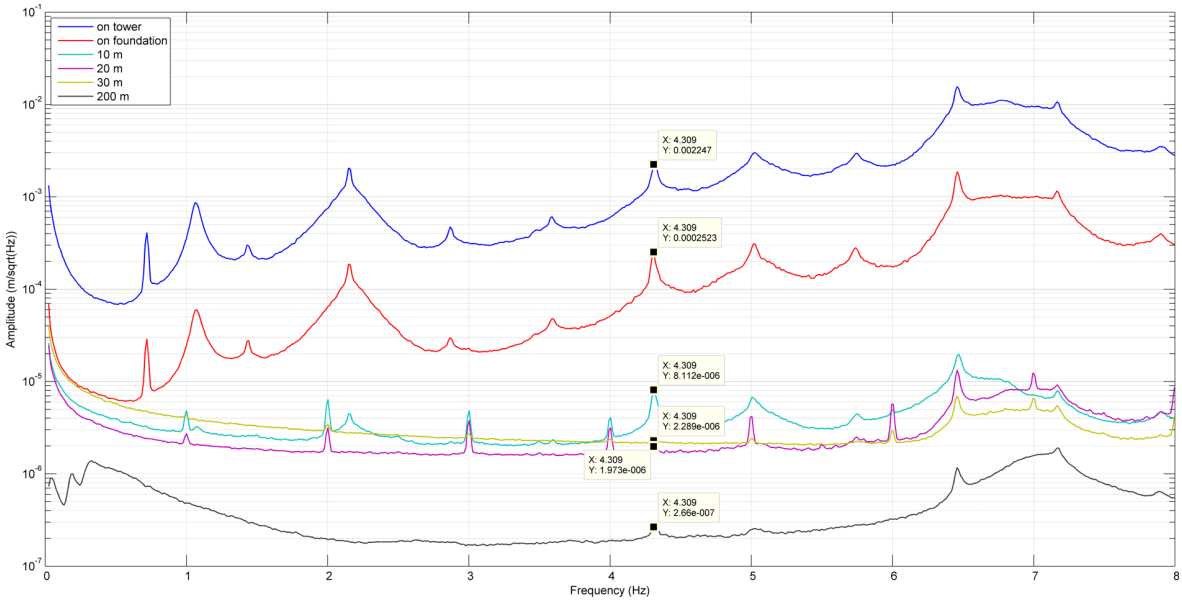

a. Picked peaks at 4.3 Hz peak

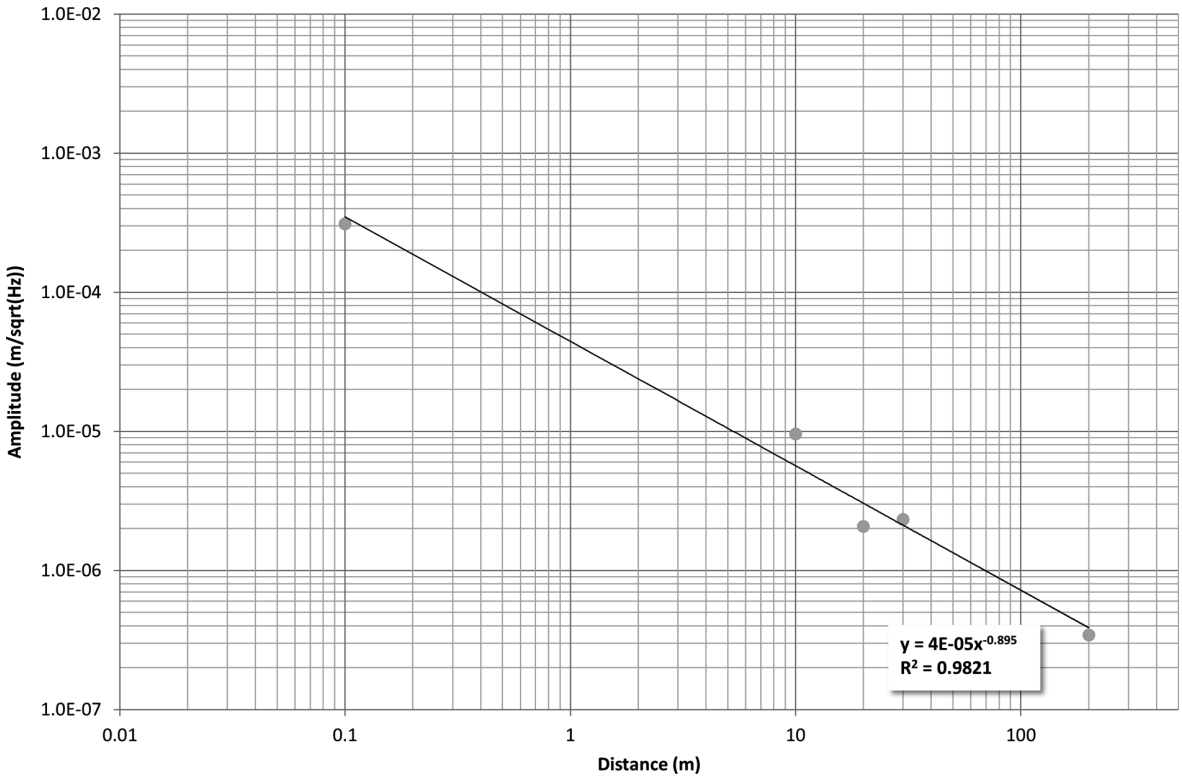

b. The log-log of distance to amplitude for the 4.3 Hz peak

Figure 5-53: *The distance-amplitude log-log plot and picked peaks at 4.3 Hz when the wind speed is between 3.5 m/s and 10 m/s*

The plot in figure 5-54 shows how wind speed affects the displacement spectrum on the tower. The colour indicates amplitude with the light areas being the frequencies and wind speed of highest amplitude and the dark areas the lowest. The most prominent area of high amplitude occurs across all wind speeds between 6 Hz and 7 Hz, with the highest area of the band at 6.3 Hz. Other areas of high amplitude occur at 19.2 Hz, also across all wind speeds and at 8.6 Hz, however although this frequency is present across all wind speeds, the amplitude increases at 2 m/s. There are no obvious shifts in frequency with wind speed.

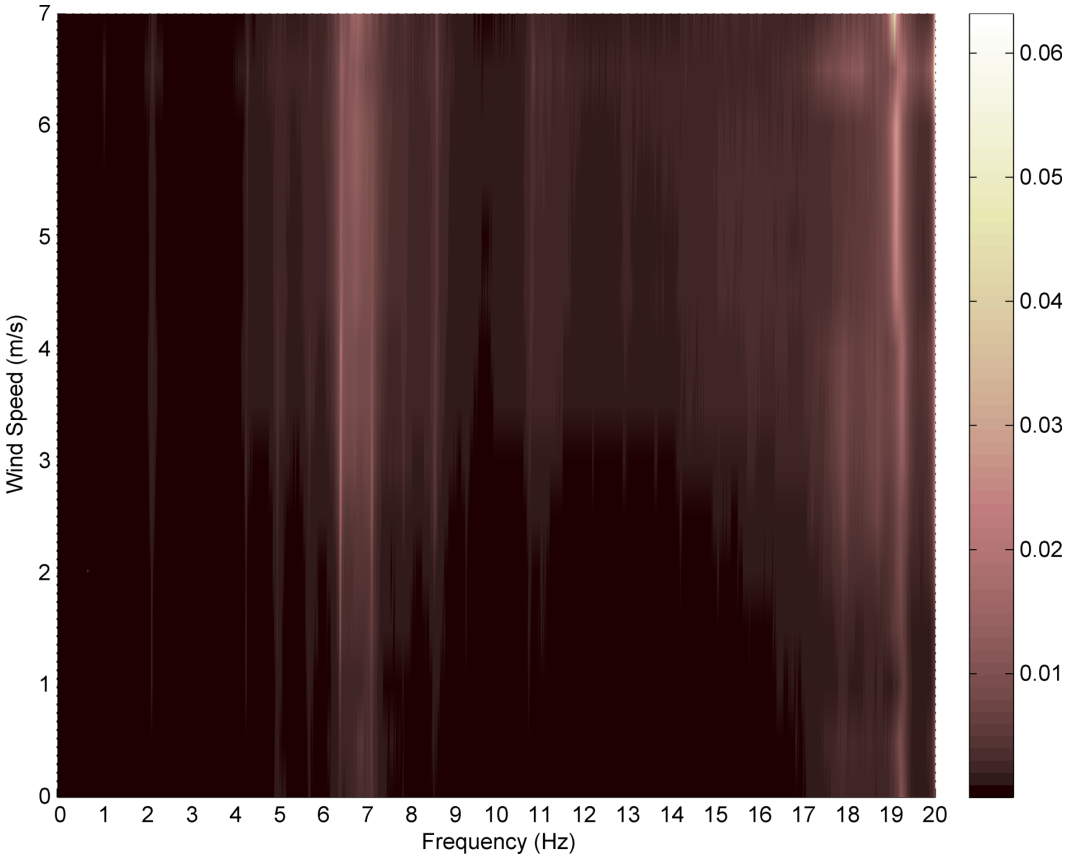

Figure 5-54: *A waterfall plot of wind speed and frequency with colour representing amplitude (m/sqrt(Hz)) from the on-tower accelerometer of the Endurance E-3120*

5.5 Discussion

Four wind turbines have been monitored; a Gaia-Wind 133 lattice tower, a Gaia-Wind 133 tubular tower, a Proven P35-2 and an Endurance E-3120. Each were monitored for a period of seven days. In addition to the seismic monitoring, wind speed and direction were also recorded throughout the monitoring period. Table 5-5 shows the maximum wind speed obtained during each of the monitoring periods and a brief description of the distribution of the wind speeds. At three of the sites, a power-cut occurred part way through monitoring, leading to the accelerometers only recording for part of the week. However, at each site enough data was gathered in order to complete an analysis.

Turbine	Month of monitoring	Max Wind Speed	Wind speed distribution
Gaia-Wind 133 lattice tower	Aug 2010	9.5 m/s	low wind speeds for most of the week (<5m/s) then picking up during the last twenty-four hours
Gaia-Wind 133 tubular tower	Sept 2010	7.8 m/s	even distribution of speeds
Proven P35-2	May 2011	18.2 m/s	Wind speeds <8 m/s for the first four days, then twenty-fours of high wind speeds, before returning to the previous levels.
Endurance E-3120	Sept 2011	10.3 m/s	even distribution of speeds

Table 5-5: *A summary of the wind speed information for all sites*

The prominent frequencies in each of the respective on-tower spectra are shown in table 5-6. All of the data recorded on the tower of the fixed speed wind turbine contain the blade rotation rates as prominent spikes in the spectrum and therefore contain many more peaks than the variable speed Proven.

The data from the sensors mounted on the Gaia-Wind tubular tower, show a large difference (a factor of 100) in amplitude between the turbine being stationary and turning, with a slight increase between turning and non-generating and generating. However, for the lattice tower the largest difference occurs between turning but not generating and generating with around the same factor of one hundred. For the Endurance, the data shows a gradual change in amplitude with wind speed, although the spectra are much more 'spikey' than the other three turbines. On the Proven 35-2, up to 9.5 m/s,

Gaia-Wind 133 Tubular	Gaia-Wind 133 Lattice	Endurance E-3120	Proven 35-2
0.9	0.9	0.7	1.1
1.3	1.4		
1.6			
1.87	1.87	2.15	
	2.5		2.6
2.8	2.8	2.9	
	3.2		3.3
3.7	3.75	3.6	
4.1		4.3	
4.65	4.65		
4.9		5.0	5.2
5.6	5.6	5.7	
6.0			
6.5	6.5	6.5	6.6
7.45	7.5	7.2	
7.7		8.0	7.8
8.6	8.4	8.6	
9.4	9.4	9.3	
9.6			
	10.3	10.1	
10.45	10.5	10.8	10.8

Table 5-6: *The frequencies visible in the spectrum from data gathered on the tower of each of the turbines. The highlighted numbers indicate blade rotation frequency harmonics*

a 'shifting' effect is visible at some frequencies, whereby the frequency gradually shifts with wind speed with a range of about 1 Hz.

In the data from the sensors on the Gaia-Wind tubular tower, peaks are visible at 0.9 Hz, 1.1 Hz, 6.1 Hz and 8.4 Hz at all wind speeds. However when the turbine is operational, additional peaks can be seen at 1.86 Hz, 2.8 Hz, 3.7 Hz, 5.6 Hz, 6.7 Hz, 7.47 Hz, 8.1 Hz and 9.3 Hz. Of these, all but the 6.7 Hz and 8.1 Hz peaks are harmonics of the blade rotation rate. Further away from the turbine, some of the signal is either not being efficiently transferred to the ground or is being masked by background noise. Peaks are visible at a distance of 190 m away at frequencies of 4.2 Hz, 6.7 Hz, 8.1 Hz and 9.5 Hz when wind speeds are greater than 2.5 m/s. The Endurance displays a similar loss of signal, possibly due to the same reasons. On the sensors at 10, 20 and 30 m from this turbine, there is a 1 Hz artefact in the data (due to the time synchronisation pulse from the GPS combined with a grounding issue), although some signal can still be seen above 1 Hz at 10 m and above 4 Hz at 20 and 30 m. At a distance of 200 m, when the wind speed is greater than 3 m/s, peaks are visible at 4.2 Hz, 5 Hz,

6.3 Hz, 7.1 Hz, 7.9 Hz and 8.6 Hz, as well as other frequencies above 10 Hz.

At high wind speeds, the sensor 200 m from the Proven 35-2 shows only one prominent peak, at 7 Hz. This frequency does not feature prominently in the on-tower spectrum, so is likely to originate from a source other than the turbine. However, the source is constant as because it is visible within the median, it cannot be a single solitary value. At low wind speeds, the signal contains more noise. The same loss of signal is seen in the data for the Gaia-Wind lattice tower at 190 m, with peaks at 4.8 Hz and 5.2 Hz visible in one of the horizontal components of the sensor. On the vertical component additional peaks are also seen at 7.5 Hz, 9.2 Hz and 11.5 Hz.

The reduction in amplitude with distance of the most prominent peak in the spectra for each turbine at wind speeds when the turbine is operational, show that the attenuation of the signal is kr^{-1}, where k is dependent upon turbine type, wind speed and frequency and r is the distance from the wind turbine.

These results are analysed further in chapter 6.

Chapter 6

An Analysis of the Similarities and Differences Between the Turbines

This chapter brings together the results from monitoring the four small wind turbines as described in chapter 5, to try and resolve issues relating to wind speed, structure, wave type and attenuation.

6.1 The Effect of Tower Design on the Vibrations

The Gaia-Wind 133 is available in a choice of two types of tower; a tubular monopole or a lattice. The nacelle and blades are identical on both, which is ideal in order to compare the effects of tower structure on the generated vibrations. Details of the turbines and the monitoring procedure for each of the tower designs are provided in sections 5.1 and 5.2. This section discusses the results from the two monitoring periods and the different effects the tower structure can have on the vibrations generated by the turbine.

There is a difference in seismic amplitude between the two tower types dependent upon the operational state of the turbine. Figure 5-8 (page 94) and figure 5-23 (page 107) show the on-tower spectrum for each turbine over three wind speed ranges; when the turbine is stationary (wind speed less than 2.5 m/s, hereafter referred to as wsLow), starting to turn (wind speeds of 2.5 m/s - 3.5 m/s, hereafter

referred to as wsMid) and generating (wind speeds greater than 3.5 m/s, hereafter referred to as wsHigh). In figure 5-8 (the tubular tower) the amplitude of the wsMid spectrum is close to wsHigh, whereas for the lattice tower it is closer to the wsLow spectrum. Figure 6-1 shows a comparison of the on-tower spectra from each tower for the three wind speed ranges. At high and low wind speeds, the lattice tower amplitude is higher than the tubular, especially at frequencies over 10 Hz where the difference is a factor of 10-100, depending upon frequency. However, for the wsMid range, the opposite occurs, with the tubular tower amplitude higher than the lattice tower, especially at low frequencies.

Figure 6-2 shows wind speed against amplitude for the 9.3 Hz peak on the lattice tower and the 8.5 Hz peak on the tubular, both of which are visible in the data through all three wind speed ranges. The difference in amplitude between the lattice and tubular tower at wind speeds above 4 m/s can clearly be seen in this plot. By performing simple regression on the data, an equation can be derived to relate wind speed to amplitude. These are displayed on the graph along with the R^2 value, which is a measure of how well the equation fits the data (section 4.4.2.1). During the monitoring period for the tubular tower, the wind speed reached a maximum of 5.1 m/s before a power cut shut down the digitiser. However during the lattice tower monitoring period, the wind speed reached 9.5 m/s. From the graph, it can be seen that the lattice tower data displays two trends, one over the wind speed range 0-4 m/s and the other for 4-9.5 m/s. At low wind speeds the relationship is linear, however at high wind speeds there are two possible trends, one linear with a different gradient to the low wind speeds and the other a power law. Although there are less data points, the data from the tubular tower could also contain two laws over the same wind speed ranges as the lattice. The trend at low wind speeds is again linear, but for the higher wind speeds there are not enough data points to calculate an accurate equation. Alternatively, a power law can fit all of the data points, such that

$$\text{Displacement Amplitude} \propto \text{wind speed}^{2.5}. \tag{6.1}$$

Further discussion of this is provided in section 6.2, where the results are compared to the other two monitored turbines.

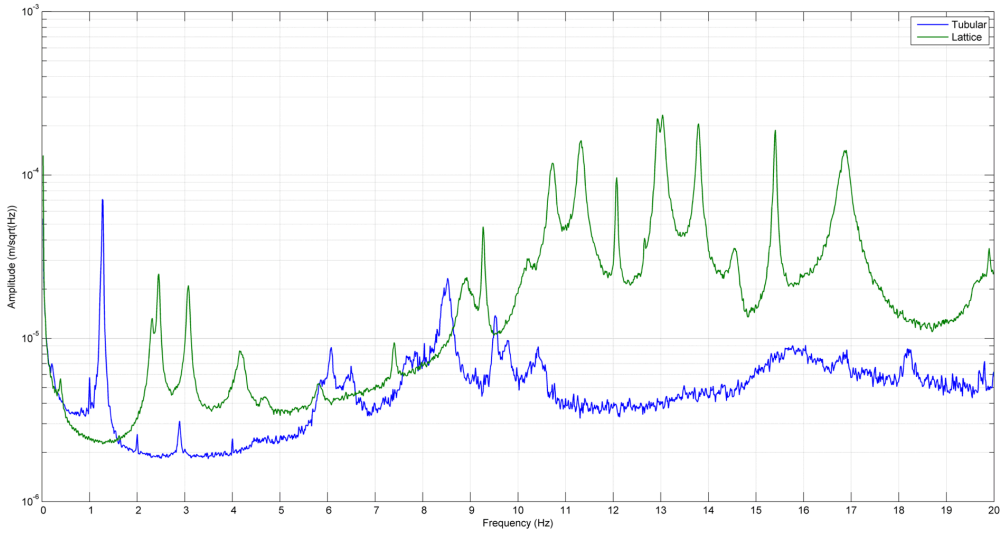

a. wind speed $<$ 2.5 m/s (wsLow)

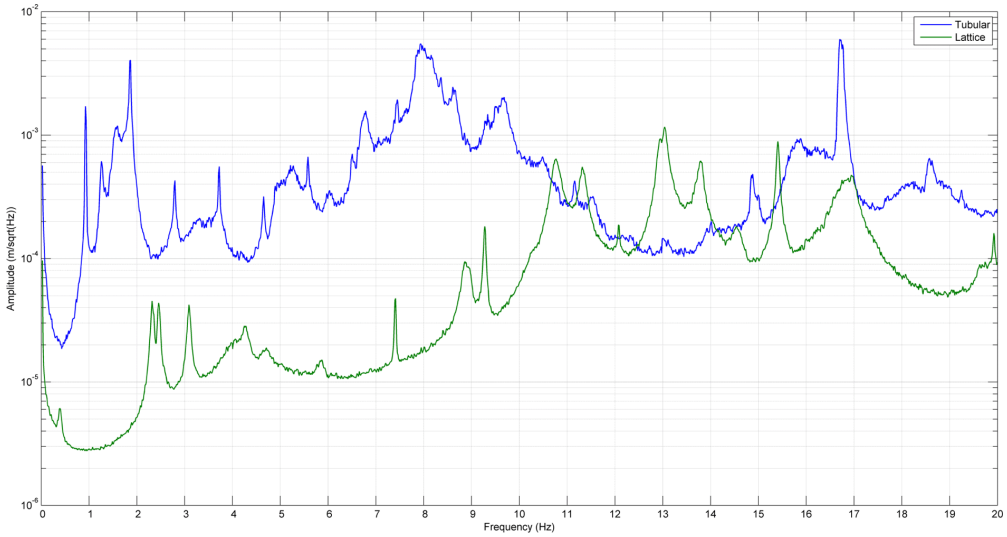

b. wind speed 2.5 - 3.5 m/s(wsMid)

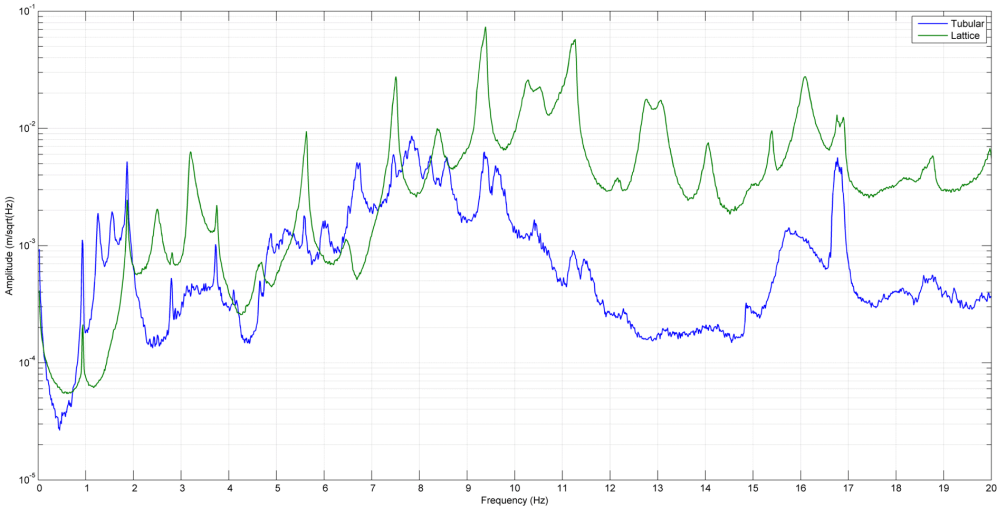

c. wind speed $>$ 3.5 m/s (wsHigh)

Figure 6-1: *A comparison of the Gaia-Wind 133 tubular (blue) and lattice tower (green) on-tower spectra at three wind speed ranges*

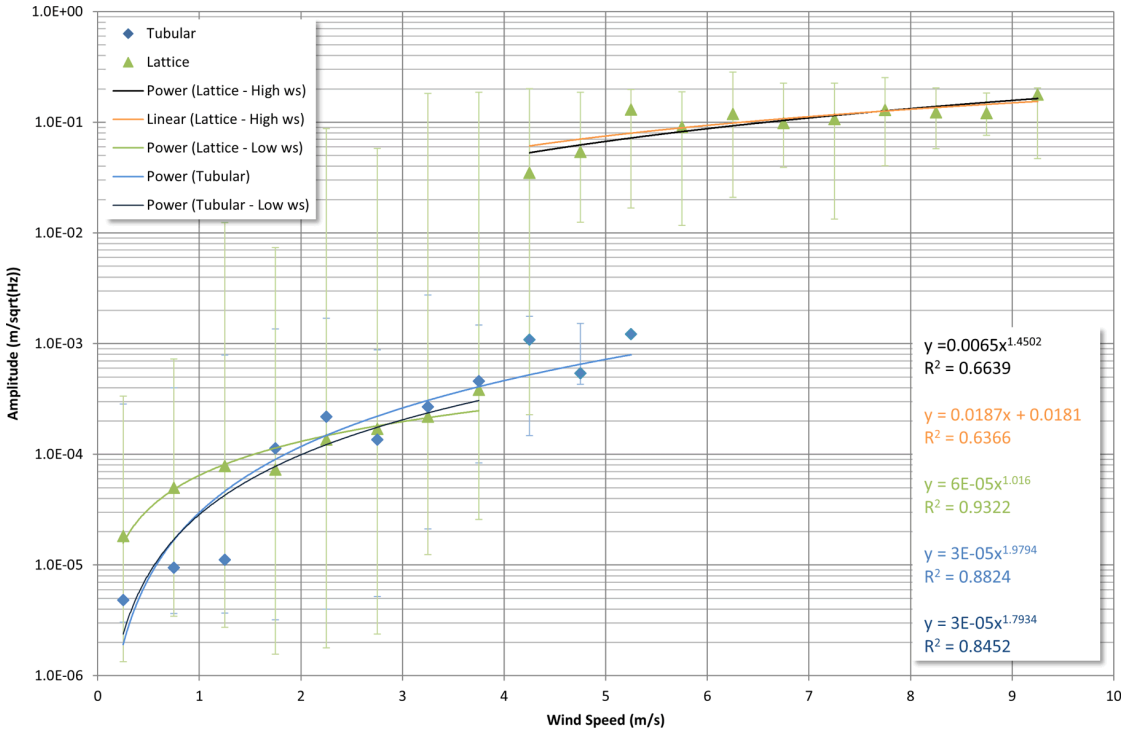

Figure 6-2: *Wind speed against amplitude for the Gaia-Wind 133 tubular tower (blue diamonds) and lattice tower (green triangles) for the 9.3 Hz peak. The error bars indicate the maximum and minimum values recorded for the frequency for each wind speed range.*

The peaks of the two spectra shown in figure 6-1a do not match perfectly. This is also true for the spectra at the higher wind speeds in figures 6-1b and 6-1c. At high wind speeds all of the rotation rate harmonics are visible (figure 5-25, page 109) on the lattice tower spectrum. There are only two peaks under 10 Hz (2.5 Hz and 3.2 Hz) which are not attributed to the blades. Neither of these feature prominently in the tubular tower spectrum at the same wind speeds and are therefore likely to be due to the structure of the lattice tower, rather than being generated by the nacelle. The clarity and size of the peaks at some of the rotation rate harmonics are probably due to modes of different parts of the tower being excited, given the many cross-beams of varying size in the lattice structure. Above 10 Hz, the harmonics start to disappear and other peaks appear, some close together, which could be linked to the bending modes of the tower. Examples of this are at 10.3 Hz, 10.5 Hz, 12.7 Hz and 13 Hz.

Rotation rate harmonics are visible in the tubular tower data under 10 Hz, however they are not as prominent as in the lattice tower data. One possible reason for this is due to the tubular structure of the tower. The lattice tower contains many components, each of which may become excited at different resonant frequencies. The tubular tower consists of only one element allowing energy to be transferred down the tower, rather than exciting modes as occurs with the lattice structure.

On the wsHigh tubular tower spectrum (figure 6-1c), peaks can be identified at 1.1 Hz and 1.3 Hz (the two first bending modes of the tower), 6 Hz, 6.7 Hz, 7.9 Hz, 8.2 Hz and 8.5 Hz which are not present on the equivalent lattice spectrum and therefore not attributable to the blade rotation harmonics. The latter peaks could be attributed to torsion, tower bending modes or vibrations from the nacelle, which are being transmitted efficiently through the tubular structure, but would be damped by the lattice structure. If the peaks are present when the blades are not turning, then they can be attributed to bending modes of the tower. From figure 6-1a, the tubular tower displays large peaks at 1.1 Hz and 8.5 Hz leading to the conclusion that these are the first and second bending modes of the tower. Some smaller peaks close to the blade passing frequencies are also present and are likely to be due to the blades turning occasionally as the wind speed starts to increase, but at a slower rate, producing a shift in frequency. This effect is demonstrated by the Proven 35-2 turbine in section 5.3 and the large turbines in Styles et al. (2005).

The displacement spectra for the sensors in the ground at wsHigh for the tubular and lattice towers are shown in figures 5-11 and 5-26 respectively. There are four small peaks at 7.5 Hz, 9.3 Hz, 11.1 Hz and 13.1 Hz visible above the sensor noise levels on the sensors at 20 m and 30 m from the lattice tower. However there are eight distinct peaks clearly visible on the same sensors at the tubular tower site, between 6 Hz and 12 Hz, as well as a large peak at 16.8 Hz. The base level amplitude is the same at both sites. This indicates signals are being transferred into the ground from the tubular tower with a higher amplitude than those from the lattice tower. This indicates that the tubular tower with a circular base, couples to the foundation better than the lattice tower, which only has four points of contact. Figure 6-3 shows the equivalent comparison graphs between towers for the three wind speed ranges using data from the seismometer located 190 m away from the turbine. At all wind speeds the lattice spectrum amplitude is a factor of ten down on the tubular spectrum.

A small peak can be seen in the tubular tower spectra, 190 m from the turbine, at 4.2 Hz across all wind speeds; this peak is not present in the on-tower spectra, which indicates it originates from a source other than the wind turbine. Styles et al. (2005) show that Vestas V47 wind turbines produce a peak at 4.2 Hz, amongst others, which can be detected up to 10 km from the turbine. Great Orton Wind Farm is located less than 5 km from the Wigton site and contains six Vestas V47 wind turbines.

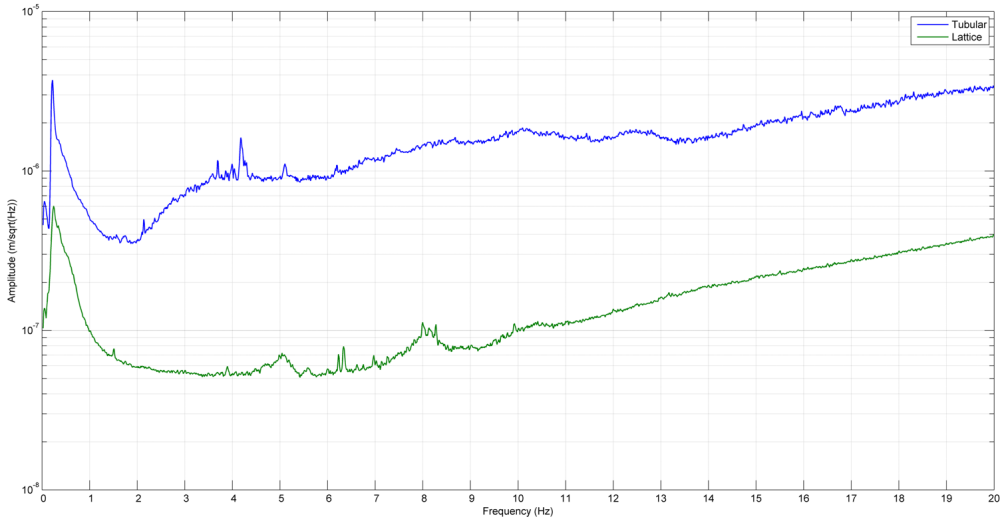

a. wind speed $<$ 2.5 m/s (wsLow)

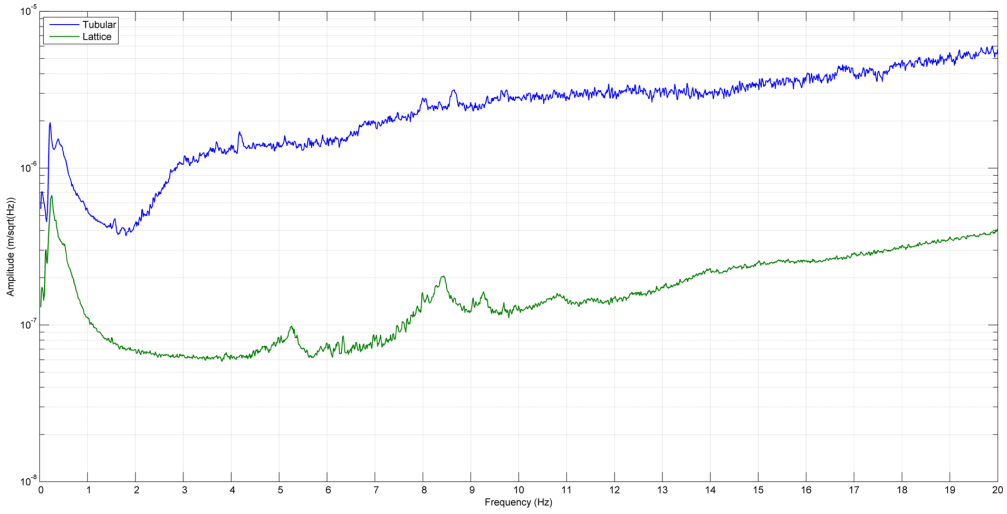

b. wind speed 2.5 - 3.5 m/s (wsMid)

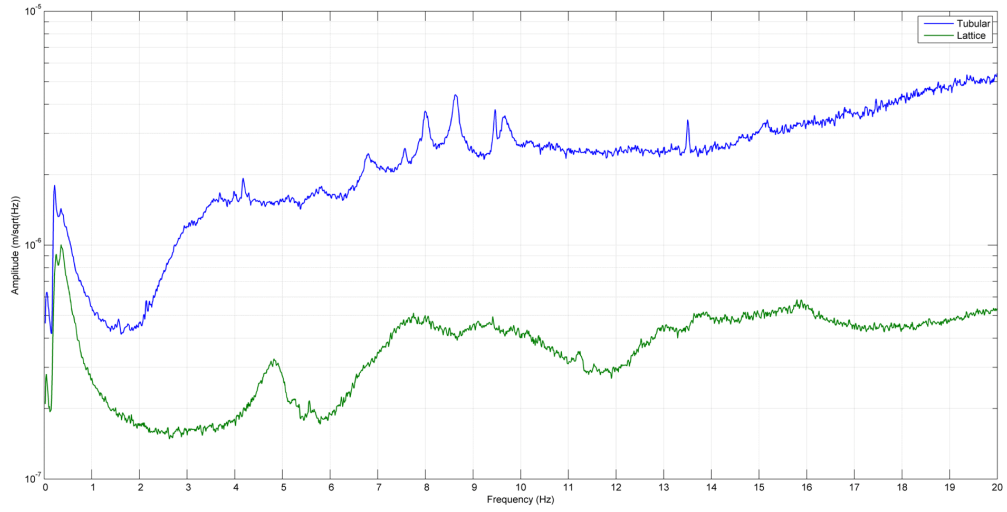

c. wind speed $>$ 3.5 m/s (wsHigh)

Figure 6-3: *A comparison of the Gaia-Wind 133 tubular and lattice tower spectra at three wind speed ranges, using data recorded on the sensor located 190 m from the turbine*

This could account for the presence of the 4.2 Hz peak in the tubular tower spectra at 190 m. Peaks at 6.8 Hz, 7.5 Hz, 8 Hz, 8.5 Hz, 9.5 Hz and 9.6 Hz emerge as the wind speed increases. The opposite is true with the lattice tower. As the wind speed increases the peaks become broader and the detail of any visible peaks disappears. A peak at around 5 Hz appears to shift with wind speed. At wsLow, the peak lies on 5 Hz, at wsMid it has shifted to the right to about 5.1 Hz and at wsHigh merges into a broader peak centred about 4.9 Hz, which is also visible in the on-tower spectra.

Figure 6-4 shows a log-log plot of the attenuation of the signal for each turbine. Both graphs show that displacement amplitude is inversely proportional to distance, such that the wave decays at r^{-1}, where r is the distance from the wind turbine. This is known as the near-field term (Chapman 2006) and is different to the Styles et al. (2005) model, which uses $r^{-0.5}$. Styles et al. (2005) calculated the model using seismometers positioned in the far-field, whereas the sensors used in this project were positioned close to the turbine. This result confirms that they were almost certainly positioned in the near-field. Further discussion on the attenuation of the signal from each of the turbines tested and the applicability of the Styles et al. (2005) model can be found in section 6.3.

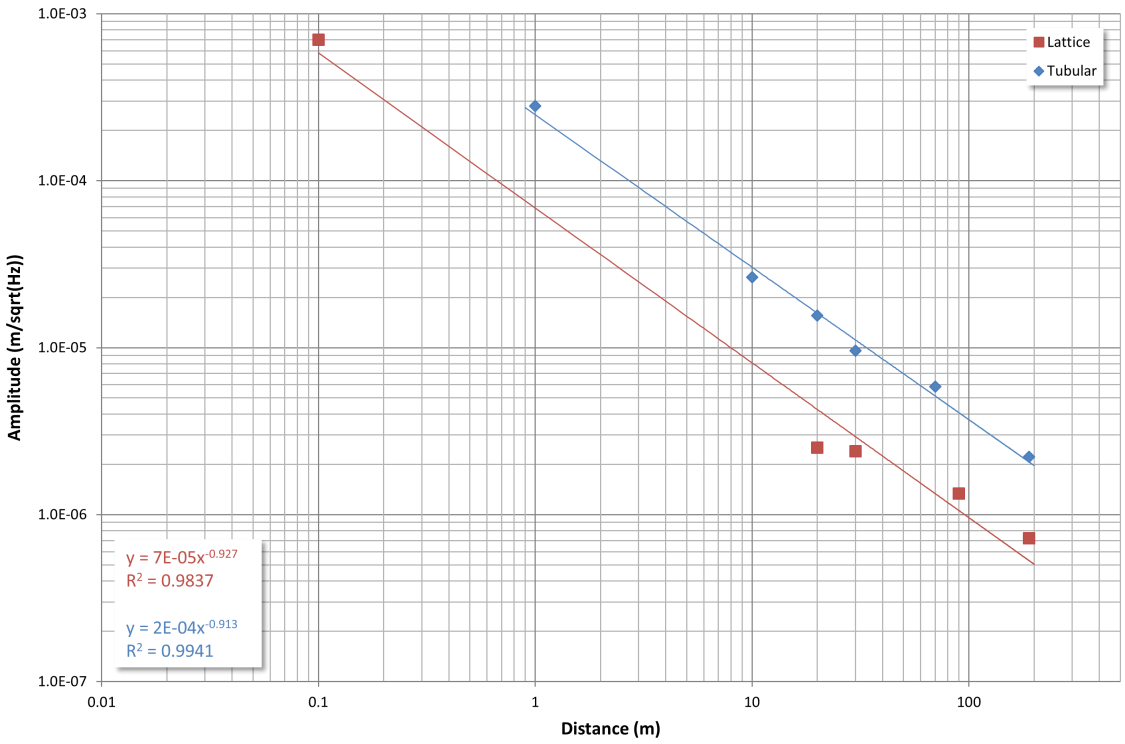

Figure 6-4: *The attenuation of the signal from the tubular tower (blue) at 7.6 Hz and the lattice tower (red) at 7.5 Hz.*

6.2 The Effect of Wind Speed

Styles et al. (2005) state that the seismic amplitude of a wind turbine is directly proportional to the wind speed. Schofield (2002) found that the amplitude increases with wind speed to the power of 3/2. This section aims to investigate whether either of these laws hold for small wind turbines.

The relationship between seismic amplitude and wind speed is calculated by identifying a peak which is visible through a range of wind speeds and performing linear regression to determine an equation from the values. The peaks tend to have a width of a fraction of a Hz and can shift slightly depending on wind speed (figure 6-5). In order to account for this, the maximum amplitude over a narrow frequency band encompassing the peak is used. Figures 6-5 to 6-8 show the on-tower spectrum of the selected peak for each wind turbine, with each line representing a 0.5 m/s bin of data. The wind data was recorded in ten minute averages, which is the standard format for the Power Predictor anemometer (section 4.2.3). Table 6-1 summarises the frequency and wind speed ranges for each of the turbines. Ideally, the frequency range for each turbine should be the same, however this is not possible, as each turbine generates a different set of frequency peaks, some of which are not visible through all wind speeds. Figure 6-7 (for the Proven 35-2) does not contain any data for wind speeds between 0 and 1 m/s, as no data was recorded for these wind speeds over the monitoring period. Additionally, the calculation for this turbine discards the 1.5 - 2 m/s bin, as it can be seen from the graph that it does not peak at the same frequency as the other wind speed ranges. Similarly, the 0 - 0.5 m/s data for the Endurance E-3120 is not used in the calculation as the peak is not visible above the background noise level.

Turbine	Frequency range	Wind speed range
Gaia-Wind 133 tubular tower	1.2 - 1.4 Hz	0 - 5.5 m/s
Gaia-Wind 133 lattice tower	9 - 9.5 Hz	0 - 9.5 m/s
Proven P35-2	1 - 1.2 Hz	1 - 15 m/s
Endurance E-3120	2 - 2.2 Hz	0 - 7.5 m/s

Table 6-1: *The frequency band and wind speed range for each wind turbine*

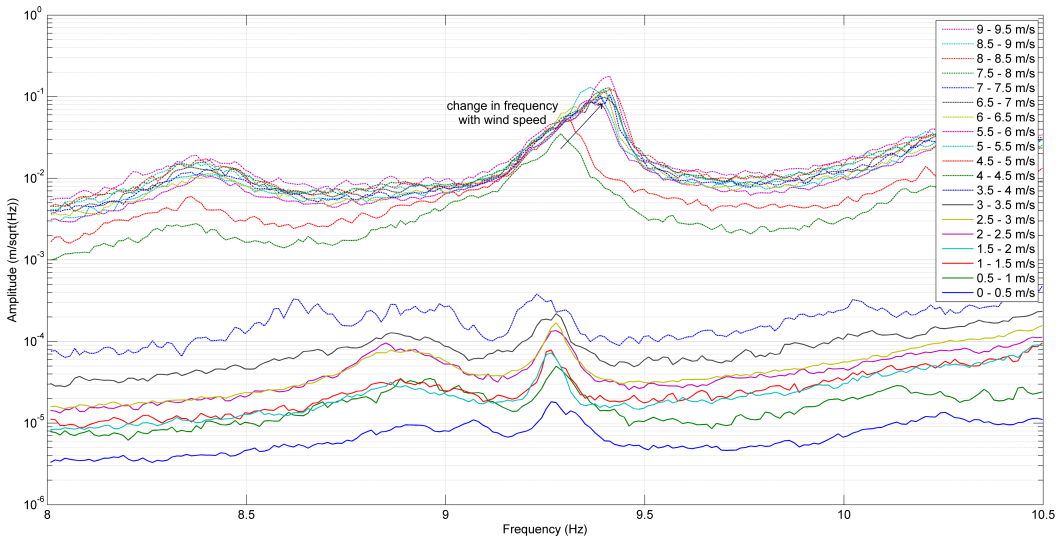

Figure 6-5: *The Gaia-Wind 133 lattice tower displacement spectra for 0.5 m/s wind speed ranges*

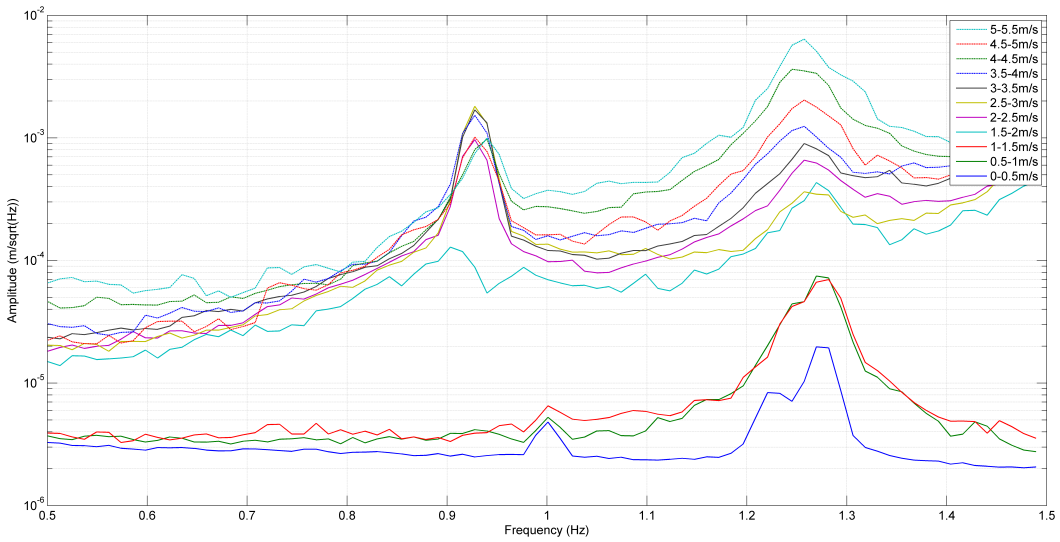

Figure 6-6: *The Gaia-Wind 133 tubular tower displacement spectra for 0.5 m/s wind speed ranges*

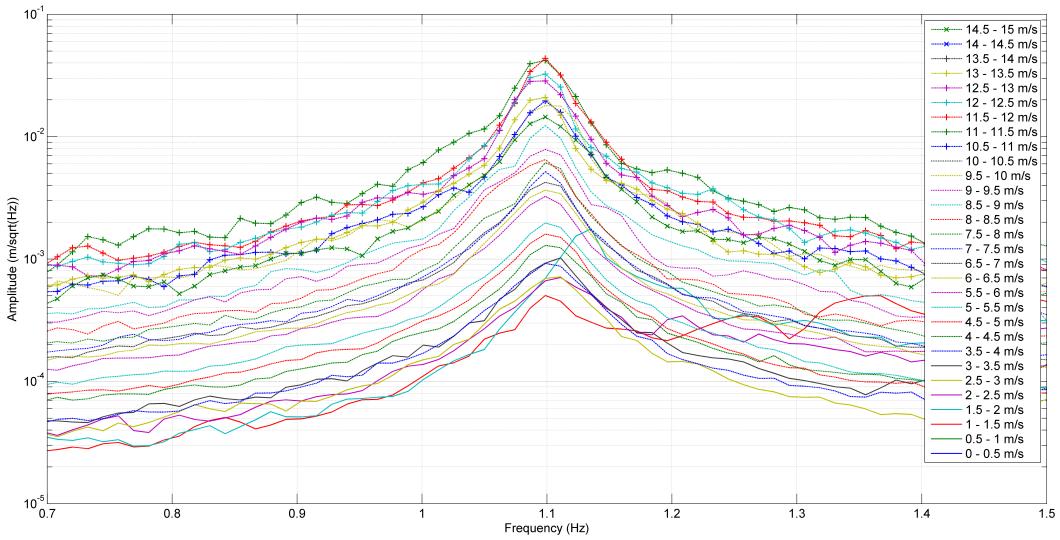

Figure 6-7: *The Proven 35-2 displacement spectra for 0.5 m/s wind speed ranges*

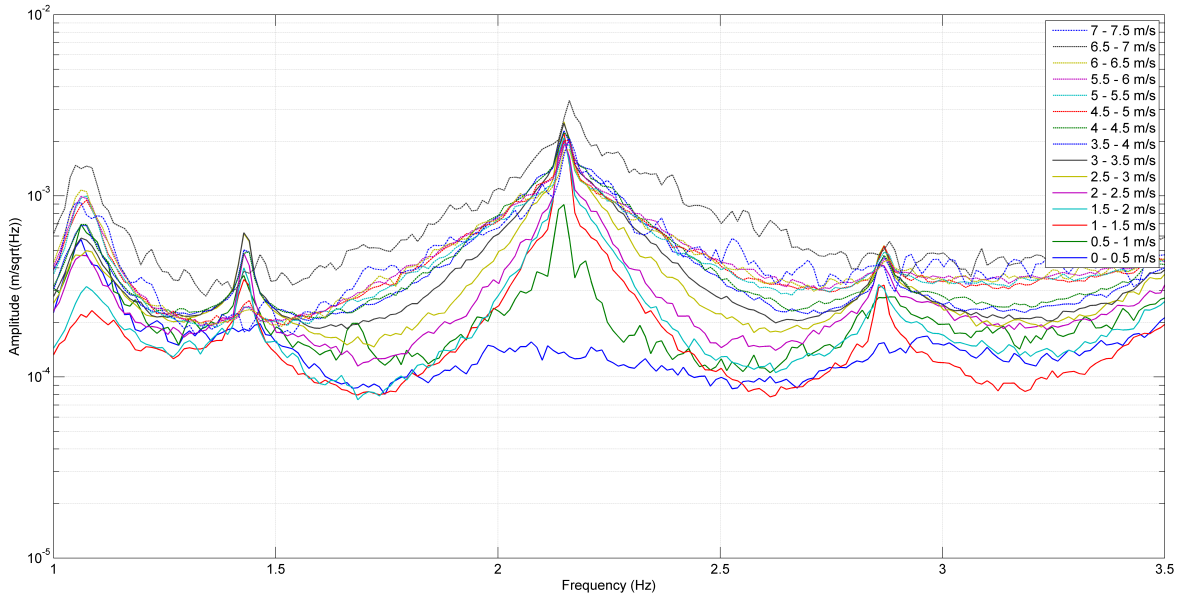

Figure 6-8: *The Endurance E-3120 displacement spectra for 0.5 m/s wind speed ranges*

Figure 6-9 shows the wind speed against amplitude plots for each of the turbines. It is clear that the wind turbines follow different trends, with wind speed affecting amplitude on some more than others. These differences could be due to the tower construction, with the most prominent difference seen between the lattice and tubular structures. Turbulence can be created inside the lattice with the wind forcing all sections of the tower in every direction simultaneously. This can be seen in the graph (figure 6-9) at higher wind speeds, where the lattice tower data has amplitudes which are a factor of ten higher than the data from the tubular tower turbines.

The data from the tubular structures each follow one trend over all wind speeds. However, the Gaia-Wind lattice tower data is bimodal and contains two separate trends for wind speeds above and below 4 m/s. This can be defined as

$$S_t \propto \begin{cases} w & \text{if } w \leq 4 \\ w^{3/2} & \text{if } w > 4 \end{cases}, \tag{6.2}$$

where S_t is the seismic amplitude on the tower and w is wind speed. For wind speeds up to 5.5 m/s, seismic amplitude on the Gaia-Wind tubular tower is proportional to wind speed squared. The maximum wind speed for this turbine only reached 5.1 m/s, therefore it is not known what the relationship is above 5.5 m/s, however figure 6-6 indicates that the results from this turbine are also bimodal.

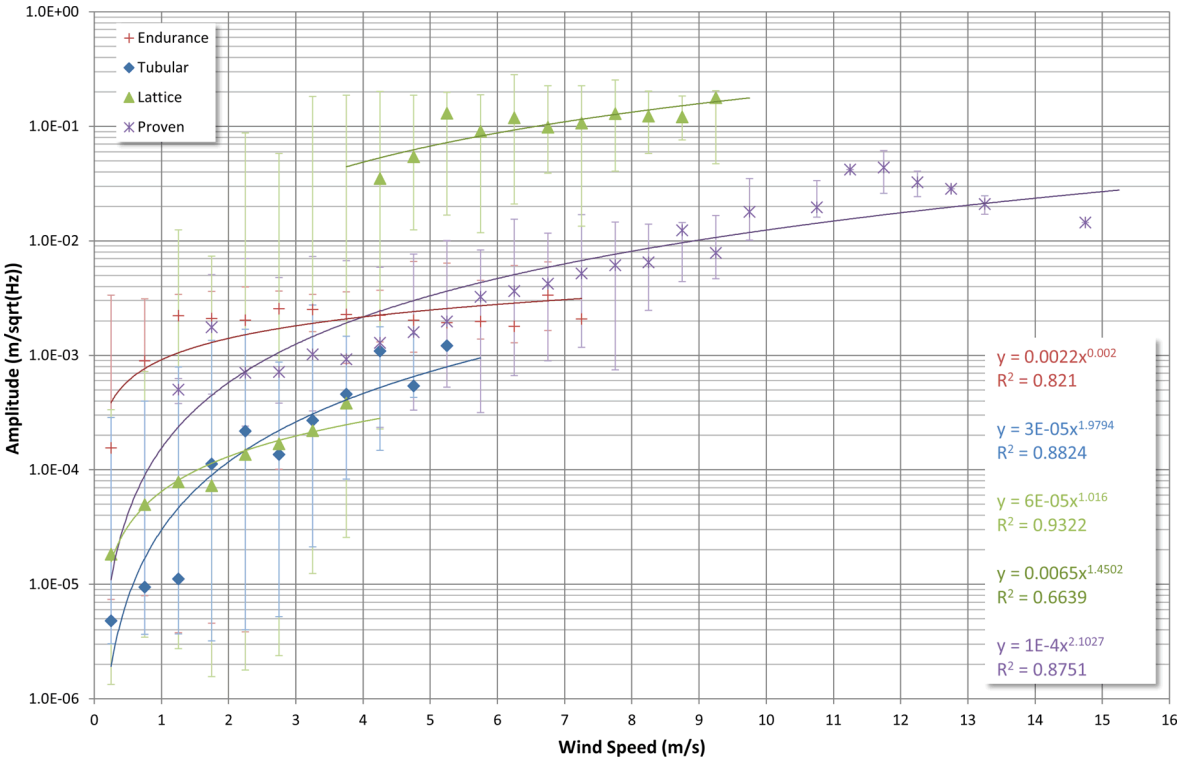

Figure 6-9: *Seismic amplitude on the tower against wind speed for all four wind turbines. The error bars indicate the maximum and minimum values recorded for the frequency peak for each wind speed range.*

The Proven 35-2 (figure 6-7) shows a much more progressive increase in amplitude with wind speed than the Gaia-Wind turbines. The wind speeds which were reached when monitoring this turbine were just under 15 m/s, the highest wind speed recorded for any of the four wind turbines while on-tower sensors were operational. The Proven 35-2 is self regulating and the blades bend and pitch in the wind to control the speed at which the turbine is rotating. There are two feasible equations; either seismic amplitude is proportional to the square of the wind speed over all wind speeds, or seismic amplitude is proportional to wind speed to the power of 3/2 for wind speeds up to 9.5 m/s (figure 6-10). Above this wind speed, the relationship is more unpredictable, probably due to the bending of the blades changing the amount of load on the turbine. The R^2 value is similar for both options, with an 88% fit of the equations to the data. It is possible that the high values are the start of the amplitude flattening off for higher wind speeds, however further monitoring would be required to confirm this. The Endurance E-3120 displays a more stable trend at wind speeds greater than 1 m/s. The amplitude remains close to constant at 0.002 m/$\sqrt{\text{Hz}}$.

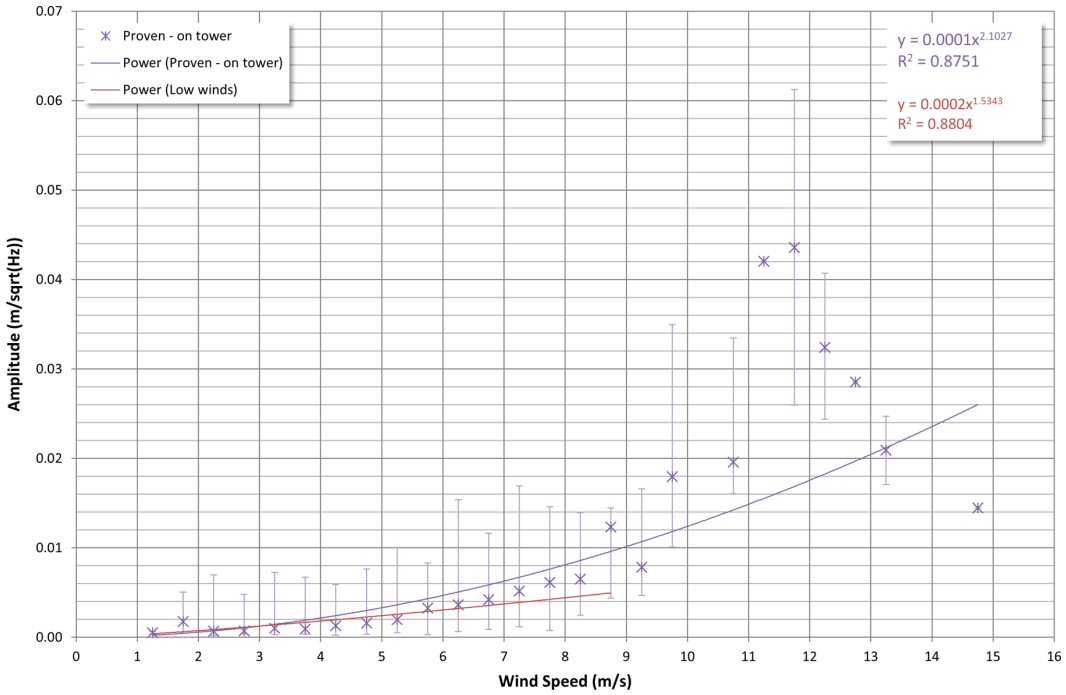

Figure 6-10: *The effect of wind speed on seismic amplitude for the Proven 35-2. The error bars indicate the maximum and minimum values recorded for the frequency peak for each wind speed range.*

Figure 6-11 shows the equivalent relationship between wind speed and the sensor in the ground at 190/200 m from the turbine. For consistency and comparison the same frequency ranges are used in this graph as for the on-tower relationship with wind speed. At 190/200 m away from the turbine the data indicates that seismic amplitude could be exponentially proportional to wind speed. As with the on-tower results, the Gaia-Wind lattice tower appears to contain two separate trends, with the separating wind speed now at 5 m/s. The data from each of the other three turbines demonstrates a single trend through all wind speeds. Unlike the measurements recorded on the tower, the Endurance data is no longer constant and the Gaia-Wind tubular tower data suggests that the trend will continue for higher wind speeds. Although each set of data demonstrates an exponential proportionality, the gradient of the exponential is not the same for any two turbines. In fact, the high wind trend in the data from the Gaia-Wind lattice tower has an exponential gradient a factor of ten lower than the low wind trend.

The relationship between seismic amplitude on the tower and at the sensor can be obtained by calculating the maximum amplitude over the same frequency band and wind speeds for the sensors on the foundation and at 190/200 m from the turbine. These results are shown in figures 6-12 and 6-13. The Proven 35-2, the Gaia-Wind 133 lattice tower and the Endurance each display directly proportional relationships between the seismic amplitudes on the tower and the foundation, showing

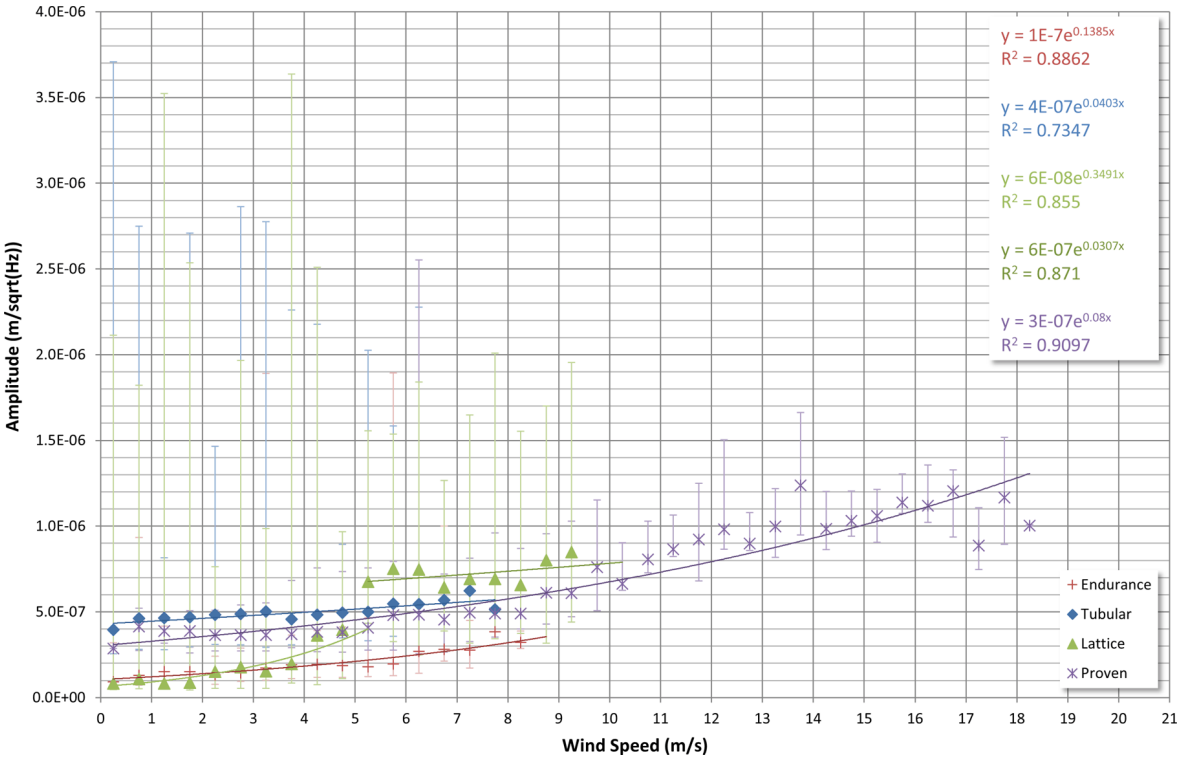

Figure 6-11: *Seismic amplitude at 190/200 m from the tower against wind speed for all four wind turbines. The error bars indicate the maximum and minimum values recorded for the frequency peak for each wind speed range.*

that the vibrations seen on the tower are transferred to the foundation. The Gaia-Wind 133 tubular tower displays a relationship where the amplitude in the ground is proportional to the amplitude on the tower to the power of 0.8. However there is less data for this turbine than the others and higher wind speeds may show that it agrees with the other three turbines.

At 200 m away the relationship between the seismic amplitude on the tower (S_t) and in the ground (S_g) is such that

$$S_g \propto {S_t}^{0.25}. \tag{6.3}$$

Equation (6.3) holds for the Proven 35-2, Endurance E-3120 and Gaia-Wind 133 lattice tower. The amplitudes in the ground for the Gaia-Wind 133 tubular tower are close to constant and display the relationship

$$S_g \propto {S_t}^{0.025}. \tag{6.4}$$

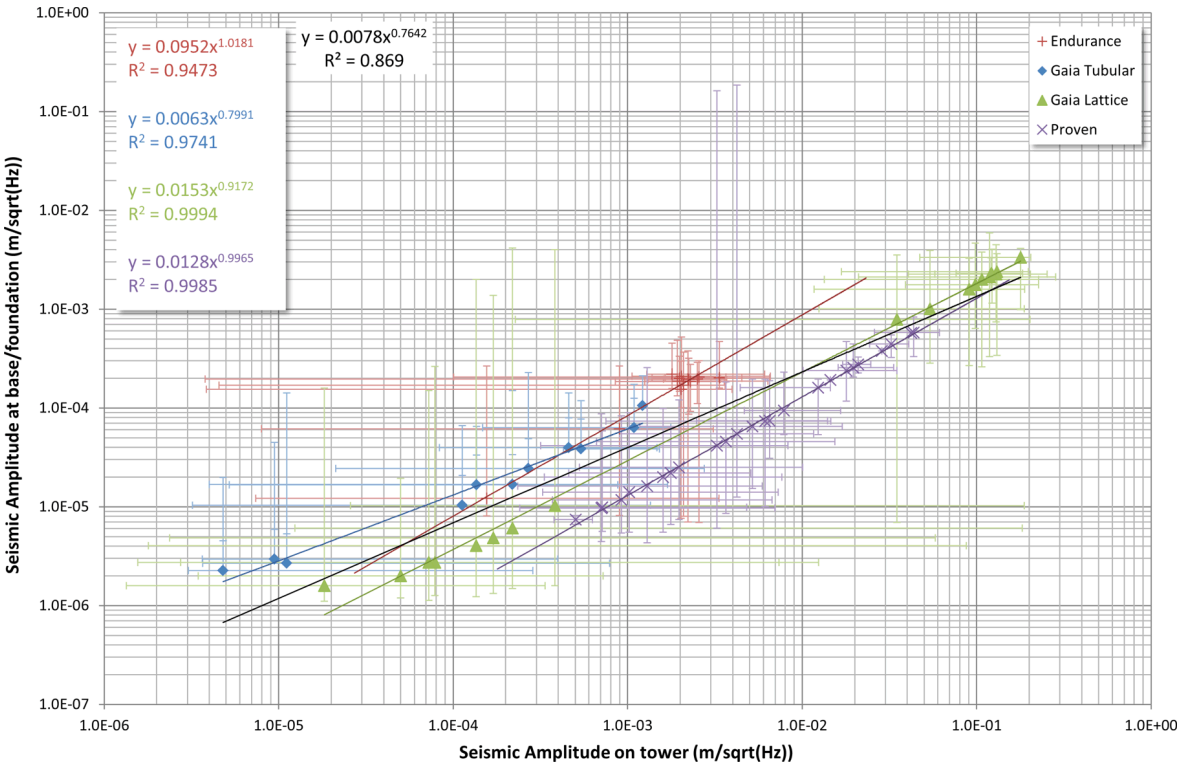

Figure 6-12: *The seismic amplitude relationship between on the tower and the foundation. The error bars indicate the maximum and minimum values recorded for the frequency peak for each wind speed range. The black line indicates the equation using all data.*

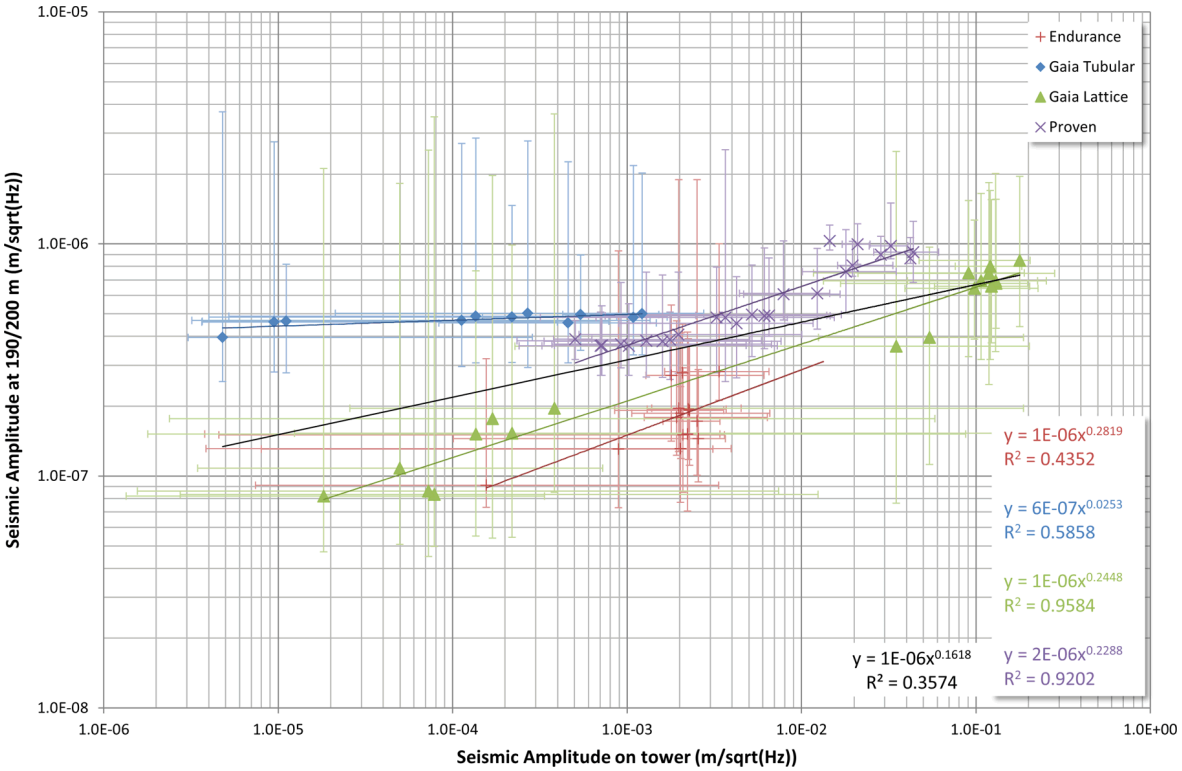

Figure 6-13: *The seismic amplitude relationship between on the tower and 190/200 m away. The error bars indicate the maximum and minimum values recorded for the frequency peak for each wind speed range. The black line indicates the equation using all data.*

Table 6-2 summarises the findings from this section. It shows that there is no one law applicable to all the turbines which can relate seismic amplitude on the tower to wind speed. Above 8.5 m/s the relationship for the Proven 35-2 cannot be predicted. This could be due to the bending of the blades creating variable loads on the tower and forcing different resonant modes. The seismic amplitude from the Gaia-Wind 133 tubular tower with respect to wind speed can only be specified for wind speeds up to 5.5 m/s due to the lack of data for high wind speeds. At low wind speeds, the lattice tower data agrees with Styles et al. (2005), before changing at wind speeds above 4 m/s to agree with the findings by Schofield (2002), with which the Proven 35-2 data also agrees. Interestingly, at wind speeds above 1.5 m/s, the Endurance maintains an almost constant amplitude.

For three out of four of the turbines, the seismic amplitude on the foundation is proportional to the seismic amplitude on the tower. Additionally, the seismic amplitude at 200 m is proportional to the seismic amplitude on the tower to the power of 0.25. The Gaia-Wind 133 tubular tower is an exception to this. The difference may be due to the high background noise of the site and the signal from the turbine being masked so that the calculation is based on background noise. Further monitoring over a larger range of wind speeds and at a seismically quieter site would confirm the relationships for this turbine. Alternatively, the soil at the site may not be creating a good coupling of the foundation to the ground, meaning the signal is not transferring well. The relationship between the seismic amplitude at 200 m and the seismic amplitude on the tower in general is unusual, as it means that although the amplitude on the tower may increase by a lot, the amplitude of the signal in the ground will increase by much less. There are a few reasons as to why this may be:

- The soil at the site may not be structurally strong enough to hold high amplitudes;
- The sensors are positioned too close to the turbine, so only direct waves are being detected and no refracted waves;
- The background noise may be to high.

Turbine	Relationship between on-tower seismic amplitude (S_t) and wind speed (w)	Relationship between seismic amplitude at 190/200 m (S_g) and wind speed (w)	Relationship between seismic amplitude on the tower (S_t) and on the foundation (S_f)	Relationship between seismic amplitude on the tower (S_t) and at 190/200 m (S_g)
Gaia-Wind 133 tubular tower	$S_t \propto w^2$ if $w < 5.5$ m/s	$S_g \propto e^{0.05w}$	$S_f \propto {S_t}^{0.8}$	$S_g \propto {S_t}^{0.025}$
Gaia-Wind 133 lattice tower	$S_t \propto \begin{cases} w & \text{if } w \leq 4 \text{ m/s} \\ 100w^{3/2} & \text{if } w > 4 \text{ m/s} \end{cases}$	$S_g \propto \begin{cases} e^{0.3w} & \text{if } w \leq 5 \text{ m/s} \\ 10(e^{0.3w})^{0.1} & \text{if } w > 5 \text{ m/s} \end{cases}$	$S_f \propto S_t$	$S_g \propto {S_t}^{0.25}$
Proven P35-2	$S_t \propto w^{3/2}$ if $w \leq 9.5$ m/s	$S_g \propto e^{0.08w}$	$S_f \propto S_t$	$S_g \propto {S_t}^{0.25}$
Endurance E-3120	$S_t \approx 0.0022$ if $w > 1.5$ m/s	$S_g \propto e^{0.15w}$	$S_f \propto S_t$	$S_g \propto {S_t}^{0.25}$

Table 6-2: *The relationship between seismic amplitudes and wind speed for each wind turbine*

6.3 Attenuation of the Measured Signals

Styles et al. (2005) describe an attenuation model for wind farms to calculate the total amount of displacement at the Eskdalemuir array (section 1.1) from a wind farm of N_j turbines, each with power P_j at a distance r_j from the centre of the array. This model is defined as

$$A_j = 0.6A_0\sqrt{\frac{r_0}{r_j}}e^{\left(\frac{-\pi f(r_0-r_j)}{Qv}\right)}\frac{P_j}{P_0}\sqrt{\frac{N_j}{N_0}}, \tag{6.5}$$

The 0.6 factor accounts for the electrical production of wind farms exceeding 60% of rated capacity only 20% of the time over a year (Styles et al. 2005). The other parameters define the velocity of the wave ($v = 2000$ m/s), the Q-factor of the ground at Eskdalemuir ($Q = 50$), the power of the turbines at the reference wind farm ($P_0 = 0.66$ MW), the number of reference wind turbines ($N_0 = 399$), the reference distance ($r_0 = 1$ km), the mid-point of the frequency pass band of interest ($f = 4.5$ Hz) and the reference displacement at the reference distance from the reference turbines ($A_0 = 24$ nm).

Table 6-3 shows the results of applying equation (6.5) for each of the small wind turbines described in chapter 5 at 190 or 200 m away, depending on the location of the 6TD seismometer. Comparison of these values to the displacement spectrum at 190 or 200 m (given in chapter 5) for each of the respective turbines indicates that the values predicted from the model are a factor of 10^4 to 10^6 lower than the measured values. This section will discuss possible reasons for this difference and will investigate the attenuation of each of the turbines to establish whether a model can be derived for small wind turbines.

One possible reason for the difference is that Styles et al. (2005) conducted their experiment using seismometers positioned in the far-field, whereas the sensors used in this project were positioned close to the turbine in the near-field.

Turbine	Distance	Model displacement result	Measured displacement result (when the turbine is operational)
Gaia-Wind 133 lattice tower	190 m	0.0309 nm = 3.09×10^{-11} m	2.57×10^{-7} m
Gaia-Wind 133 tubular tower	190 m	0.0309 nm = 3.09×10^{-11} m	1.58×10^{-6} m
Endurance E-3120	200 m	0.1367 nm = 1.367×10^{-10} m	2.98×10^{-7} m
Proven 35-2	200 m	0.0331 nm = 3.331×10^{-11} m	8.144×10^{-7} m

Table 6-3: *Styles et al. (2005) model and measured results for each of the small wind turbines at 190/200 m (and 4.5 Hz)*

Turbine	Geology	Approximate velocity (m/s)	Far-field (at 4.5 Hz)	Far-field (at 10 Hz)
Gaia-Wind 133 tubular tower	Mudstone	2500	$\gg 600$ m	$\gg 250$ m
Gaia-Wind 133 lattice tower	Shales	2000	$\gg 450$ m	$\gg 200$ m
Endurance E-3120	Slate and siltstone	3000	$\gg 700$ m	$\gg 300$ m
Proven 35-2	Mudstone	2500	$\gg 600$ m	$\gg 250$ m

Table 6-4: *The geology, velocity and approximate far-field distance for each of the wind turbines. Geology obtained through the British Geological Survey and velocity values from Mavko (2005) and Clark (1966).*

The far-field, for a seismic wave from a point source, can be defined by

$$r/\lambda \gg 1, \tag{6.6}$$

where λ is the wavelength and r the distance from the source (Madariaga 2007). Therefore, the distance at which a point is in the far-field is not fixed and varies with wavelength and rock type, which will affect the velocity of the wave. For example, a wave with a frequency of 1 Hz travelling through a rock with a shear-wave velocity of 2000 m/s will be in the far field at 2 km. Whereas at a frequency of 10 Hz, the far field will be reached at only 200 m. Table 6-4 provides information on the geology, velocity and approximate far-field distance at each of the wind turbine sites. From this, it can be concluded that the sensors were placed in the near-field at each site.

The attenuation of the wave can be obtained by plotting the amplitude of a specific peak at different distances. The result is shown in figure 6-14 for three of the turbines. Only three sensors were placed in the ground to monitor the Proven 35-2 which does not provide enough data points to

accurately predict the attenuation of the signal. A selection of peaks from the displacement spectra in figures 5-11, 5-26 and 5-52 are chosen to see if the rate of decay changes with frequency. The data from each of the turbines shows that

$$S_r \propto r^{-1}, \tag{6.7}$$

where r is the distance from the wind turbine and S_r is the seismic amplitude. In the near-field the radiation decays more rapidly than the far-field at a rate of r^{-1}, where r is the distance from the source, whereas in the far-field the decay is at a rate of $r^{-1/2}$ (Chapman 2006, Madariaga 2007).

The equations derived from figure 6-14 can be extrapolated to distances within the near-field, however once the far-field is reached it is likely that the power laws will no longer hold as the decay rate changes from r^{-1} to $r^{-1/2}$.

The change from near-field to far-field behaviour is almost certainly transitional and there is not a fixed point where the near-field becomes the far-field. In the near-field close to the source, the seismic field is more complex as the wave may still be propagating within the source zone where the vibrations are being generated. However, in the far-field, energy is either returned elastically to the propagating wave or dissipated by frictional processes and the wave is no longer propagating within a zone where permanent deformation changes can take place. There is a zone in between the near- and far-field which is not widely discussed in the literature and where the effects on the wave are not clearly understood. This makes it difficult to say at what distance one attenuation model should be substituted for another.

There are two possible attenuation models for the far-field (section 3.1.3): '$r^{-1/2}$' and '$r^{-1/2}$ with linear attenuation'. Both of these contain an $r^{-1/2}$ term, with the linear attenuation model also containing an additional exponential function to take into account damping from the material which the wave is passing through. Figure 6-15 shows the results of extrapolating the Endurance data at 7.8 Hz using each of the models. In this figure, the far-field attenuation models start at 1 km, as the far-field transition is at a distance $\gg 440$ m. A point (blue star) is also shown on the graph which is an extrapolation of the near-field term out to 1 km. The models by Styles et al. (2005) and Schofield (2002), as applied to a 50 kW wind turbine, are also shown on the graph. It can be seen that, as expected the '$r^{-1/2}$' model follows the same gradient as the Schofield (2002) model and the '$r^{-1/2}$

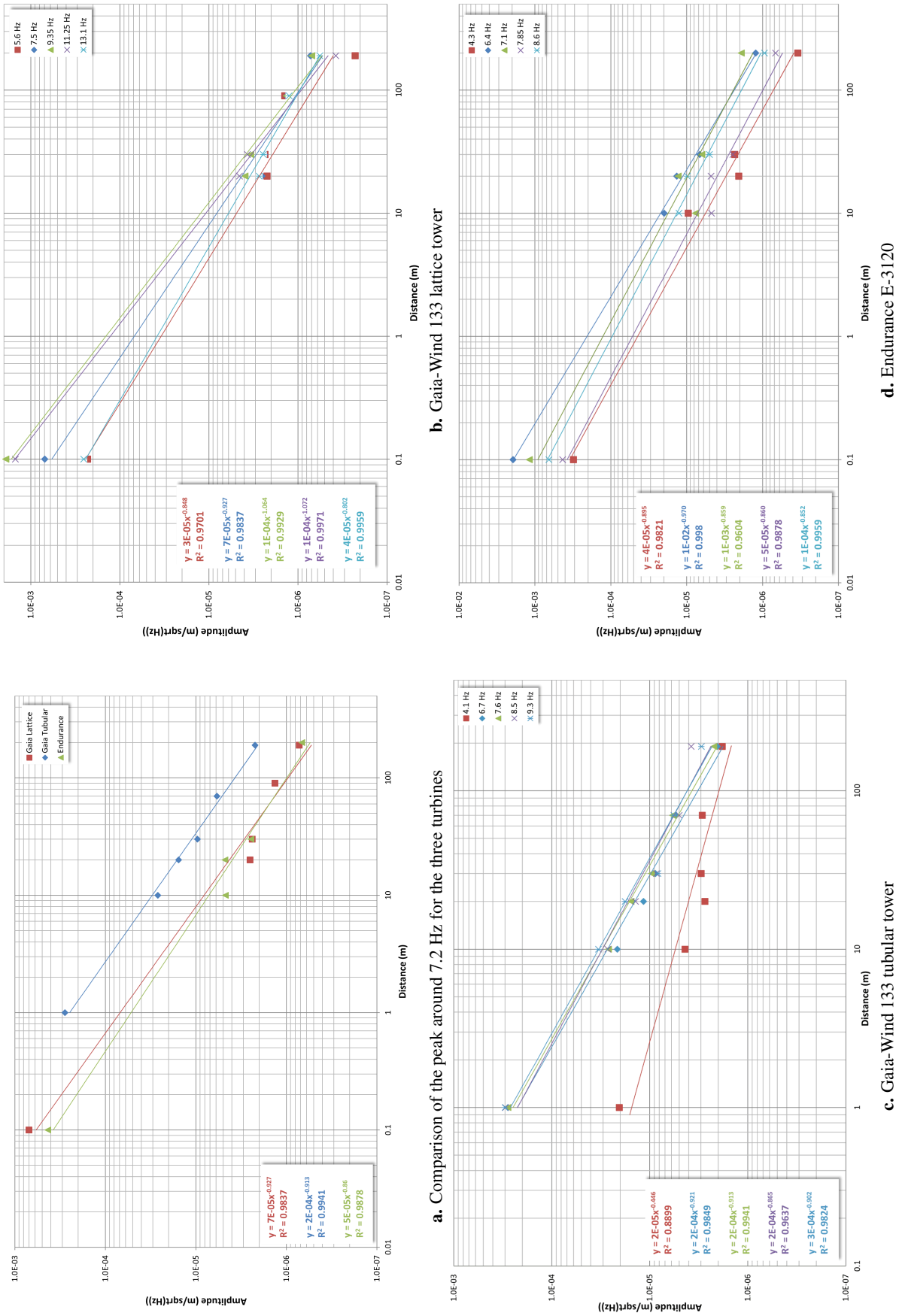

Figure 6-14: *The relationship between displacement seismic amplitude and distance for three of the wind turbines, at a variety of frequencies.*

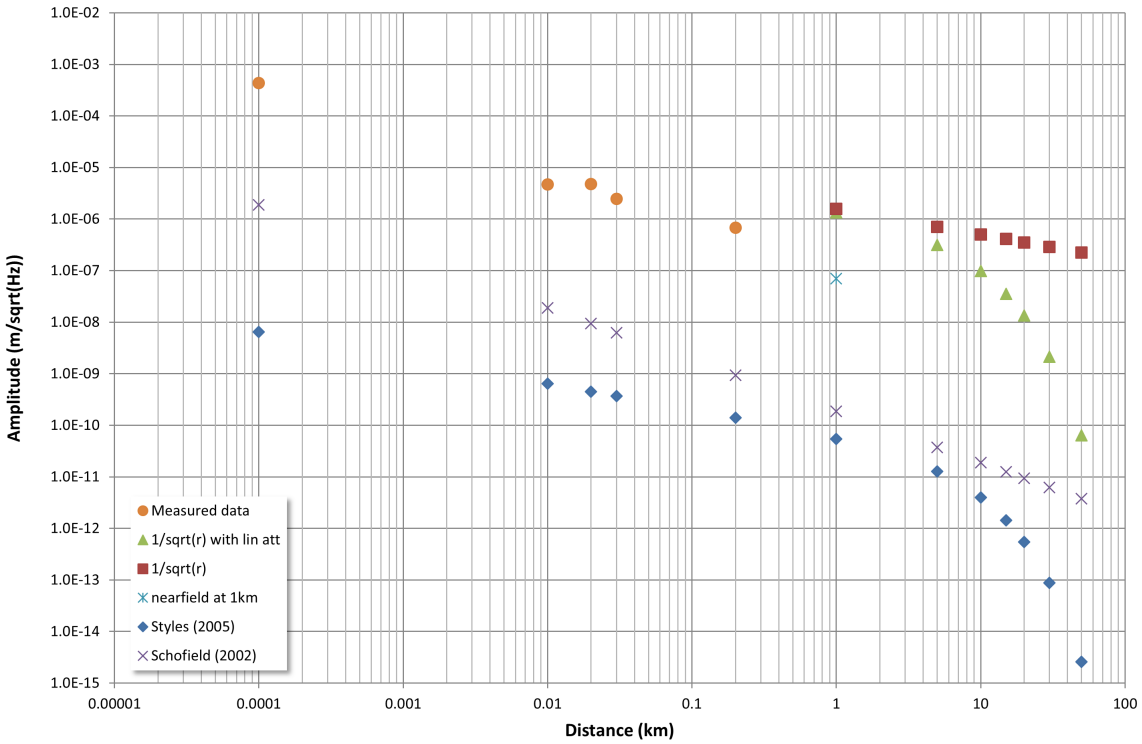

Figure 6-15: *The measured data from the Endurance E-3120 at 7.8 Hz with two possible models for the far-field, $r^{-0.5}$ and $r^{-0.5}$ with linear attenuation. Also shown are the Styles et al. (2005) and Schofield (2002) models applied to the Endurance E-3120 at Hayle.*

with linear attenuation' the same gradient as the Styles et al. (2005) model, however the measured amplitudes are around 10^4 greater than either of the published models.

Without further monitoring, it is not possible to deduce which (if either) of these models is correct, however if the $r^{-1/2}$ with linear attenuation holds at larger distances from the turbine, the amplitude will decrease more rapidly (green triangles in figure 6-15).

The decay of the 4.1 Hz peak in the Gaia-Wind 133 tubular tower data occurs at a rate of

$$S_r \propto r^{-1/2}. \tag{6.8}$$

This is representative of the sensors being placed in the far-field of the source and as such it is likely that the peak does not originate from the wind turbine.

From the results in this section and section 6.2, it can be concluded that the seismic amplitude in the ground is exponentially dependent on wind speed and in the near field decays at a rate of r^{-1}. In

the far-field this is likely to be at a rate of $r^{-1/2}$, however further experiments would be required to confirm this. The differences shown between the turbines for these parameters indicate that there is no single common simple equation to describe the amplitude at a given distance from the wind turbine for all small wind turbines.

6.4 Polarisation Analysis

Polarisation analysis quantitatively describes the particle motion of a seismic wave field. The aim of using this technique with data obtained from monitoring a wind turbine is to ascertain the type of wave the turbine is generating, which frequencies are originating from the wind turbine and which are from other nearby sources. Three-component analysis can be used to quantify the degree of linear particle movement, known as linearity. The direction of particle movement is described by the angles for dip (ϕ) and azimuth (θ) (see figure 6-16). Polarisation analysis of the wave field using data from the 6TD three component seismometer can identify whether the vibrations detected on the sensor are likely to originate from the wind turbine, as well as the type of wave that is being generated. In an isotropic homogeneous medium the basic polarisation cases are:

1. P-wave polarisation: linear and in the direction of wave propagation.
2. S-wave polarisation: linear and perpendicular to wave propagation.
3. Rayleigh wave polarisation: elliptical, perpendicular to the wave propagation direction and travelling along the surface.
4. Love wave polarisation: linear, perpendicular to the wave propagation direction and travelling along the surface.

The polarisation of the wave field is described by performing singular value decomposition (SVD) on the data. This generates an expression for the wave field (X) as a product of three matrices, such that

$$X = \mathbf{USV}'. \tag{6.9}$$

The columns of $\mathbf{V}$ contain the eigenvectors of the wave field and the diagonal elements of $\mathbf{S}$, the corresponding eigenvalues (Jackson et al. 1991). Matlab contains a built-in function which performs SVD, *svds* (MathWorks 2010c), which returns the largest three eigenvalues (λ_1, λ_2 and λ_3) and

corresponding eigenvectors. The eigenvectors are orthogonal and together completely describe the wave field. The eigenvector (x, y, z) corresponding to the largest eigenvalue (λ_1) points in the direction of the largest amount of polarisation. Using this eigenvector, the azimuth and dip can be calculated using equations (6.10) and (6.11) respectively.

$$\theta = \tan^{-1}\left(\frac{y}{x}\right), \tag{6.10}$$

$$\phi = \tan^{-1}\left(\frac{z}{\sqrt{x^2 + y^2}}\right). \tag{6.11}$$

There is an inherent 180° ambiguity in the result for the dip and azimuth, as the eigenvector (x, y, z) generates the same result as $(-x, -y, -z)$ (Hendrick & Hearn 1999, Vidale 1986).

If $\lambda_1 \geq \lambda_2 \geq \lambda_3$, then the eigenvectors corresponding to λ_2 and λ_3 point in the direction of the second and least amounts of polarisation respectively. Vidale (1986) and Nguyen et al. (1989) describe a method whereby the eigenvalues can be used to calculate the strength of the polarisation,

$$Ps = 1 - \frac{\lambda_2 + \lambda_3}{\lambda_1}. \tag{6.12}$$

If Ps is equal to 1, there is only one component of polarisation, whereas a result of 0 will mean that the largest component is as big as the sum of the other two, that is the motion is circular. For values in between, the motion is elliptical. For a polarised Rayleigh wave, λ_1 and λ_2 are much greater than

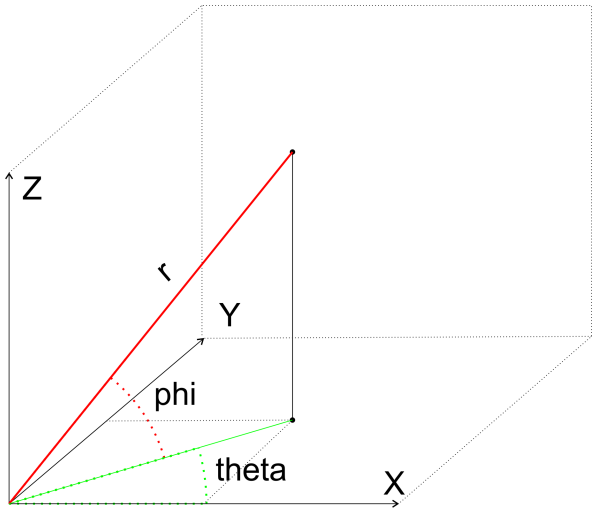

Figure 6-16: *The angles of dip (ϕ) and azimuth (θ)*

λ_3, so $Ps \geq 0.5$ (Nguyen et al. 1989). By combining the results for each of these three values, it may be possible to establish whether the signal detected at a given frequency is originating from the wind turbine, how it is travelling and what type of wave it is. Analysis is performed over time windows, the length of which is a compromise between stability and resolution. If the window length is too short the analysis becomes unstable, whereas a long window length will smooth the results and decrease the resolution (figure 6-17). After testing a range of window sizes, a 0.1 second window length was selected as optimal for analysing the data from the wind turbines.

Figures 6-18 to 6-21 show the values of θ, ϕ and Ps at a range of frequencies for each of the turbines. If the wind turbine is generating a P-wave, the azimuthal angle should be in the direction of the wind turbine, whereas a shear or surface wave will appear at 90° to the source. A 0° strike and dip represents a vector pointing horizontally toward the wind turbine. The filtered frequencies were selected by examining the results in chapter 5 and selecting peaks visible in the respective spectra on the three-component seismometer.

Unlike an earthquake, a wind turbine is a constant source. This means that there may be different types of wave arriving at the same time, as they are likely to be out of phase. The predominant azimuth angle at each of the sites over all frequency ranges is $\pm 90°$. If this is combined with a dip close to 0° and $P_s \approx 0.5$, it is likely that this is a Love wave. Rayleigh waves would also be a possibility if the azimuth is $\pm 90°$, however for this wave there is a change in azimuth with time, generating a slope between the +90° and -90°. The dip would be required to be close to 0°or slope in a similar fashion to the azimuth and $P_s \geq 0.5$. An SV-wave is indicated by an azimuth and dip each at close to 0° and a P_s equal to one. An SH-wave is the same as an SV-wave but with an azimuth between 45 and 90°.

The main wave types originating from the direction of any of the wind turbines are surface waves. However, at certain frequencies, there are also polarised signals from other sources. Figures 6-18d and 6-18e contain a mixture of azimuth angles at $\pm 90°$ and -30° to -70°. The dip is close to 0° and $Ps \geq 0.5$, indicating that there are surface waves originating from a source other than the wind turbine, as well as from the wind turbine. Figure 6-22 shows possible identification of the waves in the 11.2-11.3 Hz range from the Gaia-Wind lattice tower. The lower frequencies in figure 6-18 contain surface waves from the direction of the wind turbine. There are two time periods when the azimuth alters and the dip becomes unstable. At these times the strength of polarisation drops to less

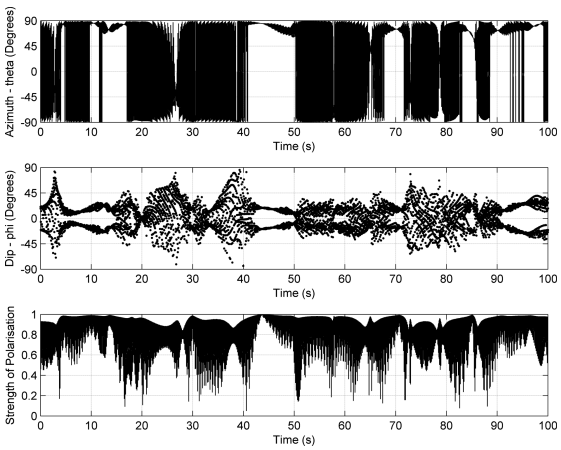

a. 0.015 sec period

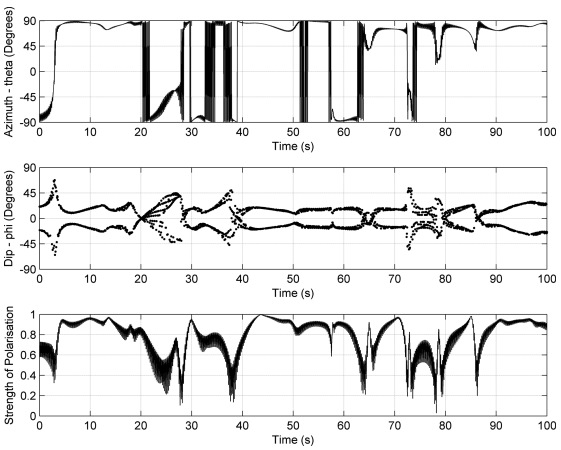

b. 0.05 sec period

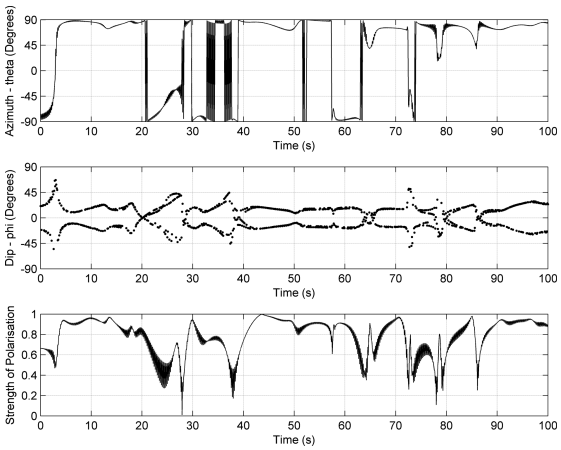

c. 0.1 sec period

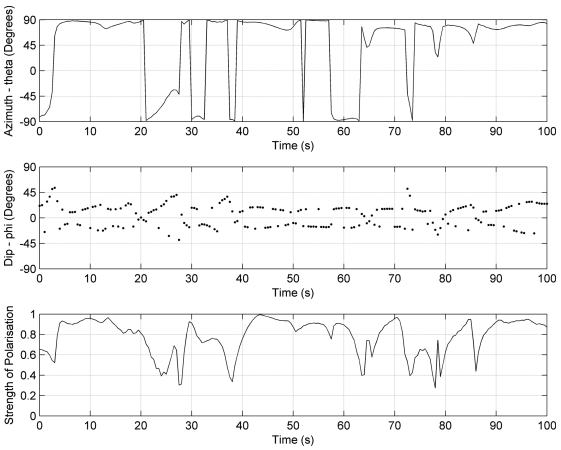

d. 0.5 sec period

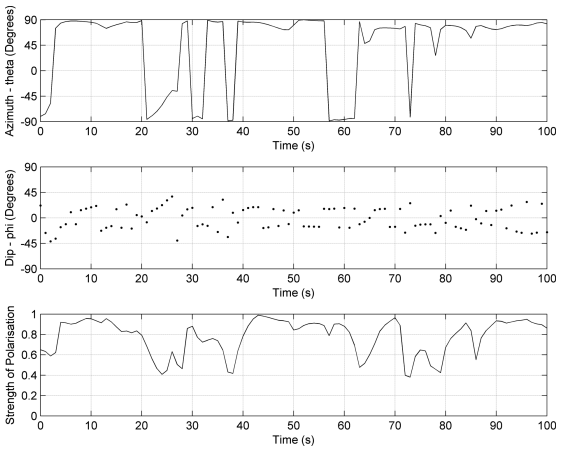

e. 1 sec period

Figure 6-17: *The effect of different period time step windows on polarisation analysis*

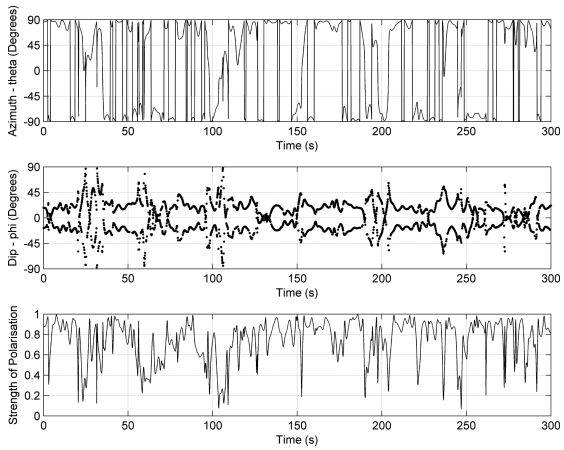

a. 4.65-5.0 Hz

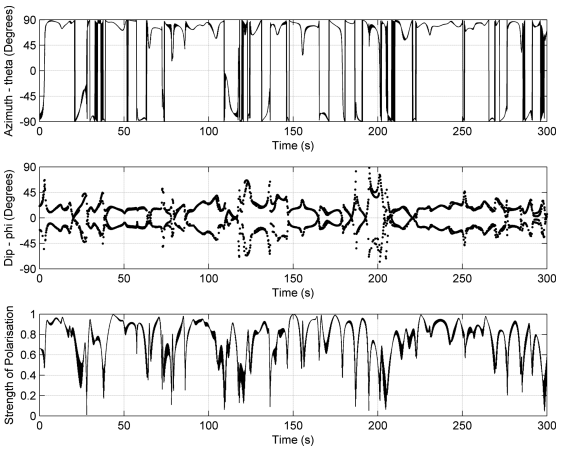

b. 7.4-7.6 Hz

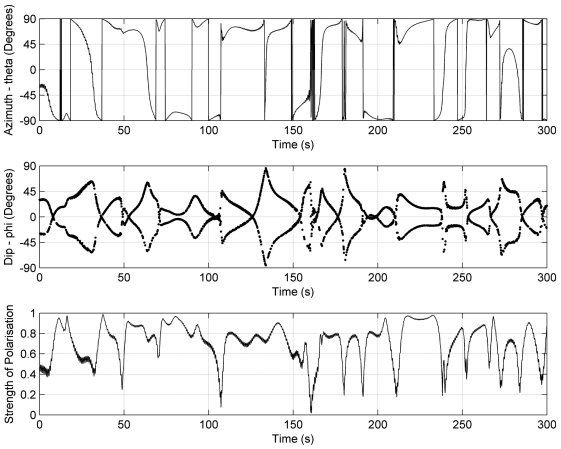

c. 9.3-9.4 Hz

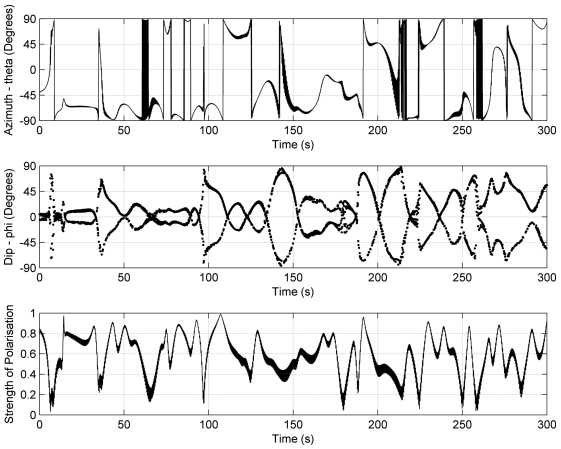

d. 11.2-11.3 Hz

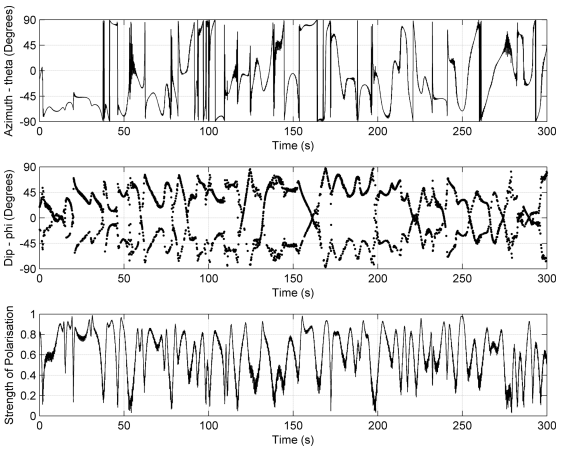

e. 13.0-13.2 Hz

Figure 6-18: *Polarisation analysis for data from the 6TD at Melrose on the Gaia-Wind 133 lattice tower site at wind speeds between 5 and 6 m/s starting on 5 September 2010 at 9.50 am. A 0° azimuth and dip indicate a vector pointing horizontally in the direction of the wind turbine.*

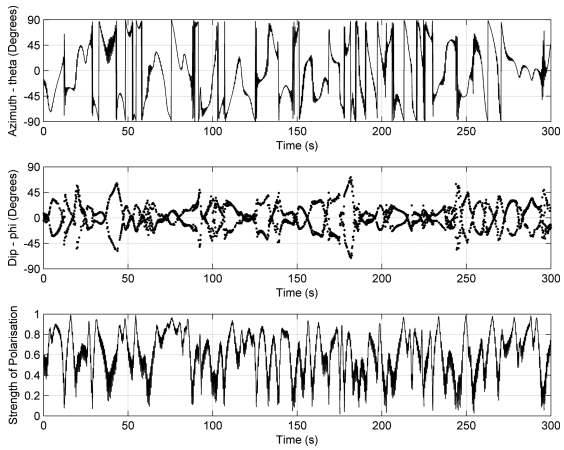

a. 4-4.2 Hz

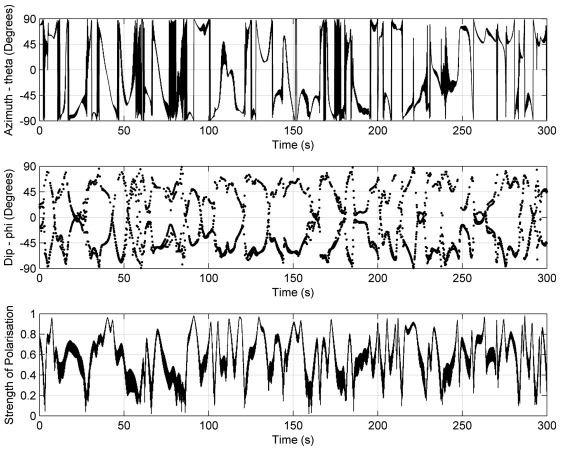

b. 6.6-6.8 Hz

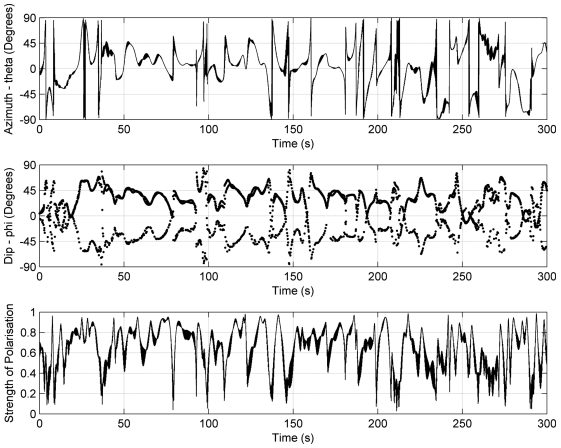

c. 7.5-7.7 Hz

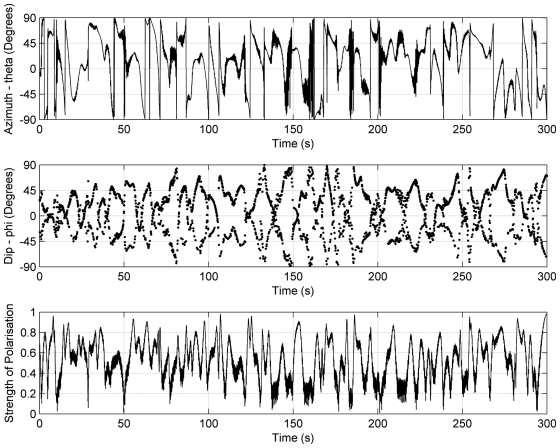

d. 8.4-8.7 Hz

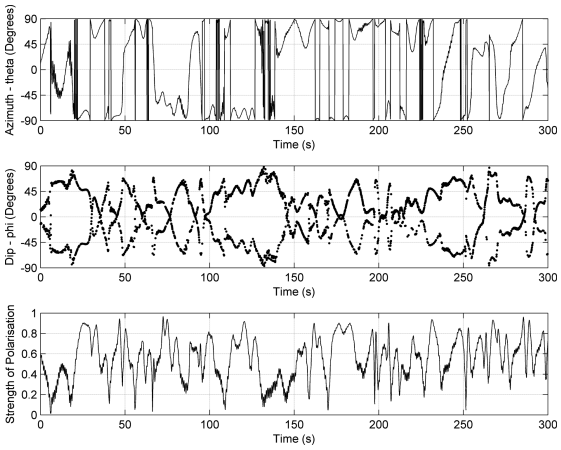

e. 9.25-9.45 Hz

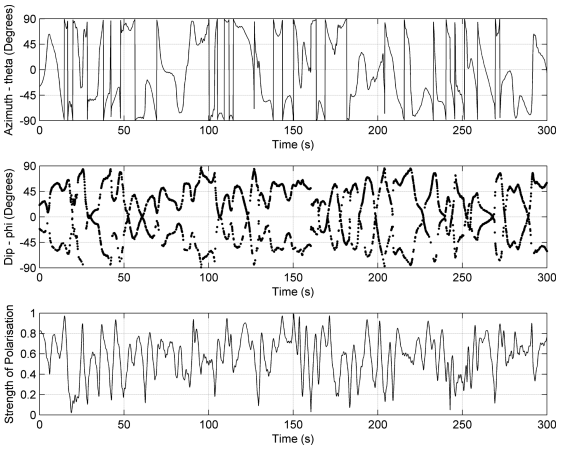

f. 10.3-10.5 Hz

Figure 6-19: *Polarisation analysis for data from the 6TD at Wigton on the Gaia-Wind 133 tubular tower site at wind speeds between 5 and 6 m/s starting on 7 September 2010 at 4.00 pm. A 0° azimuth and dip indicate a vector pointing horizontally in the direction of the wind turbine.*

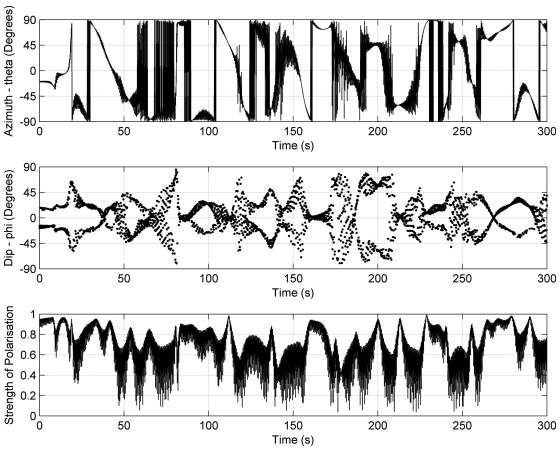

a. 3-3.1 Hz

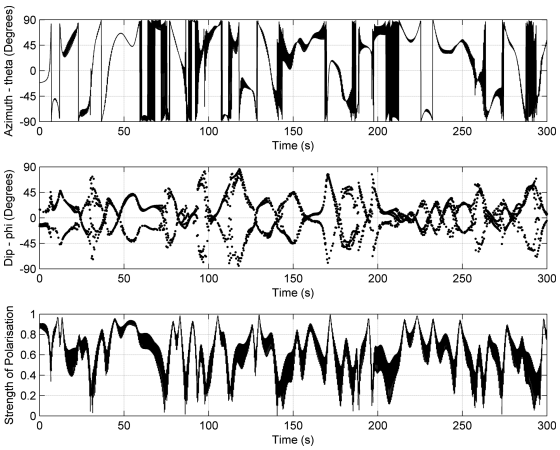

b. 3.7-3.85 Hz

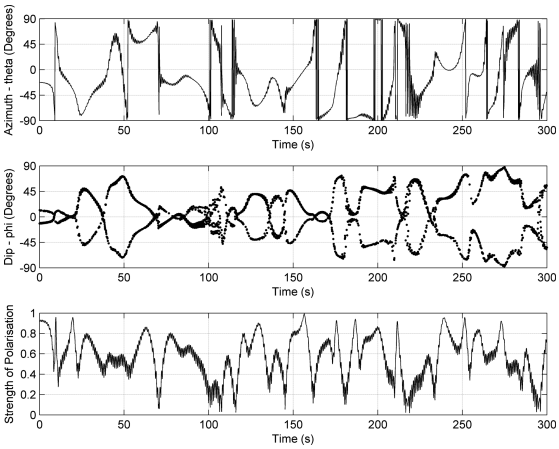

c. 4.4-4.5 Hz

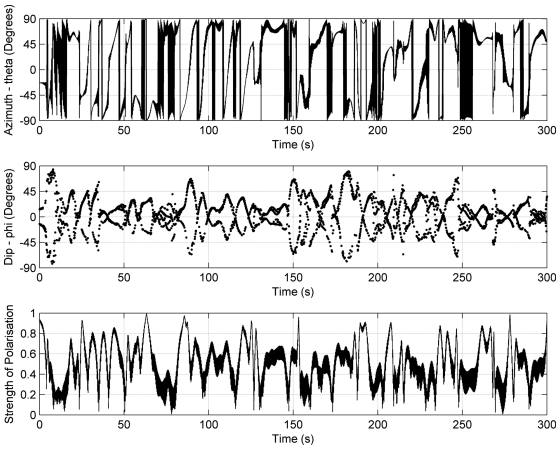

d. 6.5-6.7 Hz

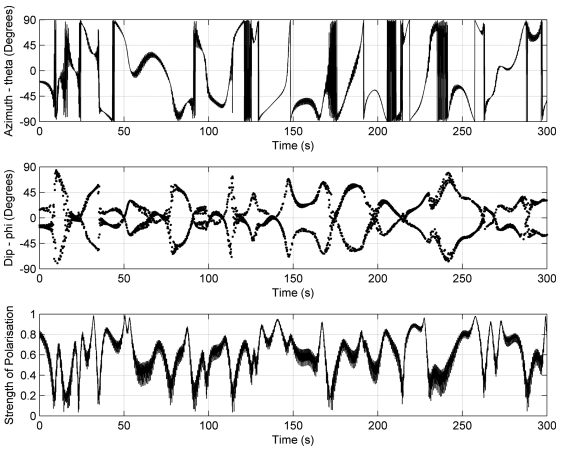

e. 7.8-7.9 Hz

Figure 6-20: *Polarisation analysis for data from the 6TD at Kilmarnock on the Proven 35-2 site at wind speeds between 5 and 6 m/s starting on 21 May 2011 at 2.30 am. A 0° azimuth and dip indicate a vector pointing horizontally in the direction of the wind turbine.*

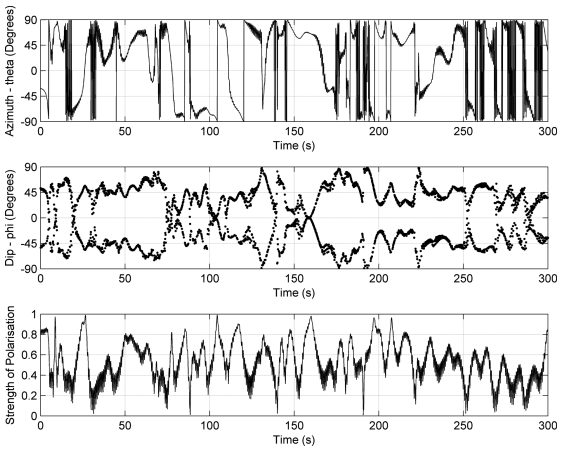

a. 4.2-4.4 Hz

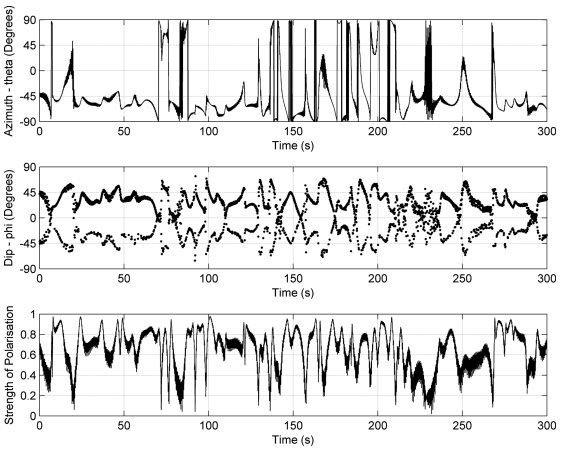

b. 6.3-6.5 Hz

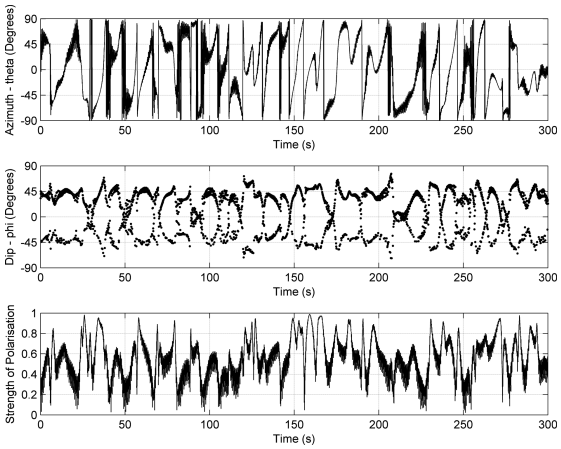

c. 7-7.2 Hz

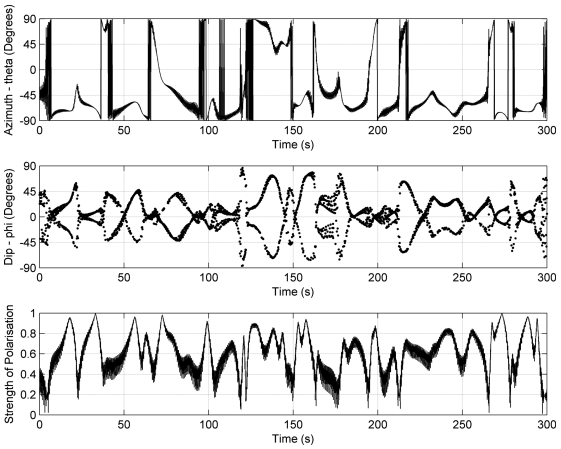

d. 7.8-7.9 Hz

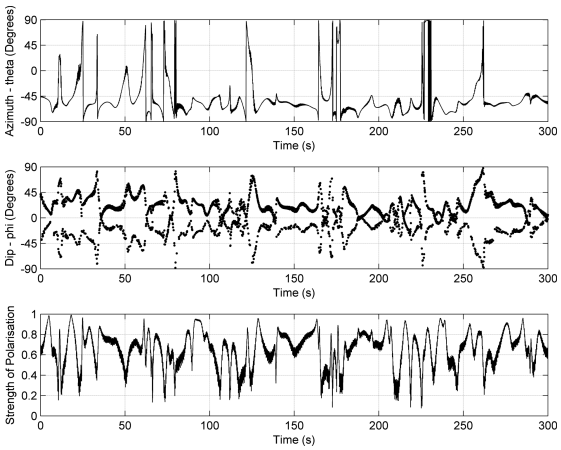

e. 8.5-8.7 Hz

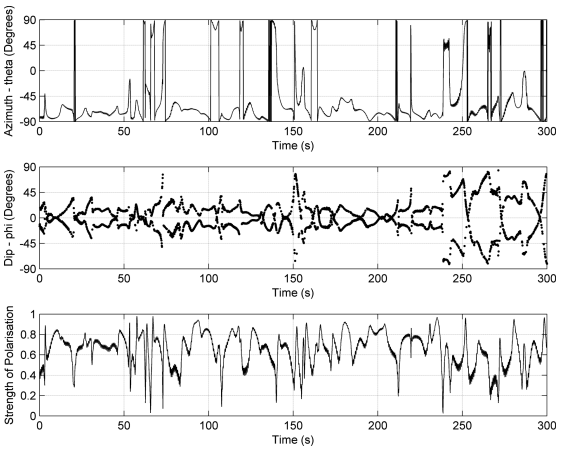

f. 10.7-10.9 Hz

Figure 6-21: *Polarisation analysis for data from the 6TD at Hayle on the Endurance E-3120 site at wind speeds between 5 and 6 m/s starting on 31st August 2011 at 1.00 pm. A 0° azimuth and dip indicate a vector pointing horizontally in the direction of the wind turbine.*

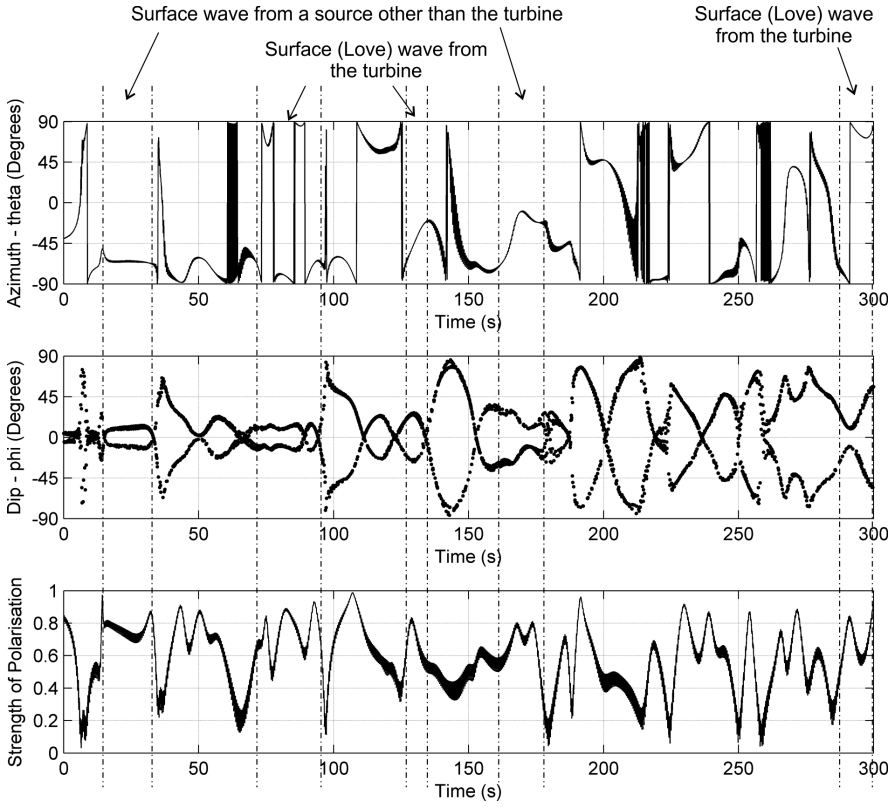

Figure 6-22: *Identification of possible wave types at frequencies between 11.2 and 11.3 Hz at the Melrose site*

than 0.5 indicating that the signal is not very well polarised and that there is not one primary direction of polarisation at this point. Examples of this occur at around 20-30 seconds and 120-130 seconds.

The signal between 13 and 13.2 Hz is less stable than the other frequencies. There is no obvious indication of surface waves from the Gaia-Wind lattice tower turbine at this frequency, as the dip is generally at around $\pm 45^{\circ}$ and Ps is frequently less than 0.5. However between 10 and 20 seconds the dip is very close to 0° and Ps increases from 0.5 to around 0.9; azimuth decreases slightly over the time period from around -85° to -60°. It is likely therefore that this is an SV or P-SV wave originating from a source other than the wind turbine. Additionally, the 13.1 Hz peak seen in the spectrum from the sensor at 190 m in figure 5-26 is not the same as the broad peak seen in the on-tower spectrum and is likely to originate from elsewhere, corroborating the polarisation analysis results.

At the site of the Gaia-Wind 133 tubular tower wind turbine in Wigton the signals are more varied, especially at 4-4.2 Hz and 7.5-7.7 Hz. Figure 6-23 shows one possible interpretation of the incoming waves for the 4-4.2 Hz frequency band. There appears to be a combination of surface waves, Love and Rayleigh, originating from the direction of the wind turbine and from a source approximately 20

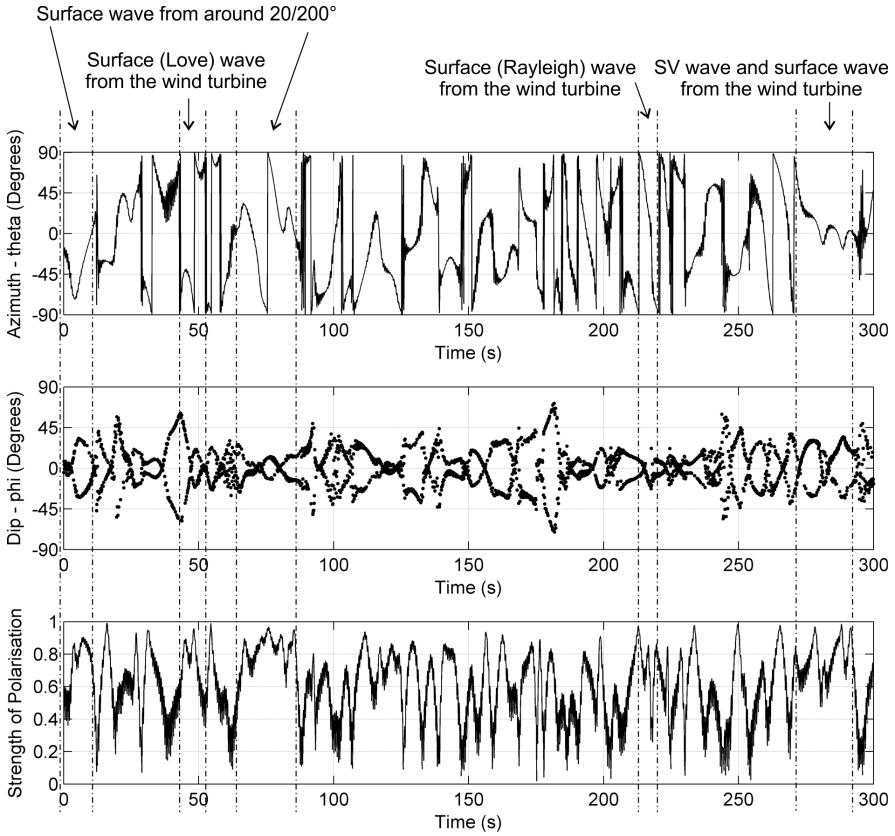

Figure 6-23: *Identification of possible wave types at frequencies between 4 and 4.2 Hz at the Wigton site*

or 200 degrees away. This is in the direction of Great Orton Wind Farm, 5 km north east of the turbine (figure 6-24).

At around 270 seconds a Rayleigh wave appears from the direction of the turbine, however an SV-wave arrives at around 280 seconds, masking the Rayleigh wave. The effect of one wave masking or interfering with another can also be seen in figures 6-20b, 6-20e and 6-21d. At 6.6 to 6.8 Hz, the azimuth is predominantly around $\pm 90°$, indicating particle motion perpendicular to the source. However, these are not all surface waves as the dip is predominantly around 45°, with some short periods close to 0°, although there are also some periods of instability. The value of Ps is generally greater than 0.5. The combination of these indicates that there are a mixture of surface waves and SH waves. It is possible that there are also other types of waves being generated by the turbine. In figure 6-19c, between 55 and 70 seconds, the azimuth is around 0° and the dip around 40°, with a high strength of polarisation. This could indicate an SV or P-SV wave generated from the direction of the turbine. These also occur at around 165-180 seconds. When comparing the prominent wave types in each analysis to the blade rotation frequency and harmonics, at the blade rotation frequencies the prominent waves appear to be surface waves, whereas more body waves are visible at the other

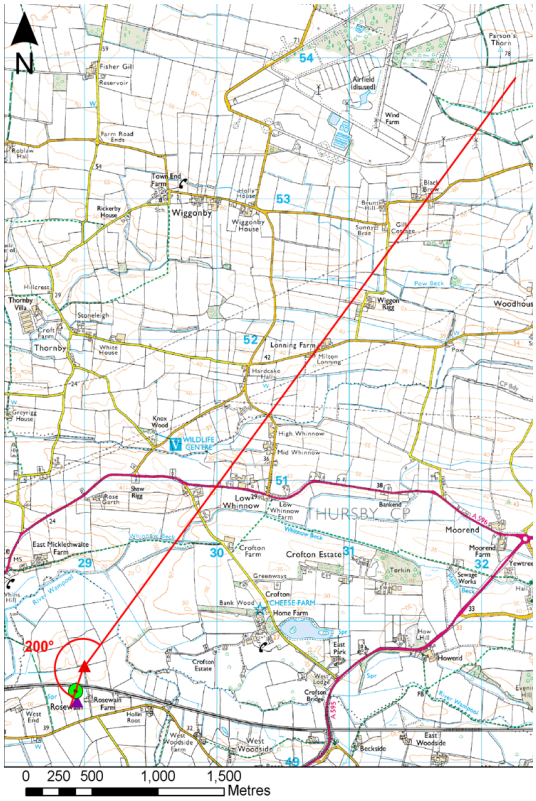

Figure 6-24: *The direction of Great Orton wind farm relative to the direction of the wind turbine (green circle) from the 6TD seismometer (red triangle). (Crown copyright/database right 2010. Ordnance Survey/EDINA supplied service).*

frequency bands (7.5-7.7 Hz and 8.4-8.7 Hz).

At Kilmarnock, the peaks at 3-3.1 Hz and 4.4-4.5 Hz can be clearly seen in the 200 m spectrum in figure 5-39, but are not visible in the on-tower or foundation spectra. However, the analysis in figure 6-20a indicates that there are surface waves originating from the direction of the tower at 3-3.1 Hz. Examples are particularly visible at around 30-45 seconds and 100-115 seconds (Rayleigh waves) and 90-100 seconds and 160-170 seconds (Love waves). At 4.4-4.5 Hz (figure 6-20c), there are few identifiable waves originating from the direction of the wind turbine, however waves originating from other sources are identifiable. Examples occur at 75 seconds, when a surface wave is apparent originating from a direction of 70° from the wind turbine and 260-280 seconds, where the dip is at close to 90° and $Ps \approx 1$, indicating a linearly polarised wave arriving almost vertically at the sensor. This could be body waves from a distant earthquake arriving at the sensor. The 7.8-7.9 Hz analysis in figure 6-20e shows similar waves from sources other than the turbine, whereas the 6.5-6.7 Hz analysis contains predominantly surface waves from the direction of the wind turbine.

The Endurance E-3120 analysis for the two highest frequency ranges (figures 6-21e and 6-21f) are dominated by surface waves which originate from very close to the direction of the turbine. The azimuths are not quite at $\pm 90^{\circ}$, which indicates either a source a few degrees away from the turbine or that the sensor was not quite aligned to north. As this azimuth dominates all the analyses for this turbine and the frequency peaks can be seen in the on-tower spectrum as well as the 200 m spectrum (figure 5-52), the latter is the most likely. Assuming this, SH waves as well as surface waves are a possibility in the 7.8-7.9 Hz range, occurring at 120-130 seconds and 160-170 seconds, when the dip is between 45 and 90 degrees and Ps close to 1. These analyses show that there may be a combination of waves originating from the wind turbines, however the predominant type appear to be surface waves, especially at frequencies which are excited by blade rotation harmonics.

Each of the analyses considered so far have used data when the wind speed was averaging between 5 and 6 m/s. Figures 6-25 to 6-28 show equivalent analyses for each turbine, for one frequency range, but over different wind speeds. The frequency range was selected based on the analysis indicating waves predominantly from the direction of the wind turbine and the peak being visible on the respective spectra in chapter 5 on the tower and in the ground.

The two Gaia-Wind 133 turbines show a distinct difference in the analyses between the turbine being operational (figures 6-25b to 6-25f and 6-26b to 6-26d) and non-operational (figures 6-25a and 6-26a). The strength of polarisation is much less when the wind turbine is not operational, indicating that the signals from the turbine are not dominating the wave field. It is likely that at this wind speed, the analysis is showing background noise. This would account for the variations in azimuth, dip and P_s. For the Proven 35-2 (figure 6-27) and Endurance E-3120 (figure 6-28) there is no distinct difference in azimuth or dip between operational and non-operational. However, as the wind speed increases, the strength of polarisation in the Proven 35-2 analyses decreases and the azimuth becomes more varied. This could be due to the background noise levels increasing with wind speed and leading to the wave field being dominated by waves from all directions.

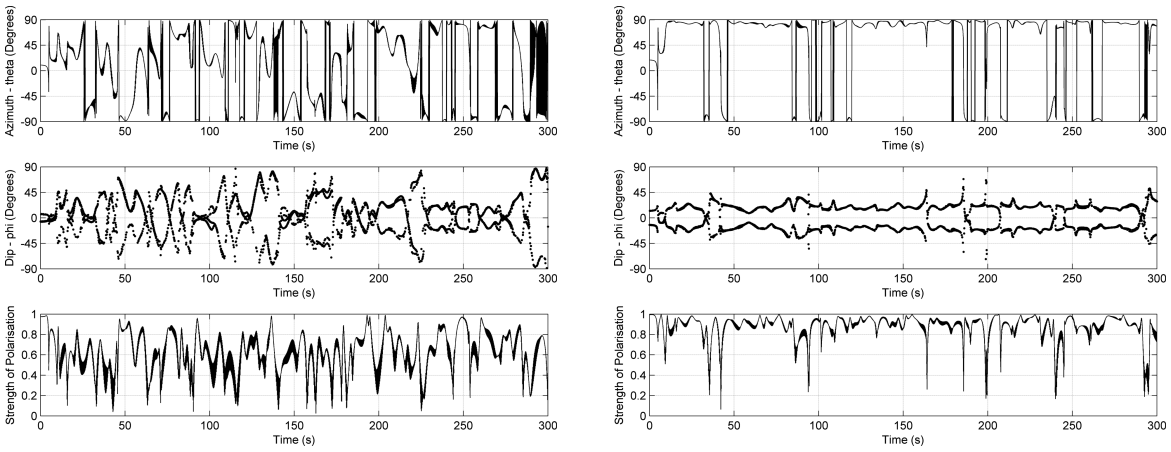

a. 1.8 m/s **b.** 2.8 m/s

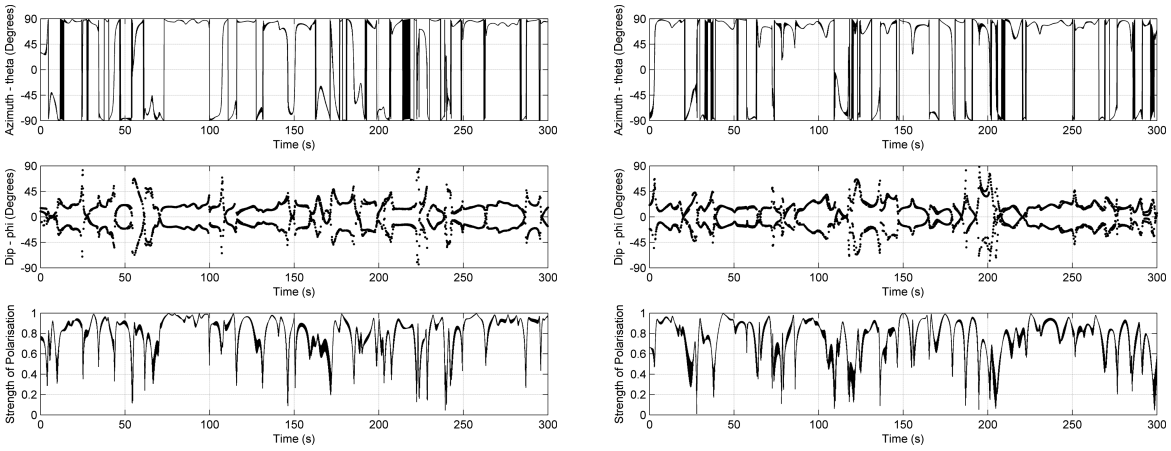

c. 4 m/s **d.** 5.5 m/s

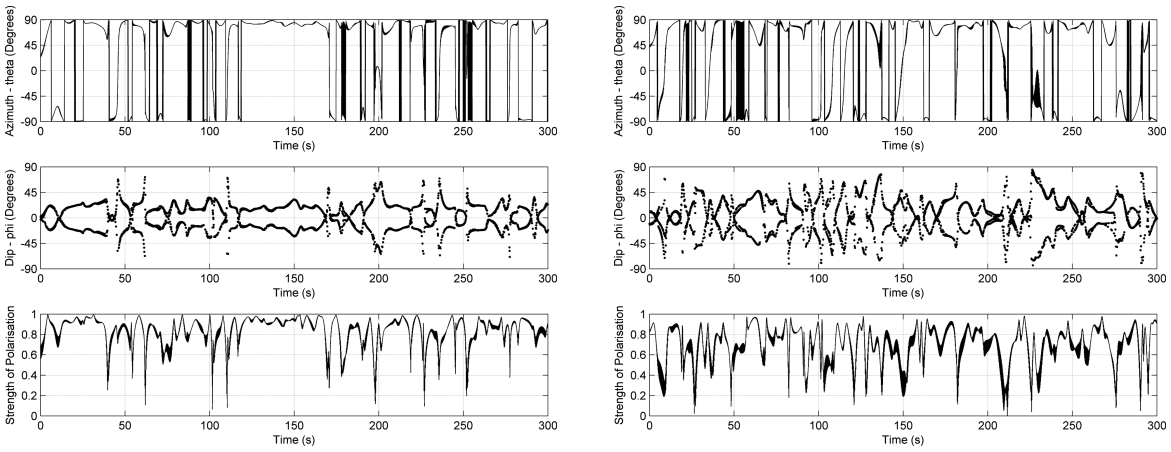

e. 7 m/s **f.** 9 m/s

Figure 6-25: *Polarisation analysis for data from the 6TD at Melrose on the Gaia-Wind 133 lattice tower site between 7.4 and 7.6 Hz for a selection of wind speeds. A 0° azimuth and dip indicate a vector pointing horizontally in the direction of the wind turbine.*

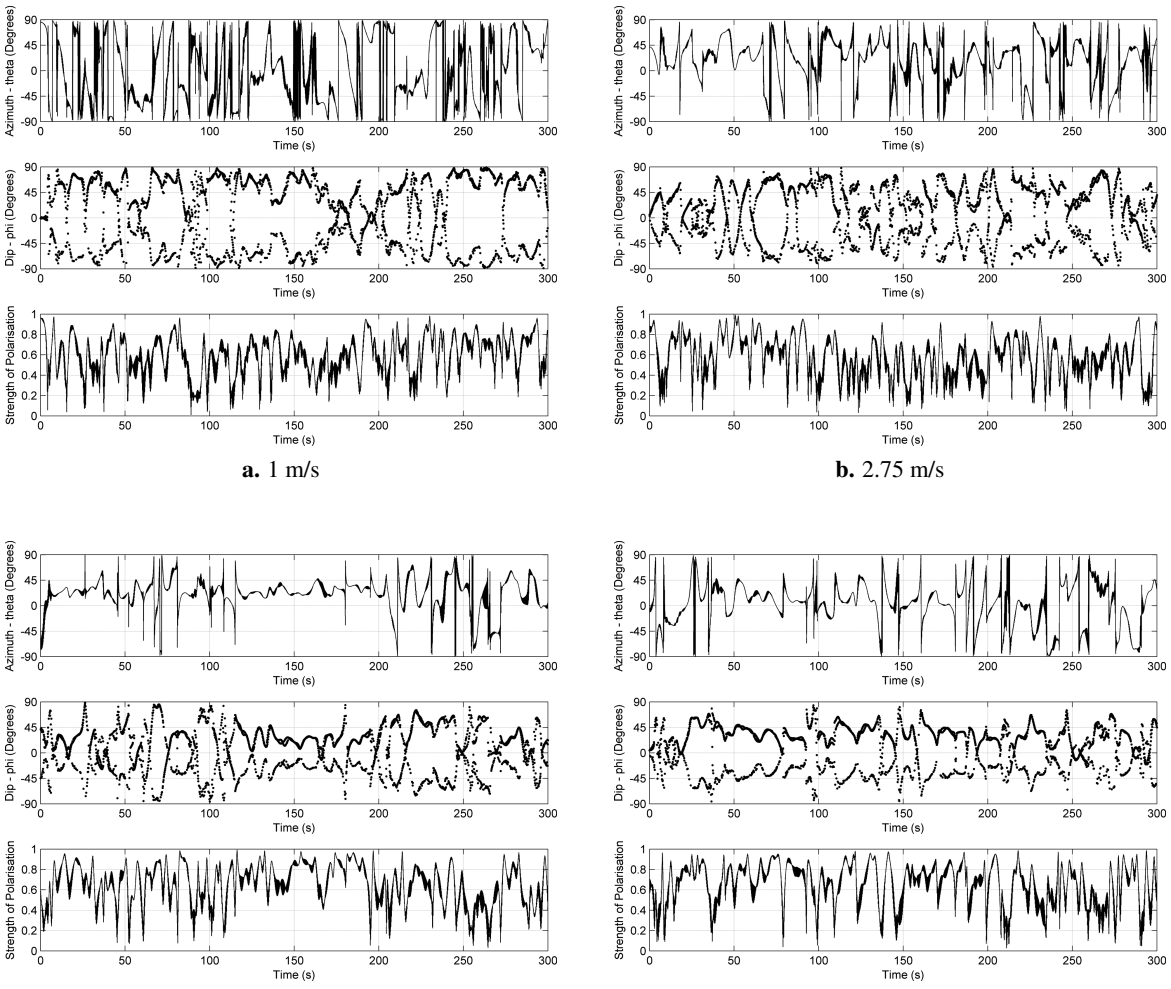

a. 1 m/s **b.** 2.75 m/s

c. 4 m/s **d.** 5 m/s

Figure 6-26: *Polarisation analysis for data from the 6TD at Wigton on the Gaia-Wind 133 tubular tower site between 7.5 and 7.7 Hz for a selection of wind speeds. A 0° azimuth and dip indicate a vector pointing horizontally in the direction of the wind turbine.*

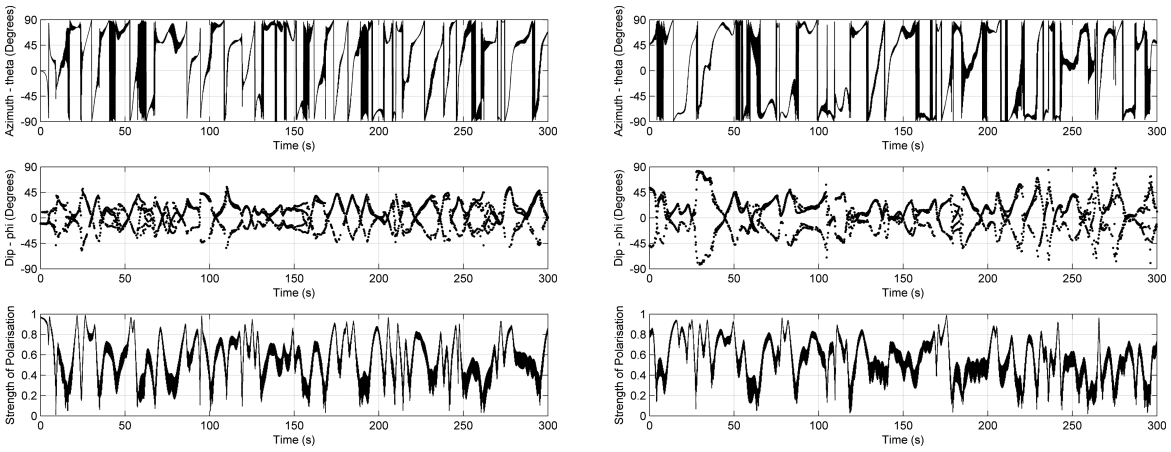

a. 1.8 m/s **b.** 4 m/s

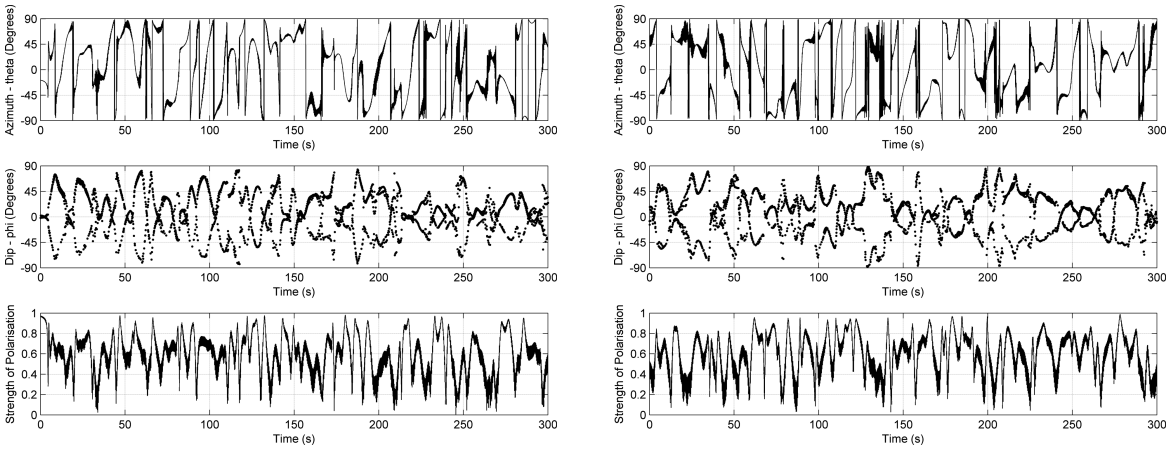

c. 7 m/s **d.** 11 m/s

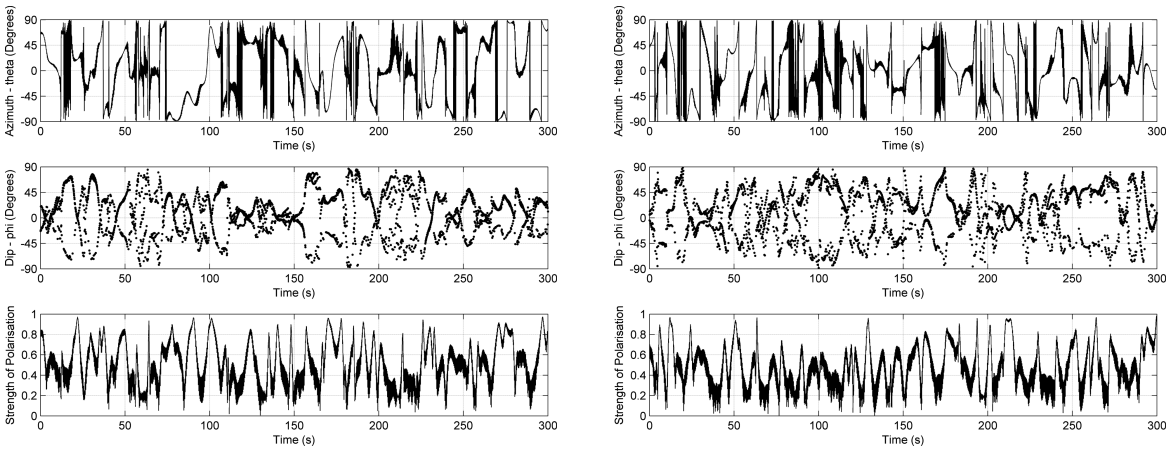

e. 15 m/s **f.** 17.5 m/s

Figure 6-27: *Polarisation analysis for data from the 6TD at Kilmarnock on the Proven 35-2 site between 6.5 and 6.7 Hz for a selection of wind speeds. A 0° azimuth and dip indicate a vector pointing horizontally in the direction of the wind turbine.*

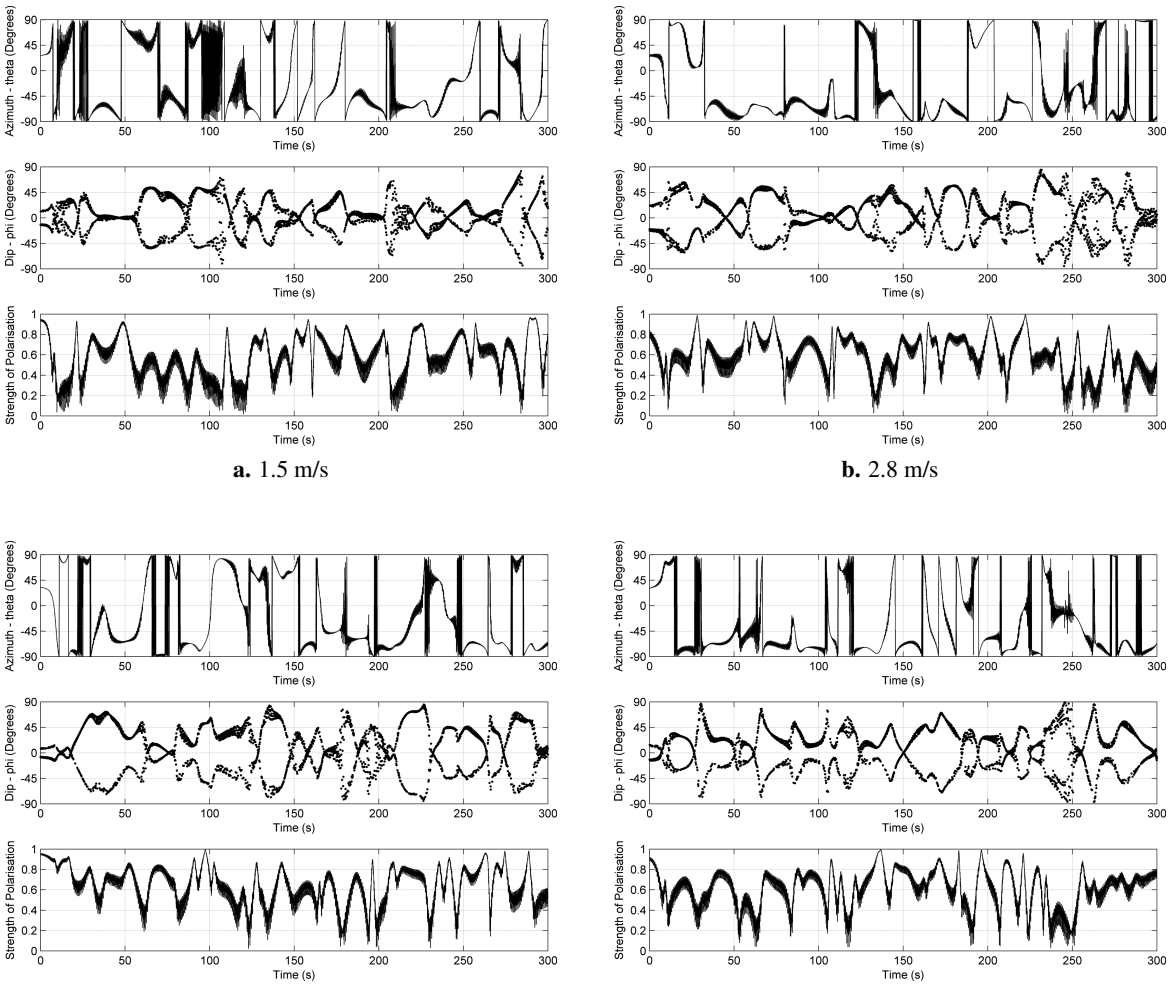

a. 1.5 m/s **b.** 2.8 m/s

c. 5 m/s **d.** 6.5 m/s

Figure 6-28: *Polarisation analysis for data from the 6TD at Hayle on the Endurance E-3120 site between 7.8 and 7.9 Hz for a selection of wind speeds. A 0° azimuth and dip indicate a vector pointing horizontally in the direction of the wind turbine.*

6.5 Discussion

This chapter has provided an analysis of the results of monitoring the four small wind turbines presented in chapter 5.

By comparing the results from the two tower types of the Gaia-Wind 133, it has been shown that tower structure does make a difference to the vibrations which are generated. On the tower, the lattice structure generates higher amplitudes at wind speeds less than 2.5 m/s and greater than 3.5 m/s, especially at frequencies above 10 Hz. Between 2.5 and 3.5 m/s, the period when the blades are rotating but the turbine is not generating, the opposite is true, with the amplitude from the tubular tower being a factor of 10 higher than the lattice tower. From measurements recorded in the ground, the tubular tower spectra consistently have an amplitude greater than the equivalent lattice tower measurements through all wind speeds.

The effect of wind speed on the seismic amplitude is different for both types of tower and indeed for each of the towers tested. However, the seismic amplitude on the foundation is directly proportional to the seismic amplitude on the tower for three out of four of the towers. For these same three towers, the seismic amplitude at 200 m is proportional to the seismic amplitude on the tower to the power of 0.25. The wind turbine which is an exception to this is the Gaia-Wind 133 tubular tower, however more testing is required to confirm the results for this turbine; as the wind speeds during the monitoring period only reached a maximum of 5.1 m/s while on-tower monitoring was operational. Table 6-2 provides a summary of the wind speed relationships which have been derived.

The polarisation analysis for the Gaia-Wind tubular tower turbine indicates that surface waves are predominantly generated at frequencies which are blade rotation rate harmonics (0.93 Hz, 1.867 Hz, 2.8 Hz, 3.73 Hz, 4.67 Hz, 5.6 Hz, 6.53 Hz, 7.47 Hz, 8.4 Hz, 9.33Hz, etc). Considering the azimuthal value of other frequencies present in the spectra with prominent peaks, there is a strong indication that they are generated along the line between the sensor and the turbine and are predominantly body waves.

The tower itself does not generate the waves in the strictest sense, as the power source for the waves is

generated by wind loading. Turbulent air created by the blade passing, combined with the rotational motion of the blades excites vibrations in the tower which are transferred into the ground creating seismic waves. However, in the same way that a clarinet generates a musical notes that is heard from it rather than assigning the music to the musicians breath, the turbine tower acts in the same capacity.

Vibrations of the tower are generated by direct broad-band, white-noise wind loading which stimulates the resonant modes of the tower. These are then coupled through the tower base into the ground as body waves and surface waves and propagate outwards with the azimuthal and amplitude variations described later in the multiphysics models (chapter 8). The difference in wave type between blade rotation rate and other frequencies is not seen in the three-blade Endurance or Proven analyses.

The sensors were located in the near-field of the seismic wave field, which is confirmed by the decay of the signal with distance at a power of r^{-1}, where r is the distance from the wind turbine. This has been shown for a range of prominent frequencies for each of the turbines (figure 6-14). However, the exception to this is the 4.2 Hz peak visible in the Gaia-Wind tubular tower data, which decays at a rate of $r^{-0.5}$, indicating that the sensors are probably located in the far-field of the source. Additionally, polarisation analysis indicates that the source is located 20° or 200° (due to a 180° ambiguity) to the direction of the wind turbine from the 6TD seismometer. This azimuth is close to the direction of Great Orton wind farm, 5 km NE of the wind turbine, this make of turbine has been shown to generate vibrations at this frequency (Styles et al. 2005, Schofield 2002).

Polarisation analysis of a particular frequency band can show that there are vibrations being generated from the wind turbine at that frequency which have peaks visible in the on-tower spectrum but not in the in-ground spectrum, as the amplitude of the peak is such that it is masked by background noise Alternatively polarisation analysis may suggest that some waves at particular frequencies originate from the wind turbine, where the frequency peak is prominent in the ground spectrum but not in the on-tower spectrum, eg 3-3.1 Hz at Kilmarnock. In this case, the frequency peaks in the on-tower spectrum may be masked by a broader peak or have originated on the tower at a different frequency and shifted during transfer from the tower to the ground.

Chapter 7

Multiphysics Modelling

The previous chapters have shown how vibrations from wind turbines can be characterised through monitoring. Multiphysics modelling, which will never replace the requirement for monitoring, can help characterise these vibrations further and enable the effects on the turbine and in the ground to be visualised. The modelling of a wind turbine can be performed in any multiphysics software capable of computing a frequency response and structural analysis of the eigenfrequencies of the model through finite element analysis (section 2.3). The modelling for this project was conducted in Comsol, as a licence had already been purchased for the software and it was capable of carrying out the required analysis. Further explanation on Comsol is provided in section 7.2.

Section 7.1 provides a review of literature which have used finite element analysis to model wind turbines or similar lattice structures. The results of the modelling and comparison with the monitored results is shown in chapter 8.

7.1 A Review of Related Work

The use of finite element analysis methods to analyse wind turbines is a large and developing field, with applications including

- Fatigue analysis (Sutherland 1999, Lacalle et al. 2011);

- Design optimisation of the tower (Lavassas et al. 2003, Uysa et al. 2007), blade design (Bechly & Clausen 1997, Jureczko et al. 2005, Paquette et al. 2006) and foundation design (AlHamaydeh & Hussian 2011);
- Wind loading response (Harikrishna et al. 1999, Savory et al. 2001);
- General vibrational and modal analysis (Lobitz 1981, Carne et al. 1982, Bazeos et al. 2002, Murtagh et al. 2004).

7.1.1 Vertical Axis Wind Turbines

Work was carried out in the early 1980s at the Sandia National Laboratories in the USA on the prediction of resonant frequencies from a vertical axis wind turbine (VAWT). A finite element method code, written in MSC-Nastran, was used for the dynamic analysis of a Darrieus VAWT and a Sandia 2-m variable speed VAWT. The method consisted of modelling the turbine in a reference frame which rotated at the same speed as the turbine. The theory is described in detail in Lobitz (1981) and Carne et al. (1982). The models of the VAWT were constructed using beam elements, with a mass placed on the top to represent the upper bearing and tie down connections, which were modelled as horizontal linear springs with a downward force applied to them. The rotor was defined as a solid mass.

Carne et al. (1982) refined the model using experimental data from a parked turbine, collected using accelerometers which were attached to the blades, tower and base (figure 7-1). By adjusting various parameters within the model, the average errors were reduced to less than 1%. The comparison between the experimental and modelled results is shown in figure 7-2. The two sets of data matched relatively well, especially for the lower modes. Mode 8, which relates to a symmetric 'butterfly' mode, is the only mode to have an error between the two sets of data greater than 1%. Carne et al. (1982) attribute this to inaccuracies in the model at the joint between the blade and the tower.

7.1.2 Horizontal Axis Wind Turbines

With the exception of the previous section, most of the work in this field is focused on the analysis of horizontal axis wind turbines, with particular emphasis on the blades or tower.

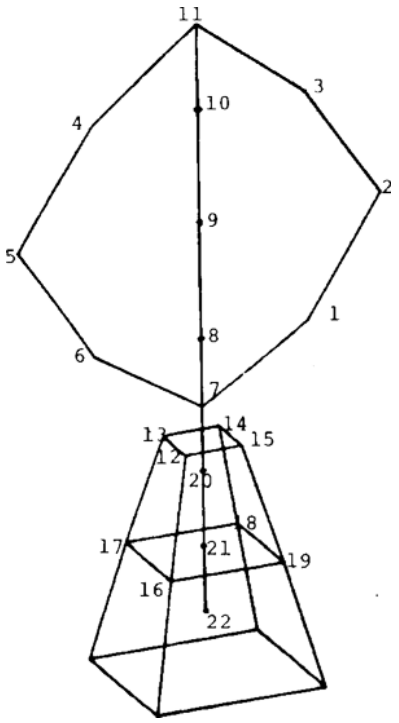

Figure 7-1: *Locations of the sensors on the parked Sandia 2-m VAWT (Carne et al. 1982).*

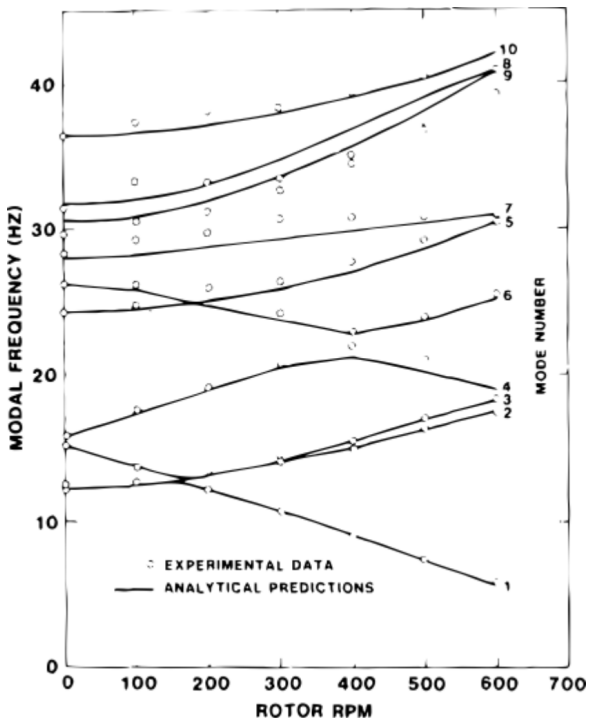

Figure 7-2: *Comparison of the predicted data from the Sandia 2-m model and the measured data (Carne et al. 1982).*

7.1.2.1 Tubular Towers

Tubular towers generally consist of two or three conical sections welded along the perimeter and which vary in diameter and wall thickness according to height. Each section is connected together using flanges, which are also used to connect the tower to the foundations. Modelling of a tubular tower has been included in studies by

- Bazeos et al. (2002), who considered a 38 m steel tower for a prototype 450 kw turbine developed in Greece;
- Lavassas et al. (2003), who modelled a prototype 1 MW wind turbine also from Greece, with a tower height of 44.075 m;
- Lacalle et al. (2011), who use FE methods to study cracks in a tower;
- Marmo & Carruthers (2010), who modelled a tower and rotor to locate the source of excessive tonal noises emitted from a 1 MW turbine.

Bazeos et al. (2002) modelled a turbine under two types of static loads, one simulating gravity, which was applied to the top of the tower to represent the weight of the nacelle and the tower itself. The other had an aerodynamic load concentrated at the top of the tower, simulating wind resistance and the operation of the turbine. The values of the loads applied to the tower are shown in table 7-1.

	Aerodynamic loading (wind velocity = 25m/s)	Gravity and mass loading
F_x (kN)	75.87	-
F_y (kN)	-0.23	-
F_z (kN)	-226.25	236
M_x (kN)	161.29	-
M_y (kN)	-95.4	-
M_z (kN)	4.88	-

Table 7-1: *Loads on a 38m prototype tower. For aerodynamic loads, the x-axis is horizontal in the direction of the wind and the z-axis is vertical up. For loads due to gravity there is a -0.75 m eccentricity along the x-axis. The weight of the tower ($78500N/m^3$) is spread out along its height. (After Bazeos et al. 2002).*

The model was defined directly as a mesh, with the shell wall constructed from quadrilateral elements. Trapezoidal elements were applied on the tower around the flange connections, which were made from solid hexahedrals. In total the model consisted of 3763 elements with a total of 69,186 degrees of freedom. Finite element modelling, using MSC-Nastran software, was used to perform a variety of analyses, including a fixed-base analysis, where as the name suggests, the boundary conditions on the base of the tower were defined as fixed. The first four bending modes of the tower obtained with the fixed-base analysis are shown in figure 7-3. For static and buckling analyses, Bazeos et al. (2002) find that a refined finite element model is required, due to the high degree of accuracy which is necessary for these analyses. An accurate seismic analysis can be obtained using approximate numerical models.

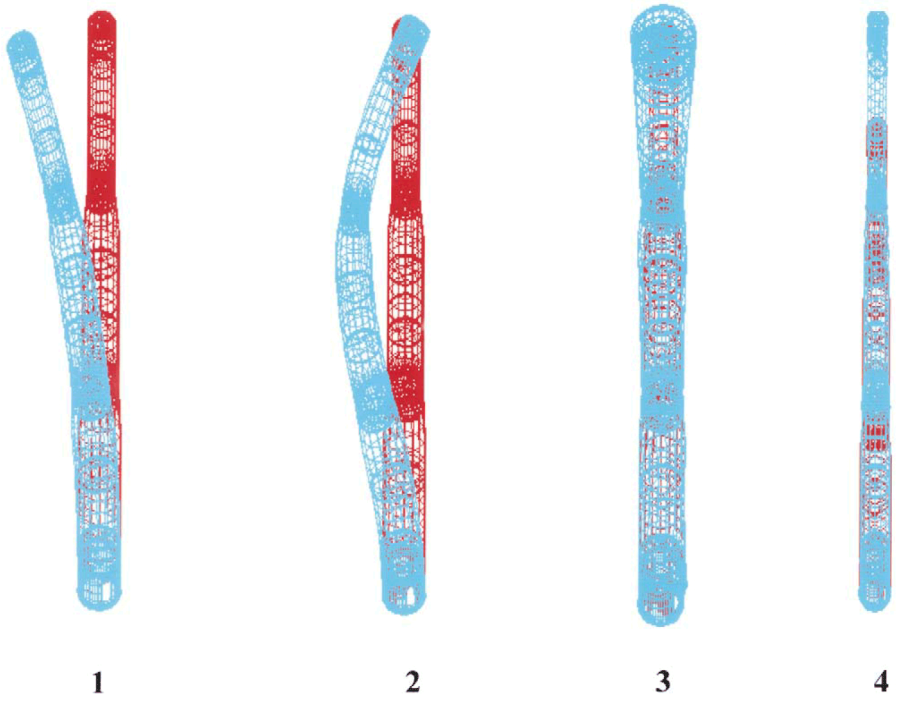

Figure 7-3: *First four modes of the 38m prototype tower. Eigenvalues from left to right are 0.937Hz, 7.4Hz, 14.631Hz and 18.984Hz (Bazeos et al. 2002).*

The tower modelled by Lavassas et al. (2003) was constructed from only two sections, connected together with internal flanges. Two models were investigated (figure 7-4), the first involved just the tower and consisted of a total of 5208 quadrilateral shell elements. The boundary conditions applied to this model defined the base edge as fixed. The second model incorporated the foundations in addition to the tower and consisted of 3270 hexahedral and tetrahedral solid elements as well as the tower shell elements. The boundary conditions described the contact of the foundations with the

ground elastically. Gravity loads, representing the weight of the tower, wind pressure and earthquake loading, were applied to the model. Finite element analysis was performed using Strand7 software. Lavassas et al. (2003) concluded that the predominant load combination comes from extreme winds unless the turbine is to be sited in a seismically active and hazardous area. In terms of fatigue analysis, the design of the tower should be influenced by the dynamic characteristics of the turbine as a whole.

Finite element analysis is being used increasingly for fatigue analysis of wind turbines. Sutherland (1999) examined bending loads on a bond joint and created both a 2D and 3D model to analyse peel stress on the structure. More recently, Lacalle et al. (2011) used a finite element model of the cracked section of a tower, to look at the stresses on a welded joint, as cracks had appeared in the joints between the lower section of a turbine and the flange connecting the tower to the foundations. The simulation was performed in ANSYS under stresses of 10, 50, 100 and 200 MPa, where it was found that high stress concentrations are located on the inner part of the tower due to the profile of the weld joint and a differences in the thickness of the materials used for the tower and flange.

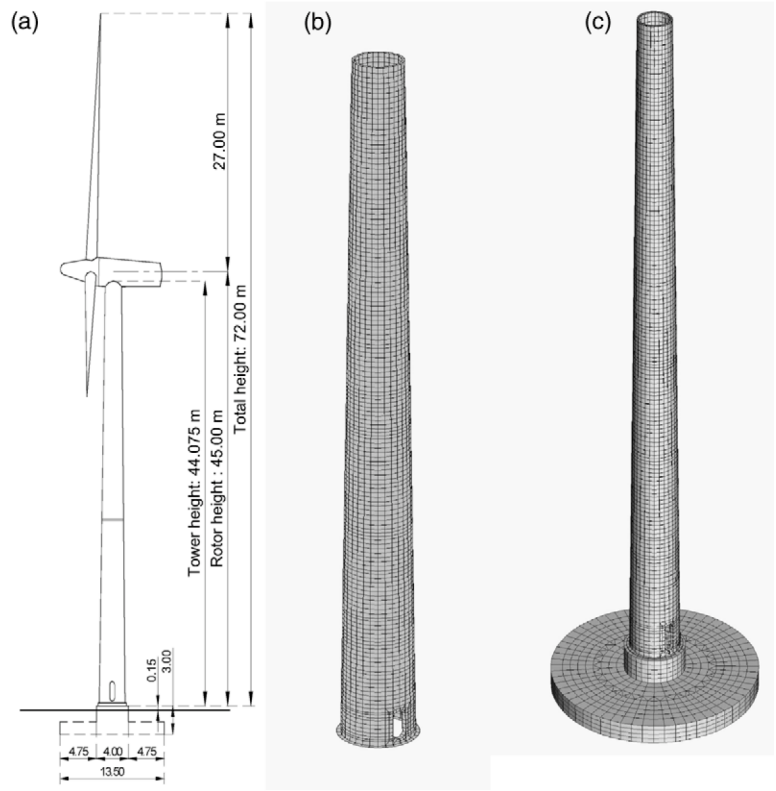

Figure 7-4: *The wind turbine dimensions and meshed models of a 44m tower used for a finite element analysis (Lavassas et al. 2003).*

7.1.2.2 Lattice Towers

Lattice towers were popular on early turbines, although it was found that they were more prone to corrosion and wind excitation than their tubular equivalents due to the exposure of the structure to the weather (Ciang et al. 2008). Consequenctly, there is little previous published work using finite element analysis on lattice tower wind turbine structures.

Due to their design, lattice towers can prove a bigger challenge to model using finite elements than tubular towers. Murtagh et al. (2004) compare two methods for obtaining the natural frequencies of the tower. These two models were compared these for accuracy with an FEA model. The first method is similar to the one applied by Bazeos et al. (2002) and Lavassas et al. (2003), described in section 7.1.2.1, where the tower was modelled with a mass weight on the top, reducing the computational complexity of the model. The second method modelled the tower as a cantilever beam with a mass at the free end, and concentrated on the fundamental bending mode only. The FEA was performed in ANSYS using a 20 degree of freedom model constructed from truss elements, meaning that each element has only two degrees of freedom at each node. Comparison of the two alternative methods with the FEA results showed that all three methods produce very similar results for the natural frequency (figure 7-5) and fundamental frequency values respectively.

Savory et al. (2001) have modelled a lattice transmission tower (CEGB type Blaw Knox L6, with a standard height of 50.5m) using ABAQUS to investigate the effects of a tornado and wind loading on the structure. The principles used may be applicable to wind turbine lattice towers. Each element of the tower was modelled using a three-dimensional beam element, with a minimal torsional stiffness applied at each end to simulate the pinning of the elements in the actual structure. Mass damping was applied to the tower at time zero to damp any initial vibration in the model. Three wind loads were applied to the model to assess the response. Figure 7-6 shows the shape of the tower upon failure under a tornado equivalent wind load, where the shear force from the turbine creates compression in some of the horizontal supports of the tower, causing them to buckle.

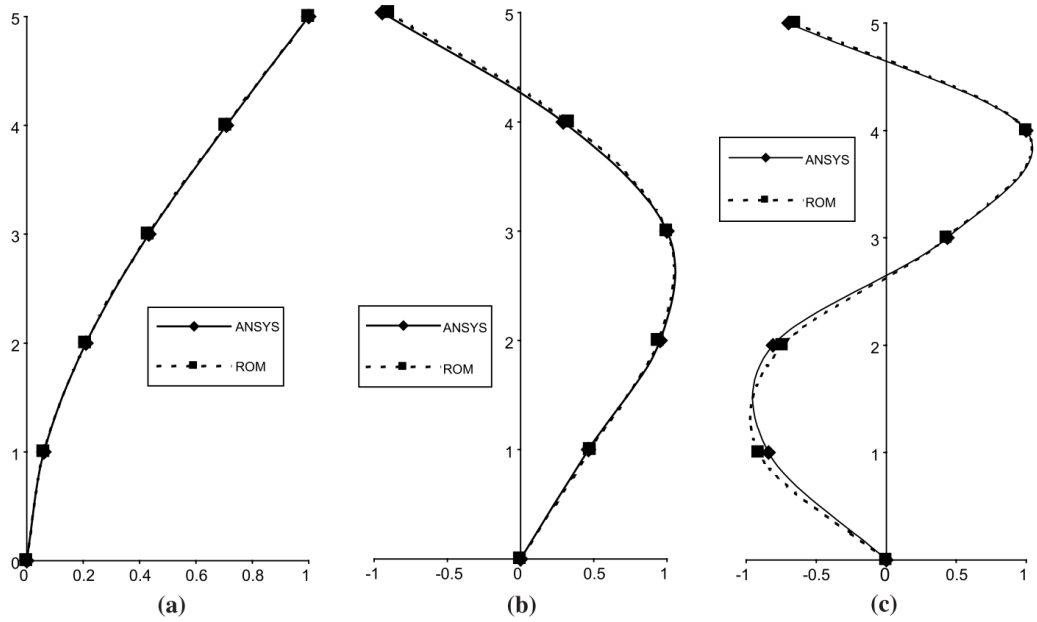

Figure 7-5: *Comparison of FEA with the reduced complexity order model for (a) the first bending mode, (b) the second bending mode and (c) the third bending mode (Murtagh et al. 2004).*

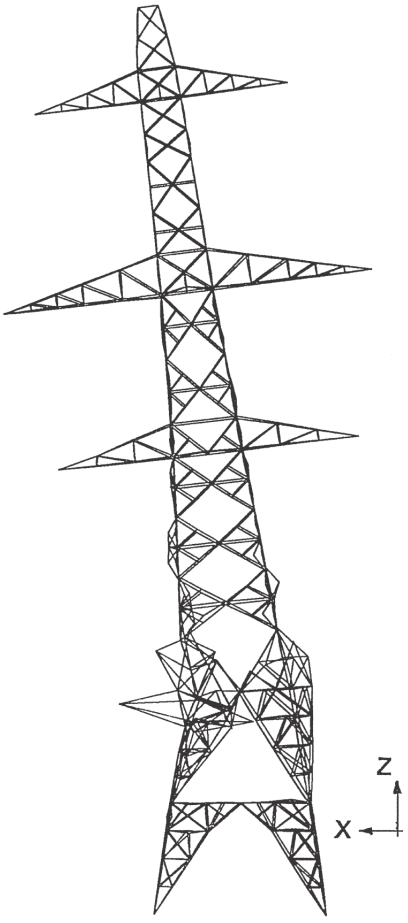

Figure 7-6: *The lattice transmission tower modelled by Savory et al. (2001) buckling under a tornado wind load*

7.1.3 Summary

Finite element modelling of wind turbines has become increasingly popular over recent years and is used for a range of techniques including fatigue analysis, vibration and modal analysis and design optimisation. Most of this work is focused on horizontal-axis wind turbines. However, the Sandia Laboratories have conducted experiments and generated models of vertical-axis wind turbines. Indeed in the 1980s they were amongst the first to work on finite element modelling of wind turbines.

Lavassas et al. (2003) and Bazeos et al. (2002) both modelled tubular towers using tetrahedral shell elements. Bazeos et al. (2002) found that for different analyses, different mesh refinements were required. Lattice towers are not as popular as their tubular equivalents and as such there is not as much literature on the finite element modelling of such structures. The lattice structure makes finite element modelling much more challenging than a tubular tower. Murtagh et al. (2004) overcome this issue by simplifying the structure so that it contains only 20 degrees of freedom. Their results look promising, however the model has not been compared to field data. Savory et al. (2001) used a more complex model of a lattice transmission tower. They used three dimensional beam elements, with torsion and stiffness properties applied to each element. This makes the model much more realistic, however the complexity increases compared to the approach by Murtagh et al. (2004).

7.2 Comsol

Comsol is a multiphysics modelling software package which provides an interface for mathematically modelling and solving scientific and engineering problems, including those related to geophysics, which are based on partial differential equations (PDEs). The software contains different application modes, which can be coupled together to create complex models. By using these modes, the underlying PDEs do not have to be defined explicitly, instead the user inputs physical values such as material properties, constraints and loads dependent on the application modes in use.

The process of modelling a wind turbine is iterative and consists of four phases (figure 7-7). First, the geometry is created and material properties and boundary conditions applied. Then the mesh is applied to the structure, before an eigenfrequency analysis can be performed. The results of the model are finally compared to field measurements in order to verify the model. The model is subsequently refined to achieve a better correlation with the results (Westwood et al. 2011).

At the time of writing, the current version of Comsol is 4.2a, however the models described in this thesis are created using version 3.5a, which was the current version at the start of the project.

The model geometry can be imported into Comsol from external computer-aided design (CAD) software packages or generated using the built-in CAD tool. Multiphysics modelling requires a balance between complexity and accuracy; the more complex the model, the more processing power and time it will take to compute a solution. For example, it is not necessary to model individual nuts and bolts or the internal workings of the nacelle, if the model is looking at the overall turbine. If the model was to examine fatigue in a certain area of the turbine, then it may be necessary to model to a higher degree of detail.

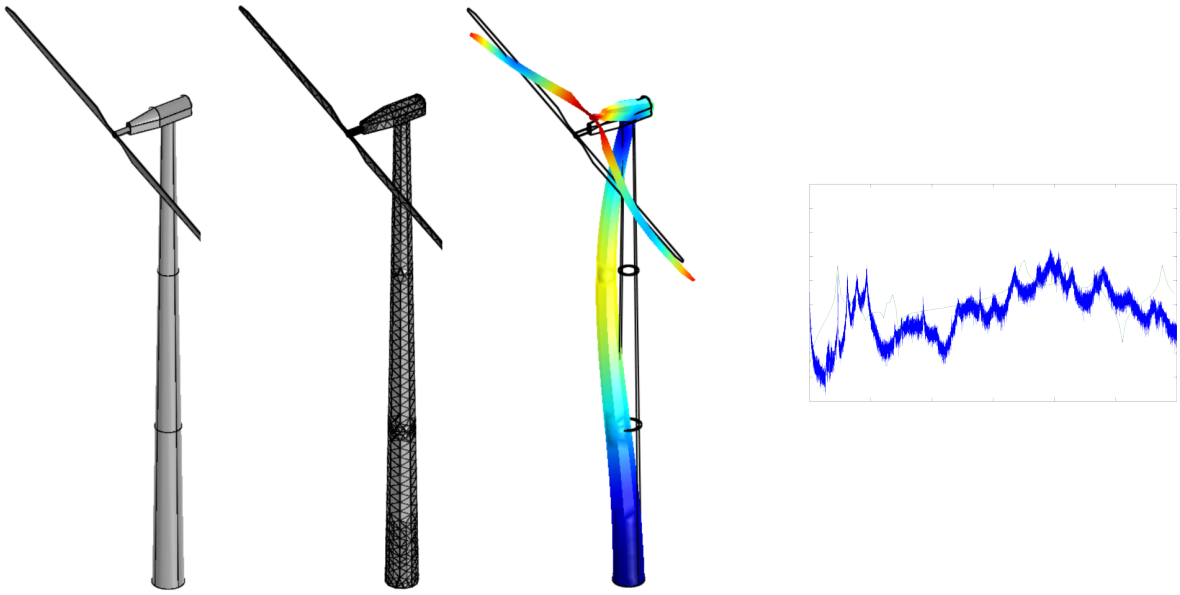

Figure 7-7: *The four phases involved in the finite element modelling of a small wind turbine. From left to right: 1. Creating the geometry and assigning boundary conditions; 2. applying the mesh; 3. running an eigenfrequency analysis; 4. comparing model results with the monitored data (Westwood et al. 2011)*

The modelling work described in this thesis makes use of the Structural Mechanics Module. The module uses specialist elements, including solids, shells, trusses and Euler beams to solve problems related to solid and structural mechanics (Comsol Multiphysics 2008c). It contains a set of application modes which can perform static, eigenfrequency, damped eigenfrequency, parametric, frequency response, transient and quasi-static transient analyses (figure 7-8).

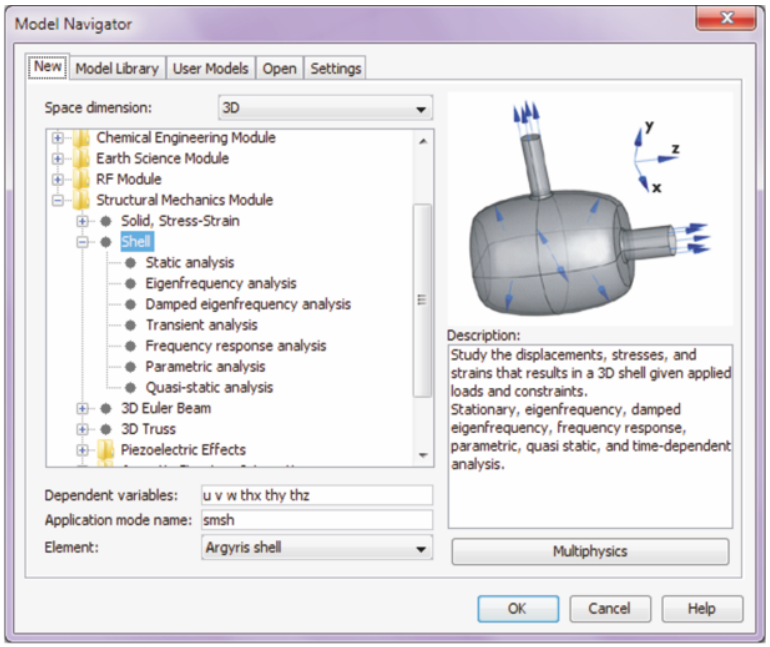

Figure 7-8: *The application modes available within the Structural Mechanics Module in Comsol 3.5a*

7.2.1 Structural Mechanics Modelling

Modelling a wind turbine in Comsol requires knowledge of the dimensions and materials of the turbine, especially the tower. The resonant frequencies can change, simply by adding or removing flanges or changing the type of material the tower is constructed from. Figure 7-9 shows frequency spectra for four models which differ only in the material of the tower. It can be seen that by changing to alternative material from steel, the large peak visible at 5 Hz on the steel tower has been damped and shifted down in frequency. The overall amplitude of the acceleration is lowest for the concrete model. In order to obtain a precise model, as much information as possible about the structure is required.

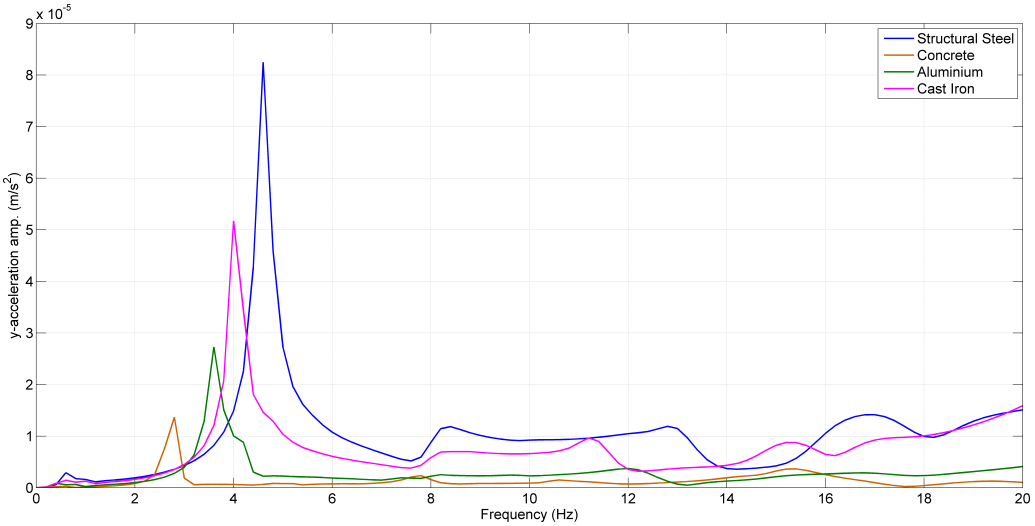

Figure 7-9: *An example of how changing the material of a wind turbine tower affects the vibrational characteristics*

Generally, wind turbine towers are hollow tubular structures (an exception would be a lattice tower). The simplest way to model these is by using shell elements. Bars, cables and the cross-beams of the lattice structure are modelled using truss elements. The foundation of the turbine and surrounding ground are solid and modelled either as a 2D plane with a thickness or with 3D solid stress-strain elements. All of which are contained within the Structural Mechanics module.

When using any of these elements, it is necessary to define the density (ρ), Young's modulus (E) (see section 2.2.4) and Poisson's ratio (ν) (see section 2.2.3). On shells and solids these are defined as boundary conditions and on trusses they are edge settings. Comsol contains a library of common materials and their properties, which can be added to for use in multiple models. In addition to these elastic properties, the shell element also requires definition of a thickness and trusses and beams a cross-section area. Rayleigh damping parameters for mass (α_{dM}) and stiffness (β_{dK}) can be applied to solids, shells and beams.

Constraints on the model can be defined on faces, edges and points. A constraint specifies the amount of displacement and rotation on a part of the shell. This is particularly useful if the model is symmetrical as it may only be necessary to define half or even a quarter of the model (figure 7-10). When choosing the correct constraint it is important to define the loads on the model (the application of forces and moments). Although, with a symmetrical geometry, it is possible to have asymmetrical loading, in which case the constraint would have to be defined as *antisymmetrical*. Loads can be applied to points, edges and boundary faces.

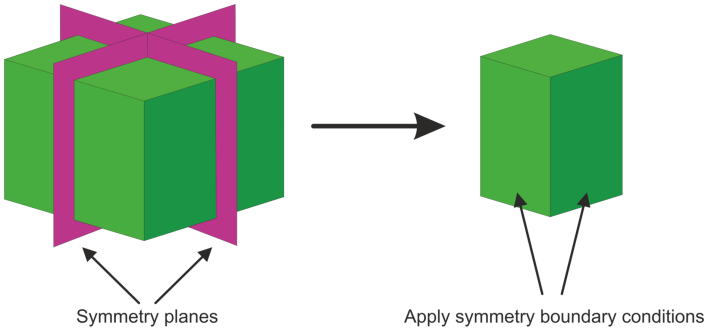

Figure 7-10: *An illustration of how symmetry plane constraints can be used to simplify models (After Comsol Multiphysics 2008c).*

When modelling a wind turbine, if the foundation is included in the model, then loads on the external faces should represent interaction with the surrounding ground. Similarly, if the foundation is not included, the base edge of the turbine, should represent the interaction with the foundation. This can be achieved using Hooke's Law (section 2.2). Forces acting on the blades and tower (section 2.5) which are generated by the wind are represented by loads on the relevant element (eg blades).

Truss elements can only be applied to edges and support axial forces which determine the amount of rotation and movement of the element. Damping parameters can be specified for each of the element types. The options available are no damping, Rayleigh and loss factor. If selecting Rayleigh, damping factors for mass (α_{dM}) and stiffness (β_{dK}) should be defined.

Chapter 8

Comsol Models of Two Small Turbines

This chapter describes the finite element modelling, using Comsol multiphysics software, of the two tower types of the Gaia-Wind 133 11 kW wind turbine, which are described at the start of sections 5.1 and 5.2.

An explanation of the models, the parameters they require and the stages of development are explained in sections 8.1 to 8.4. The results of the modelling are presented in section 8.5 and the findings discussed further in section 8.6.

8.1 Model Development

The Gaia-Wind 133 wind turbine is available with a choice of either a lattice or tubular tower type, however the nacelle and blades are identical irrespective of the choice. This simplifies the modelling process, as the same geometries and boundary conditions for the nacelle and blades can be used in each model. Simplifications have been made when creating the models in order to reduce complexity and therefore the computing power and time required to calculate eigenfrequencies and perform a frequency response analysis. The ladder, maintenance platform and internal workings in the nacelle and tower are not included in the model, as their mass is not large enough to significantly affect the resonant frequencies of the tower.

The models are developed in stages from a simple hammerhead model containing the tower (and flanges) with a mass on top; through adding the blades and foundation to a full model with the surrounding ground and bedrock. Figures 8-1 and 8-2 show each model phase prior to adding the surrounding ground. Constructing models in this way enables the changes in the resonant modes of the tower, by adding or changing components, to be investigated and visualised.

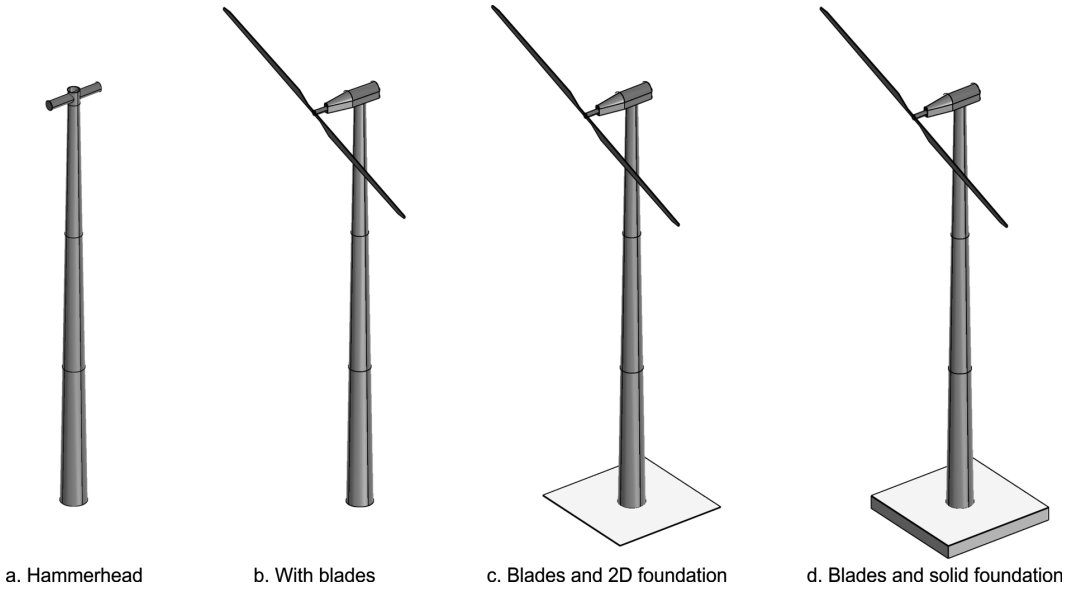

Figure 8-1: *The models of the Gaia-Wind tubular tower turbines prior to including soil and bedrock*

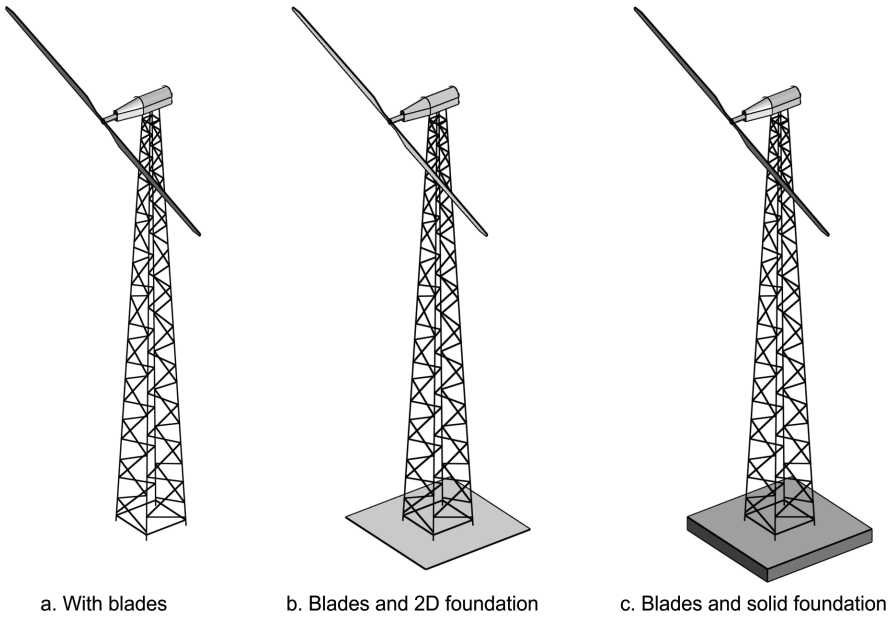

Figure 8-2: *The models of the Gaia-Wind lattice tower turbines prior to including soil and bedrock*

8.2 Material Properties and Boundary Conditions

Each component of the model is constructed from either a shell, 3D truss or solid element. The nacelle and tubular tower are constructed from shell elements and the cross-section braces and uprights of the lattice tower from 3D truss elements. In Comsol, a 3D truss is defined as a solid tube. This means that it is not a completely accurate representation of each brace as they are actually L-shape solid entities. However, it is a relatively good approximation and reduces the solving time and computational complexity of the model. An alternative design technique would involve constructing the tower from individual solid L-shaped components. This option was attempted; however, due to the complexity of the model there were issues with meshing and solving.

The blades of the wind turbine are constructed from fibre glass and have a length of 6.5 m. Besides this, the only other information known about the design of the nacelle and blades is that they have a combined mass of 900 kg (Gaia-Wind, pers. comm.), with 700 kg of this being attributed to the nacelle (Gaia-Wind Ltd 2008). Wind turbine manufacturers are very cautious about the information they release, especially with respect to the blades. This means that the shape and thickness of the blades (and the nacelle) have to be approximated from photos and basic drawings provided by Gaia-Wind.

The turbines are constructed from steel and the tower defined using the values from Comsol's material library. The material properties for the nacelle also use the values of Young's modulus and Poisson's ratio for steel, however the density is calculated from the known mass of the nacelle, area of the nacelle in the model and a given thickness using the equation

$$\text{density} = \text{mass}/(\text{model\_area} * \text{thickness}). \tag{8.1}$$

The most basic model of the tubular tower wind turbine approximates the detail of the nacelle by defining the wind turbine purely as a tower with a hammerhead on it (figure 8-1a). The tower is constructed in three sections using shell elements, making a tapered hollow tube which is assigned the material properties for structural steel from the Comsol materials library, with a thickness of 6 mm. The sections are connected by two flanges which also increases the rigidity of the structure. When calculating the density of the nacelle (the hammerhead) using equation (8.1), the mass should

equate to the sum of the nacelle and blades.

For the models which do not contain a foundation, Hooke's law is defined on the base edge of the tubular tower (figure 8-3a) and the feet of the lattice (figure 8-3b). This represents the interaction of the tower with the concrete foundation.

When the foundation is added to the model, it is initially represented by a square plate in the x-y plane with sides of length 5 m, a thickness of 0.55 m and the material properties for concrete. This is a simplification of the actual foundations, but speeds up the calculations as the square can be defined using a shell element. The boundary settings placed on the base edge or feet are removed and Hooke's law defined on the edges of the foundation, to represent interaction with the surrounding soil. The solid foundation has the same dimensions in the x-y plane; however it has been extruded down to a depth of 0.55 m. Hooke's law is applied to all boundaries except the top to define the interaction with the surrounding soil or bedrock. The solid, stress-strain application mode must be added to the model and the boundaries of the foundation defined as 'not active' in the shell application mode so that calculations will only be performed on the foundation as a solid entity. The subdomain of the foundation is defined as concrete, using Comsol's built-in values from the Material Library.

The models each contain a collection of constants and expressions shown in table 8-1. They are used to control the forces acting on the wind turbine and the material properties of the structure.

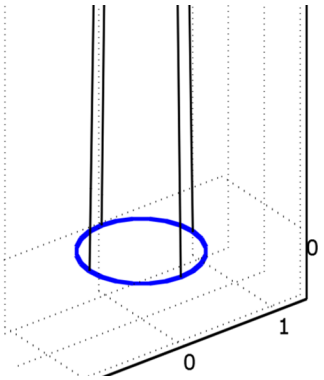

a. The tubular tower has Hooke's Law applied to the base edge

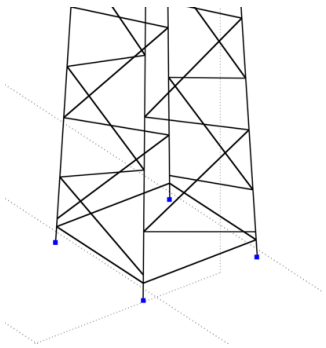

b. The lattice tower has Hooke's Law applied to bottom of the feet

Figure 8-3: *The edges/points on which Hooke's Law is defined for models which do not include the foundation*

Name	Description	Model
Turbine Properties		
n_mass	Mass of the nacelle	both
n_area	Area of the nacelle	both
n_density	Density of the nacelle = n_mass/(n_area*n_thick)	both
n_thick	Thickness of the nacelle	both
n_back_area	Area of the back of the nacelle	both
b_mass	Mass of the blades	both
b_area	Area of the blades	both
b_density	Density of the blades	both
b_thick	Thickness of the blades	both
f_thick	Thickness of the flanges	tubular
t_mass	Mass of the tower	lattice
t_length	Length of the tower	lattice
t_xsection	Cross section area of the tower	lattice
t_density	Density of the tower	lattice
Ground Properties		
concrete_ym	Young's modulus of concrete	both
concrete_pr	Poisson ratio of concrete	both
concrete_sw	Specific weight of concrete	both
concrete_sm	Shear modulus of concrete	both
concrete_density	Density of concrete	both
soil_ym	Young's modulus of soil	both
soil_pr	Poisson ratio of soil	both
soil_sw	Specific weight of soil	both
soil_lambda	$\gamma/(1-\gamma)$ of soil	both
soil_density	Density of soil	both
Load Properties		
z_hub	Height of hub (reference height)	both
v_ref	Reference wind velocity	both
rho	Density of air	both
c	Thrust coefficient	both
g	Acceleration due to gravity	both
z0	Surface roughness	both

Table 8-1: *The constants which are defined for each of the Gaia models*

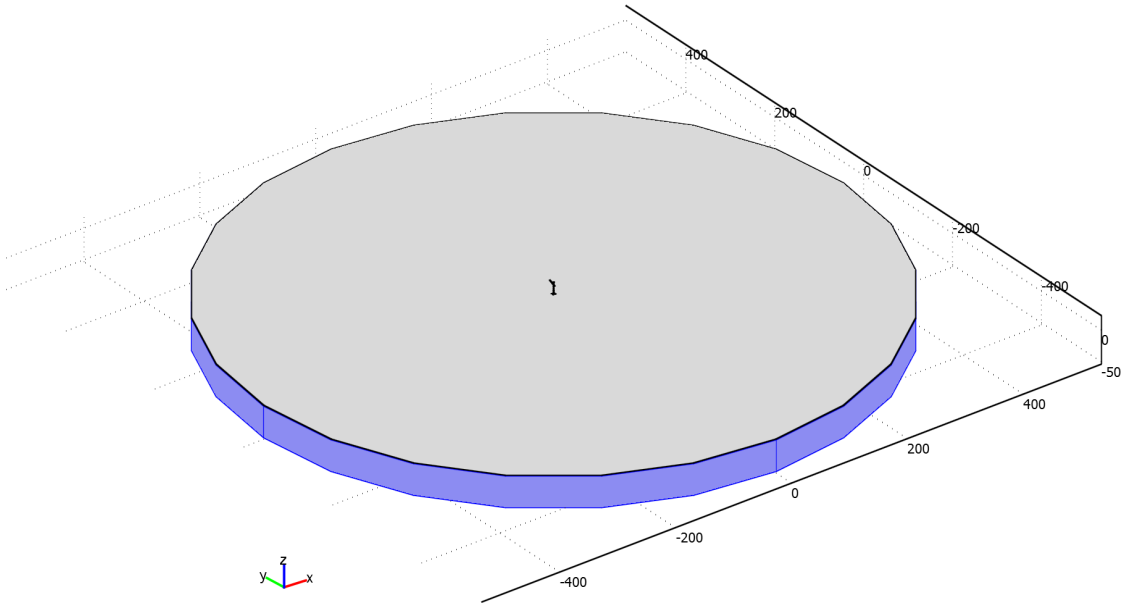

Figure 8-4: *The boundaries which have a roller constraint applied to them (shown with the blue highlight)*

Gravitational forces are applied to the nacelle and to the blades, in addition to aerodynamic loading, which uses the equations described in section 2.5.3.

Comsol contains multiple boundary constraints. For the turbine itself, this is set to *free*, meaning that the boundary is completely unconstrained. However, when the surrounding ground is added the edges are set to *roller* (figure 8-4). This means that displacement is constrained in the normal direction and that the waves cannot rebound off the boundary, as the edge should be continuous and not representative of a physical boundary in the ground.

8.3 Geology of the Surrounding Ground

The ground surrounding each of the wind turbines is modelled in three ways; bedrock and soil, just soil and just bedrock. Both soil and bedrock are modelled as a cylinder with a radius of 500 m. The sides of the cylinder have a roller boundary applied to prevent reflection of the waves. When modelling only the soil, the bottom of the cylinder has Hooke's Law applied to represent the interaction with the bedrock at the location of the monitoring site. When bedrock is a base layer, the bottom edge is defined with a roller boundary. The soil layer is modelled as a 1 m thick cylinder and represents the top layer of soil in which the sensors are placed when monitoring the turbine. When this layer is not included in the model, the bedrock interacts directly with the foundations. The aim of these three

models is to determine whether adding a top layer of soil makes a substantial difference to the results and their accuracy.

The bedrock underlying the site of the tubular tower at Wigton is the Mercia Mudstone Group (MMG) of Triassic age. Hobb et al. (2002) describe an extensive study to discover the engineering properties of the mudstone. Based on their findings, three additional constants for the engineering properties of the rock are added to the tubular model (table 8-2).

The geology underlying the site of the lattice tower near Melrose is that of the Gala Group and Hawick Group, which is a greywacke of Silurian age. This is similar to the geology at Eskdalemuir. The same engineering properties as those for the greywacke at Eskdalemuir (Marmo & Buckingham 2011) are added to the lattice model (table 8-3).

Name	Value	Description
merciaMS_ym	42[MPa]	Young's modulus of the MMG
merciaMS_pr	0.2	Poisson's ratio of the MMG
merciaMS_density	2470[kg/mˆ3]	Density of the MMG

Table 8-2: *The engineering properties for the Mercia Mudstone Group*

Name	Value	Description
greywacke_ym	16[GPa]	Young's modulus of greywacke
greywacke_pr	0.25	Poisson's ratio of greywacke
greywacke_density	2500[kg/mˆ3]	Density of greywacke

Table 8-3: *The engineering properties for greywacke*

8.4 Meshing

The models shown in figures 8-1 and 8-2 are meshed automatically with the Comsol predefined Normal mesh size. When the ground is included, interactive meshing is required to ensure that the mesh is fine enough to produce accurate results, but coarse enough to be able to be solved with limited processing capacity. Figure 8-5 shows the resultant meshed 'no foundation' model for the two tower types and a model with the soil and bedrock included.

Table 8-4 provides the mesh statistics for each of the tubular tower models and shows how the complexity of the model increases substantially with the addition of the solid, stress strain application

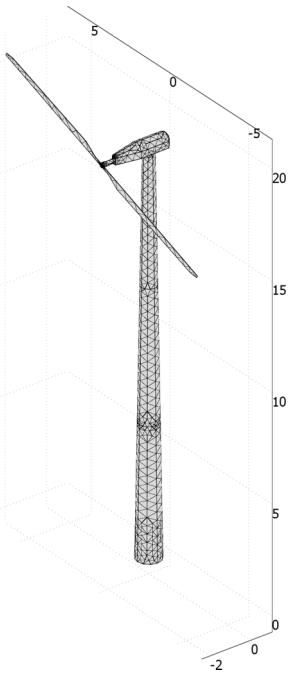

a. Tubular ‘no foundation’

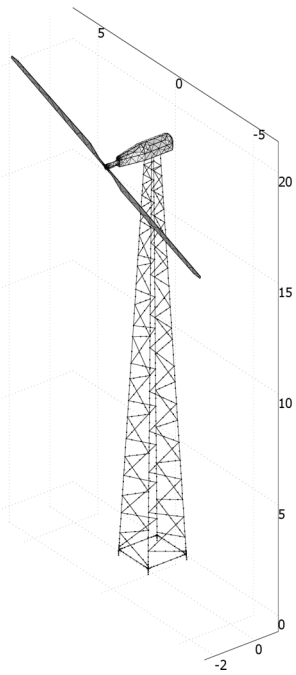

b. Lattice ‘no foundation’

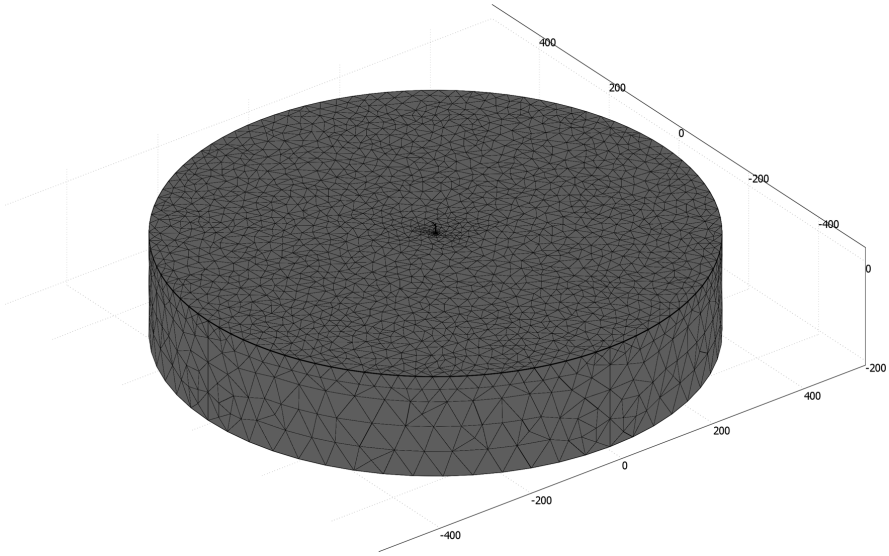

c. Tubular ‘soil and bedrock’

Figure 8-5: *Meshed models*

mode for the solid foundation and again once the ground is included. Table 8-5 provides the equivalent information for the lattice tower models. The reasons for not expanding the lattice models to include the ground are explained in section 8.5.3.

Model	degrees of freedom	mesh points	number of elements			
			tetrahedral	triangular	edge	vertex
Hammerhead	5790	965	0	1942	404	52
No foundation	5430	905	0	1747	510	77
Simple foundation	5940	990	0	1913	526	81
Solid foundation	8682	1125	471	2203	569	85
Soil only	279606	15961	45956	31806	900	98
Bedrock only	125931	6574	26981	6005	732	100
Soil and bedrock	186072	8724	41838	9439	609	112

Table 8-4: *The mesh statistics for each of the tubular tower models*

Model	degrees of freedom	mesh points	number of elements			
			tetrahedral	triangular	edge	vertex
No foundation	3129	735	0	559	745	161
Simple foundation	3948	824	0	905	674	165
Solid foundation	15 651	1573	2114	1857	900	169

Table 8-5: *The mesh statistics for each of the lattice tower models*

8.5 Results

8.5.1 The Blade Angle

The eigenfrequency analysis and frequency response analysis of a wind turbine model in Comsol are performed on a static model, where the blades are fixed at a rotation angle about the x-axis. For the models described earlier in this section, the blades were rotated at an angle of 20 degrees from the horizontal.

In order to investigate whether the rotation angle affects the resonant frequencies, the blades were positioned horizontally and an eigenfrequency analysis performed, after which the bending mode frequencies are recorded. The blades are rotated 10° (figure 8-6) and the analysis repeated. This is performed for all rotation angles between -90° and 90°.

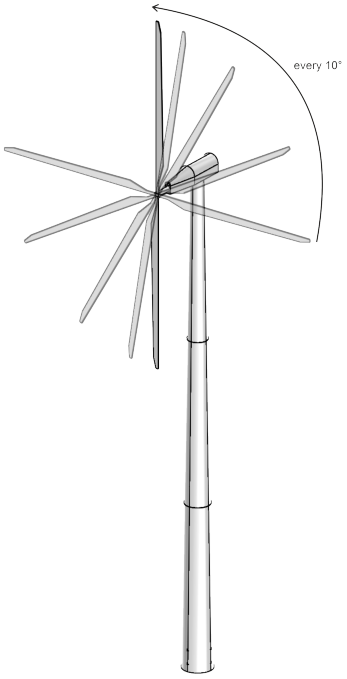

Figure 8-6: *Example of various blade positions for testing the variation of resonant frequency with blade angle*

The graph in figure 8-7 shows the resultant first and second bending mode frequencies after rotating the blades through intervals of 10 degrees.

Both of the first bending modes appear close to linear, but the second bending modes display a sinusoidal affect with a 90 degree period and are symmetrical about $0°$. The maximum amplitude difference is 1 Hz. Therefore when comparing the modelled data to the measured data, this should be kept in mind.

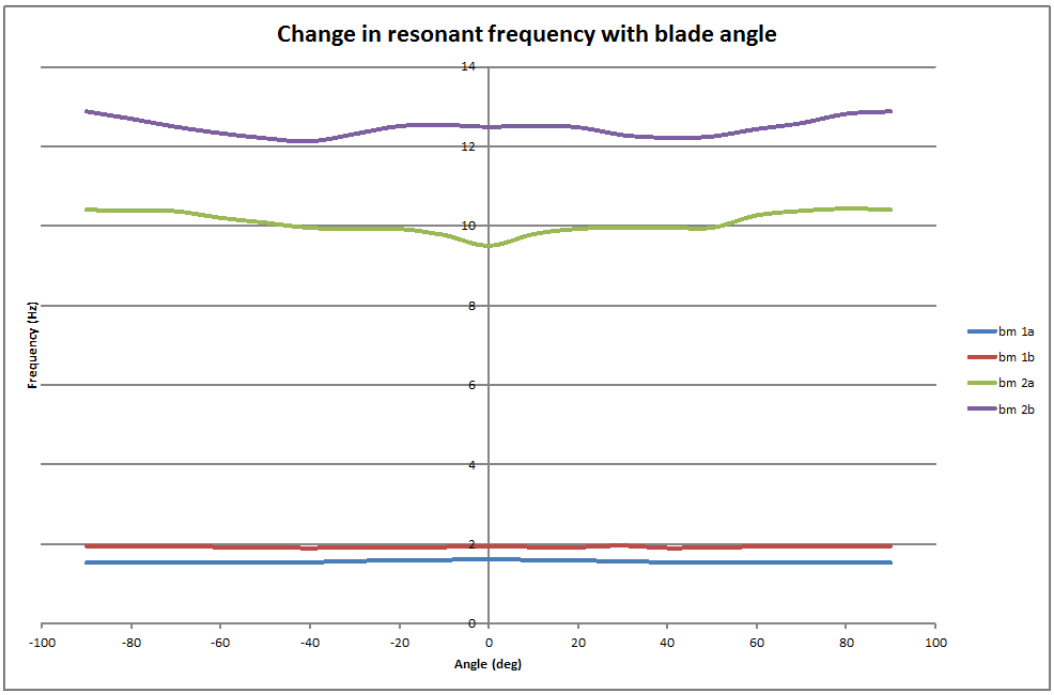

Figure 8-7: *Change in resonant frequency for the first and second bending mode of the Gaia tubular tower wind turbine dependent on the rotation angle of the blades*

8.5.2 Eigenfrequency Analysis to Calculate the Resonant Modes

The models for each turbine have an eigenfrequency analysis performed on each prior to adding the surrounding ground. The eigenfrequency analysis enables the resonant modes of the tower to be calculated and visualised. A tubular tower generally has two 1st bending modes, where the turbine bends about one node and two second bending modes, where the turbine bends about two nodes. Additionally, there may be a torsional mode, depending upon the design of the turbine. This is where the turbine appears to twist or yaw. Examples of the modes are shown in figures 8-8 to 8-10 using the hammerhead model. Table 8-6 shows the frequencies at which the 1st and 2nd bending modes occur for each of the models (images showing the modes for each model can be found in appendix B).

Model	1st bending mode		2nd bending mode	
Hammerhead	1.799 Hz	1.805 Hz	10.433 Hz	10.649 Hz
No foundation	1.578 Hz	1.911 Hz	9.836 Hz	12.386 Hz
Simple foundation	1.507 Hz	1.821 Hz	9.234 Hz	11.371 Hz
Solid foundation	1.556 Hz	1.888 Hz	9.73 Hz	11.647 Hz

Table 8-6: *The calculated eigenfrequencies of the Gaia-Wind tubular tower models*

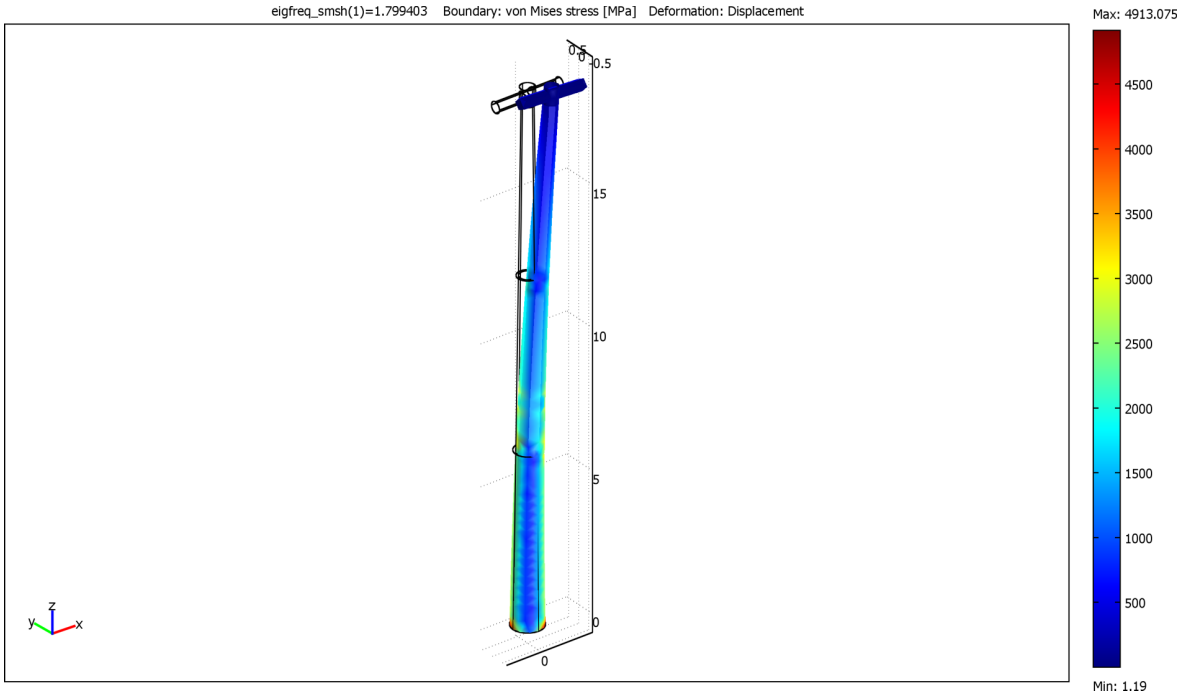

a. 1st bending mode a at 1.799 Hz

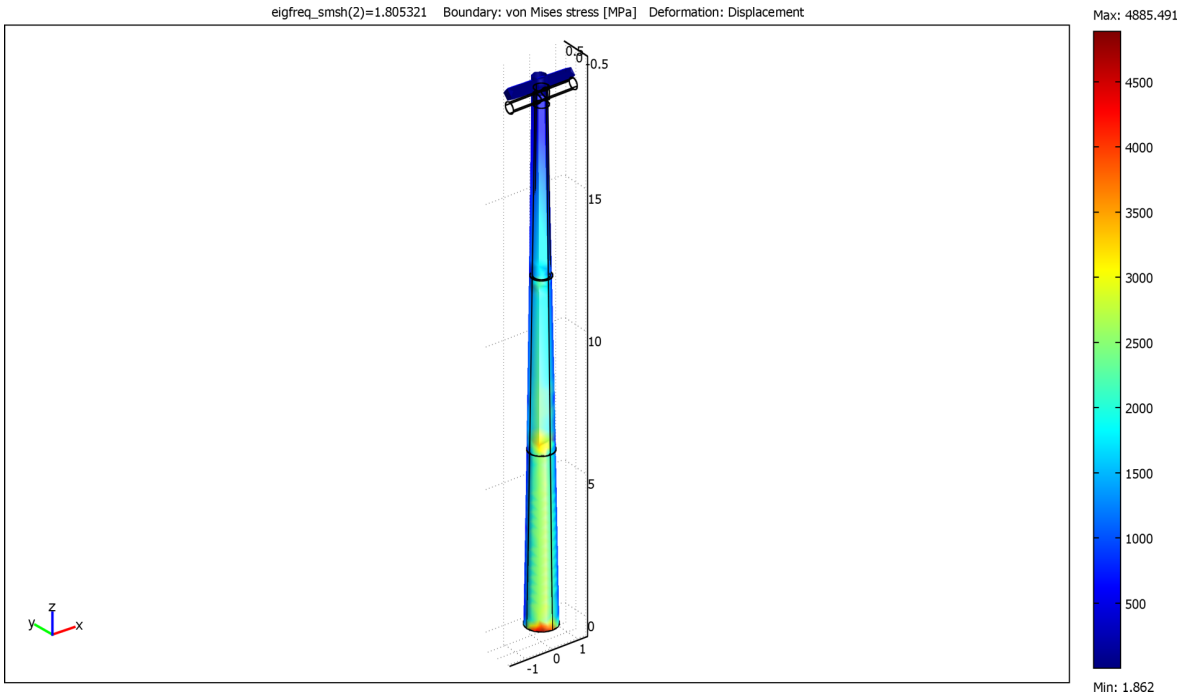

b. 1st bending mode b at 1.805 Hz

Figure 8-8: *The first bending modes of the Gaia tubular tower hammerhead model. The colour scale indicates the amount of stress on the turbine (in megapascals [MPa]) and the deformation an indication of the displacement (scaled for visual effect).*

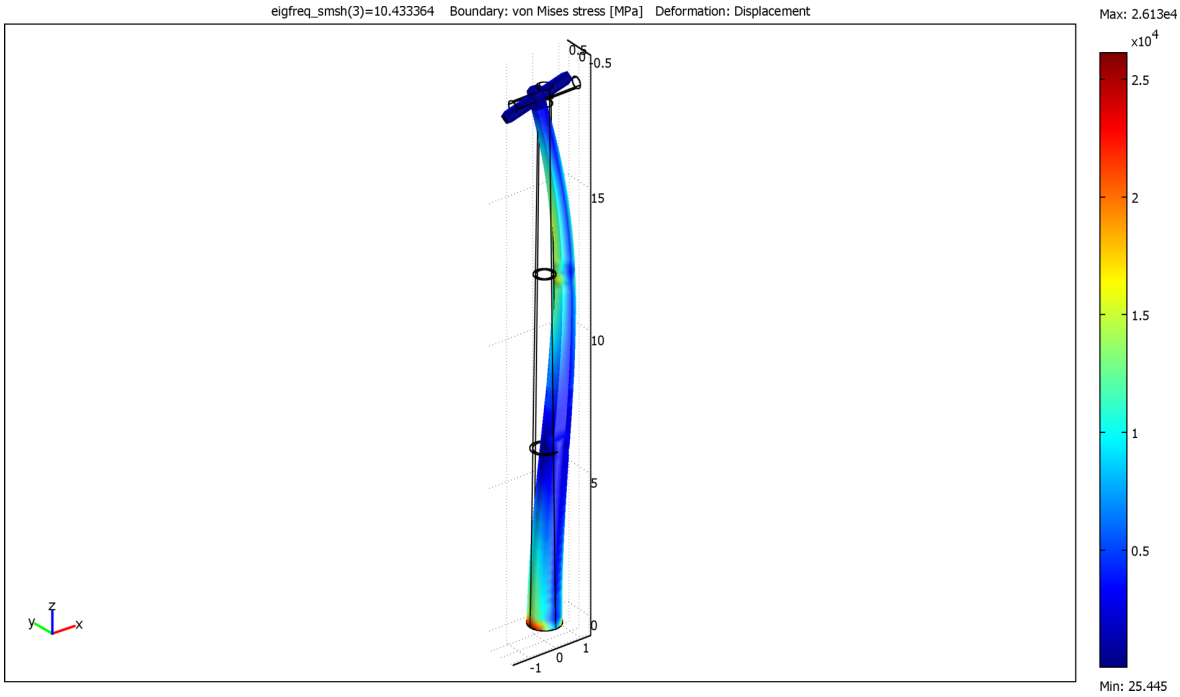

a. 2nd bending mode a at 10.433 Hz

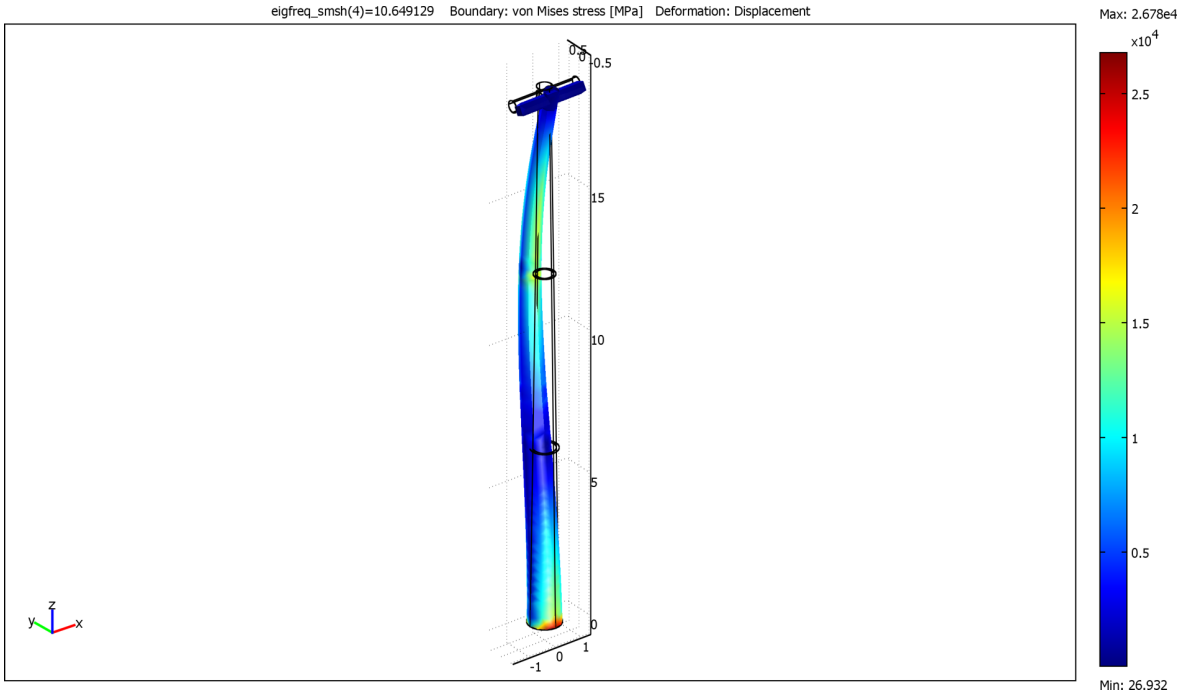

b. 2nd bending mode b at 10.649 Hz

Figure 8-9: *The second bending modes of the Gaia tubular tower hammerhead model. The colour scale indicates the amount of stress on the turbine (in megapascals [MPa]) and the deformation an indication of the displacement (scaled for visual effect).*

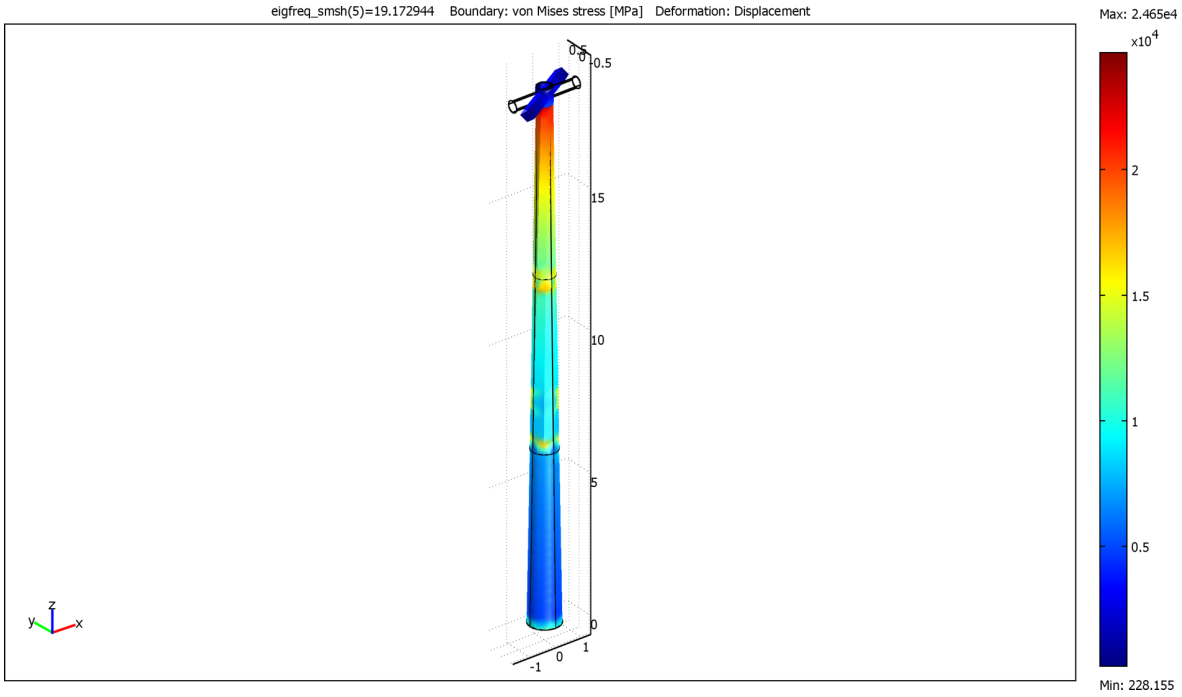

Figure 8-10: *The torsional mode of the Gaia tubular tower hammerhead model at 19.173 Hz. The colour scale indicates the amount of stress on the turbine (in megapascals [MPa]) and the deformation an indication of the displacement (scaled for visual effect).*

Higher bending modes of the tower exist at frequencies greater than those for the second bending mode and are caused by the tower bending between multiple nodes (figure 8-11). Additionally tubular towers also have breathing modes, where parts of the tower look as though they are expanding in the way lungs do when full of air (figure 8-12). These also occur at higher frequencies.

The lattice tower does not bend in the same way as the tubular tower. The eigenfrequency analysis for the 'no foundation' model returns ten eigenfrequencies between 1 and 20 Hz. Unlike the tubular tower, due to the structure of the lattice, it is not possible to clearly make out which (if any) of these frequencies are bending modes, or indeed whether the lattice structure has true bending modes at all. Two examples which could be bending modes are shown in figures 8-13 and 8-14. Arrows have been included to show the direction of displacement and are scaled proportionally to the amplitude of the displacement. At 1.88 Hz the nacelle appears to be yawing (figure 8-13), this is similar to the torsional mode of the tubular tower. At 7.71 Hz, the nacelle is pitching. Initially, this may be conceived as a first or second bending mode, however a closer inspection of the directional arrows shows that at the top of the tower the arrows point backward, but slightly further down they are pointing forward, toward the blades. This alternation repeats itself down the tower.

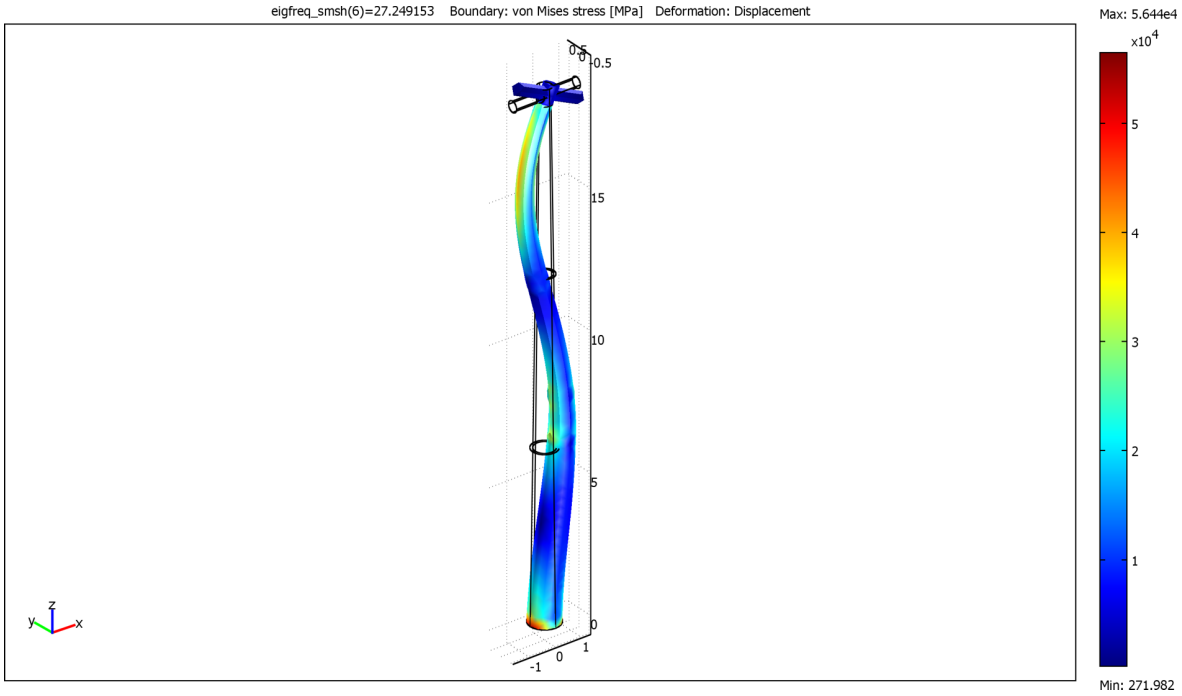

Figure 8-11: *The third bending mode of the Gaia tubular tower hammerhead model. The colour scale indicates the amount of stress on the turbine (in megapascals [MPa]) and the deformation an indication of the displacement (scaled for visual effect).*

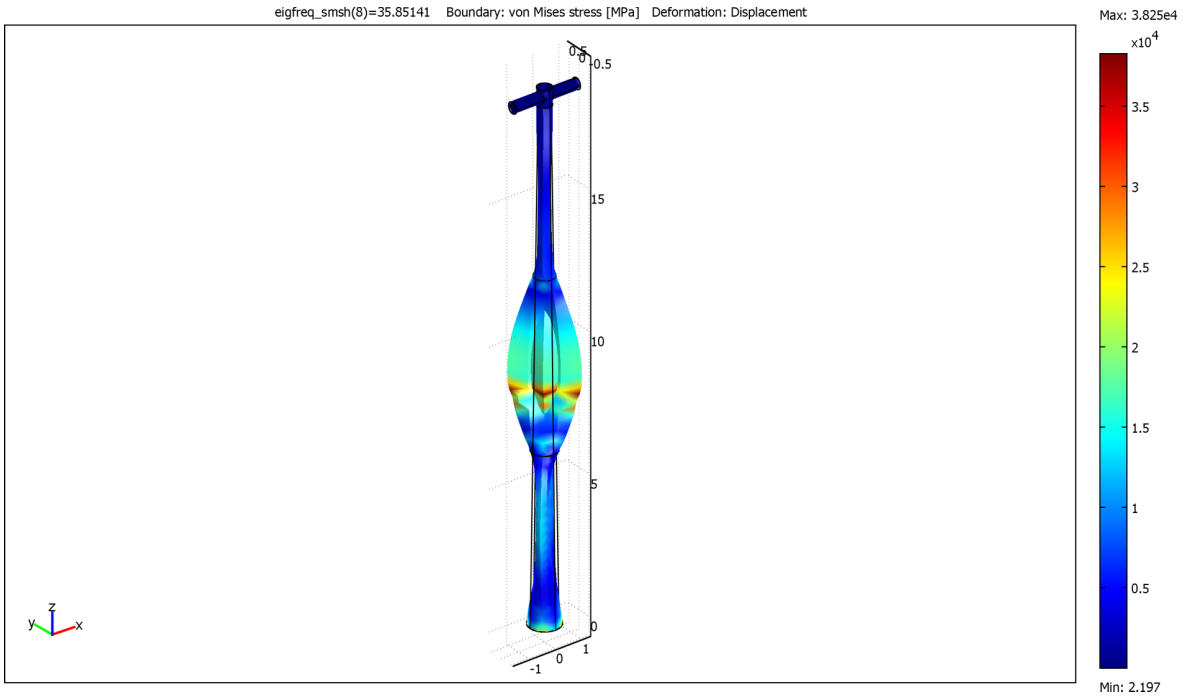

Figure 8-12: *A breathing mode of the Gaia tubular tower hammerhead model. The colour scale indicates the amount of stress on the turbine (in megapascals [MPa]) and the deformation an indication of the displacement (scaled for visual effect).*

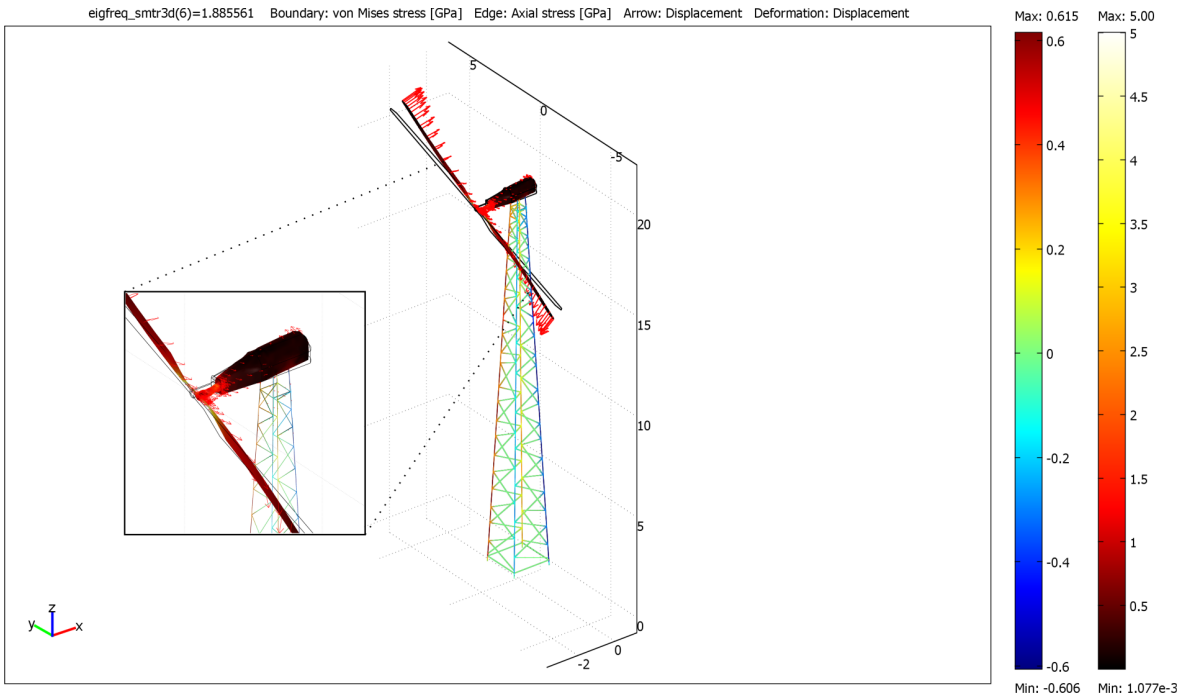

Figure 8-13: *The displacement, deformation and stress of the Gaia-Wind lattice model with no foundation at 1.88 Hz. The rainbow colour scale (blue to red) indicates the amount of stress (in gigapascals [GPa]) on the truss sections of the turbine, the thermal colour scale (black through red to white) the amount of stress (in gigapascals [GPa]) on the shell sections, the deformation an indication of the total displacement (scaled for visual effect) and the arrows the direction of displacement.*

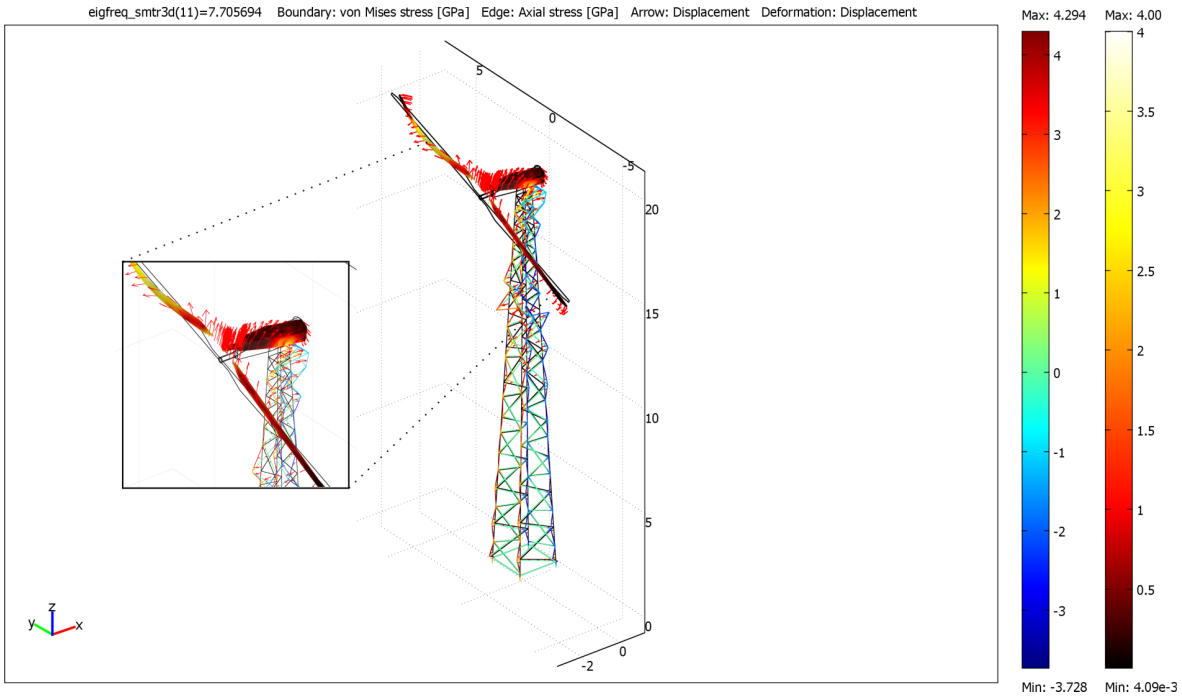

Figure 8-14: *The displacement, deformation and stress of the Gaia-Wind lattice model with no foundation at 7.71 Hz. The rainbow colour scale (blue to red) indicates the amount of stress (in gigapascals [GPa]) on the truss sections of the turbine, the thermal colour scale (black through red to white) the amount of stress (in gigapascals [GPa]) on the shell sections, the deformation an indication of the total displacement (scaled for visual effect) and the arrows the direction of displacement.*

	Eigenfrequencies (Hz)							
No foundation	Below 10 Hz	1.219	1.885	2.596	2.878	7.037	7.245	7.706
	Above 10 Hz	16.462	19.875	19.893				
Simple foundation	Below 10 Hz	1.219	1.884	2.591	2.875	7.031	7.243	7.659
	Above 10Hz	16.236	19.6136	19.875				
Solid foundation	Below 10 Hz	1.214	1.873	2.574	2.809	7.005	7.224	7.592
	Above 10 Hz	16.212	19.753	19.799				

Table 8-7: *The calculated eigenfrequencies of the Gaia-Wind lattice tower models*

The eigenfrequencies calculated for each of the lattice models are shown in table 8-7. The frequencies are comparable for all the models and the visualisations show that the movement of the tower is comparable through all three models at each of the frequencies. An example of this provided in figure 8-15 for the 16.3 Hz eigenfrequency. Additionally, visualisation of the frequencies shows that the displacement of the tower is predominantly in the nacelle, blades and top of the tower for all frequencies apart from 16.3 Hz.

8.5.3 Frequency Response Analysis

There are two reasons for performing a frequency response analysis. The first is to verify the accuracy of the model by comparing a frequency response sweep of displacement data with a frequency spectrum generated using measured data. Once the models are verified and some confidence is obtained about the modelling process, a frequency response analysis can provide an indication of the amplitude and frequency of the resonant modes. The modelling process will never replace monitoring the turbine in the field, however a frequency analysis of a model can provide a good initial estimate of the amplitude and resonant frequencies. The frequency response is calculated every 0.1 Hz between 0 and 20 Hz.

The frequency response analysis at two points on the tubular tower (0.3 m and 0.8 m from the base, figure 8-16a) was compared to the power spectrum density function of the measured data, as shown in figure 8-17. The points are selected at positions as close as possible to the sensor location of the measured data. The highlighted areas in the plots show where the peaks in the measured and modelled data correspond.

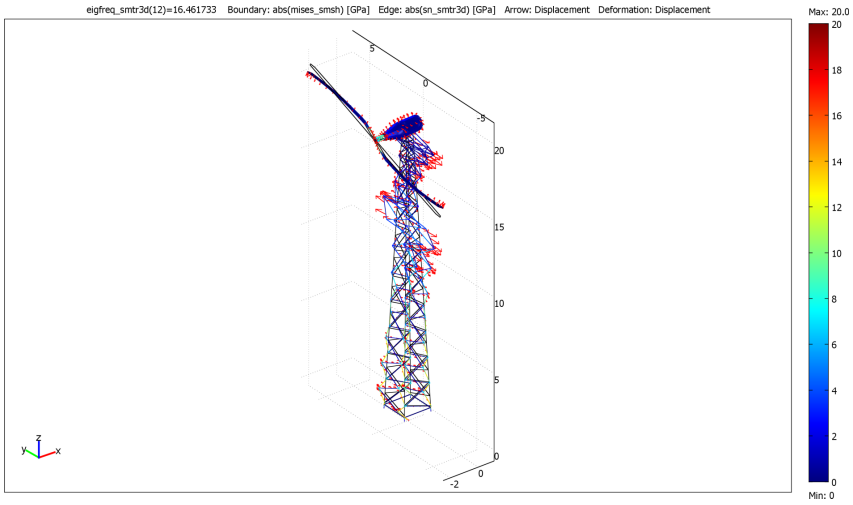

a. No foundation model at 16.462 Hz

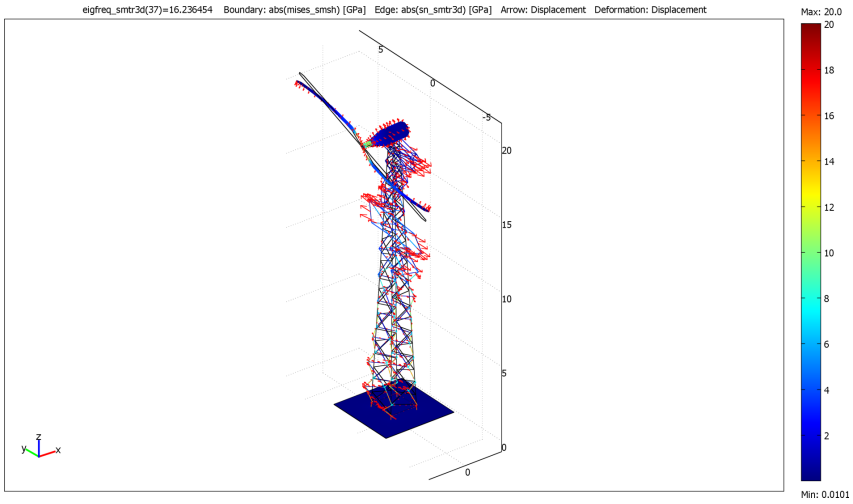

b. Simple foundation model at 16.236 Hz

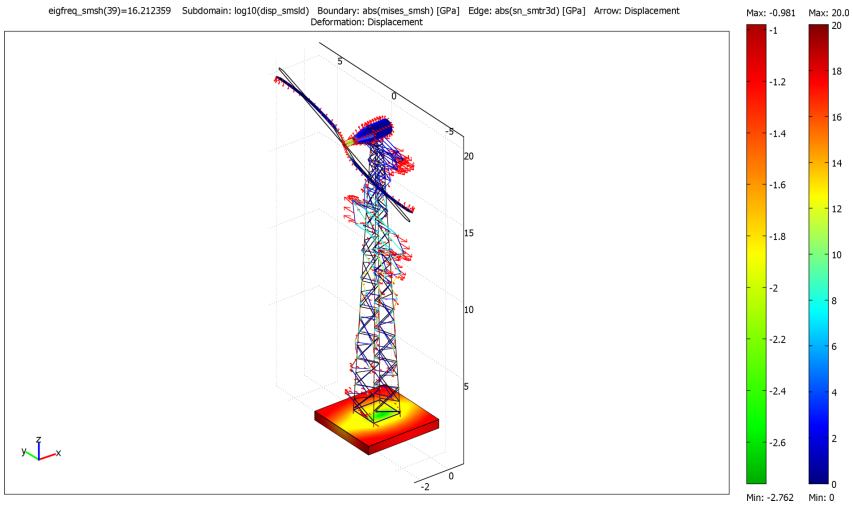

c. Solid foundation model at 16.212 Hz

Figure 8-15: *The 16.3 Hz eigenfrequency visualisation for the no foundation and solid foundation models. The rainbow colour scale (blue to red) indicates the amount of absolute stress (in gigapascals [GPa]) on the truss and shell sections of the turbine; the traffic light colour scale (green through yellow to red) the amount of total displacement (in* $\log_{10}$ *meters) on the foundation; the deformation an indication of the total displacement (scaled for visual effect) and the arrows the direction of displacement.*

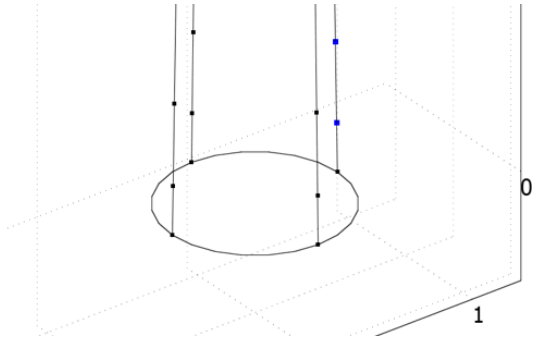

a. Points used for the tubular tower frequency response

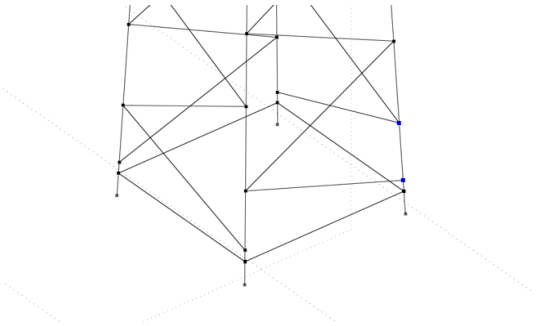

b. Points used for the lattice tower frequency response

Figure 8-16: *The points on the tower, indicated by the blue dots, used for the frequency response plots.*

In each of the plots, the 1st and 2nd bending modes, as indicated in table 8-6, are visible in the frequency response, of which the bending modes 1a, 1b and 2a each correspond to peaks in the measured spectrum. Given the static nature of the models, the blade rotation frequencies visible in the spectrum (section 5.1.3) are only seen in the modelled data if the blade rotation excites a mode of the tower.

The frequency responses for the lattice tower models (figure 8-18) at both heights on the tower (0.4 m and 1 m) and for each of the models contain no peaks below 10 Hz. The measured spectrum does not agree with this. However, as discussed in section 5.2.3, the peaks in the measured spectrum relate to blade rotation frequencies, which will not be seen in the static model, unless they excite the tower. The match of the peaks which are visible in the frequency response with the measured is not as good as the tubular tower. Although they are close to peaks to which they could correspond, the difference is attributed to the approximations in the cross-braces of the tower.

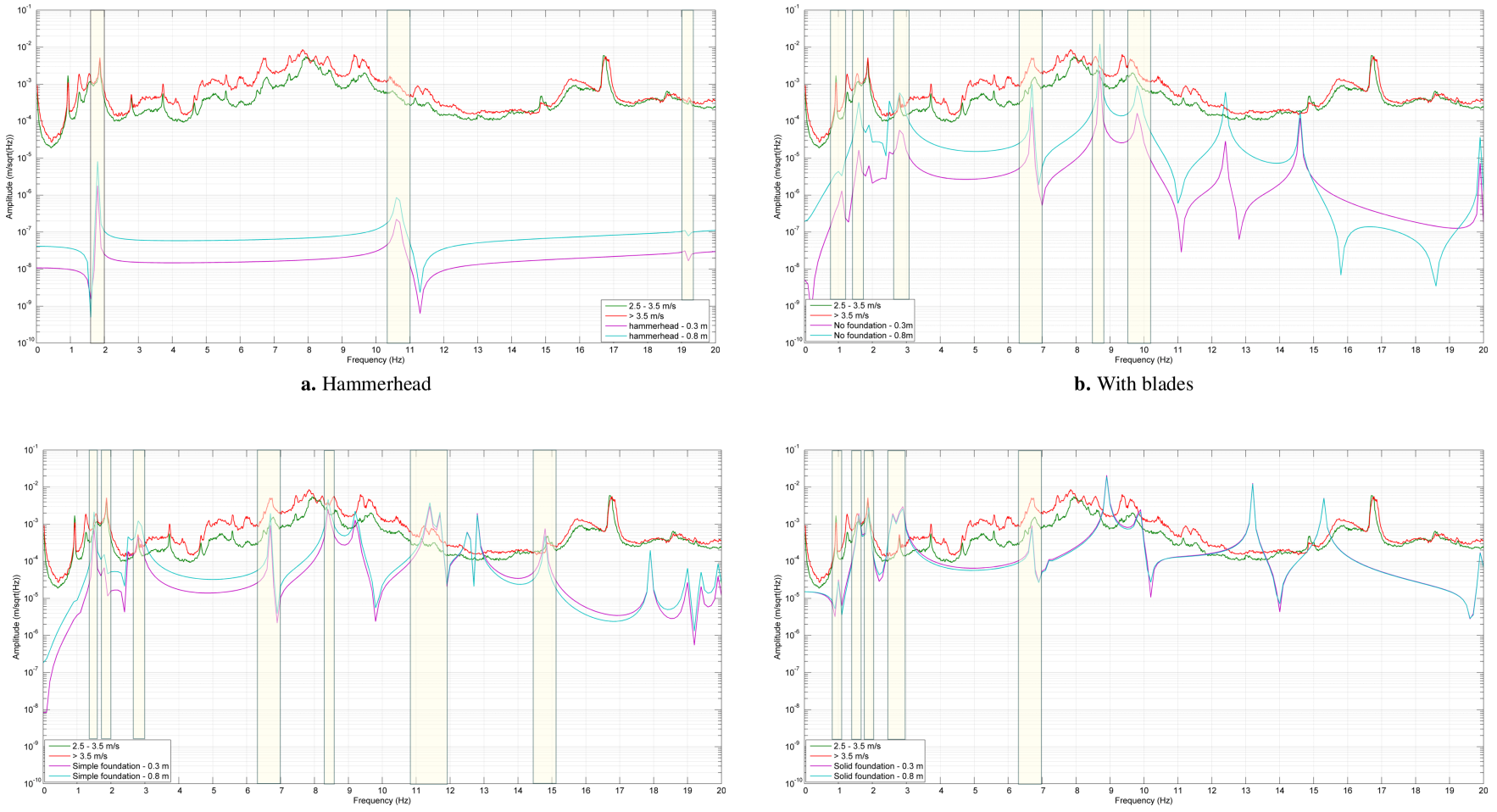

a. Hammerhead

b. With blades

c. Blades and 2D foundation

d. Blades and solid foundation

Figure 8-17: *Comparison of the frequency response analysis and the monitored spectrum for the Gaia-Wind tubular tower models prior to adding the ground. The highlighted areas are where the peaks in the two graphs correspond.*

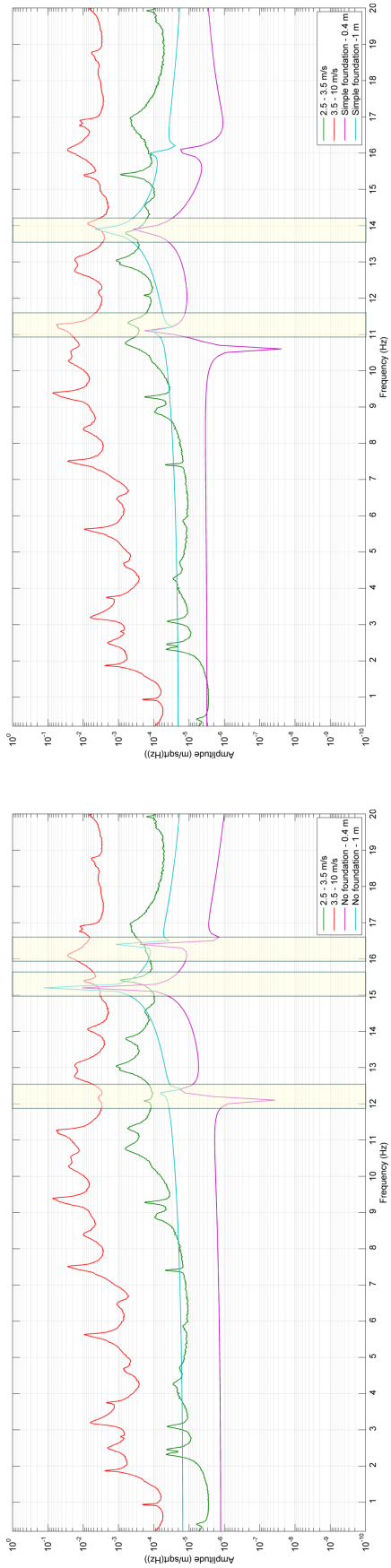

a. With blades

b. Blades and 2D foundation

c. Blades and solid foundation

Figure 8-18: *Comparison of the frequency response analysis and the monitored spectrum for the Gaia-Wind lattice tower models prior to adding the ground*

8.5.4 Ground comparison

Based on the results of the frequency response, the complexity of the lattice model and surrounding issues with Comsol and meshing, only the effect of different ground models on the tubular tower is investigated.

At each monitoring site the coordinates of each sensor, as well as the turbine, are recorded as standard. This enables points to be added to each of the ground models by calculating the easting and northing coordinates relative to the turbine (table 8-8). All sensors were buried, therefore points are placed 0.5 m below the surface in the 'soil only' model and 'soil and bedrock' model. The latter contains an additional set of points at 2 m down (1 m into the bedrock layer). The model with only a bedrock layer contains a set of points on the surface and a set 1 m down. Examining the results for multiple depths will see whether depth positioning makes a significant difference to the results. Figure 8-19 shows the results from the different depths. This shows that the frequency response does not alter by a large amount with changing depth, however the amplitude is affected greatly by the make-up of the ground. Having 'soil only' over predicts the amplitude, while for 'bedrock only' the calculated amplitude is less than the measured data and lower still for the model including combined bedrock and soil.

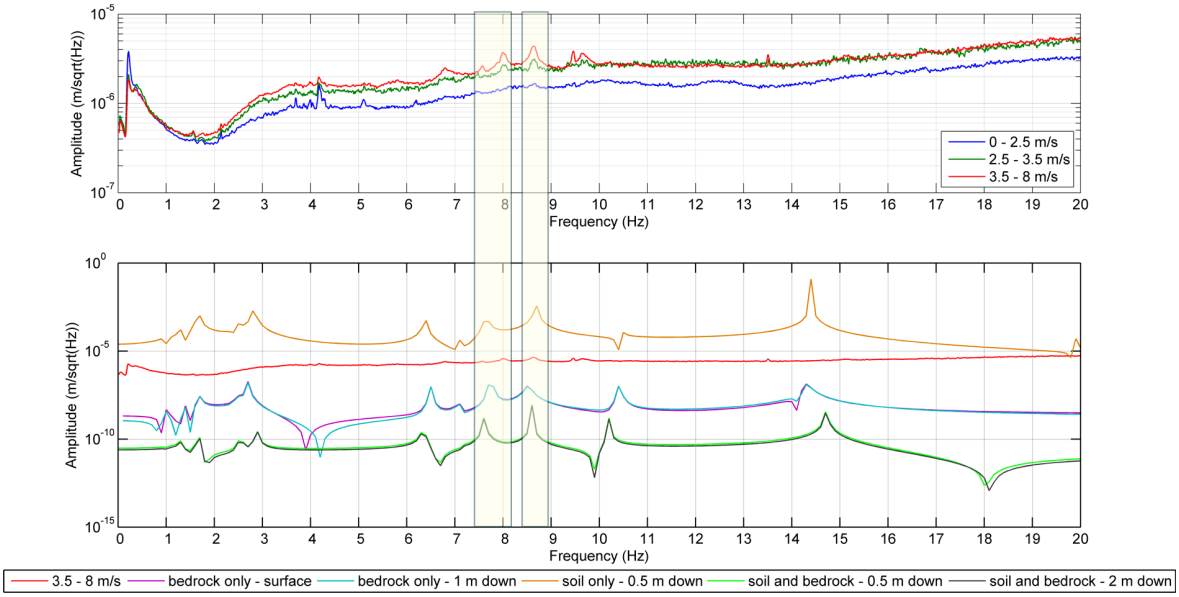

Figure 8-19: *The measured data from the 6TD (top) and frequency response results for the three ground models from points at different depths*

Description	Northing	Easting	rel. Northing to turbine	rel. Easting to turbine
Turbine	328932	549504	0	0
Accelerometer @ 10 m	328927	549514	-5	10
Accelerometer @ 20 m	328923	549522	-9	18
Accelerometer @ 30 m	328919	549532	-13	28
5TD	328944	549434	12	-70
6TD	329001	549683	69	179

Table 8-8: *Actual and relative coordinates for the sensors at the Wigton site*

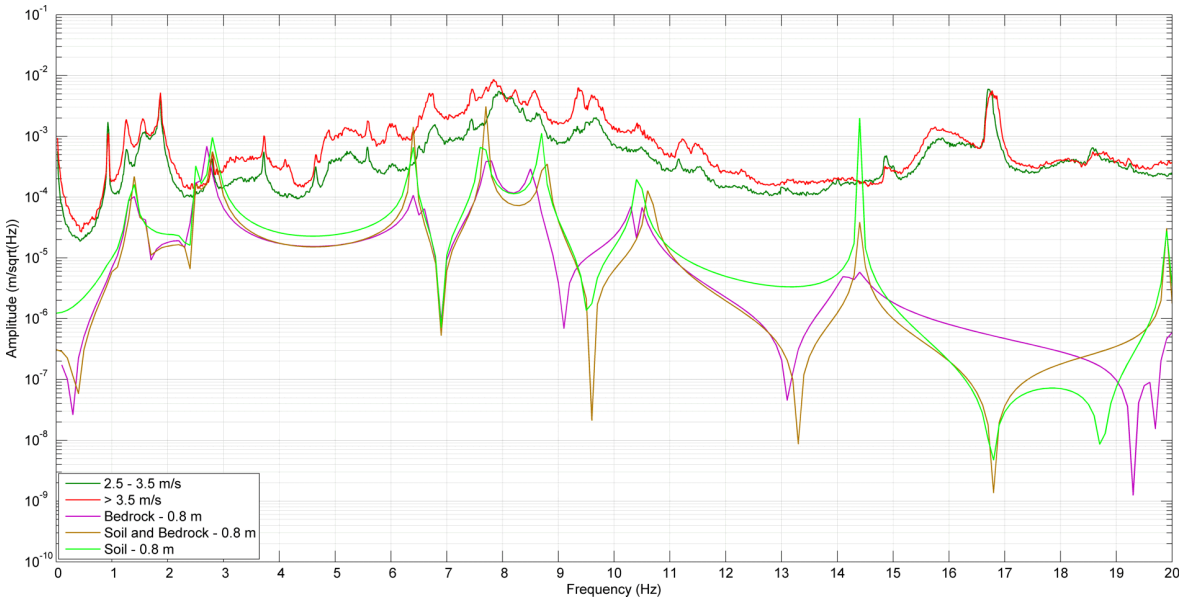

Figure 8-20: *The frequency response of each of the ground models at a point 0.8 m up the turbine*

On the turbine, each of the models generate a similar frequency response in terms of amplitude and shape. This is shown in figure 8-20 for the point 0.8 m up the tower. Adding a soil layer to the bedrock does not make a difference to what is seen on the tower.

The radiation patterns for the 'soil and bedrock' and 'bedrock only' models for the second bending mode at 9.5 Hz are shown in figures 8-21 and 8-22 respectively and slices through the model at varying depths are shown in figures 8-23 and 8-24. For both of the models it can be seen that amplitude decreases with depth, as would be expected with an attenuating signal. Both models also clearly show an asymmetry in the radiation pattern with the area behind the turbine (and the bend) having a higher amplitude.

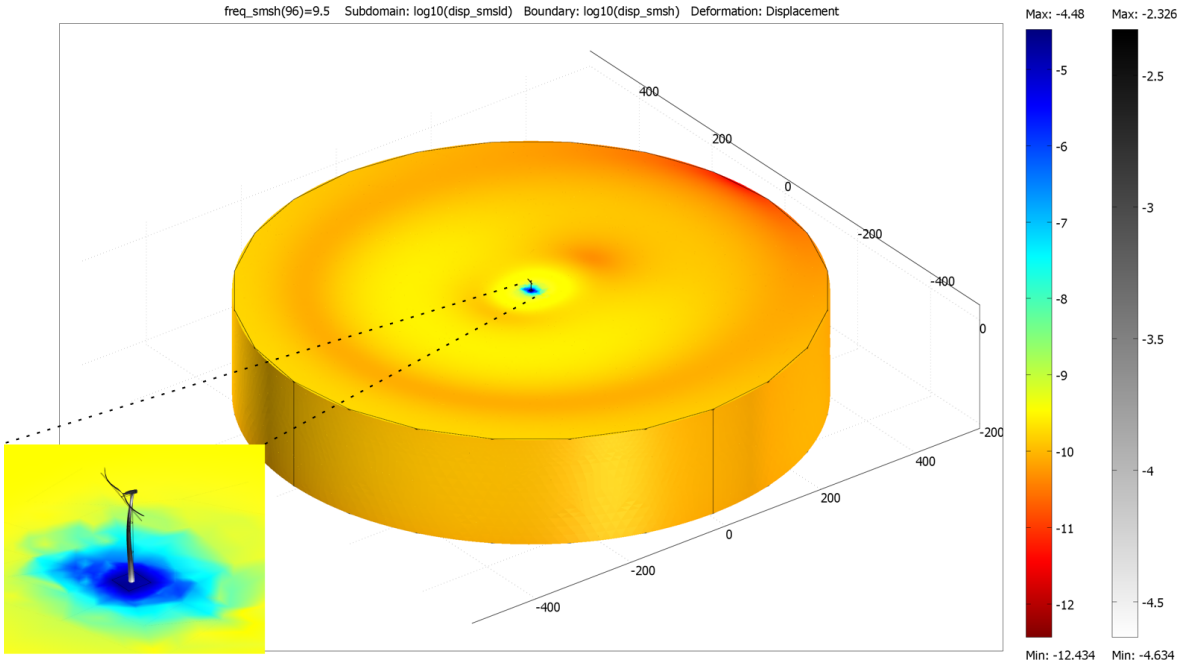

Figure 8-21: *The soil and bedrock model for the second bending mode at 9.5 Hz. The rainbow colour scale (blue to red) indicates the amount of total displacement (in $\log_{10}$ metres) in the ground and the grey scale the amount of total displacement on the turbine (in $\log_{10}$ metres). The deformation on the turbine also gives an indication of the total displacement (scaled for visual effect)*

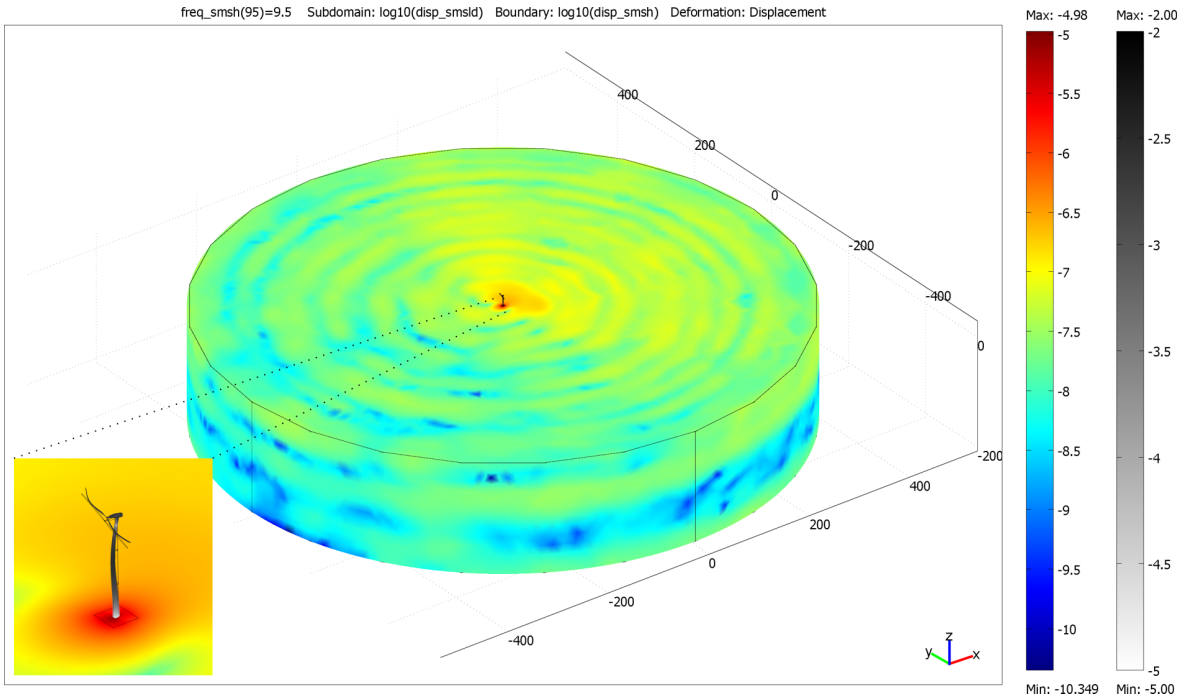

Figure 8-22: *The bedrock only model for the second bending mode at 9.5 Hz. The rainbow colour scale (blue to red) indicates the amount of total displacement (in $\log_{10}$ metres) in the ground and the grey scale the amount of total displacement on the turbine (in $\log_{10}$ metres). The deformation on the turbine also gives an indication of the total displacement (scaled for visual effect)*

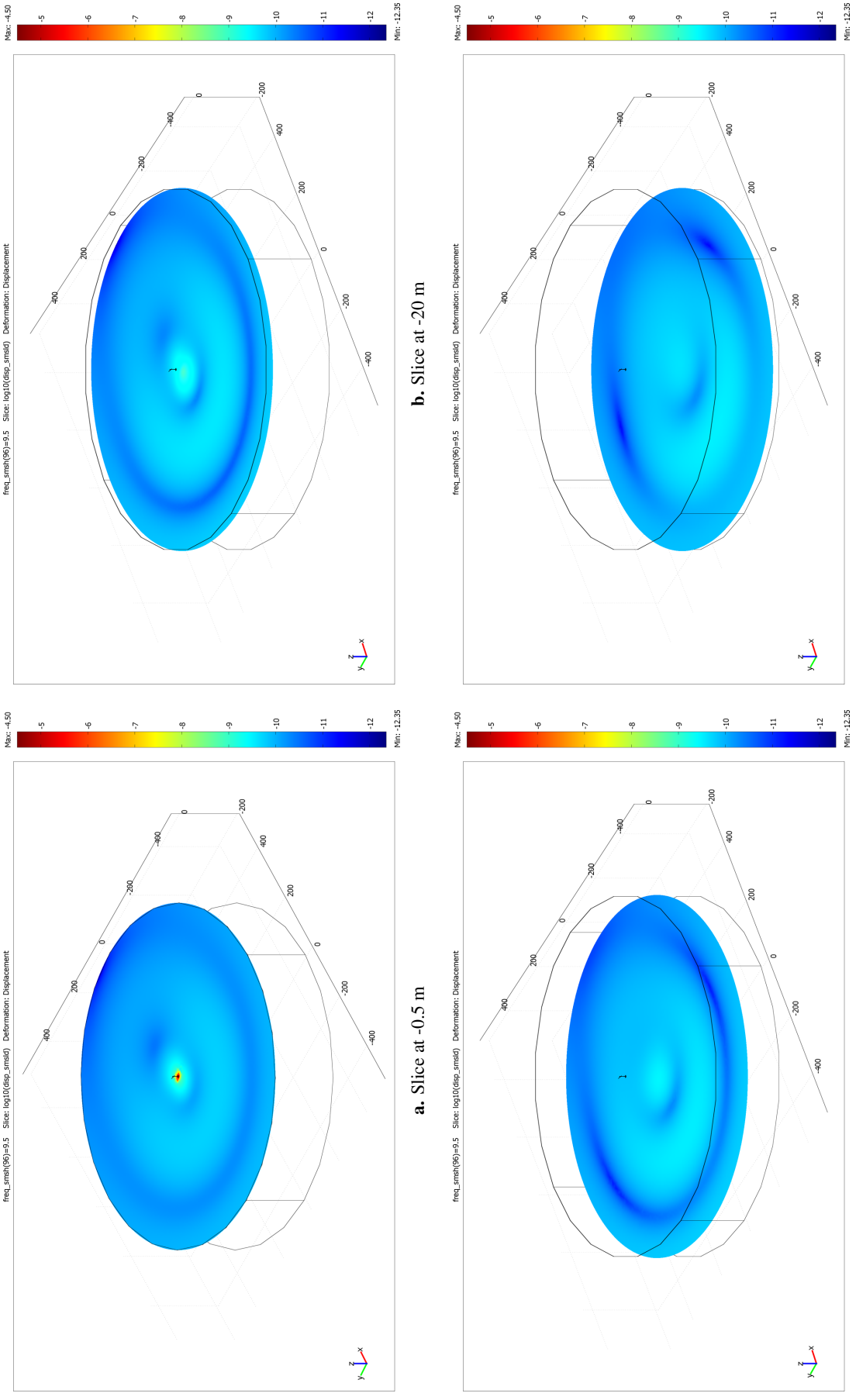

Figure 8-23: *Slices through the soil and bedrock model at various depths. The rainbow colour scale (blue to red) indicates the amount of total displacement (in* $\log_{10}$ *metres) in the ground*

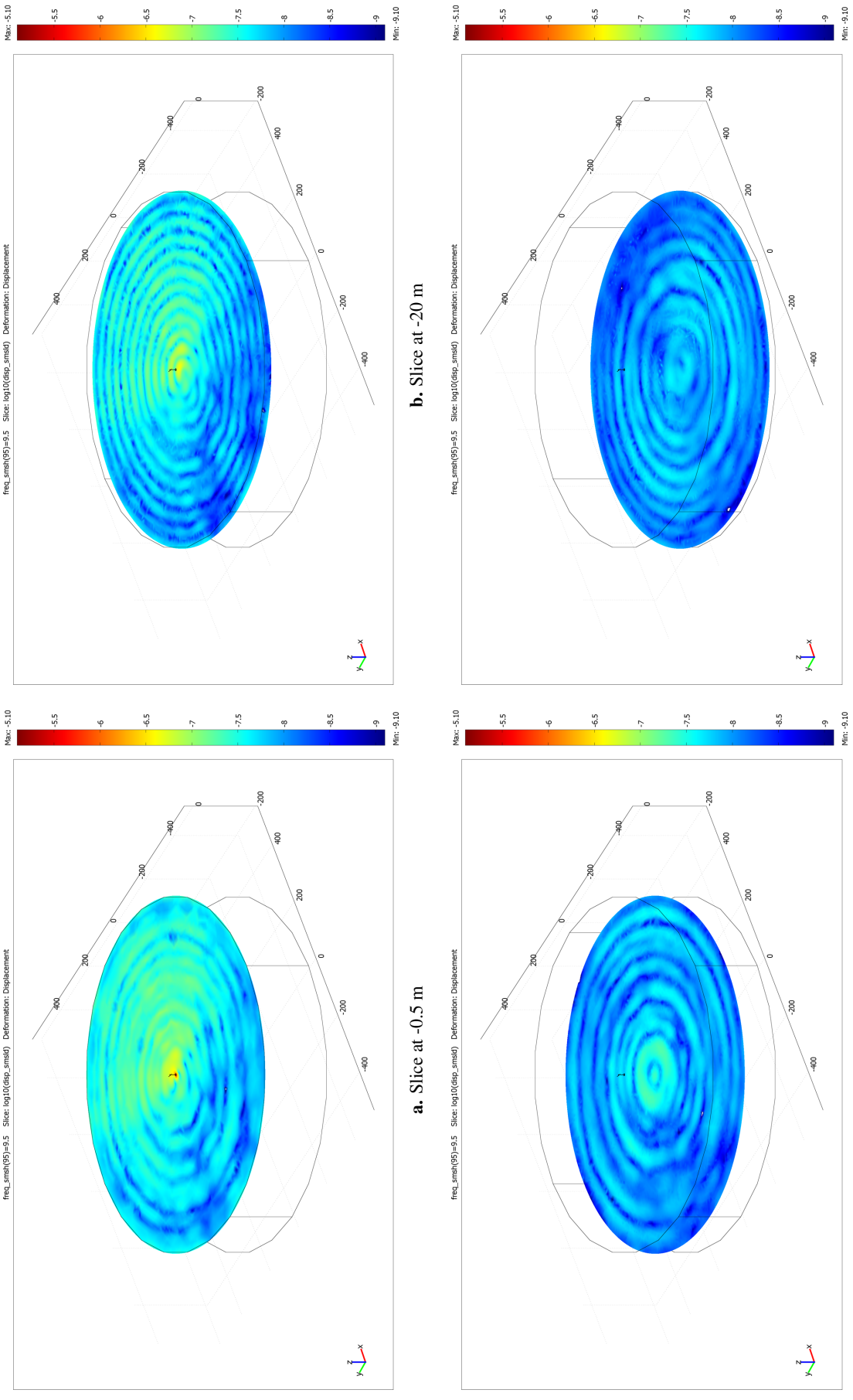

Figure 8-24: *Slices through the bedrock only model at various depths. The rainbow colour scale (blue to red) indicates the amount of total displacement (in $\log_{10}$ metres) in the ground*

8.6 Discussion

This chapter has presented models of both tower types of the Gaia-Wind 133 wind turbine. The models were created in Comsol, initially without surrounding ground and developed in stages from a simple hammerhead to a full turbine with blades and a solid foundation. After analysing these results, the surrounding ground was added to the model. This section discusses the models, results and key issues arising from the results.

8.6.1 The Results and Peak Identification

An eigenfrequency analysis was conducted on each of the the models, prior to including the ground, to establish the bending and torsional modes of the turbine. These frequencies can be transmitted down the tower to the ground or be damped by the structure, depending on where the eigenfrequency originates. The frequency response analysis calculates the vibrations at a given point on the model over a range of frequencies.

Based on the results shown in section 8.5.1 the frequency peaks can have a difference of as much as 1 Hz from the measured data for the second bending mode and 0.1 Hz for the first bending mode, depending on what angle the blades are set to in the model. Each of the models, display frequencies in the spectrum which match with frequencies in the measured data, within these tolerances. There are certain peaks visible in the measured data which are not visible in any of the model frequency responses or eigenfrequency analyses. This could be due to the frequencies originating from sources other than the wind turbine and propagating up the tower. Alternatively, inaccuracies in the model from approximations due to the turbine complexity (see section 8.6.3) could cause the frequency to not be calculated or the frequency may be attributed to a blade rotation harmonic, which will not be seen in the model due to its static nature.

From the eigenfrequency analysis, the tubular tower has 1st bending modes at around 1.5 Hz and 1.9 Hz and 2nd bending modes at around 9.6 Hz and 11.5 Hz. There is also a torsional-bending mode at around 7.8 Hz. Combining this with the blade rotation frequencies which, due to the static nature of the model, will not be visible unless one of the frequencies excites a mode of the tower, the

peaks in the measured data can be identified. Modelling in itself will not replace monitoring a wind turbine. However, when combined with the measurements and the polarisation analysis discussed in section 6.4, a greater confidence can be gained about which peaks originate from the tower and what mode of the tower they are (or blade rotation harmonic). Identification of the peaks in the tubular tower measured data is shown in figure 8-25. The measured data was recorded at wind speeds greater than 3.5 m/s, when the wind turbine was operational and the median value across all power spectrum density functions for the wind speed obtained (see section 4.4.2.1). The peak at 4.2 Hz is not present in the model, further adding to the conclusions made in chapter 6 that this frequency originates from a source other than the turbine, most likely Great Orton Wind Farm. The wind farm is located less than 5 km NW of the turbine and contains six Vestas V47s. This type of turbine has been shown by Styles et al. (2005) to generate a 4.2 Hz peak (the 2nd bending mode of the tower), which can be detected up to 10 km away.

The difference in amplitude between the frequency response of the model and the measured data for the tubular tower decreases as the model complexity increases (figure 8-17). The choice of model complexity should therefore depend on the desired outcomes from the model. If it is only the frequency of the peaks which is required, then a model with nacelle and blades, but no foundation will provide this, however the amplitude will be significantly underestimated. For a more reliable estimation of both the frequencies of the peaks and amplitude, a solid foundation should be included

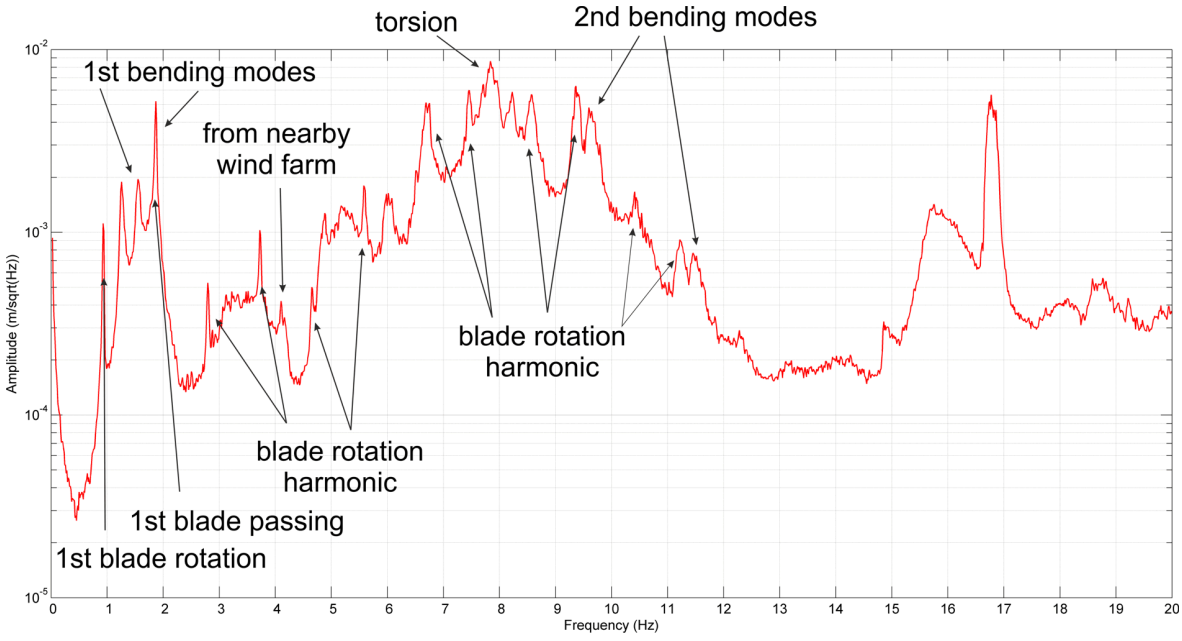

Figure 8-25: *Identification of the peaks in the measured on-turbine data for the Gaia-Wind tubular tower wind turbine, when the wind speed was greater than 3.5 m/s*

in the model to produce a much closer match between the two graphs. The difference between the amplitudes of the frequency response at different heights up the tower also decreases with complexity.

The peaks which are present in the frequency response of each of the lattice tower models match a peak in the measured data. Although there are no peaks below 10 Hz in the modelled response, when examining the measured data, all but two of the peaks in the power spectrum up to 10 Hz can be attributed to blade rotation harmonics. These harmonics would not be visible in the model as they are caused by the dynamic movement of the blades. The amplitude difference between the modelled and measured data may be due to inaccuracies in the tower model which are discussed further in section 8.6.3.

The eigenfrequency analysis of the lattice tower model presents consistent results for all the models, some of which are present in the measured data. Identification of the peaks in the lattice tower measured data is shown in figure 8-26. The blade rotation harmonics are the same as for the tubular tower and account for most of the peaks present in the data. The peaks at 11.2 Hz, 14.1 Hz and 16 Hz are close to the peaks visible in the frequency response analysis of the models.

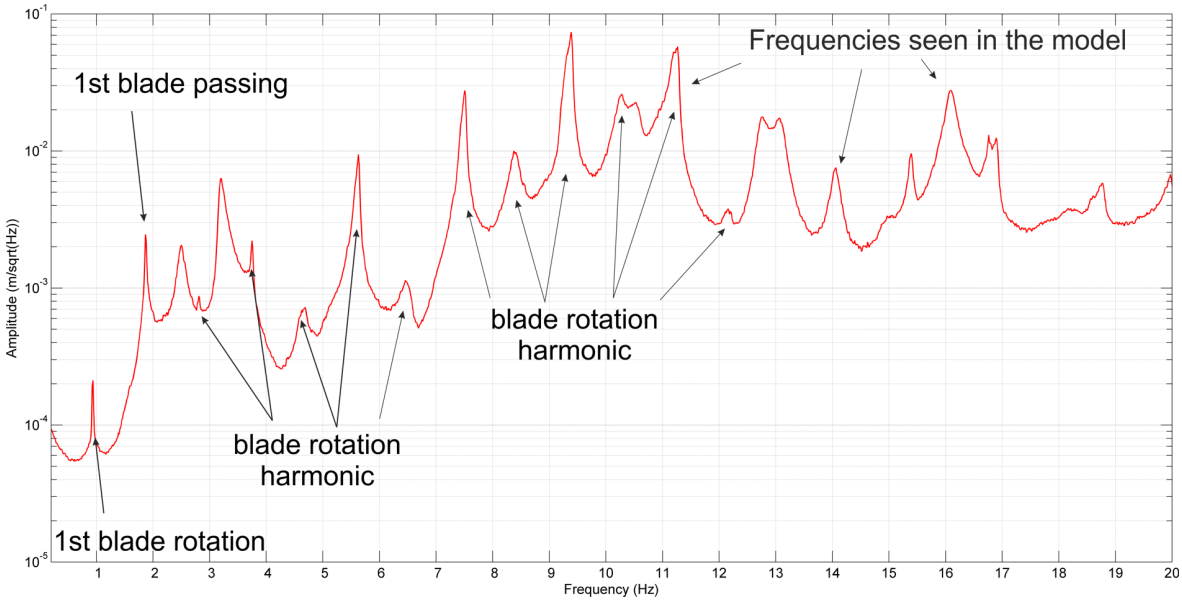

Figure 8-26: *Identification of the peaks in the measured on-turbine data for the Gaia-Wind lattice tower wind turbine, when the wind speed was greater than 3.5 m/s*

Three different approaches to including the surrounding ground have been modelled in order to investigate if adding a soil layer makes a substantial difference to the results. Figure 8-20 shows that the frequency response for each of the models at a point 0.8 m up the tower is almost identical. This indicates that the addition of a soil layer to the bedrock does not affect what is seen on the tower. However the layering structure of the ground does make a difference to what is seen at a point representative of a buried sensor, with a significant difference in amplitude between the models, although none are representative of the amplitude seen in the measured data. There are some peaks which correspond across all models and the measured data, with the most predominant occurring at 8.6 Hz.

8.6.2 Frequency Response Step Sizes

The frequency response analysis was performed every 0.1 Hz between 0 and 20 Hz. For the tubular tower, there are a number of prominent peaks displayed in the results between 0 and 10 Hz, which could have been used solely as a comparison with the measured data. However, for the lattice tower, there are no peaks visible in the analysis below 10 Hz at the selected points on the tower. Therefore, it was necessary to calculate over a larger frequency range. For consistently and applicability, the range of 0 to 20 Hz was selected for both tower types.

The step size determines at what frequencies the response should be run. Decreasing the step size increases the number of calculations which have to be performed and the length of time the analysis will take. Figure 8-27 shows the frequency response of the Gaia-Wind tubular tower for the 'no foundation' model at 0.8 m up the tower, with the step size set at a range of values. From this, it can be seen that the larger the step size gets, the more detail is missed by the solver, with peaks getting sharper as the step size decreases. A 0.1 Hz step size can be calculated in a sensible length of time, requiring 201 calculations between 0 and 20 Hz. For the larger models including the ground, this still takes many hours. A step size of this value calculates enough detail for an analysis, only cropping a couple of the peaks.

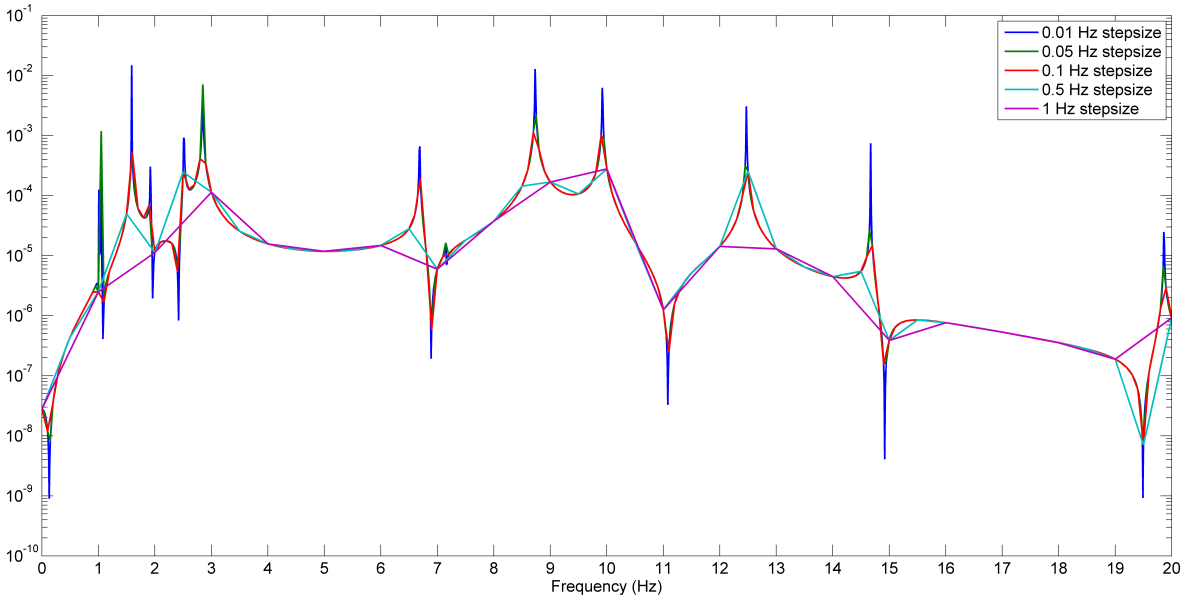

Figure 8-27: *A comparison of the frequency response results of the model of the Gaia-Wind tubular turbine, using different frequency step sizes.*

8.6.3 Model Complexities

The tubular tower model is a less complex model than the lattice. The tower is straightforward to model as a tapered cylinder and the uncertainties lie in the nacelle and blades. Manufacturers are very reluctant to give out any structural details of their wind turbine, especially with regard to the nacelle and blades. All that is known about the Gaia-Wind turbines is the mass of the nacelle and the blades, the blade length and that they are constructed from glass fibre (Gaia-Wind Ltd 2011b). The shape of the nacelle is approximated from a simple drawing provided by Gaia-Wind. This means that the nacelle may not be balanced correctly on the tower or may not be scaled properly, which could shift, add or remove frequencies. As it is only the blade length which is known, the width and shape are approximated from photographs. Making the blades too narrow and/or too thin can cause additional bending, as they will not be stiff enough to withstand the forces applied upon them and could cause the nacelle to be unevenly balanced in the model and excess stress to be formed on the front of the the nacelle. Alternatively making the blades too wide and/or too thick could mean that they do not bend as much and that some of the nacelle movement of the bending modes may not be seen. Both of these can have an influence on the resonant frequencies, as can be seen in figure 8-17, which shows that by changing the hammerhead to a nacelle and blades (figures 8-17a and 8-17b), more peaks appear in the analysis and the amplitude increases.

The lattice structure provides additional uncertainties to the model with respect to the tower. The complexity of the lattice means that it has to be simplified in order to create a model which can be interpreted and calculated by Comsol. Prior to deciding on the geometry, described in this chapter, more complex geometries were generated in AutoCAD. They were still simplified CAD (computer aided design) models and did not contain elements like nuts, bolts or washers, nor the maintenance platform, ladder or internal workings. However, the detail of the L-shape of the braces and uprights was included. The geometry of such a model is shown in figure 8-28. When Comsol attempts to mesh the model, it can fail due to some boundaries not quite touching or by generating singular matrices which cannot be solved. A successfully generated mesh at a Comsol defined Normal mesh size of the tower alone would contain over 700,000 triangular boundary elements. A frequency response analysis would likely take a few hours to run a 0.1 Hz sweep between 0 and 20 Hz. An alternative model, using the same geometry as described in the chapter would involve using the 3D Euler beam application mode instead of the 3D truss mode. Euler beams require the material properties of Young's modulus, Poisson's ratio and the density to be defined in the same way as the other Structural Mechanics application modes. In addition to the cross-section area, which is required for the 3D truss mode, 3D Euler beams also require the area moments of inertia about the y and z axes, the torsional constant and a definition of the local xy plane to be defined for each edge. This would require separate calculations for each of the braces and uprights, given that they are each at different angles and have varying lengths and are thought to be beyond the computational resources available.

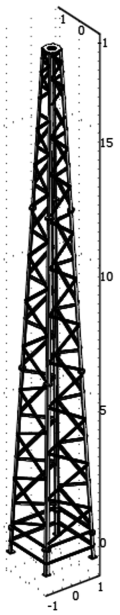

Figure 8-28: *Lattice complex CAD model for the tower only. All L-shape braces are constructed as solid steel sections.*

Chapter 9

Summary, Conclusions and Recommendations

With high topography and prevailing high winds, the southern uplands of Scotland are a prime location for wind energy from both large and small wind turbines. Situated in the middle of this area is the Eskdalemuir Seismological Recording Station (EKA). The station is a component of the International Monitoring System (IMS), which is part of the verification regime for the Comprehensive Nuclear-Test Ban Treaty (CTBT); an international treaty banning all nuclear explosions. The UK is obliged by the treaty to ensure that the seismic array's detection capabilities are not compromised.

A study by Styles et al. (2005) on the vibrations from wind turbines found that low frequency vibrations from a wind farm containing 26 Vestas V47 (660 kW, 40 m hub height and 47 m rotor diameter) turbines situated on similar geology and topography to Eskdalemuir, could be detected on seismometers located several kilometres away. From the results, a model was derived to predict the aggregate vibration contribution from any planned wind farm in the vicinity of EKA.

Previous work on the vibrations from wind turbines has focused on the effects from large (some now defined as medium) wind turbines. Styles (1996) conducted a study at a wind farm of 11 Bonus 450 kW turbines at St Breock's Down in Cornwall (reported by Snow (1997), Manley & Styles (1995) and Legerton et al. (1996)) and found that vibrations were transmitted into the ground at

certain harmonics of 0.5 Hz. In 2002, Schofield monitored the vibrations from the Stateline Wind Project, which consisted of the same Vestas V47 turbines (399 of them) as studied later by Styles et al. (2005) and found results consistent with the work carried out at St Breock's Down. Since the research in 2005, little additional work has been published, with none specifically on the vibrations from small wind turbines. Fiori et al. (2006, 2009) confirm the conclusions of Styles et al. (2005) in a study conducted in 2005 on the vibrations from a wind farm near Hannover, Germany containing three 2.3 MW 100 m turbines and five 1.5 MW 85 m turbines.

This project has investigated the vibrations generated from four small wind turbines through an integrated approach of measurement analysis and multiphysics finite element modelling.

9.1 Field Setup & Instrumentation

Four small wind turbines were monitored at locations around the UK; a Gaia-Wind 133 lattice tower in Southern Scotland, a Proven 35-2 in Ayrshire, a Gaia-Wind 133 tubular tower in Cumbria and an Endurance E-3120 in Cornwall. The monitoring setup included a combination of multiple single-component CMG-5U accelerometers, a three-component CMG-5TD accelerometer, a three-component CMG-6TD broadband seismometer, a Güralp digitiser and an anemometer.

At each site, two single-component accelerometers were attached horizontally to the turbine and aligned perpendicular to each other, with a third buried shallowly at the base. The sensors were placed to measure the vibrations on the tower and foundation. At three of the sites, three single-component accelerometers were positioned in the ground in a line at 10 m, 20 m and 30 m from the turbine. These sensors were all attached to either a CMG-DM24S12AMS or CMG-DM24S6EAM digitiser. The CMG-5TD was positioned 70 - 100 m from the wind turbine and the CMG-6TD 190 - 200 m away. The sensors were positioned, as far as possible, in a line with each other and the wind turbine. By placing the sensors in a line, the attenuation of the signal from the turbine could be calculated. The location of the CMG-6TD at Wigton for the Gaia-Wind tubular tower is not quite aligned with the other sensors, as the locations also had to be convenient for the landowner, at a site where they would not be disturbed for the monitoring period by either people or livestock. The accelerometers in the ground were not deployed to monitor the Proven 35-2, as the digitiser was found to be faulty

prior to monitoring.

The equipment is portable and can be deployed quickly. Two different Güralp digitisers were used during this project. The CMG-DM24S12AMS must be powered through the mains, which means that the digitiser has to be positioned within 100 m of a power supply. The digitiser and power reels have to be kept dry and were placed in a tent. The CMG-DM24S6EAM can be powered from a single 12v battery. This has the advantage that the equipment can be sited anywhere and is small enough to fit into a large plastic box, without the need for a tent. This also makes the location of the equipment less obvious to any passer-by. Additionally, should a power-cut occur due to stormy conditions, as in the case when monitoring the Gaia-Wind tubular tower, the CMG-DM24S6EAM will not be affected and will continue monitoring.

Once locations for the sensors have been determined, the sensors can be installed within a few hours. Installation involves digging holes at each site and lining the base with sand prior to placing the sensor. Each sensor must be levelled on the sand and cables and peripherals (GPS antennae, break-out boxes, data download cables) attached to the sensor or digitiser, prior to powering the equipment. Data acquisition starts immediately, but a series of tests must be carried out before leaving the site to ensure all are responding well and that both the CMG-6TD and digitiser have good GPS fixes.

The CMG-6TD seismometer has a lower instrument noise level than the accelerometers. This was clearly visible in the results. This means that the seismometer can record signals at lower amplitudes, which would be masked by noise levels if recorded on the accelerometers. The results show that the CMG-6TD is the better instrument to use for monitoring in the ground.

The anemometer was mounted on a five metre monopole and secured with guy ropes. The location of the anemometer varied from site to site and was dependent on the surrounding area and use of the land.

9.2 Site Location & Monitoring

Site selection was based on a set of ideal criteria, which were matched as closely as possible to a limited number of available sites provided by the turbine manufacturers. The sites of the Gaia-Wind lattice wind turbine at Melrose and the Endurance E-3120 near Hayle were ideal; located away from roads, livestock and other possible sources of vibration. The Gaia-Wind tubular tower site was more noisy, with the turbine standing just 40 m from the Carlisle to Barrow-on-Furness rail line and on the site of a working farm. This raised the background noise levels and introduced peaks to the spectrum from the sensors in the ground which originated from sources other than the turbine.

At three of the sites, power was lost to the digitiser part way through monitoring. This meant that although data from the seismometer was collected for the entire monitoring period, accelerometer data was only available up to the power cut. However, enough data was successfully gathered in order to complete an analysis. Stormy weather caused the power cut at two of the sites and meant that the highest wind speed of the period occurred after the power cut. This only affected the analysis of one of the turbines, the Gaia-Wind tubular tower, where data recorded on the turbine was only recorded for low wind speeds. This meant that calculation of the amplitude with respect to wind speed could only be predicted for these wind speeds. This turbine produced a different result to the other three when relating seismic amplitude on the tower to seismic amplitude on the foundation and in the ground. This could be a real affect with this turbine behaving differently to the others. Alternatively, with the low wind speed leading to fewer data points, the results may be biased and adding more data points through further monitoring at higher wind speeds could bring the results in line with the other three turbines.

9.3 Modelling

Multiphysics finite element models of the two Gaia-Wind 133 turbines were developed using Comsol Multiphysics software. Comsol is a commercial software package which can be used for solving mathematical problems in science and engineering. The software lends itself well to vibration analysis of wind turbines, as the Structural Mechanics module includes application modes for solids, shells and trusses and has built-in solvers for eigenfrequency and frequency response analysis.

One of the characteristics of finite element analysis is the necessity to simplify a model according to the desired outcome. As it was the turbine as a whole which was analysed, details such as nuts, bolts, washers, the maintenance platform, ladder and internal workings were not included in the model as individually they would not affect the bending modes of the tower.

The lattice tower cross-braces and uprights were modelled using 3D truss elements and the structure based on a simplification of a CAD model provided by Gaia-Wind and some basic engineering drawings. The results indicate that this may be an over-simplification, however an alternative method of modelling the tower using solid elements with the correct L-shaped design generated errors when meshing and/or solving. Using a 3D truss defines each cross-brace as a solid cylindrical rod and although this is not the L-shape of the actual braces, the cross-section area was defined as the same. The adjustments and approximations required to transform the CAD model with solid entities into a model using only lines for each brace may cause some inaccuracies in the results, but were necessary in order to be able to solve a model.

Modelling was carried out in stages from a rudimentary hammerhead model through to a full turbine with blades and a foundation. At each stage, an eigenfrequency analysis and frequency response analysis were performed on the model. This determined the frequencies of the bending modes of the turbine as well as a frequency spectrum at a certain point on the model. Combining these results with the analysis of the measurements helped determine which peaks in the measured frequency spectrum originate from the wind turbine and if they relate to a bending mode.

Three different models were used to investigate how geology affects the transfer of vibrations from the turbine to the ground and the propagation of the signal. The ‘soil only’ model contained a solid cylinder with 500 m radius, depth of 1 m and the material and elastic properties for soil. The ‘bedrock only’ model contained a solid cylinder with 500 m radius and depth of 200 m with the material and elastic properties for the underlying bedrock. The ‘soil and bedrock’ model combined the previous two models using a layer of soil with the bedrock underneath. The mesh for these models increased considerably in complexity from the previous ‘turbine only’ models and required interactive meshing on the ground elements in order to generate a mesh which was fine enough to be able to solve the problem with a confident degree of accuracy and with the computational power available (Intel i7 with 16GB RAM). A mesh which is too coarse introduces discretisation errors into the results.

Points were identified in the models at locations equivalent to where the sensors were placed during monitoring. Although these locations were accurate, the wind turbine in the model was always aligned along the x-axis. This may account for some of the discrepancies shown in the results, as during monitoring the nacelle yaws depending on wind direction. This may change the direction of the bending modes and any azimuthal effects generated by this could affect the results at these points.

9.4 Analysis Techniques and Interpretation

Power spectrum density (PSD) functions were calculated on ten minute blocks of the measured data using Welch's method (Welch 1967), then filtered on wind speed. After consideration of a selection of averaging techniques, the median was selected as the the most representative method to use in order to obtain a single PSD vector.

The averaged PSD vector from the data recorded on the tower was compared against the modelled frequency response results in order to verify the models and identify peaks in the PSD. As the height of the sensor positioning up the tower was not recorded for the Gaia-Wind turbines, multiple points on the modelled tower were compared against the measured data. This showed that the higher the point on the tower, the greater the amplitude, however, the difference in amplitude between the two points varies depending on the model and which type of foundation is used, if any.

Using non-linear regression, a relationship between wind speed and the seismic amplitude on the turbine and in the ground was determined. These were found to differ for each of the turbines. At high wind speeds the background noise levels increase, therefore at these wind speeds it is possible that the the signal is being masked by the noise and that the amplitudes which are being selected are actually the background noise. This may explain some of the unpredictability in the Proven 35-2 results at these wind speeds. Additionally this turbine uses self-regulating blades which bend to control rotation speed. It is possible that this effect may be changing the loads on the tower, shifting the peaks and affecting the amplitude up to the wind speed for rated power. Further analysis provided relationships between the seismic amplitude on the turbine, the foundation and in the ground.

Each of the monitored small wind turbines are downwind machines, meaning that the blades point

in the opposite direction to the source of the wind. This is the opposite of large wind turbines which are upwind. The wind will generate a constant force on the back of the tower of a downwind machine, whereas the blades would disrupt the force upwind, causing turbulence. This could result in downwind turbines generating vibrations with higher amplitude than an equivalent upwind turbine and may be one possible explanation for why the measured values of the small wind turbines are considerably higher than the Styles et al. (2005) model predicts. Additionally, each of the sensors were shown to have been positioned in the near-field of the wind turbine with an attenuation factor of r^{-1}, whereas the experiment by Styles et al. (2005) used sensors located in the far-field (with an attenuation factor of $r^{-1/2}$) which may also account for some of the discrepancy between the measured and predicted values.

Polarisation analysis was performed using the data from the seismometer at each site to quantitatively describe the particle motion of the surrounding wave field. The analysis provides an indication of the azimuth, dip and linearisation of the waves. The technique is normally used for identifying the location of a seismic event, where certain wave types are expected in a specific order, based on ground type and velocities. Unlike a seismic event, a wind turbine is a continuous source and therefore waves of different types appear concurrently and may mask each other. The analysis was performed over limited bandwidths and showed that some of the signal detected on the sensor originated from the direction of the wind turbine and that surface waves were the predominant wave type from each of the turbines, although at certain frequencies shear waves were also visible. The technique also proves useful in showing whether signals at a specific frequency are present in the ground that are visible as a peak in the on-tower spectrum but masked by background noise in the in-ground spectrum. However, polarisation analysis cannot provide any indication of amplitude.

9.5 Conclusions

This research has found that small wind turbines generate vibrations which are transferred into and propagate through the ground. However, the frequencies of these signals, their amplitudes and the relationship between the amplitude and wind speed varies for each type of turbine.

Multiphysics modelling of a wind turbine will not replace collecting and analysing field measurements.

However, by combining the two techniques and the analyses conducted on the data, a higher level of confidence can be reached as to which frequencies are generated by the turbine and which originate from other sources. The analyses have revealed the prominent frequencies of the vibrations generated by the turbine, the type of wave being generated and the direction from which it originates (ie the likelihood of it originating from the wind turbine). Additionally, by using modelling, visualisations of the bending modes can be obtained, allowing for peaks seen in the measured data to be matched with the bending modes of the tower.

Model complexity can be adjusted depending on the desired outcomes. If it is only the resonant frequencies of the tower which are required, then a model with blades and nacelle will suffice, however this will not give an accurate estimation of amplitude. For this, the model should also include a solid foundation. Visualisation of the radiation patterns at different frequencies can be obtained by adding a ground layer of bedrock.

The structure of the tower has been shown though modelling and monitoring to make a difference to the vibrations which are generated. The two Gaia-Wind 133 turbines were compared and differences found between the on-tower spectra at various wind speeds in terms of amplitude and shape of the spectrum. Additionally differences were also seen in the effect of seismic amplitude on the tower and in the ground with respect to wind speed. Indeed, this was true for all four wind turbines. However, all of these were found to have a power curve relationship between seismic amplitude on the tower and wind speed and an exponential curve for seismic amplitude on the ground as a function of wind speed. The findings are summarised in table 9-1.

Turbine	Relationship between on-tower seismic amplitude (S_t) and wind speed (w)	Relationship between seismic amplitude at 190/200 m (S_g) and wind speed (w)
Gaia-Wind 133 tubular tower	$S_t \propto w^2$ if $w < 5.5$ m/s	$S_g \propto e^{0.05w}$
Gaia-Wind 133 lattice tower	$S_t \propto \begin{cases} w & \text{if } w \leq 4 \text{ m/s} \\ 100w^{3/2} & \text{if } w > 4 \text{ m/s} \end{cases}$	$S_g \propto \begin{cases} e^{0.3w} & \text{if } w \leq 5 \text{ m/s} \\ 10(e^{0.3w})^{0.1} & \text{if } w > 5 \text{ m/s} \end{cases}$
Proven P35-2	$S_t \propto w^{3/2}$ if $w \leq 9.5$ m/s	$S_g \propto e^{0.08w}$
Endurance E-3120	$S_t \approx 0.0022$ if $w > 1.5$ m/s	$S_g \propto e^{0.15w}$

Table 9-1: *The relationship between seismic amplitude and wind speed for each wind turbine*

For three out of the four turbines, the seismic amplitude on the foundation was shown to be directly proportional to the seismic amplitude on the tower and the seismic amplitude in the ground at 200 m from the turbine (S_g) to be related to the seismic amplitude on the tower (S_t) such that

$$S_g \propto S_t^{0.25}.$$

However, these two relationships did not hold for the data from the Gaia-Wind tubular tower.

By combining the monitoring and modelling results, the first bending modes of the Gaia-Wind 133 tubular tower were identified as occurring at 1.1 Hz and 1.8 Hz; the latter is very close to the blade passing frequency of 1.87 Hz. The second bending modes occur at 9.6 Hz and 11.5 Hz, which are outside the band of interest for Eskdalemuir. A torsional mode is present at around 7.8 Hz. The blade rotation frequencies are visible in the measured spectrum of each of the fixed speed turbines from the sensors located on the tower, but are not visible in the models due to their static nature. For this turbine, peaks at 4.2 Hz, 6.7 Hz, 8.1 Hz and 9.5 Hz are seen on the tower and at 190 m.

Polarisation analysis, modelling and attenuation analysis each indicated that the 4.2 Hz peak seen in the frequency spectrum for the Gaia-Wind tubular tower originated from a source other than the turbine: most likely from the direction of a wind farm less than 5 km NE of the wind turbine. The peak is visible in the spectrum from the sensor attached to the tower as well as those in the ground, which indicated that the wind turbine absorbs energy and vibrations as well as generating them.

Modelling of the Gaia-Wind lattice tower revealed no peaks in the frequency response analysis below 10 Hz. From the monitoring results, all peaks apart from two (under 10 Hz) are attributed to blade rotation rate harmonics. However these two frequencies are not transmitted into the ground. Frequencies at 9.35 Hz and 11.2 Hz are visible at 190 m and originate from the direction of the turbine. Interestingly these are close to the frequencies of the two second bending modes of the Gaia-Wind tubular tower.

The Endurance E-3120 wind turbine generates frequencies at 4.2 Hz, 5 Hz, 6.3 Hz, 7.1 Hz, 7.9 Hz and 8.6 Hz (plus others greater than 10 Hz) which are visible 200 m from the turbine. These frequencies each occur very close to blade rotation frequencies and the source of each is in the direction of the

wind turbine. It is not clear which frequencies correspond to bending and torsional modes.

The Proven 35-2 is a variable speed wind turbine, regulated by the pitching of the blades. This causes frequencies to shift with wind speed up to the speed at which rated power is recorded. Frequencies at 1 Hz (most likely the first bending mode), 3.0 Hz, 4.45 Hz, 5.1 Hz and 6.4 Hz have each been shown to originate from the direction of the wind turbine.

It is predominantly surface waves which are generated by the wind turbines. However, shear waves are also detected at some frequencies, especially those which are not attributed to blade rotation harmonics.

The Styles et al. (2005) model does not hold for these small wind turbines, with the estimation of the amplitude much lower than was measured. One possible reason for this is the noise model contained within the measured data being a much more important component than for the large wind turbines. It is unclear from the measured data whether small turbines generate vibrations at similar amplitudes to large turbines, as measurements have not been obtained in the far-field for small wind turbines and conversely the near-field for large wind turbines. However, using the measurements of the small wind turbines as a basis and applying a $1/\sqrt{r}$ with linear attenuation model (as used in the Styles et al. (2005) model), at 50 km for a 50 kW wind turbine, the predicted amplitude would be 0.06 nm which would add considerably to the noise budget around the Eskdalemuir station and is much more than the 0.00001 nm limit suggested by Bowers and Styles (2010 to MoD).

The combination of techniques explored in this thesis have been proven to be able to successfully identify the frequencies of the vibrations originating from a wind turbine, the rate at which these decay, the relationship of the amplitude with respect to wind speed, the corresponding bending mode, visualisation of the radiation pattern, the type of wave and confirmation of the direction of the source.

9.6 Recommendations

Following this research, it has been shown that not all small wind turbines generate the same vibrations, in terms of frequency and amplitude. The project has raised many more questions then originally

envisaged, many of which will require additional monitoring or more computing power than was available for this project. On this basis the following additional areas of research are recommended.

9.6.1 Monitoring

The results show that at some sites the instrument noise of the accelerometers is masking the low amplitude signal. For this reason, it is advisable that for any further monitoring, seismometers are used for all in-ground monitoring. As each sensor is self-contained there are no cables trailing across the ground. The system will also be more resilient, as should one sensor fail, data can still be obtained from the others; whereas with the system used in this project, should the digitiser fail, data is lost across all accelerometers.

Using seismometers at all locations will also increase the amount of data gathered, with the ability to record three components at each location. This will increase the confidence levels of any polarisation analysis, as it can be performed on each sensor and the azimuthal results cross-referenced to find the source of the signal.

A short period of monitoring prior to the full monitoring process, using a seismometer which can be quickly deployed, will provide information on the background noise levels of the site. Based on the levels seen at the four sites used in this research, a decision could be made as to whether the site is too noisy and if so monitoring ceased there and an alternative site found.

Monitoring for a longer period of time will produce a larger range of wind speeds. This is essential for establishing equations which relate wind speed to amplitude. Ideally, wind speeds should be comparable to those at Eskdalemuir, so that a more accurate estimation of amplitude can be gained. Regular checks on what wind speeds have been achieved during monitoring will enable a decision to be made as to whether a large enough variation and maximum wind speed has been achieved or whether monitoring should continue. Ideally, monitoring should continue until a large enough range has been obtained.

Some of the turbine manufacturers have data from the wind turbine transmitted back to them so that

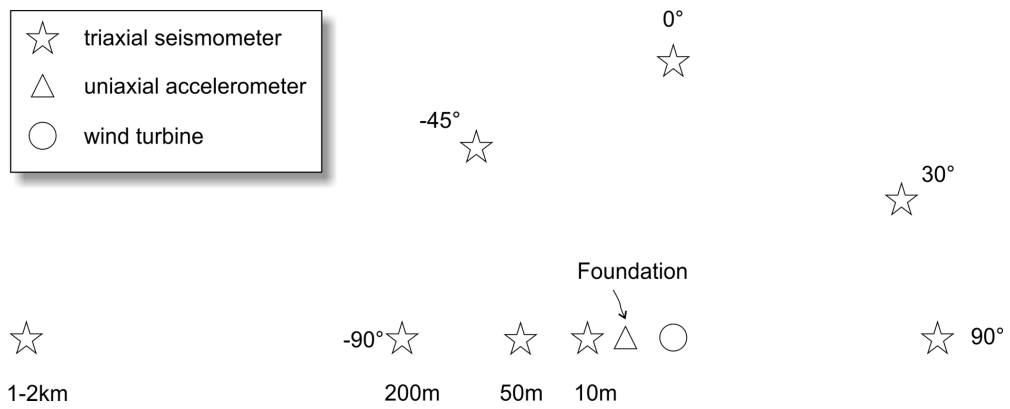

Figure 9-1: *Possible sensor layout for further monitoring using three-component seismometers*

constant health monitoring can be carried out. The Endurance E-3120 also has a wireless network to transmit data from the nacelle to the control box on the ground. A telemetry setup using mobile phones or the internet, transmitting data back to Keele, would enable longer periods of recording to be carried out without the need to visit the site and download wind speed and vibration data. Such a system would enable a decision to be made remotely as to when best to withdraw the equipment as well as being able to detect if there are issues with the monitoring (eg power cuts) and to respond accordingly.

This project only investigated sensors located in a straight line. Adding more sensors at alternative locations will help to understand the radial effects from the wind turbine and can be used to further verify models incorporating the ground. Figure 9-1 shows one possible layout using five three-component seismometers, arranged at various degrees in an arc with the turbine in the centre. Three additional seismometers are located in a line at 10 m, 50 m and 1-2 km, so that attenuation can be calculated. The more sensors positioned on this line, the more accurate the attenuation calculation will be. In addition a single-component accelerometer would be positioned on the foundation, as well as the two attached to the tower. In order to get the maximum amplitude, it is hypothesised that the line of sensors should be placed along the dominant wind direction or at 90°to this (along the lines of the two variations of bending mode).

Placing a seismometer at 1 km or further will allow the far-field to be examined. However, based on the PSD plots at 200 m, it is unlikely that much signal would be seen above background noise levels; although polarisation analysis may still reveal a signal.

Only one of each type of turbine was monitored for this project. Performing the same analysis on an additional turbine of the same specifications at an alternative location will allow comparison of the two spectra. This will reveal which peaks are common to both turbines, increasing the confidence that the peak originates from the turbine. If the second turbine is located on different geology to the original, the effects of geology can also be investigated.

Monitoring a site prior to the installation of a wind turbine will provide an 'image' of the background noise. This could then be 'subtracted' from the monitored data post-installation to find the vibrations generated by the turbine, removing any vibrations from other sources. Removing this will also provide a true amplitude of the signal from the turbine, possibly showing that the amplitudes are not high enough to have a significant effect on the capabilities of the Eskdalmuir seismic array.

9.6.2 Data Analysis

Statistical analysis of the data will examine confidence levels of the seismic amplitude and whether it can be confirmed with 90 or 95% confidence that the amplitudes will not have a detrimental effect on the capabilities of Eskdalemuir. It can also show that the relationship derived between seismic amplitude and wind speed is within a 90 or 95% confidence level.

9.6.3 Further Modelling

The multiphysics modelling in this project has only examined a single turbine. This can be taken further by adding multiple turbines to the model in order to answer questions including

- How do multiple turbines interfere (or resonate) with each other? Does the geometry of the wind farm change this?
- If a force is added to one turbine, but not to the other, can the vibrations still be seen on the second? This will show that the turbines absorb energy as well as generate it.
- Does placing wind turbines in a line create an antennae affect, directing the vibrations at a specific angle?

Comsol is capable of running models to answer each of the questions posed above, however as the complexity of the model increases, memory and CPU demands will also increase.

The effects of geology on the amplitude and frequency peaks have only been touched on in this project. Further modelling using precise depths of soil and superficial deposits at sites will provide a better understanding of the effects of geology on the signal from the wind turbine.

Each of the turbines analysed during this project has a different ratio of mass of nacelle and blades to mass of tower. Modelling can be used to investigate what effect this ratio has on the frequency and amplitude of the vibrations.

9.6.4 Other Applications of the Data

Seismic interferometry uses passive seismic background noise to generate virtual sources. Signals from two sensors are cross-correlated to generate a new virtual source which is the response that would appear if one location was a source and the other a receiver. The technique is a large and relatively young area of research which can have many uses. Shapiro et al. (2005) and Gerstoft et al. (2006) use the process to obtain velocity models and tomographic images of the medium between the sensors. Other practical applications of the technique include reservoir modelling (Bakulin & Calvert 2006), salt edge imaging (Willis et al. 2006, Hornby & Yu 2007) and estimating building responses to ground motion (Snieder & Safak 2006). With continuous data, this dataset lends itself to an analysis using interferometry.

The Applied and Environmental Geophysics group at Keele has access to large amounts of data from previous studies of large wind turbines. Combining this data with the data from this research, comparison can be performed to see if there are any common relationships which link hub height, power or rotor diameter between turbines with seismic amplitude. This will help gain a broader understanding of whether there is a cut off in these parameters between large and small (and possibly medium) wind turbines and what this value is.

9.7 Consequences for Eskdalemuir

Prior to this research, small wind turbines were bound by the same planning guidelines as the large turbines with regard to the Eskdalemuir Seismic Array (EKA), with a 50 km consultation zone around the station and a maximum permissible background noise budget of 0.336 nm in place.

In February 2010, with the noise budget close to filled, the MoD placed a blanket ban on all new wind turbines, large and small, within 50 km of EKA. In light of the large number of applications for small wind turbines within the zone, it was suggested by Bowers and Styles (2010 to MoD) that an interim guideline for small wind turbines might be as follows;

> *We recommend that contributions with a predicted level of less than 0.00001 nm can be considered negligible. This recommendation for contributions from small- and micro-wind turbines should be considered interim, until trials have quantified the source term from such turbines and the 2005 model and guidelines adjusted if necessary. The 0.00001 nm level is roughly equivalent to one micro turbine (1.5 kW) at 30 km, or one small turbine (50 kW) at 50 km. The interim level should allow consent for small turbines with $<$ 10 kW in the zone 40-50 km from the seismometer array.*

This assumed that micro and small turbines generated vibrations in the 4-5 Hz frequency band of interest, which are transferred into the ground and propagate to Eskdalemuir.

Following the research on the two Gaia-Wind turbines, new interim guidelines were introduced by the MoD to determine whether specific design-types of small wind turbines could be permitted in the consultation zone. These guidelines state that

> *The 10 km exclusion zone for building wind turbines around EKA remains. The interim limit of 0.00001 nm remains for the statutory consultation zone from 10 to 50 km around EKA unless after appropriate research [by] AEG... suitable report-based evidence... [will] allow assessment of the vibration frequency-response for a specific design-type of small wind turbine. [If] the assessment... confirms that the specific small*

> *turbine design-type presented has been shown to excite negligible seismic energy in the frequency passband of interest for EKA, and therefore does not contribute to the noise budget, then MoD will... confirm [this] specific design-type of small wind turbine... can now be accepted in the statutory consultation zone from 10 to 50 km around EKA.*

This project set out with the aim of attempting to determine whether small wind turbines generate vibrations at frequencies in the band of interest for Eskdalemuir and whether the Styles et al. (2005) model was correct in its estimation of their amplitudes. It has been found that there is no common set of frequencies generated by small wind turbines and that some do generate vibrations in the frequency band of interest. Additionally, the measured vibration amplitudes considerably exceed those predicted by the Styles et al. (2005) model.

The Styles et al. (2005) model was originally derived from one type of turbine, and applied to other large machines with the assumption that the design specifications with regard to vibration, which has significant implication for maintenance and lifetimes, of all large turbines was relatively similar. As might be expected, large wind turbines appear to be constructed to higher design specifications than small wind turbines. They are designed to very high precision standards to minimise risk of failure and error in design and production.

Small wind turbines are produced for different markets on a much smaller budget and at much lower eventual price points and do not contain a lot of the technology required to ensure the design life-times and noise and vibration minimisation which is required for the large turbines. This may account for some of the difference in the model estimation and measurements. Additionally, this means that there is a great deal of variety in the design of small wind turbines.

Due to this variability, confirmed by the results of this study, it is not possible to recommend that small wind turbines be automatically allowed to be constructed within the consultation zone simply because they fall below the 50 kW generation level. Each machine-type should be considered on an individual basis, examining the frequencies generated and the transfer of the signal into the ground. Further work may then allow the consultation zone to be reconsidered on a per-turbine basis. However, it is unlikely that one common vibration model, similar to the Styles et al. (2005) model, which in itself is likely to be re-examined in the light of more recent work, can be derived for all small turbines.

Appendix A

Bespoke Matlab Classes for Processing Field Data

Since version R2008a, it has been possible to programme objects in Matlab. This object-orientated approach means that the code only needs to be written once and an object created specific to each turbine. An additional advantage to this approach is that each set of data will be processed identically.

Five classes have been developed to aid the data processing; superseismic, seismic, chunked, weather and weatherType. Each class is summarised in the following sections.

A.1 *Superseismic*

The *superseismic* class is a top level class which contains basic information about seismic data. The class contains a combination of public, private and abstract properties. The two abstract properties, *data* and *ns* must be defined in any class which inherits *superseismic*.

The main properties which are publicly available outside of this class are:

- *startTime* - the start time of the data (a Matlab date number), by default this is set to midnight on 1 January 1970.

- *fs* - the sampling frequency, by default this is set to 1.

Additionally there is a virtual property, which does not contain data directly, instead data is retrieved from other properties and used to calculate the value of this property when the property is used.

- *time* - a time vector, this is constructed from *startTime*, *fs* and *ns* when the property is used.

Trying to set the value of this property manually will result in an error.

The three abstract properties are:

- *data* - the seismic data, this is defined as necessary in subclasses to contain the required number of channels.
- *ns* - the number of samples of data held within the class in any one component.
- *endTime* - the time of the last sample of data, this is a Matlab date number.

The class contains just one constructor

S = SUPERSEISMIC(STARTTIME, FS) which creates a new superseismic object *S* with a sampling rate of *FS* and a start time of *STARTTIME*.

The only methods associated with this class are two static methods: *fileList, readGCFList.*

The methods associated with the superseismic class are written to assist with adding data into Matlab from Güralp GCF files (section 4.4.1.1), the data files generated by the digitiser. They do not act upon a specific instance of the class and do not perform any action on an individual class, as such they do not require an instance of the class as an input, unlike ordinary methods.

The main file associated with the task is *readGCFList*, which takes as input arguments, a list of files contained within a cell array and the sample rate (samples per second) of the data. If the sample rate provided is an empty vector, the value is set to that provided by the first file read. For each file which is read, the sample rate is checked against the value held from the input argument or first file and

an error returned if there is not a match. For each stream ID (which includes the instrument serial number and component) the initial start time (ist) and sample rate are returned. The recorded data is returned in a matrix, sorted into time order, with each column representing a unique stream ID. Should an error occur, the id of the error is returned, otherwise 0 is returned if the method completed successfully. The command for calling this function is:

[errorid, data, sps, ist, streamid] = superseismic.readGCFlist(filelist, sps);

The function uses the Güralp *readgcffile()* function, which is available from their website (www.guralp.com/support/software) and allows GCF files to be read directly into Matlab. This function requires a filename as an input argument and returns the samples, stream ID, sampling rate and initial start time.

The file list supplied to *readGCFlist* as an argument is generated using the command:

newfilelist = superseismic.fileList(folder, channel);

The function creates a list of GCF files contained within the root folder and subfolders passed as an argument, these are filtered based on the channel value also provided as an argument.

A.2 *Seismic*

The *seismic* class stores a set (or sets) of seismic data in vectors sampled over a given time period. It contains functions and properties relevant to the processing of such data and is a subclass of *superseismic*, inheriting its properties and methods.

There are four possible constructors for the *seismic* class:

S = SEISMIC creates an empty seismic object.

S = SEISMIC(DATA) creates a seismic object *S* using *DATA*. *DATA* can be a structure or 3xn matrix. By default, the start time is set to 0 and the frequency rate to 1 sample a second.

S = SEISMIC(DATA, STARTTIME) creates a seismic object *S* using *DATA* and the start time in *STARTTIME*. By default, the frequency rate is set to 1 sample a second.

S = SEISMIC(DATA, STARTTIME, FS) creates a seismic object *S* using *DATA*, the start time in *STARTTIME*, and the frequency rate in *FS*.

The empty vector [] can be used for any of the above arguments if the default value is required.

Property-value pairs can be added after the *DATA*, *STARTTIME* and *FS* arguments in the form

'PropertyName1', PropertyValue1, ...

that set the following additional properties of the seismic object:

- 'name' - a string that specifies the name of this seismic object.
- 'endTime' - this sets the end time of the data if only the start and end times are known. The sampling frequency will be calculated from this.
- 'nanorzero' - This should be NaN or 0, depending on which the empty values for the data arrays should be set to. The default is NaN.
- 'xdata' - a vector containing data values just for the x direction.
- 'ydata' - a vector containing data values just for the y direction.
- 'zdata' - a vector containing data values just for the z direction.
- 'units' - the units data is measured in.
- 'comment' - a string containing any applicable comments.

The class contains a selection of methods for processing the data:
detrend, filtfilt, norm, plot, psd, toAcceleration

The methods contained within the class exist to simplify the post processing procedure of the data for each instance. Some of the methods simply overload the already built-in Matlab functions, eg *plot, detrend* and *filtfilt*, others are additional functions for performing specific calculations.

The raw data must be converted into acceleration data before any processing is performed on it. This is performed using the *toAcceleration* method, which multiplies the raw data by a calibration factor dependant on the stream id contained within the specific seismic object.

Power Spectrum density plots are generated using the *psd* method. In addition to the seismic object, this method also requires a start and end time for generating a plot using data only between these times. The method calls the Matlab built-in *pwelch* function from the Signal Processing toolbox (MathWorks 2010b). Full details of the Welch method can be found in section 2.4.4. The function is called using the command:

[Pxx, f] = pwelch(data, window, noverlap, nfft, fs);

The method is called twice using an eight segment Hamming window with a 50% overlap. The value of *nfft* (the length of the fft) is 4096 on the first occasion and the total number of samples contained with the time period on the second run. The sampling rate (*fs*) is obtained from the seismic object. The two variables returned by the function are the power spectrum (*Pxx*) and the corresponding frequencies (*f*).

The *seismic.psd* method is called using the command:

[XF, f, XF2, f2, t, h] = S.psd(startTime, endTime, print)

This populates the Matlab workspace with six additional variables

- *XF* - the power spectrum of the data in *S* between *startTime* and *endTime* using an *nfft* of 4096.
- *f* - the frequencies corresponding to *XF*.
- *XF2* - the power spectrum of the data in *S* between *startTime* and *endTime* using an *nfft* of *S.ns*.

- *f2* - the frequencies corresponding to *XF2*.
- *t* - the time vector from *startTime* to *endTime*.
- *h* - a figure handle for viewing the results.

A.3 *Blocked*

The *blocked* class is similar to the *seismic* class and is a subclass of *superseismic*. It contains functions and properties for storing data in blocks of a given time interval, eg 10 minutes. It inherits the properties and methods of the superclass.

The class contains a combination of public and private properties. The main properties required by the class, listed below, are available publicly to use, however, attempting to set the values of the properties explicitly is restricted. The values are set internally through public methods within the class, eg on instantiating the class or using *generatePSD*.

- *data* - the blocked data matrix. Each column contains data for one block, eg 10 minutes.
- *blockinterval* - the length of the block in seconds.
- *psd* - a matrix containing the psd for each block in each column.
- *f* - the frequency vector relating to the psd matrix.
- *ns* - the total number of samples contained in the data matrix.

Additionally there are three dependant properties which do not physically store data, but rely on data stored in other properties to calculate the output each time the property is used.

- *blockTimes* - a vector containing the start times of each block.
- *numblocks* - the number of blocks contained in the data matrix.
- *dispPSD* - the displacement PSD matrix.

To instantiate the class, there are three possible constructors:

C = BLOCKED creates an empty blocked object.

C = BLOCKED(ROOT, SENSOR, STARTDATE) creates a blocked object *C* using data from a sensor with stream ID *SENSOR*, stored in the *ROOT* directory from a particular *STARTDATE*.

C = BLOCKED(ROOT, SENSOR, STARTDATE, ENDDATE) creates a blocked object *C* using data from a sensor with stream ID *SENSOR*, stored in the *ROOT* directory between a *STARTDATE* and *ENDDATE*.

The empty vector [] can be used for any of the above arguments, except *ROOT*, if the default value is required. In the case of *SENSOR*, using the empty vector would prompt the program to ask the user to chose the correct file based on those stored in the directory.

Property-value pairs can be added after the required arguments allowing the following additional properties of the blocked object to be set.

- 'name' - a string that specifies the name of this object.
- 'blocklength' - the length of each block in seconds.
- 'units' - the units the data is measured in.
- 'comment' - a string containing any applicable comments.

As with the *seismic* class, the *blocked* class contains a selection of methods for processing the data: *boxcarpsd, generatepsd, integratepsd, toAcceleration*

The *toAcceleration* method converts the raw data into acceleration by multiplying it by a calibration factor. If the data is originally from a seismometer it is also differentiated to transform the velocity data into acceleration.

The remaining three methods are all focused on generating and manipulating the power spectrum density (psd) of the blocked data. The psd is stored within the *psd* property in the class and generated with a call to the *generatepsd* method. The method calls the Matlab built-in *pwelch* function with

a 60 second hamming window and 50% overlap. See appendix A.2 for more details on the pwelch function and section 2.4.4 for an explanation of Welch's method.

The root mean squared (rms) value between two frequencies is generated using the displacement psd property, *dispPSD* and the *boxcarpsd* and *integratepsd* methods. When the *dispPSD* property is used the psd stored in the *psd* property is converted into a displacement psd (section 2.4.5). A box car window between two frequencies is applied to the psd using the function call

bc = C.boxcar(freqRange, displacementPSD)

which will return a matrix the same size as the displacement psd matrix, but containing zeros for all values outside of the frequency range. The integration of the psd is performed using the *integratepsd* method, which takes as arguments the blocked object and the matrix containing the psd's to integrate, eg the *boxcar* output. The built-in Matlab function *trapz* is used to calculate the integration numerically using the trapezoidal method and called using the command

Z = trapz(frequencies, psd)

The function returns a vector of values Z equating to the root mean squared value for each block (see MathWorks (2010d) for more details of the *trapz* function.)

A.4 *WeatherType*

The *weatherType* class is a simple class which holds weather data, with each instance of the class relating to a specific type, eg solar, wind speed. The class contains four public properties:

- *data* - a vector containing the data, by default this is empty.
- *units* - the units the data is in, by default this is set to 'not assigned'.
- *name* - a string that specifies the name of this weatherType object.
- *comment* - a string containing any applicable comments.

The only value which is required within the constructor of the class is a vector containing the data. The remaining three values can be set as property value pairs in a similar fashion to those with the previous classes already discussed or by using the set method. The class contains one virtual property, *ns*, the number of samples.

The class has been created purely for data storage and the only additional method associated with it is *notempty()*, which returns a true or false value dependant on whether the class contains data or not.

A.5 *Weather*

The *weather* class is designed to specifically deal with data collected using a Power Predictor. It can contain data relating to wind speed, wind direction, solar and temperature, each of which are stored as a separate instance of the *weatherType* class. All data contained within a instance of the *weather* class should be for the same time period, which is stored in the property *startTime* and have the same sampling rate, stored in the property *fs*.

There are four possible constructors for the *weather* class:

W = WEATHER creates an empty weather object.

W = WEATHER(DATA) creates a weather object *W* using *DATA*, which should be a structure. By default, the start time is set to '01/01/1970' and the frequency rate to 1 sample a second.

W = WEATHER(DATA, STARTTIME) creates a weather object *W* using *DATA*, which should be a structure and the start time defined by *STARTTIME*.

W = WEATHER(DATA, STARTTIME, FS) creates a weather object *W* using *DATA*, which should be a structure, the start time defined by *STARTTIME* and the frequency rate as defined by *FS*.

As with the *seismic* and *blocked* classes, the empty vector [] can be used for any of the above arguments if the default value is required. Additional properties can be entered as property value

pairs. The available options are:

- 'name' - a string that specifies the name of this weather object.
- 'endTime' - this sets the end time of the data if only the start and end times are known. The sampling frequency will be calculated from this.
- 'windspeed' - a vector containing data values just for the wind speed.
- 'winddirection' - a vector containing data values just for the wind direction.
- 'solar' - a vector containing data values just for the solar power.
- 'temperature' - a vector containing data values just for the temperature.
- 'windspeed units' - the units wind speed is measured in. The default is 'm/s'.
- 'winddirection units' - the units wind direction is measured in. The default is 'degrees'.
- 'solar units' - the units solar is measured in. The default is 'Kwh/m2'.
- 'temperature units' - the units temperature is measured in. The default is 'C'.
- 'comment' - a string containing any applicable comments.

The power predictor data file is a simple ascii file containing seven columns of data (see section 4.4.1.2 for more information). The method *readPowerPredictor()* reads in the data from a specific file, passed in as an argument and adds a populated *weather* object to the Matlab workspace.

Reading of the input text file is simplified using the Matlab built-in function *textscan()* called with the command:

```
data = textscan(fopen(txtfile, 'r'), '%s %f %f %f %f %f %f', 'HeaderLines', 8,...
    'Delimiter', '\t', 'ReturnOnError', true, 'CommentStyle', '**');
```

Once in Matlab, the data is calibrated to ensure it is in the correct units before being included in the new *weather* object.

Appendix B

Additional Images of Gaia-Wind 133 Tubular Tower Models

This appendix contains a selection of images of the results of the Gaia-Wind 133 tubular tower models which are discussed in chapter 8.

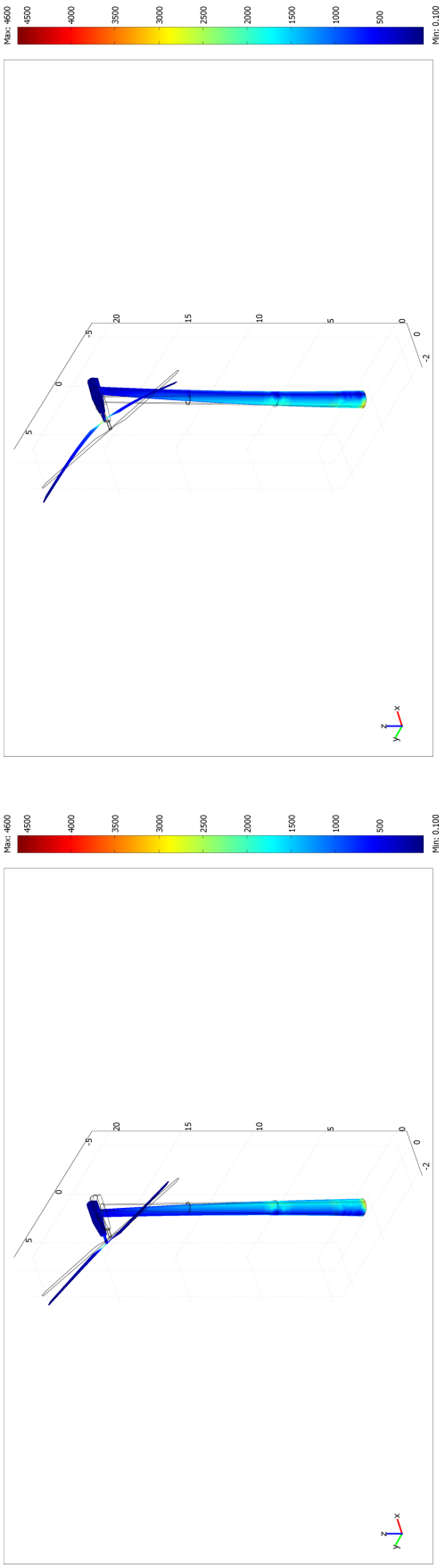

a. First bending mode A

b. First bending mode B

c. Second bending mode A

d. Second bending mode B

Figure B-1: *The first and second bending modes of the tubular tower model with no foundation. The colour scale indicates the amount of stress on the turbine (in megapascals [MPa]) and the deformation an indication of the displacement (scaled for visual effect).*

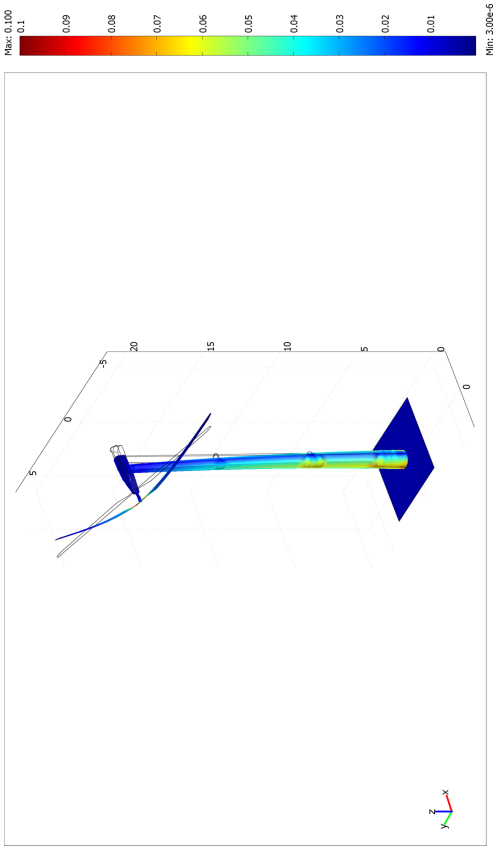

a. First bending mode A

b. First bending mode B

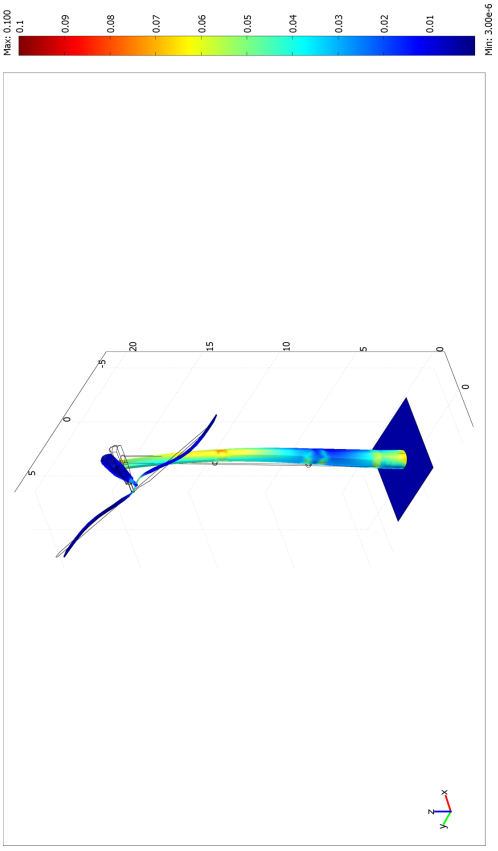

c. Second bending mode A

d. Second bending mode B

Figure B-2: *The first and second bending modes of the tubular tower model with a shell foundation. The colour scale indicates the amount of stress on the turbine (in megapascals [MPa]) and the deformation an indication of the displacement (scaled for visual effect).*

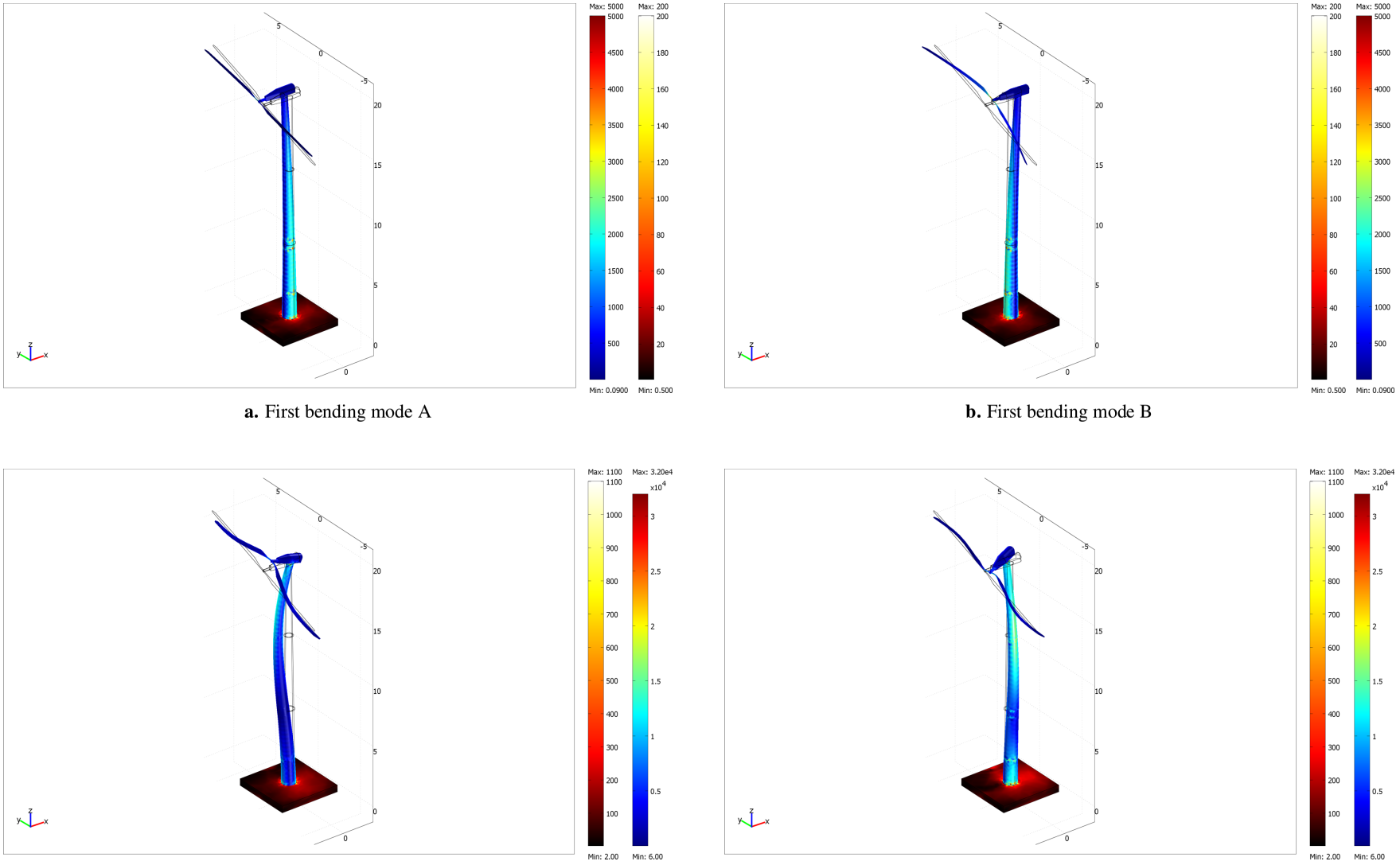

a. First bending mode A

b. First bending mode B

c. Second bending mode A

d. Second bending mode B

Figure B-3: *The first and second bending modes of the tubular tower model with a solid foundation. The rainbow colour scale indicates the amount of stress on the turbine (in megapascals [MPa]) and the thermal colour scale (black through red to white) the amount of stress on the foundation (in megapascals [MPa]). The deformation gives an indication of the displacement (scaled for visual effect).*

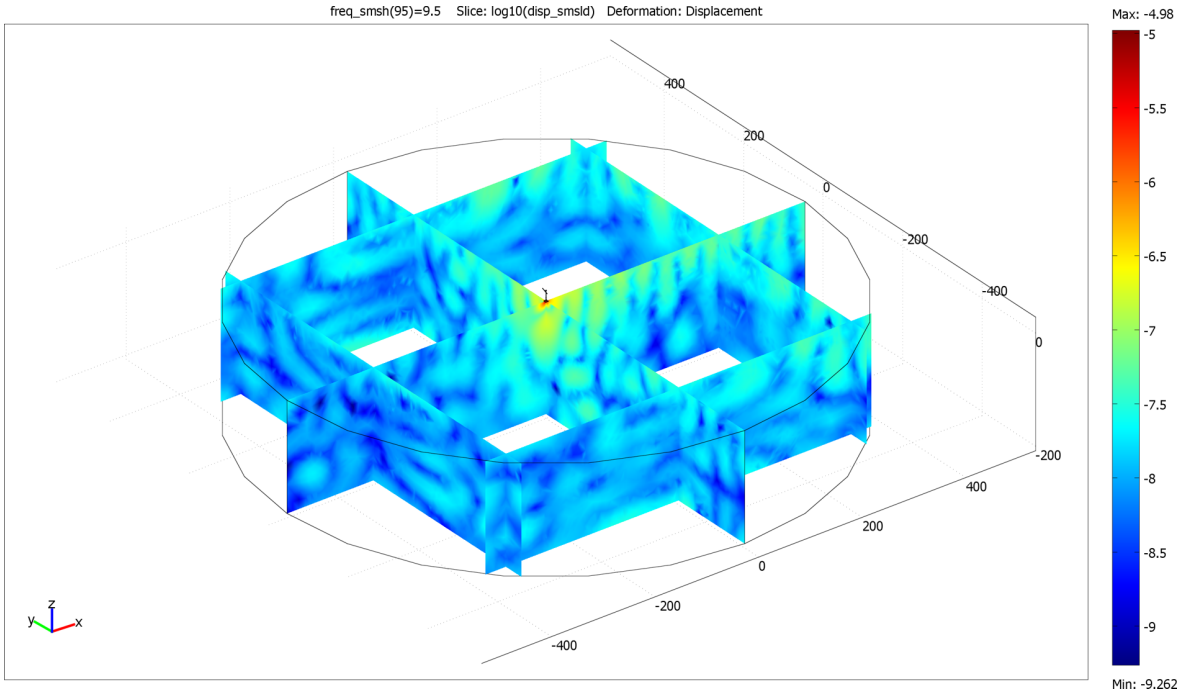

Figure B-4: *Three slices in the x and y directions through the ground of the bedrock model (no soil layer) at 9.5 Hz. The rainbow colour scale (blue to red) indicates the amount of total displacement (in* $\log_{10}$ *metres) in the ground.*

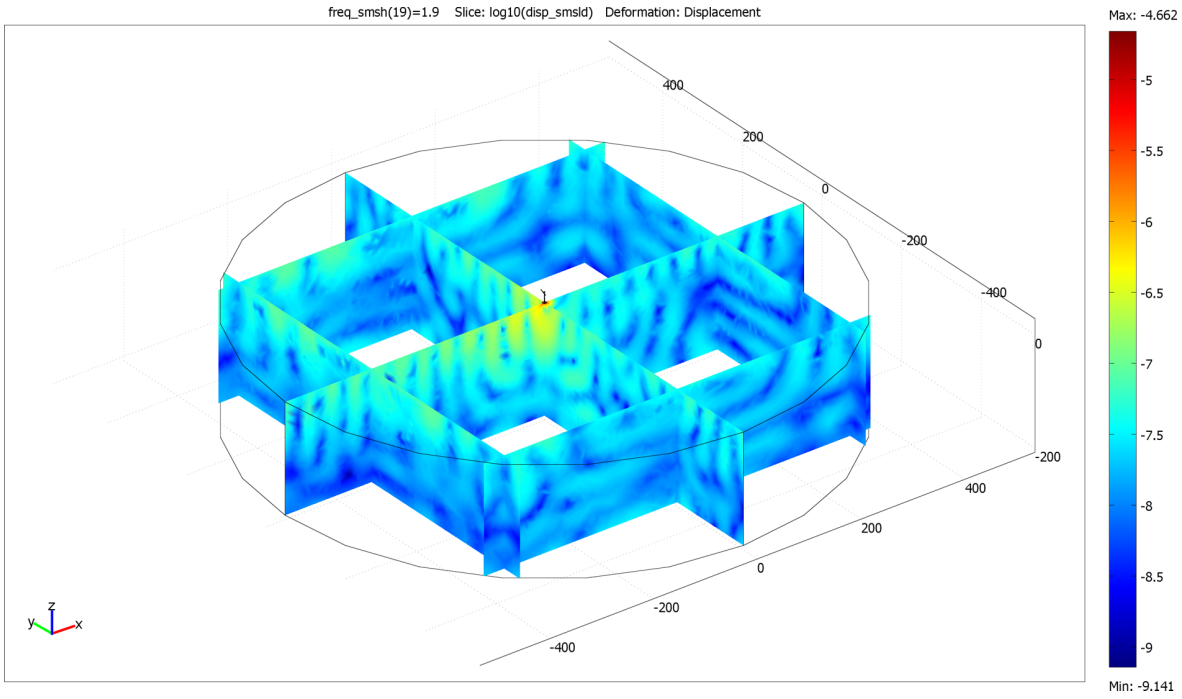

Figure B-5: *Three slices in the x and y directions through the ground of the bedrock model (no soil layer) at 1.9 Hz. The rainbow colour scale (blue to red) indicates the amount of total displacement (in* $\log_{10}$ *metres) in the ground.*

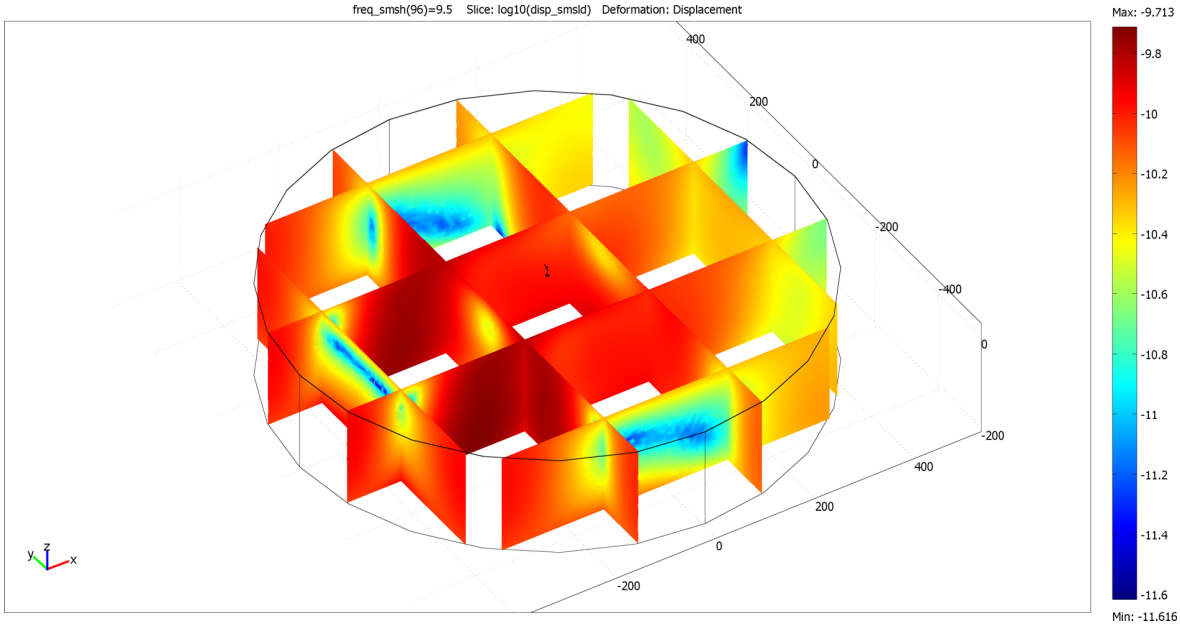

Figure B-6: *Three slices in the x and y directions through the ground of the soil and bedrock model at 9.5 Hz. The rainbow colour scale (blue to red) indicates the amount of total displacement (in* $\log_{10}$ *metres) in the ground.*

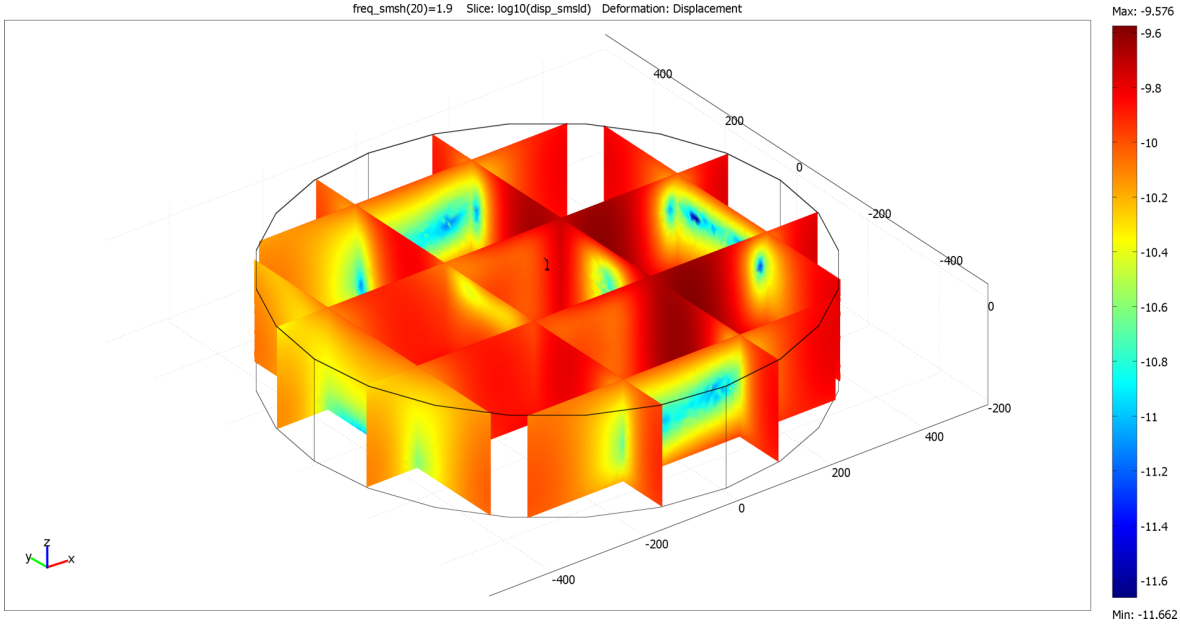

Figure B-7: *Three slices in the x and y directions through the ground of the soil and bedrock model at 1.9 Hz. The rainbow colour scale (blue to red) indicates the amount of total displacement (in* $\log_{10}$ *metres) in the ground.*

References

Aki, K. & Richards, P. G. (1980), *Quantitative Seismology*, volume 2, W. H. Freeman and Company, ISBN 0716710595.

AlHamaydeh, M. & Hussian, S. (2011), Optimized frequency-based foundation design for wind turbine towers utilizing soil-structure interaction, *Journal of the Franklin Institute*, *348*(7), 1470–1487, doi:10.1016/j.jfranklin.2010.04.013.

Bakulin, A. & Calvert, R. (2006), The virtual source method: Theory and case study, *Geophysics*, *71*, SI139, doi:10.1190/1.2216190.

Balmer, J. A., Holder, D. J. & Owen, H. L. (2000), Measurement of Ground Vibrations and Calculation of their Effect on the Diamond Light Source, *Proceedings of EPAC 2000*, pp. 2328–2330, Vienna, Austria.

Bartolini, R., Huang, H., Kay, J. & Martin, I. (2008), Analysis of Beam Orbit Stability and Ground Vibrations at the Diamond Storage Ring, *Proceedings of EPAC 2008*, pp. 1980–1982, Genoa, Italy.

Bazeos, N., Hatzigeorgiou, G. D., Hondros, I. D., Karamaneas, H., Karabalis, D. L. & Beskos, D. E. (2002), Static, seismic and stability analyses of a prototype wind turbine steel tower, *Engineering Structures*, *24*(8), 1015–1025, doi:10.1016/S0141-0296(02)00021-4.

Bechly, M. E. & Clausen, P. D. (1997), Structural Design of a Composite Wind Turbine Blade Using Finite Element Analysis, *Computers and Structures*, *63*(3), 639–646, doi:10.1016/S0045-7949(96)00387-2.

Bowers, D. (2010), The Seismometer Array at Eskdalemuir, Scotland (EKA).

Brisbourne, A., Horleston, A., Hawthorn, D. & Lane, V. (2010), *6TD & ESPD Field Methods*, SEIS-UK. Version 5.6.

Burton, T., Sharpe, D., Jenkins, N. & Bossanyi, E. (2001), *Wind Energy Handbook*, John Wiley & Sons Ltd, ISBN 0471489972.

Butterworth, S. (1930), On the Theory of Filter Amplifiers, *Wireless Engineer*, *7*, 536–541.

BWEA (2005), BWEA Briefing Sheet: Small Wind Energy Systems.

Carne, T. G., Lobitz, D. W., Nord, R., Arlo & Watson, R. A. (1982), Finite Element Analysis and Modal Testing of a Rotating Wind Turbine, Technical Report SAND82-0345, Sandia National Laboratories. Contract DE-AC04-76DP00789.

Chapman, C. (2006), *Fundamentals of Seismic Wave Propagation*, Cambridge University Press, ISBN 9780521815383.

Cheung, Y. K. & Yeo, M. F. (1979), *A Practical Introduction to Finite Element Analysis*, Pitman Publishing Ltd, ISBN 0273010832.

Ciang, C. C., Lee, J.-R. & Bang, H.-J. (2008), Structural health monitoring for a wind turbine system: a review of damage detection methods, *Measurement Science and Technology*, *19*(12), IOP Publishing Ltd, doi:10.1088/0957-0233/19/12/122001.

Clark, S. P. (editor) (1966), *Handbook of Physical Constants*, Memoir 97, The Geological Society of America, revised edition.

Clough, R. W. (1960), The Finite Element Plane Stress Analysis, *Proceedings of the 2nd ASCE conference on Electronic Computation*, pp. 345–378, Pittsburgh, Pa.

Comsol Multiphysics (2008a), *Comsol Reference Guide*, Version 3.5a.

Comsol Multiphysics (2008b), *Comsol User's Guide*, Version 3.5a.

Comsol Multiphysics (2008c), *Structural Mechanics Module User's Guide*, Version 3.5a.

Cooley, J. W. & Tukey, J. W. (1965), An algorithm for the machine calculation of complex Fourier series, *Mathematics of Computation*, *19*(90), 297–301, doi:10.1090/S0025-5718-1965-0178586-1.

Coulson, C. A. & Jeffrey, A. (1977), *Waves: A mathematical approach to the common types of wave motion*, Longman Mathematical Texts, Longman, 2nd edition, ISBN 0582449545.

CTBTO (2009), AS104, Eskdalmuir, Scotland, Online. URL http://www.ctbto.org/the-treaty/status-of-signature-and-ratification/.

CTBTO (2012), Status of Signature and Ratification, Online. URL http://www.ctbto.org/the-treaty/status-of-signature-and-ratification/.

Danish Wind Industry Association (n.d.), Wind Turbines: Horizontal or Vertical Axis Machines?, Online. URL http://wiki.windpower.org/index.php/Horizontal/vertical.

Davies, A. J. (1980), *The Finite Element Method*, Oxford Applied Mathematics and Computing Science Series, Oxford University Press, ISBN 0198596308.

Diamond Light Source (2011), Online. URL http://www.diamond.ac.uk/.

Endurance Windpower Ltd (2011a), Online. Last accessed: 26/08/2011, URL www.endurancewindpower.co.uk/.

Endurance Windpower Ltd (2011b), E-3120 50kW Wind Turbine, Product Brochure.

Enercon GmbH (2010), ENERCON Wind energy converters: Product overview.

England, R. J. E. (2007), *Microseismic and Infrasound Monitoring of Low Frequency Noise and Vibration from Windfarms*, Ph.D. thesis, Keele University.

Felippa, C. A. (2010), Introduction to Finite Element Methods. URL http://www.colorado.edu/engineering/cas/courses.d/IFEM.d/.

Fiori, I., Giordano, L., Hild, S., Losurdo, G., Marchetti, E., Mayer, G. & Paoletti, F. (2006), Study of the Seismic Disturbances Produced by the Wind Park Near GEO600 and a Prediction for the Wind Park "il Faldo" Considered for Installation Near VIRGO., Technical Report VIR-NOT-PIS-1390-317, VIRGO.

Fiori, I., Giordano, L., Hild, S., Losurdo, G., Marchetti, E., Mayer, G. & Paoletti, F. (2009), A Study of the Seismic Disturbance Produced by the Wind Park Near the Gravitational Wave Detector, *Proceedings of the Third International Meeting on Wind Turbine Noise*, Aalborg, Denmark.

Gaia-Wind Ltd (2008), *Installation Manual: Gaia-Wind 11 kW Turbine*, Gaia-Wind Ltd, 1 Ainslie Road, Hillington Park, Glasgow G52 4RU, gw-uk-18-0808 user manual edition.

Gaia-Wind Ltd (2011a). Last accessed: 16/08/2011, URL www.gaia-wind.com.

Gaia-Wind Ltd (2011b), Gaia-Wind 133-11kW Data Sheet. URL www.gaia-wind.com/index.php/download_file/159/98/.

Gerstoft, P., Sabra, K. G., Roux, P., Kuperman, W. A. & Fehler, M. C. (2006), Green's functions extraction and surface-wave tomography from microseisms in southern California, *Geophysics*, *71*(4), SI23–SI31, doi:10.1190/1.2210607.

Gubbins, D. (1990), *Seismology and Plate Tectonics*, Cambridge University Press, ISBN 0521379954.

Gubbins, D. (2006), *Time Series Analysis and Inverse Theory for Geophysicists*, Cambridge University Press, ISBN 0521525691.

Guralp (2008), Guralp Compressed Format (GCF) Specifications, Online. URL http://www.guralp.com/articles/20080313-howto-gcfreference/support.

Güralp Systems Limited (2004), The Eskdalemuir Seismic Array, Online. URL http://www.guralp.com/articles/20040400-casestudy-eskdalemuir/support.

Güralp Systems Limited (2010), CMG-6TD Digital broadband seismometer. Data Sheet.

Hansen, M. O. L. (2008), *Aerodynamics of Wind Turbines*, Earthscan, second edition, ISBN 9781844074389.

Harikrishna, P., Shanmugasundaram, J., Gomathinayagam, S. & Lakshmanan, N. (1999), Analytical and experimental studies on the gust response of a 52 m tall steel lattice tower under wind loading, *Computers & Structures*, *70*(2), 149 – 160, doi:10.1016/S0045-7949(98)00156-4.

Hendrick, N. & Hearn, S. (1999), Polarisation Analysis: What is it? Why do you need it? How do you do it?, *Exploration Geophysics*, *30*(4), 177–190, doi:10.1071/EG999177.

Hobb, P. R. N., Hallam, J. R., Forster, A., Entwisle, D. C., Jones, L. D., Cripps, A. C., Northmore, K. J., Self, S. J. & Meakin, J. L. (2002), Engineering geology of British rocks and soils - Mudstones of the Mercia Mudstone Group, Research Report RR/01/02, British Geological Survey, Keyworth, Nottingham.

Hornby, B. E. & Yu, J. (2007), Interferometric imaging of a salt flank using walkaway VSP data, *The Leading Edge*, *26*(6), 760–763, doi:10.1190/1.2748493.

Hrennikoff, A. (1941), Solutions of Problems in Elasticity by the Framework Method, *Journal of Applied Mechanics*, *A8*, 169–175.

Jackson, G. M., Mason, I. M. & Greenhalgh, S. A. (1991), Principal component transforms of triaxial recordings by singular value decomposition, *Geophysics*, *56*(4), 528–533, doi:10.1190/1.1443068.

Jureczko, M., Pawlak, M. & Mezyk, A. (2005), Optimisation of wind turbine blades, *Journal of Materials Processing Technology*, *167*(2-3), 463 – 471, doi:10.1016/j.jmatprotec.2005.06.055. 2005 International Forum on the Advances in Materials Processing Technology.

Lacalle, R., Cicero, S., Álvarez, J. A., Cicero, R. & Madrazo, V. (2011), On the analysis of the causes of cracking in a wind tower, *Engineering Failure Analysis*, *In Press*, doi:10.1016/j.engfailanal. 2011.02.012.

Lavassas, I., Nikolaidis, G., Zervas, P., Efthimiou, E., Doudoumis, I. N. & Baniotopoulos, C. C. (2003), Analysis and design of the prototype of a steel 1-MW wind turbine tower, *Engineering Structures*, *25*(8), 1097–1106, doi:10.1016/S0141-0296(03)00059-2.

Legerton, M. L., Manley, D. M. J. P., Sargent, J. W., Snow, D. J. & Styles, P. (1996), Low Frequency Noise and Vibration Levels At A Modern Wind Farm, *Proceedings of Inter-Noise 96*, Liverpool.

LIGO (2010), LIGO Hanford Observatory, Online. URL http://www.ligo-wa.caltech.edu/welcome.html.

Lobitz, D. W. (1981), Dynamic Analysis of Darrieus Vertical Axis Wind Turbine Rotors, Technical Report SAND80-2820, Sandia National Laboratories, Albuquerque, NM, USA.

Madariaga, R. (2007), Seismic Source Theory, G. Schubert (editor), *Earthquake Seismology*, volume 4 of *Treatise in Geophysics*, chapter 4.02, pp. 59–82, Elsevier, ISBN 9780444519283.

Manley, D. M. J. P. & Styles, P. (1995), Infrasound Generated By Large Sources, *In Proceeding of the Institute of Acoustics*.

Manwell, J., McGowan, J. & Rogers, A. (2002), *Wind Energy Explained: Theory, Design and Application*, John Wiley & Sons Ltd, ISBN 0470846127.

Marmo, B. & Buckingham, M. P. (2011), Wind direction and ground vibration II, Technical report, Xi Engineering Consultants.

Marmo, B. A. & Carruthers, B. J. (2010), Modelling and Analysis of Acoustic Emissons and Structural Vibration in a Wind Turbine, *Comsol Conference 2010*, Paris, France.

MathWorks (2010a), *Mode*, The MathWorks, Inc. URL http://www.mathworks.com/help/releases/R2010a/techdoc/ref/mode.html.

MathWorks (2010b), *Pwelch*, The MathWorks, Inc. URL http://www.mathworks.com/help/releases/R2010a/toolbox/signal/pwelch.html.

MathWorks (2010c), *svds*, The MathWorks, Inc. URL http://www.mathworks.co.uk/help/releases/R2010a/techdoc/ref/svds.html.

MathWorks (2010d), *Trapz*, The MathWorks, Inc. URL http://www.mathworks.com/help/releases/R2010a/techdoc/ref/trapz.html.

MathWorks (2011), *Linear Regression*, The MathWorks, Inc. URL http://www.mathworks.co.uk/help/techdoc/data_analysis/f1-5937.html.

Matthews, M. C., Hope, V. S. & Clayton, C. R. I. (1997), The Geotechnical Value of Ground Stiffness Determined Using Seismic Methods, D. M. McCann, M. Eddleston, P. J. Fenning & G. M. Reeves (editors), *Modern Geophysics in Engineering Geology*, volume 12 of *Geological Society Engineering Geology Special Publications*, pp. 113–123, Geological Society of London, doi:10.1144/GSL.ENG.1997.012.01.10.

Mavko, G. (2005), Conceptual Overview of Rock and Fluid Factors that Impact Seismic Velocity and Impedance, Lecture Series. Last accessed:28/01/2012, URL http://pangea.stanford.edu/courses/gp262/Notes/8.SeismicVelocity.pdf.

McHenry, D. (1943), A Lattice Analogy for the Solution of Plane Stress Problems, *Journal of the Institution of Civil Engineers*, *21*, 59–82.

Murtagh, P. J., Basu, B. & Broderick, B. M. (2004), Simple models for natural frequencies and mode shapes of towers supporting utilities, *Computers and Structures*, *82*(20-21), 1745–1750, doi:10.1016/j.compstruc.2004.04.005.

Nguyen, D. T., Brown, R. J. & Lawton, D. C. (1989), Polarization filter for multi-component seismic data, Research report, Consortium for Research in Elastic Wave Exploration Seismology.

Nixon, N. (2008), Timeline: The history of wind power, The Guardian. Last accessed 9/3/2012, URL http://www.guardian.co.uk/environment/2008/oct/17/wind-power-renewable-energy.

Oden, J. T. (1981), *Finite Elements*, volume 1, Prentice-Hall, ISBN 0133170578.

Paquette, J., Laird, D., Griffith, D. T. & Rip, L. (2006), Modeling and Testing of 9m Research Blades, *44th AIAA Aerospace Sciences Meeting and Exhibition*, Reno, Nevada, USA.

Pickering, M. (1986), *An Introduction to Fast Fourier Transform Methods for Partial Differential Equations, with Applications*, Applied and Engineering Mathematics Series, Research Studies Press, ISBN 0863800459.

Proven Energy (2010), Proven 35-2 Planning Support Document, Online. URL hwww.provenenergy.co.uk/index.php/download_file/view/484/.

Ragheb, M. (2012), Wind Shear, Roughness Classes and Turbine Energy Production. University of Illinois.

Rayleigh, L. (1887), On Waves Propagated along the Plane Surface of an Elastic Solid, *Proceeding of the London Mathematical Society*, *s1-17*(1), 4–11.

RenewableUK (2011a), Small Wind Systems: UK Market Report. April 2011.

RenewableUK (2011b), State of the Industry Report. October 2011.

Rushforth, I. M., Styles, P., Toon, S., Manley, D. M. J. P. & Bryan-Jones, A. (1997), Seismic Investigations of Low-Frequency Vibrations Generated by Wind Turbines, Poster Presentation. U.K. Geophysical Assembly, Southampton.

Saccorotti, G., Piccinini, D., Cauchie, L. & Fiori, I. (2011), Seismic Noise by Wind Farms: A Case Study from the Virgo Gravitational Wave Observatory, Italy, *Bulletin of the Seismological Society of America*, *101*(2), 568–578, doi:10.1785/0120100203.

Savory, E., Parke, G. A. R., Zeinoddini, M., Toy, N. & Disney, P. (2001), Modelling of tornado and microburst-induced wind loading and failure of a lattice transmission tower, *Engineering Structures*, *23*(4), 365 – 375, doi:10.1016/S0141-0296(00)00045-6.

Scherbaum, F. (1994), *Basic Concepts in Digital Signal Processing for Seismologists*, number 53 in Lecture Notes in Earth Sciences, Springer-Verlag, ISBN 3540579737.

Schofield, R. (2002), Seismic Measurements at the Stateline Wind Project - And a Prediction of the Seismic Signal that the Proposed Maiden Wind Project Would Produce at LIGO, Technical Report T020104-00-Z, LIGO.

Schuster, A. (1898), On The Investigation Of Hidden Periodicities With Application To A Supposed 26 Day Period Of Meteorological Phenomena, *Terrestrial Magnetism*, *3*(1), 13–41, doi:10.1029/TM003i001p00013.

Scottish Natural Heritage (2011), Scotland Scottish Windfarm Proposals, ESRI Shapefile. Last accessed: 07/03/2012, URL http://www.snh.gov.uk/publications-data-and-research/snhi-information-service/naturalspaces/.

Scottish Renewables (2012), Submission of written evidence to inquiry into the Scottish Governments renewable energy targets, Online. URL http://www.scottishrenewables.com/news/scotland-track-hit-2011-renewables-target/.

Shapiro, N. M., Campillo, M., Stehly, L. & Ritzwoller, M. H. (2005), High-Resolution Surface-Wave Tomography from Ambient Seismic Noise, *Science*, *307*(5715), 1615–1618, doi:10.1126/science.1108339.

Shaw, G. & Wheeler, D. (1994), *Statistical Techniques in Geographical Analysis*, David Fulton Publishers, ISBN 1853462292.

Shearer, P. (1999), *Introduction to Seimology*, Cambridge University Press, ISBN 0521669537.

Siemens (2009), Outstanding efficiency: Siemens Wind Turbine SWT-2.3-93. Last accessed 9/3/2012, URL http://www.energy.siemens.com/mx/pool/hq/power-generation/wind-power/E50001-W310-A102-V6-4A00_WS_SWT-2.3-93_US.pdf.

Snieder, R. & Safak, E. (2006), Extracting the Building Response Using Seismic Interferometry: Theory and Application to the Millikan Library in Pasadena, California, *Bulletin of the Seismological Society of America*, *96*(2), 586–598, doi:10.1785/0120050109.

Snow, D. (1997), Low Frequency Noise and Vibration Measurements at a Modern Wind Farm. ETSU W/13/00392/REP.

Stein, S. & Wysession, M. (2002), *An Introduction to Seismology, Earthquakes, and Earth Structure*, Wiley-Blackwell, ISBN 978-0-86542-078-6.

Stoica, P. & Moses, L., Randolph (1997), *Introduction to Spectral Analysis*, Prentice Hall, ISBN 0132584190.

Styles, P. (1996), Low Frequency Wind Turbine Noise and Vibration: Microseismic Investigations. Contract Number 503922: ETSU/Powergen.

Styles, P., Stimpson, I., Toon, S., England, R. & Wright, M. (2005), Microseismic and Infrasound Monitoring of Low Frequency Noise and Vibrations from Windfarms: Recommendations on the Siting of Windfarms in the Vicinity of Eskdalemuir, Scotland, Technical report, Applied and Environmental Geophysics Research Group, Keele University.

Sutherland, H. J. (1999), On the Fatigue Analysis of Wind Turbines, Technical Report SAND99-0089, Sandia National Laboratories, Albuquerque, New Mexico 87185-0708.

Trodd, H. (1998), Variation in Amplitude of Seismic Noise at Eskdalemuir Array, AWE Internal Technical Note /97/DFS/AG/391 HT052.

Truscott, J. R. (1964), The Eskdalemuir Seismological Station, *Geophysical Journal of the Royal Astronomical Society*, *9*(1), 59–68, doi:10.1111/j.1365-246X.1964.tb06314.x.

Udías, A. (2000), *Principles of Seismology*, Cambridge University Press, ISBN 9780521624787.

Uysa, P. E., Farkasb, J., Jármaib, K. & van Tondera, F. (2007), Optimisation of a steel tower for a wind turbine structure, *Engineering Structures*, *29*, 1337–1342, doi:10.1016/j.engstruct.2006.08.011.

Vidale, J. E. (1986), Complex polarization analysis of particle motion, *Bulletin of the Seismological Society of America*, *76*(5), 1393–1405.

Welch, P. D. (1967), The Use of Fast Fourier Transform for the Estimation of Power Spectra: A Method Based on Time-Averaging Over Short, Modified Periodograms, *IEEE Transactions on Audio and Electroacoustics*, *15*(2), 70–73, doi:10.1109/TAU.1967.1161901.

Westwood, R., Styles, P. & Toon, S. (2011), Monitoring and Modelling the Vibrational Effects of Small (< 50 kW) Wind Turbines on the Eskdalemuir IMS Station, *Fourth International Meeting on Wind Turbine Noise*.

Willis, M. E., Lu, R., Campman, X., Toksoz, M. N., Zhang, Y. & de Hoop, M. V. (2006), A novel application of time-reversed acoustics: Salt-dome flank imaging using walkaway VSP surveys, *Geophysics*, *71*(2), A7–A11, doi:10.1190/1.2187711.

Wilson, S. A. (1994), *A Study of Microseismicity and Attenuation in Unstable Soil Selopes*, Ph.D. thesis, University College of Swansea.

Wind Energy Facts (2009), Brief History of Wind Energy, Online. Last accessed: 9/3/2012, URL http://windenergyfacts.eu/brief-history-of-wind-energy.html.

Wood, D. (2011), *Small Wind Turbines: Analysis Design and Application*, Springer-Verlag London Limited, ISBN 9781849961745, doi:10.1007/978-1-84996-175-2.

Zhang, L. (2000), Ground Vibration at the Site of ESRF and Comparison With Some Other Places, *22nd Advanced ICFA Beam Dynamics Workshop on Ground Motion in Future Acelerators*, Stanford.

Zhang, L. & Lesourd, M. (2005), Vibration and Stability Issues at ESRF, *Workshop on Ambient Ground Motion and Civil Engineering for Low Emittance Electron Storage Ring*, Hsinchu, Taiwan.

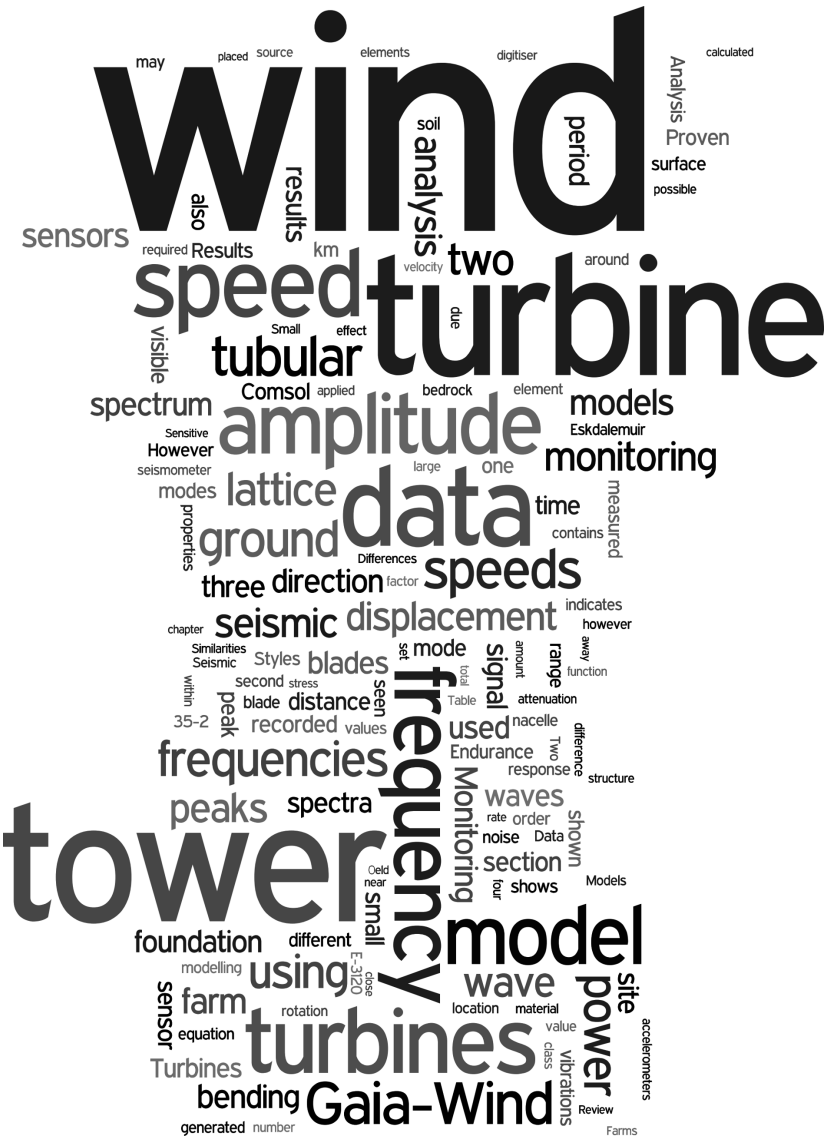
wind
turbine
speed
tower
frequency
model
turbines
data
amplitude
tubular
Comsol
spectrum
lattice
ground
displacement
seismic
blades
frequencies
peaks
spectra
foundation
using
farm
sensor
Turbines
bending
Gaia-Wind
wave
power
site
vibrations
accelerometers
Monitoring
waves
section
shows
Models
Data
noise
order
rate
shown
Endurance
response
structure
used
nacelle
attenuation
signal
range
distance
recorded
peak
blade
blades
Styles
Seismic
Similarities
mode
speeds
direction
three
time
measured
contains
monitoring
models
Eskdalemuir
However
Sensitive
seismometer
modes
properties
Differences
factor
chapter
however
indicates
function
away
amount
set
total
Table
seen
within
35-2
values
second
stress
Two
difference
four
near
Oeld
small
different
modelling
close
E-3120
location
material
value
class
rotation
equation
generated
number
Review
Farms
sensors
required
Results
km
velocity
around
two
analysis
results
also
soil
period
Proven
surface
possible
Analysis
calculated
digitiser
elements
source
placed
may
visible
Small
effect
due
applied
bedrock
element
large
one
Table